DEVELOPMENT OF PROTEIN NANOPARTICLE BASED COMPOSITE MATERIALS

by

Janice Elizabeth Lucon

A dissertation submitted in partial fulfillment
of the requirements for the degree

of

Doctor of Philosophy

in

Chemistry

MONTANA STATE UNIVERSITY
Bozeman, Montana

January 2013

©COPYRIGHT

by

Janice Elizabeth Lucon

2013

All Rights Reserved

APPROVAL

of a dissertation submitted by

Janice Elizabeth Lucon

This dissertation has been read by each member of the dissertation committee and has been found to be satisfactory regarding content, English usage, format, citation, bibliographic style, and consistency and is ready for submission to The Graduate School.

Dr. Trevor Douglas

Approved for the Department Chemistry and Biochemistry

Dr. Mary Cloninger

Approved for The Graduate School

Dr. Ronald W. Larsen

STATEMENT OF PERMISSION TO USE

In presenting this dissertation in partial fulfillment of the requirements for a doctoral degree at Montana State University, I agree that the Library shall make it available to borrowers under rules of the Library. I further agree that copying of this dissertation is allowable only for scholarly purposes, consistent with "fair use" as prescribed in the U.S. Copyright Law. Requests for extensive copying or reproduction of this dissertation should be referred to ProQuest Information and Learning, 300 North Zeeb Road, Ann Arbor, Michigan 48106, to whom I have granted "the exclusive right to reproduce and distribute my dissertation in and from microform along with the non-exclusive right to reproduce and distribute my abstract in any format in whole or in part."

Janice Elizabeth Lucon

January, 2013

ACKNOWLEDGEMENTS

I would like to thank some of the many people who from the begininning of this work have been instrumental in its final success. Without the continual guidance, support, and training from Trevor Douglas this work would never have come to fruition. The assistance and camaraderie of all the Douglas group members over the years have made this a joyous labor. In particular, through discussions and joint project efforts Masaki Uchida and Sebyung Kang have significantly contributed to my development. Additionally, the interesting and challenging variety of projects fostered by the Douglas group made it a pleasure to contribute to the group efforts.

Before joining the Douglas group, the recruitment efforts of Stephanie Cunningham and the Molecular Biosciences Program brought me to Montana State University and without their financial support, it would not have been as possible to start and finish strong. Generous funding from the NSF Graduate Fellowship Program and the Douglas group made it so greater project risks and subject flexibility could be investigated resulting in the variety of publications contained here.

Without the support of my family, who has always made education a priority, this work would not have been completed. Peter, especially, was and always is a constant source of encouragement, who through all the miles maintained our life in Butte, so I could focus on this endeavor.

Finally, I would like to dedicate this to Helen, for you are a precious living example of a bottom-up composite.

TABLE OF CONTENTS - CONTINUED

TABLE OF CONTENTS

TABLE OF CONTENTS - CONTINUED

TABLE OF CONTENTS - CONTINUED

LIST OF FIGURES

LIST OF FIGURES - CONTINUED

Figure Page

LIST OF FIGURES - CONTINUED

LIST OF FIGURES - CONTINUED

Figure Page

LIST OF FIGURES - CONTINUED

Figure Page

LIST OF FIGURES - CONTINUED

Figure Page

LIST OF FIGURES - CONTINUED

Figure Page

ABSTRACT

Inspired by the core-shell composite structures found in nature, a range of protein based composites have been developed. These materials were made using synthetic approaches, which utilized the native protein architecture as an initiation point and size constrained reaction vessel for the piecewise formation of the second material. In the first illustration of this approach, a protein-Pt composite was formed, where the protein cage has been modified to include a metal binding moiety for improved synthesis of metallic Pt nanoclusters, which were shown to be an active H_2 catalyst. This composite was analyzed by native mass spectrometry to determine the number of Pt ions bound prior to mineralization and to measure the distribution of species after mineralization, which provided a unique view into the mineralization process. The second illustration was a material synthesized using the cage-like protein architecture as an internal guiding synthetic scaffold for the formation of a coordination polymer core inside the protein cage. The construction of this coordination polymer was unusual in that unlike normal coordination polymer synthesis, coordination of the metal preceded formation the ditopic ligands, which were afterwards completed using azide-alkyne click chemistry. Finally, a collection of protein-polymer composites were developed, which utilized a living radical polymerization method, atom transfer radical polymerization, to form internal polymer cores. By labeling one of these protein-polymer constructs with a Gd based MRI contrast agent a material with vastly improved relaxivity was made. The development of each of these three types of composites served to improve our understanding of the natural systems, from which they are derived, and provide a basis for further development of advanced multicomponent nanomaterials.

CHAPTER 1

INTRODUCTION

Drawing Inspiration from Biological Composites

We are surrounded by, and composed of, composite materials both biotic and abiotic across an incredible size range. These materials are tuned and designed to the degree required for their purpose where the characteristics of the composite are controlled by the arrangement and properties of the component materials. For example chip board is a simply constructed composite of brittle resin and relatively pliant wood flakes, but the combination results in the desired strength and flexibility, at the tolerances necessary, required for building materials. In this case flaws in the material, though potentially bothersome, are rarely catastrophic. In contrast, the nacreous layer of the mollusk shell (Figure 1.1), though a similarly layered composite, of protein and aragonite, has no room for error and is composed on a much finer scale to attain the desired macroscopic material properties. Here the mineral component interpenetrates the pores formed by a protein network leading to a phase controlled laminated composite, with nanoscale control, giving the shell increased strength over non-laminated aragonite.[1,2] If the shell where flawed, resulting in a weak material, death of the mollusk would potentially occur. Because reduced viability or death may result from an imperfect material, biologic composites have developed with exquisite control, which engineers and scientist desire to better understand and mimic.

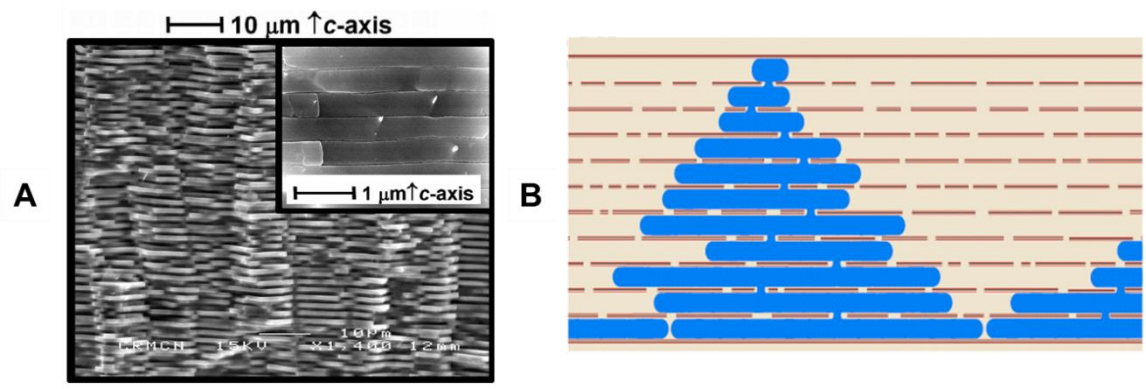

Figure 1.1: A) SEM images of a side view of the freshly fractured nacreous layer of the mollusk *Trochou niloticus*. B) Cartoon of the brick and mortar structure of this composite, which consists of the mineral component (blue) interlayered with the organic matrix (tan lines). Adapted from Bruet (2005) and Addadi(1997).[3] [4]

As more composites are used in biomedical applications, and devices become smaller, materials property control at the nanoscale, which biology does so well, becomes increasingly imperative. By establishing a fundamental understanding of the manner in which biosystems maintain spatial and morphological control, prevent modulus mismatch, impart hardness, and respond to the environment, new materials with improved tolerances can be constructed. In a recent example, by building on the principles, which cause the interpenetrated protein-calcite skeleton of the Brittlestar (Ophiocoma *wendtii*) a monocrystalline structure of calcite several millimeters square interpenetrated with photoresist features, can be formed (Figure 1.2). [5] This bioinspired controlled arraying of components opens up the possibility of making monocrystalline materials for technological applications, which are built from the bottom-up rather than being ground down to size from larger materials.

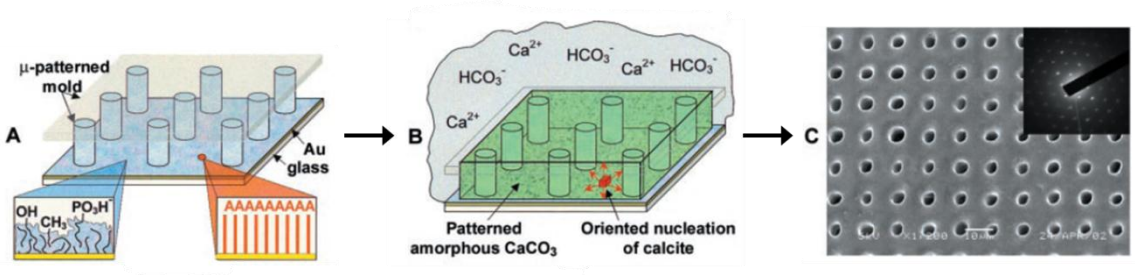

Figure 1.2: Bioinspired formation of monocrystalline calcite. A) The reaction platform consisted of micropatterned photoresist posts covered in gold and subsequently coated with polymer (blue), which inhibits crystal formation. A single polymer region (red), which induces crystallization, was added to the slide via AFM. B) Incubation of the surface with amorphous calcium carbonate resulted in crystal growth initiated only at the engineered nucleation site (red dot). C) A SEM of the resulting crystal. The inset is a TEM diffraction, which shows that the material is a single crystal over the ~50 μm^2 sampled area. Adapted from Aizenberg (2003).[5]

Biological Encapsulation

In addition to interpenetrated structures, another common biological composite arrangement is the formation of spatially controlled core-shell like structures. In some instances this compartmentalization of the composite components is essential for the resulting material property or for protection of the cell (itself a type of compartmentalized composite). For instance the complex multicomponent protein-lipid vesicles surrounding the magnetite particles found in magnetotactic bacteria, control the size, shape, and morphology of the particles, which allows these magnetic particles to be synthesized at ambient conditions and serve as nanoscopic compasses for the bacteria. A more simple form of compartmentalization occurs in systems like ferritins and some viruses, where the core material is simply surrounded and protected by just a multimeric protein shell. It is these protein cage coated structures that have provided the inspiration for a wide range of work on protein based core-shell materials.

Although both ferritin and viruses are essentially protein based containers, the different natures of their cargo, ferrihydrite (Fe(O)OH) or nucleic acid, determine the possible mechanisms by which the final composites can be formed. In the case of viruses, because the nucleic acid polymer must be constructed prior to packaging and is released all at once, it is packaged as the completed polymer becomes available. Depending on the type of virus two basic means of packaging are employed. In the most mimicked mechanism electrostatic interactions between the positively charged interior face of the protein subunits with the negatively charged nucleic acid induce controlled formation of the multimeric protein shell around the nucleic acid. It is this mechanism which drives the formation of the 180 subunit widely studied RNA containing plant virus Cowpea chloric mottle virus (CCMV). In the second mechanism, found in phages like P22 bacteriophage, a protein motor located at one of the vertices of the completed protein shell threads in the nucleic acid in an energy intensive ATP driven process. Due to the specificity and energy required this method is not currently mimicked for engineered composites. In contrast ferritin protein surrounds a nanoscopic ferrihydrite core. This protein shell serves to sequester and perhaps provide a molecular controlled release of iron in both eukaryotes and prokaryotes. Thus it is essential for protein functionality that the iron be added and released from the internal protein-mineral composite in a piecewise manner. In most ferritins iron enters through a pore in the cage at the 3-fold axis and is subsequently oxidized to build up a ferrihydrite core within the ferritin cage with subsequent reduction allowing release of the stored iron from the mineral core. Together,

both of these systems provide inspiration for the use of protein cages for materials exploration and design.

Bioinspired Encapsulation

Protein cages have been used as a model system for understanding biomineralization processes. They provide an unparalleled view of these processes and are useful for the development of improvements and expansion of the range of protein-material composites for materials applications and to gain insight into the biological processes. Much of the previous work has been tied to understanding how bioprocesses work including the forces and factors at play and the steps or order in which the composite is built. These protein based shell structures provide a superior system for study of compartmentalized materials, compared to their lipid based counterparts such as vesicles, due to lower particle-to-particle variability. These cage-like protein assemblies, of which virus-like particles (VLPs) are a class, are small enough for many types of solution phase molecular analysis and yet are large enough to be readily isolated from solution. But, spatial control in proteins with subunits arranged into cage-like architectures provide special challenges as the protein shell defines an interior space, subunit interface, and exterior surface all of which can be modified. The interface interaction can be modified to strengthen or weaken the subunit interactions, and thereby the cage stability, and to alter the final cage morphology. The exterior surface can be modified to make unique core-shell structures and to display molecules for cell signaling. But it is the interior space that really sets this class of proteins apart from other multimeric protein assemblies.

Synthetic, encapsulated, protein-composites have been made either by building the protein around or actively packaging a preformed cargo molecule as observed in viruses or alternatively by assembly of the cargo material piece-wise within the protein architecture, as observed in ferritins. In the former method the protein cage is often disassembled into subunits or dimers or made porous by a trigger such as a pH or salt content change and then the cage is reassembled in the presence of the cargo by a return to cage conformation favoring solution conditions. In the piece-wise method the protein cage structure is rigorously maintained during composite synthesis, so that the growing core material cannot develop beyond the dimensions prescribed by the protein shell. In both packaging cases, often, concentration and electrostatic interactions determine whether the desired packaging is attained. Both methods have been used to make protein-metal, protein-mineral, and protein-polymer constructs, which both provide insights into the biological processes from which they are derived and also result in useful materials.

Preformed Cargo

Packaging of synthetic polymers via the virus inspired mechanism of assembly is perhaps the most intuitive use of this bioinspired pathway and is one which can provide insights into the specificity for both the type and size of polymers that can accommodate proper assembly by this pathway. The first report of packaging a synthetic polymer was described for the introduction of an anionic polymer, poly(anetholesulfonic acid), within the CCMV virus capsid. In this approach the CCMV was not completely disassembled, rather it was converted to its swollen porous form at pH 7.5 and incubated with PAS then converted to the closed (T=3) virion form via pH adjustment down to pH 4.5.[6]

Subsequently, CCMV has been used extensively for studying non-native DNA and synthetic polymer packaging. For example, rather than drive packaging of the CCMV capsid using pH, fluorescein-PEG was added to lysine residues on the exterior which destabilized the cage to form individual subunits. When polystyrene sulfonate (PSS) was added to the mixture, the capsid reformed, but this time into T=1 (18 nm) spherical particles (Figure 1.3). [7] Similarly, using oligionucleotide amphiphile constructs to make small micelles, CCMV could be template at pH 7.5 forming T=1 and T=2 sized CCMV capsids.[8] In an example of further control over the capsid morphology of the CCMV, the final structure of the CCMV coat was determined by the morphology (extended or globular) of the packaged fluorescent polyanionic semiconducting polymer MPS-PPV (poly-2-methoxy-5-propyloxy sulfonate phenylene vinlyene). This was possible because the structure of the polymer changes in the assembly solution from rods (0.0 M NaCl) to spheres (1.0 M NaCl).[9] Further work has demonstrated that not only the structure, but also the total size of the packaged polymer can have a significant effect. Using PSS of 5 different masses, ranging from 400 kDa to 3400 kDa, the size of the final CCMV particle could be controlled to be either T=2 (22nm) or the native T=3 (27 nm) size, where the smaller form was obtained when the polymer was less than 2000 kDa.[10] From these studies it is clear that electrostatics can be used to drive assembly of these protein-polymer composites and that the system is surprisingly accommodating to both size and type of non-native polymers.

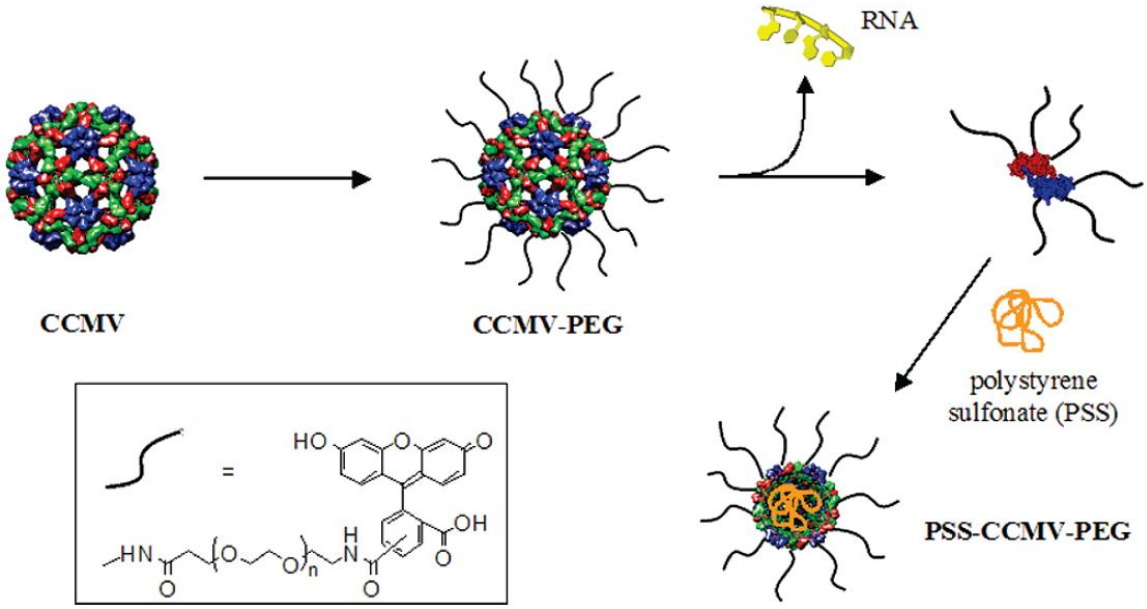

Figure 1.3: Scheme for reassembly of CCMV coat protein around the negatively charged polymer PSS. In the first steps lysines on CCMV are labeled with a fluorescein-PEG followed by removal of the native RNA, which causes the VLP cage to disassemble into dimers. Introduction of PSS in the final step causes the dimers to reassemble into a T=1 capsid.[7]

Using similar principles, cargo peptides and proteins have been selectively packaged inside protein cages demonstrating that electrostatic interactions are not the only useful interaction that can be used to drive assembly and to study the effect of packaging on the proteins and as a means to deliver active proteins. In these composites, much like the protein-nucleic acid interaction, to drive effective packaging the protein of interest is modified to provide a strong interaction with the cage coat protein (or modified coat protein). For example, if the interior surface residues of lumazine synthase are genetically modified to be negatively charged and the purified protein is combined with the positively charged GFP(+36) protein, which has additional positive residues on its surface compared to standard GFP, then about 74 GFP are sequestered inside the 36 nm diameter lumazine synthase cage. [11] An alternative interaction was used to package GFP

in CCMV, rather than rely on electrostatics, a coil-coil motif peptide was genetically engineered onto the N-termini of the CCMV coat and the guest protein. Each protein was individually expressed and purified and the CCMV coat was disassembled (pH 7.5) and reassembled (pH 5.0) in the presence of the GFP-coil protein yielding a packaging of 15 GFP per 28 nm capsid.[12] Yet another, different, strong interaction was used to package GFP and enzymes in Qβ capsids. Using a RNA aptamer bridge with one end consisting of the Qβ packaging sequence, which has a strong affinity for the interior of the coat protein, and the other end with an affinity for the genetically engineered N-termini of the guest protein, these interactions resulted in the encapsidation of 10-11 GFP per 28 nm Qβ particle.[13,14] More recently fluorescent proteins, enzymes, and peptides have been packaged inside the P22 phage derived VLP. This packaging method takes advantage of the native coat-scaffold protein interaction, allowing the protein or peptide of interest to be expressed and encapsidated in vivo (Figure 1.4), unlike the methods previously described, which are all constructed exclusively in vitro. [15-18] When comparing the amount of GFP packaged to other similar approaches, this method leads to highest packaging (150 GFP or per 58 nm cage). Each of these studies has led to insights into the effect individual cargo size and shell-cargo interactions have upon the final compartmentalized structure and the ability of these systems for directed assembly and encapsulation.

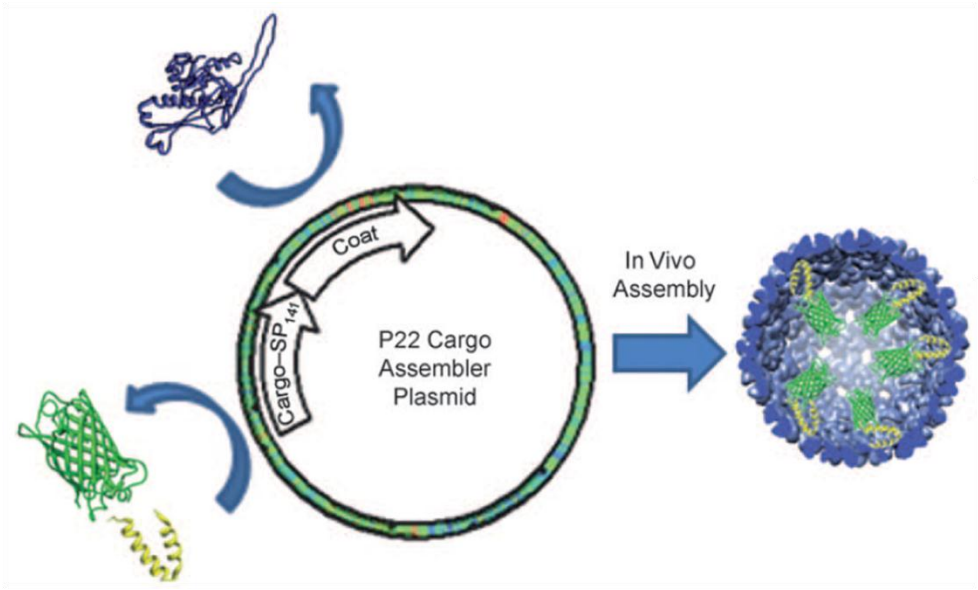

Figure 1.4: Schematic representation of the encapsulation of the GFP by heterologous co-expression of scaffold protein (yellow) and GFP (green) fusions with P22 coat protein (blue). Adapted from O'Neil (2011).[15]

Stepping into the hard material realm, the ability to build protein cages around existing metal nanospheres has proven particularly useful for the study of the driving principles that determine virus symmetry and overall size. This work has largely been advanced by the Dragnea group with the study of the assembly of brome mosaic virus (BMV) coat protein around peg-coated gold nanospheres. In this system, the BMV is dissociated and reassembled around the metal core in a pH driven process much like the polymer encapsulation methods (Figure 1.5). [19] Small changes in the encapsulation conditions for the formation of BMV around 12 nm carboxylated peg Au nanospheres, results in two mechanisms, which can be followed using intrinsic fluorescence quenching of the metal center. These two regimes (cooperative or non-cooperative) adsorption observed give insight into the types of condition specific pathways by which some

viruses may assemble. [20] This process is not limited to just Au nanospheres, but also CdSe and ZnS quantum dots coated in the same manner can be encapsidated with BMV coat proteins to make core-shell structures.[21] Although this method is rarely used for making protein-mineral composites, there are a few instances of other protein cages being constructed around preformed mineral particles. Electrostatic driven assembly around a core is not limited to virus based proteins as citrate capped Au spheres can also be encapsulated inside ferritin by low salt driven disassembly of the ferritin cage followed by introduction of the Au nanospheres.[22] Recently maghemite particles were synthesized using coprecipitation of iron salts in aqueous conditions to preform a colloid solution of nanoparticles 4-6 nm in diameter. Subsequently horse spleen ferritin at pH 2 (disassembled) was added and the pH was titrated up to pH 7 (assembled) leading to the encapsulation of the preformed maghemite nanoparticles into about 75% of the assembled cages. [23] In a similar manner PbS quantum dots have been trapped inside ferritin using pH driven disassembly (pH 2) and reassembly (pH 9.5) of the ferritin in the presence of PbS quantum dots. [24] These studies together further demonstrate the flexibility of the electrostatic driven assembly of protein based core-shell structures and in the carefully designed experiments serve to quantify the forces involved in assembly.

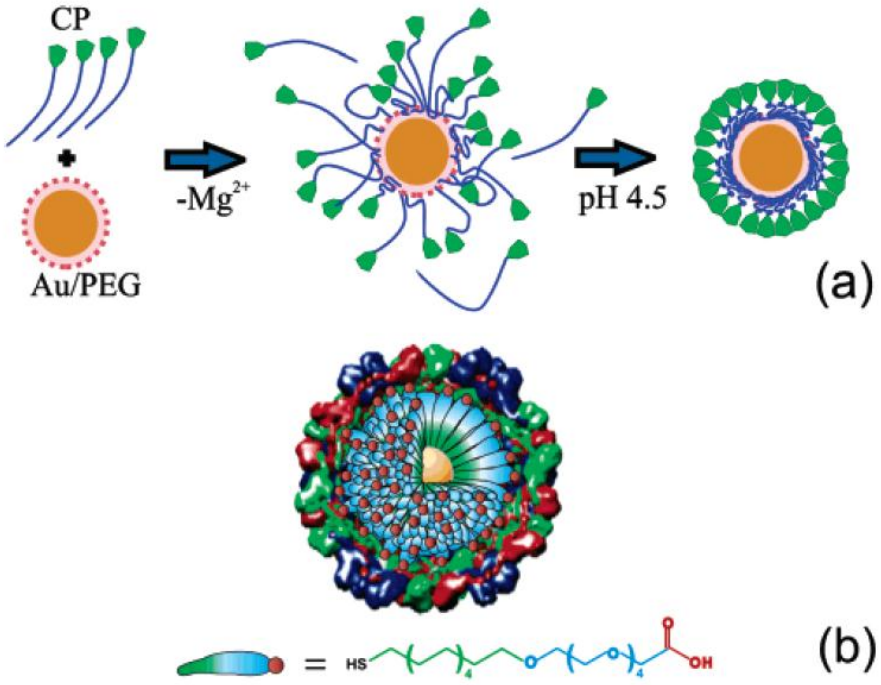

Figure 1.5: A) Proposed mechanism of VLP assembly (CP capsid protein). First, electrostatic interaction leads to the formation of disordered protein-Au nanoparticle complexes. The second step is a crystallization phase in which the protein-protein interactions lead to the formation of a regular capsid. B) Schematic depiction of the encapsidated nanoparticle functionalized with carboxylterminated TEG chains.[19]

Piecewise Cargo

Taking inspiration from the ferritin ferrihydrite mineralization mechanism, a wide range of minerals have been synthesized not only in ferritin, but also in other protein cages, which serve to inform the native mineralization process and drive the development of new spatially controlled composites. Each synthetic procedure used to make these materials relies largely on electrostatic interaction of the precursor molecule with the protein interior, which is then nucleated and mineralized inside the protein sphere at a rate greater than the exterior process. These minerals include Fe_3O_4, Co_3O_4, Mn_3O_4, Mn(O)OH, Co(O)OH, $Cr(OH)_3$, $Ni(OH)_3$, In_2O_3, FeS, CdS, CdSe, ZnSe, $CaCO_3$, $SrCO_3$,

$BaCO_3$,TiO_2, tungstates, molybdates, and vanadates.[25] The range of materials speaks to the robust nature of electrostatic interactions essential to this mineralization route, but the careful selection of the nanoreactor protein cage can be instrumental to successful spatial control or formation of the desired mineral phase. For example to obtain the necessary electrostatic driven interactions the negatively charged tungstate, molybdate, and vanadate precursors demand a positively charged protein cage interior like that found in the CCMV plant virus. [6] Other minerals require special conditions such as the formation of hematite (α-Fe_2O_3) from ferrihydrite cores in ferritin which involves prolonged treatment at 97 ºC to elicit the conversion, thus formation of this mineral requires a theromostable ferritin such as *Pyrococcus furiosis* ferritin.[26] From these studies the importance of interactions between the interior of the protein and the mineral precursors for successful spatially controlled mineralization has become abundantly clear.

Using mineralization related methods, metal cores have been grown within protein cages for structural, catalytic, magnetic, and electron transmission applications. In initial studies Pd, Ag, and CoPt cores were formed inside ferritin nanoreactors. [27-29] The Pd cores formed in ferritin (Figure 1.6) were catalytic for olefin hydrogenation and the successful formation of the Pd core has inspired subsequent metal binding studies using x-ray crystallography to determine the binding locations for precursor metal ions in this protein. [27,30] Much like with mineralization, reaction conditions can be used to modify the composite structure. If both Au and Pd are used, depending on the order of metal introduction and reduction, either an alloy of the two metals or a Au core-Pd shell particle can be synthesized inside the ferritin.[31] Although some mineralization processes are

extremely robust others require extensive optimization of reaction conditions. For instance, only one particular synthetic route where Pt and the reducing agent (DMAB) are added concurrently in a rapidly stirred reaction solution warmed to 65º C results in Pt nanospheres formed in the small heatshock protein cage (sHsp). This specific synthesis proved worthwhile as the resulting composite showed an improvement in catalytic activity compared to Pt particles synthesized via traditional methods.[32] Other metal cores could not be made simply through condition manipulation and instead genetic engineering of the protein was required. In one example, genetically engineering a peptide to the N-terminus of sHsp specific to the L_{10} phase (magnetic phase) of CoPt allowed ferromagnetic nanospheres to be synthesized. When the native protein was used, CoPt nanospheres still formed, but were not of the proper phase for room temperature hysteresis to be observed.[33] One advantage of using a non-spherical protein cage is that methods to obtain longitudinal control can be explored. Taking advantage of the anisotropy of tobacco mosaic virus (TMV), reduction of Ni and Co ions doped into the virus lead to protein encapsulated nanowires of about 3 nm in diameter and over 100 nm in length.[34] In comparison, using photoreduction Ag nanoparticle clusters rather than nanowires could be formed in a similar manner inside TMV. [35] Together each of these new application driven protein-metal combinations has helped lead to new means to control compartmentalization of the metal core.

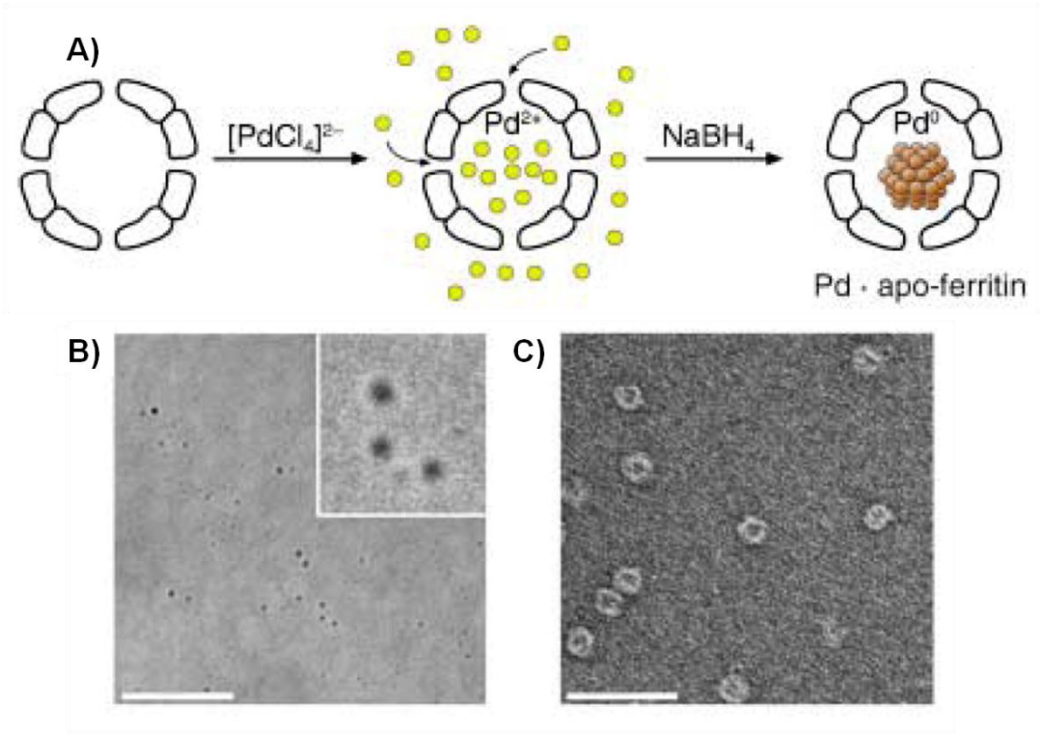

Figure 1.6: Synthesis of Pd inside ferritin A) Reaction scheme for formation of Pd nanoparticles inside ferritin. B) Unstained TEM image of the material in vitreous ice showing the presence of electron dense particles. C) Uranyl acetate negatively stained TEM image of the material demonstrating that the protein shell is still present. Both scale bars are 50 nm. Adapted from Ueno (2004).[27]

Unlike mineral synthesis, the piecewise formation of organic polymers inside protein cages has not been as widely investigated. Only two basic examples have been described for interior piecewise construction of polymers and each relies on the specificity of the polymerization reactions to control the location of the finished polymer core. In the first instance, using L-chain horse liver ferritin with a Rh-norbornadiene catalyst attached to any of three locations on the interior of the ferritin through cysteine or histidine residue interactions, the selective polymerization of phenylacetylene to form poly(phenylacetylene) has been described (Figure 1.7). It is the dependency on the Rh

catalyst, which allows this reaction to be confined to the interior of the protein as the synthesized polymer is not attached to the protein and can therefore be subsequently released by disassembly of the ferritin at pH 2.[36] In the other method a covalently attached polymer was made using azide-alkyne click chemistry to construct a polymer in a stepwise manner inside sHsp and was afterwards modified with Gd-chelates to make an improved MRI contrast agent.[37,38] The fidelity of the click chemistry reaction ensures that this generational polymer only grows from the interior located initiation site limiting the polymer growth to the interior of the protein. Together these initial studies provide inspiration for pursuing new materials requiring specific reaction stimuli which can be compartmentalized inside the protein prior to core material formation.

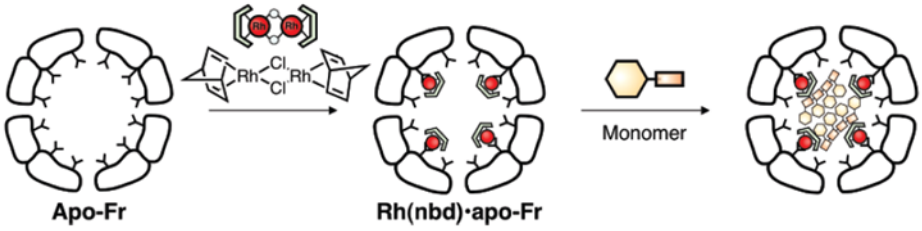

Figure 1.7: Schematic of Rh-norbornadiene binding to ferritin and the subsequent polymerization of phenylacetylene. [36]

Research Directions

Inspired by piecewise method found in ferritins for forming interior protein composite materials, new techniques have been employed here to expand the range of synthesized protein-composite materials with medical and energy applications. In Chapter 3 Pt metallic core mineralization has been expanded to be formed inside the

LiDps protein requiring modification to the interior for success. This construct was subsequently analyzed by techniques (including native mass spectrometry) that are not well suited for free nanoparticles or other protein cages, giving new insight into the mineralization process. In Chapter 4 a metal organic polymer (MOP) was formed, with spatial control, within a protein cage (sHsp) in the first report of an internal protein-MOP composite. Protein-polymer composites were made in Chapters 5, 6, and 7 providing a new means to make piecewise-synthesized interior-confined polymers within protein cages. This method has the potential to be used for a wide variety of applications including the formation of improved MRI contrast agents as described in Chapter 6.

CHAPTER 2

FUNDAMENTALS

The composite materials described in the following chapters were made using a fundamental synthetic method and one of three proteins as a scaffold for modification. General information on each of these proteins and synthetic techniques are included here to provide additional background to that was not included in each respective chapter.

Proteins

The protein cage provides the initiation point and acts as a container for piecewise made protein composite materials. Of the many potential protein cages currently used in materials synthesis only three have been used in this work. Each of these had been used previously for materials synthesis and was selected for specific characteristics that made them particularly suited for the materials described here. The proteins chosen include the 'tiny' LiDps, the 'holey' sHsp, and the relatively 'large' P22 phage derived VLP.

Listeria Dps (LiDps)

The Dps (DNA binding protein from starved cells) originated from the Gram-positive bacterium Listeria innocua where it prevents oxidative damage to DNA by accumulating iron atoms within its central cavity to produce an iron oxide core similar to that of ferritins.[39,40] The assembled LiDps consists of 12 identical 18 kDa subunits that self-assemble into a hollow protein cage having tetrahedral 23 symmetry (Figure 2.1).[39] Due to fewer subunits, LiDps is consequently smaller than ferritin with an outer diameter

of 9 nm and an inner cavity diameter of 5 nm with 0.8 nm pores at the three fold axis where molecules can pass through to the interior.[39]

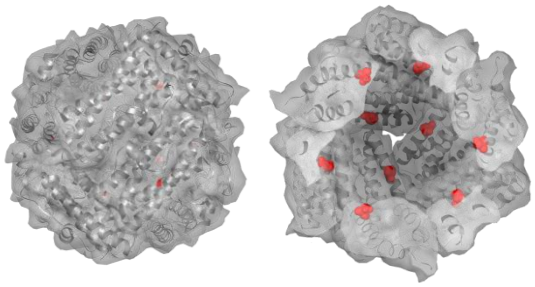

Figure 2.1: Assembled LiDps protein cage viewed from the exterior (left) and as a half-shell cut-away (right), which reveals the available interior space. The red dots are the location of the S138C mutation. PDB ID 1QGH.

The small size and ferritin-like structure of LiDps has made it a target for surface modification and for mineralizing metal oxides less than 5 nm in diameter. LiDps was first utilized as a reaction vessel for the formation of maghemite (γ-Fe_2O_3) nanoparticles with a loading of 400 Fe/cage.[41,42] This initial work was later repeated over a range of loadings (24-400 Fe/cage) and monitored via mass spectrometry to better understand the mineralization process revealing that there is a binding to the ferroxidase centers and ion accumulation phase followed by a growth phase.[43] Using LiDps as a shell, crystalline cobalt oxide (Co_3O_4) and amorphous heterogenite (Co(O)OH) can be formed inside with phase control attained by modulating the reaction temperature.[44] The crystalline Co_3O_4 particles were further characterized revealing that the small particle size has an effect on the properties of this antiferromagnetic material as compared to bulk and other small particle examples.[45] In another example, using pH control CdS quantum dots were formed inside LiDps with observed photoluminescence indicating that the cubic CdS

phase had been formed and these could be made into a hexagonal close-packed monolayer.[46,47] In addition to mineralization, LiDps is also stable to significant surface modification. For example the attachment of the photosensitizer (SnCe6, tin^{IV} chlorin e6) to lysines on the protein did not distrupt the protein architecture.[48] Together these studies demonstrate that LiDps has the necessary surface charges and stability to make it a good protein cage for selective interior directed mineralization.

One of the more unique characteristics of this protein is that it has an unusually good resolution when analyzed by native mass spectrometry, which allows for the mass of the whole protein cage to be measured. While our work in Chapter 4 was the first to exploit this property, a similar data analysis method was essential to the development of the model of maghemite formation described above.[43] Native mass spectrometry has also been exploited for the analysis of a LiDps Janus construct to verify the number of subunits in each cage modified with a biotin tag.[49] A more in depth analysis was employed to demonstrate that a LiDps chimera, made from two different labeled LiDps mutants (Figure 2.2), form cages with a composition proportional to the ratio of the mutants in the assembly solution.[50] The outstanding resolution that can be attained with this protein, including the small changes in mass from addition of metal atoms or small labels allows these difference to be observed as necessary for these applications.

Together the clean native mass spectrometry signal, small total molecular weight, and proven ability to mineralize materials, made this ‘tiny’ protein cage particularly suited for our study of Pt nanoparticle formation monitored by mass spectrometry in Chapter 4.

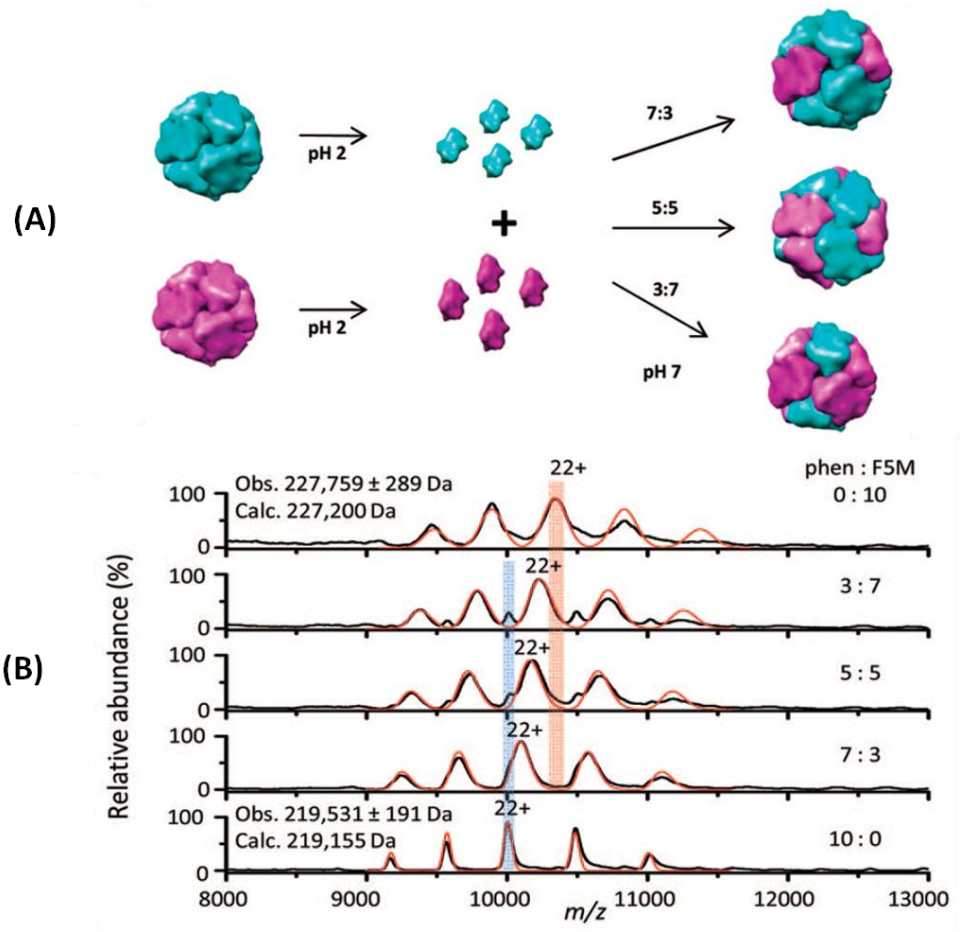

Figure 2.2: A) Chimeric cage construction scheme where the subunits are either LiDps-S138C-phen (18.30 kDa) or LiDps-KLFC-F5M (18.97 kDa). B) Mass spectra of reassembled whole cages where the charged peaks of the cages are marked by blue (LiDps-phen-S138C) and red (LiDps-KLFC-F5M) transparent bars. The experimental data (black) were modeled (red lines) using a binomial distribution model. Adapted from Kang (2008). [50]

Small Heat Shock Protein (sHsp)

The sHsp (small heat shock protein) from the hypertheromophilic Archaeon *Methanococcus jannaschii* acts as a chaperonin, which imparts thermotolerance to cells expressing the protein.[51] The sHsp consists of 24 identical 16.5 kDa subunits that self-assemble into a hollow protein cage having cubic 432 symmetry (Figure 2.3). The sHsp is

has large pores, for its size, with a diameter of only 12 nm and an inner cavity diameter of 6.5 nm, but with 3 nm triangular pores at the three-fold axis and 1.7 nm square pores at the four-fold axis.[52]

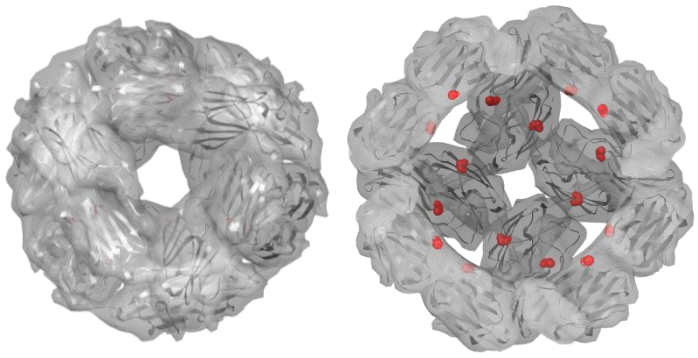

Figure 2.3: Assembled sHsp protein cage viewed from the exterior (left) and as a half-shell cut-away (right), which reveals the available interior space. The red dots are the location of the G41C mutation. PDB ID 1SHS.

Genetic mutants of the wild-type sHsp protein have been shown to be stable and have been successfully used as platforms for a range of nanomaterials synthesis. sHsp was first applied for materials synthesis with the introduction of a cysteine (G41C) which was then lableled with a fluorophore demonstrating that the site is accessable to small molecules. Additional work found that synthesis of ferrihydrate (Fe(O)OH) cores was possible in both the wild-type and this cysteine mutant. [53] This same cysteine mutant was employed to synthesize spatially controlled Pt cores with a range of loadings of Pt/cage and demonstrated catalytic activity.[32] Later using a concurrent addition scheme, CoPt cores were formed inside sHsp, but to attain the desired magnetic phase the presence of genetically engineered peptide (displayed on the interior of the cage) rather than the G41C mutation was necessary.[33] Building on the initial work, where fluorescein was

covalently attached to the G41C site, sHsp cages have been uniformly modified with a large cysteine reactive Ru based photosensitizer (Figure 2.4), both at the G41C site and at an external site (S121C), which indicated that both sites are accessable and reactive to larger molecular agents.[54]. When considered as a whole these reports demonstrate the genetic flexibility of the sHsp, the reactivity of the G41C site, and the stability of the sHsp cage to a variety of reaction conditions.

More particularly, sHsp has been used as the platform for a copper-catalyzed azide-alkyne cycloaddition (CuAAC) click chemistry based addressable organic polymer. This addressable branched polymer originated at the G41C site through attachment of a small molecule alkyne to the site. Cycling of the click chemistry components lead to a branched multimer with 144 new reactive amine sites and also imparted improved heat stability to the sHsp.[37] Labeling these new sites with a bulky Gd constrast agent, resulted in a supramolecular contrast agent with improved MRI parameters. [38] The retention of the cage architecture and internal confinement of the polymer indicated that this protein is not damaged by the click chemistry conditions and that the G41C site is suitable for internal direction of polymer growth, while labeling with the contrast agent showed that large molecules can enter the interior of the protein cage.

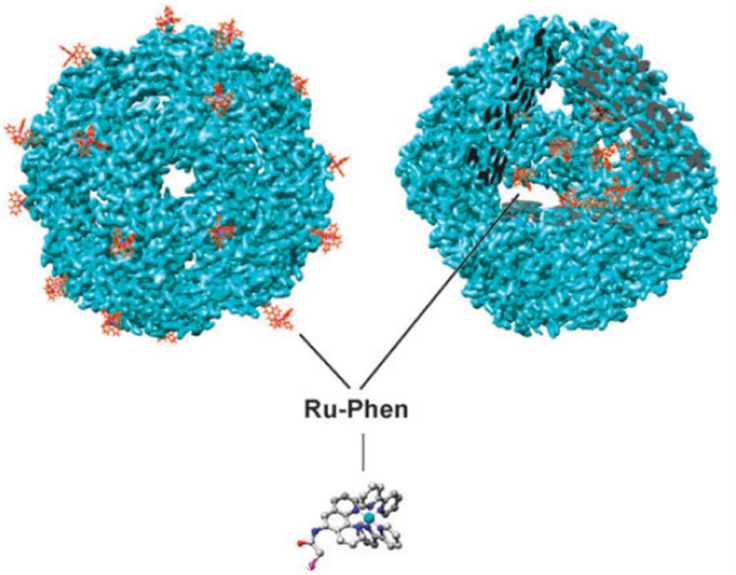

Figure 2.4: Attachment of a ruthenium complex to either the external cysteine mutant S121C (left) or the internal cysteine mutant G41C of sHsp. Adapted from Varpness (2009).[54]

The large pores for coordination complex access, demonstrated use of the G41C mutation site for labeling and polymer origination, and previous evidence of stability under click chemistry conditions made this 'holey' protein cage the selected scaffold for the formation of a protein-MOP as described in Chapter 5.

P22 Bacteriophage

The native bacteriophage P22 infects *Salmonella typhimuriam* and consists of 415 identical subunits arranged on an icosahedral lattice where one of the pentamers has been replaced by the protein portal complex, which is essential for DNA is packaging and infectivity (Figure 2.5). The virus-like particle (VLP) used for materials applications lacks the portal complex, so it consists of 420 subunits, which just like the procapsid head of the phage has an exterior diameter of 55 nm an internal cavity 48 nm in diameter.[55]

Becasuse the P22 coat protein requires the scaffold protein to guide proper assembly, recombinant expression in E. coli requires co-expression of the coat protein and scaffold protein. An important feature of this VLP is that it is capable of transformation into a series of distinct morphologies including procapsid (PC), which contains scaffold protein, empty shell (ES), where the scaffold protein has been removed, expanded (EX), and wiffleball (WB) where all 12 pentamers have been removed (Figure 2.6).[56,57] The EX morphology used in this work most closely mimics the state found in the DNA-containing infectious virion, with an exterior diameter of 64 nm and an unoccupied internal cavity 60 nm in diameter.[57,58]

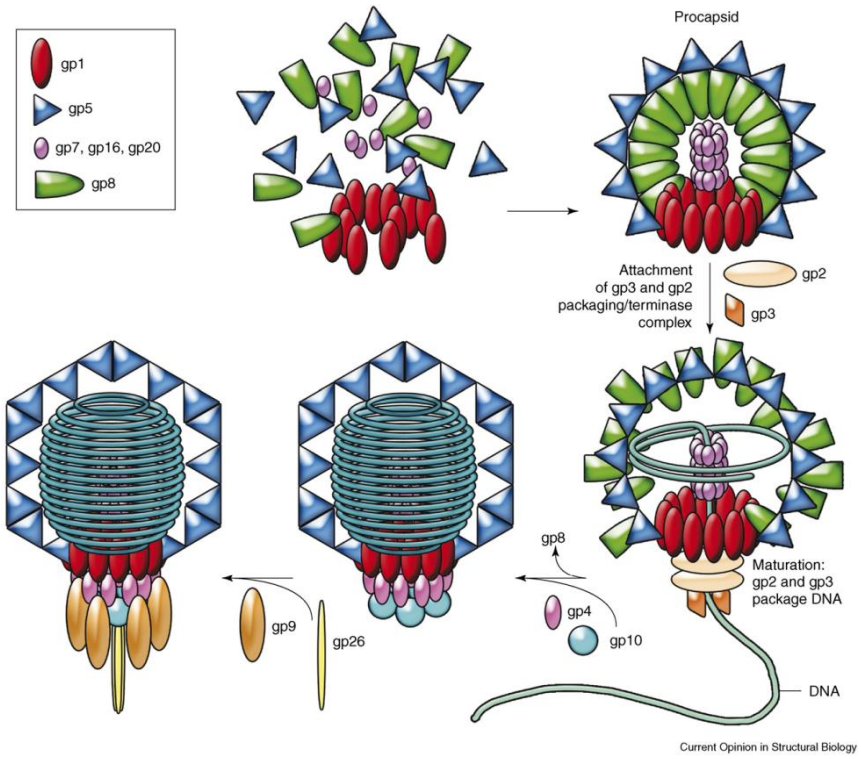

Figure 2.5: Assembly pathway for the native P22 bacteriophage. Only gp8 (scaffold) and gp 5 (coat) are necessary for the formation of the VLP.[55]

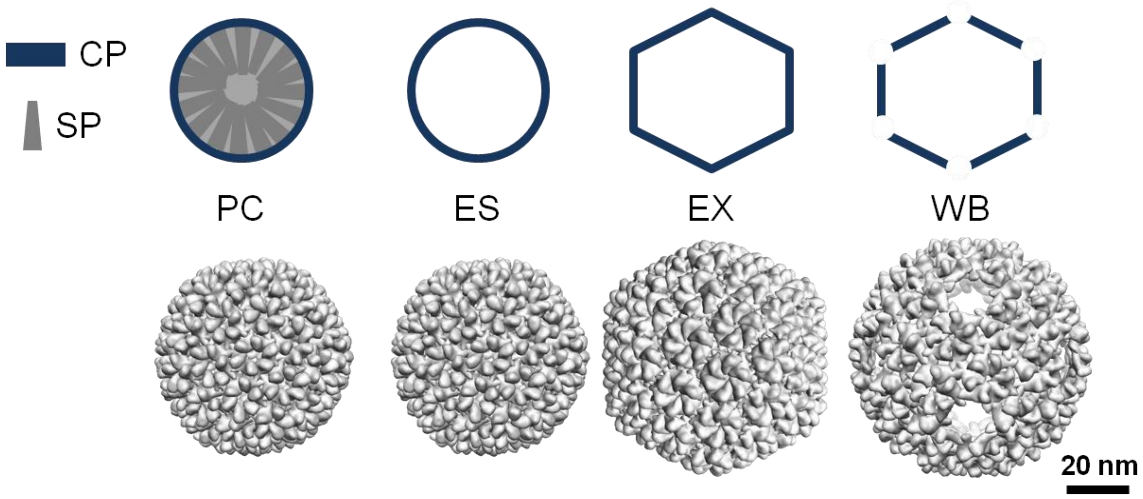

Figure 2.6: The four unique morphological forms of P22 readily accessable *in vitro*. The coat protein (CP) and scaffold protein (SP) are expressed in *E. coli*. The expressed protein is in the procapsid morphology (PC) containing both CP and SP. After extraction with guanidine•HCl only CP remains in the empty shell (ES) morphology. If the VLP is heated to 65 ºC, the shell enlarges to form the expanded shell (EX) morphology. If instead the ES is heated to 75 ºC, the wiffleball (WB) morphology can be made, where pentons are missing from the icosahedral vertices. PDB ID 3IYI, 2XYZ, 3IYH.

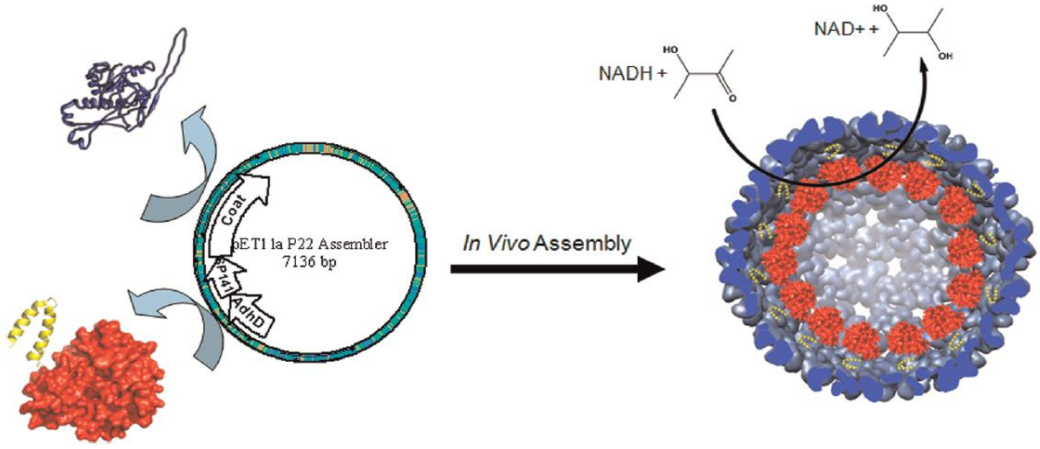

Figure 2.7: Schematic representation of *in vivo* recombinant expression and encapsulation of an alcohol dehydrogenase-scaffold protein (AdhD-SP) fusion inside of the assembled P22 capsid and the reaction catalyzed by the encapsulated enzyme. The assembly of the capsid from coat protein (blue) and the AdhD-SP fusion (red) is directed by the C-terminus of the truncated scaffold (yellow).[17]

Although the P22 architecture has only recently been utilized for use for materials purposes some methods developed with other protein cages as well as extensive genetic modification have already been applied to this cage. Prior to use as a materials scaffold point mutations in the coat protein were successfully introduced including the K118C variant used in Chapter 4.[59-62] A more extensive modification where the coat protein has been modified with a sulfide binding peptide between residues 182 and 183 has allowed the VLP exterior can be used as a template for ZnS and CdS shell formation.[63] Taking advantage of the scaffold protein for genetic modification, a poly acid peptide (ELEAE) has been attached to the scaffold to direct mineralization of ferrihydrate to the interior of the P22 capsid and without the addition of this peptide mineralization does not proceed in a spatially controlled manner. [16] The scaffold-coat protein interaction is strong enough that even larger modifications can be made to the scaffold protein including attachment of fluorescent proteins and active enzymes, which occupy the interior space of the VLP (Figure 2.7).[15,17,18] Applying previously used methods, the same procedure used to make click polymers inside sHsp, was used to make a multi generation polymer inside P22 which has been labeled to make a MRI contrast agent.[64] In a new method, a coordination polymer built by cycling a ditopic ligand and a metal ion to build an interior confined metal organic polymer has been demonstrated. [65] Together these studies support the use of P22 as a reaction platform due to the established genetic and synthetic flexibility tolerated by this protein.

The ‘large’ P22 virus-like particle was selected for demonstration of polymerization inside protein cages due to its resilence to genetic modification and

synthetic conditions as well as its relatively large size, which allows the advantage of using polymerization to occupy the interior space to be emphasized.

Synthetic Methods

Three underlying synthetic methods were employed to make the protein-metal, protein-MOP, and protein-polymer composites described in later chapters. Mineralization of Pt was used to make the LiDps-Pt construct described in Chapter 4, click chemistry was used to make the protein-MOP composite in Chapter 5, and atom transfer radical polymerization (ATRP) was used to make the protein-polymer materials in Chapters 6-8.

Platinum Mineralization

The metallic Pt surface is used extensively for catalysis and a way to increase the proportion of surface area to amount of a material used is to decrease the individual particle size. Thus, a range of synthetic methods for making nanoscale Pt have been developed either by forming the Pt on a substrate (ie Pt/carbon) or making solution phase particles (ie colloids). To make Pt colloids from Pt salts in solution a wide variety of reduction conditions have been employed from gently reducing hexachloroplatinate with ascorbic acid and light [66] to more involved treatments.[67-74] Each of these methods has the common goal of controlling the size, shape, and monodispersity of the resulting particles to obtain particles with improved activity or stability.[75] To keep the solution phase nanoparticles from coalescing, a capping agent is employed, but this agent can block the surface of the Pt reducing the activity of the particle.[32]

One alternative approach is to use a protein cage as a template for formation of the Pt nanoparticles. Although this method could be predicted to result in more monodisperse samples due to the uniform size of the protein scaffold, the nanoparticles would be expected to be polycrystalline due to multiple initiation sites inside the protein. In an example of this approach, seeding tobacco mosaic virus (TMV) with Pt nanoclusters for improved control over the synthesis of Ni and Co nanowires was accomplished. In this case the TMV was incubated in a solution of the Pt precursor ($PtCl_4^-$) followed by removal of excess Pt and reduction of the remaining TMV associated Pt using DMAB.[76] In another biotemplated example, sHsp was used as a size constrained reaction vessel for the synthesis of spherical Pt nanoparticles, which showed improved catalytic activity over particles synthesized without protein present. To produce these particles in a spatially controlled manner it was important for the Pt and reducing agent (DMAB) to be added concurrently in a rapidly stirred reaction solution warmed to 65º C.[32]

Another potential benefit of protein template synthesis is that, with appropriate protein cage selection, Pt nanoparticles synthesized in the protein cage can be analyzed with techniques not suitable for other Pt nanoparticles such as mass spectrometry. In Chapter 4 the use of mass spectrometry to get a distribution profile of the individual Pt particles formed in LiDps is described.

Click Chemistry

Click type organic reactions are both robust and very specific to the functionalities involved. Of this class, [3+2] azide-alkyne addition to form 1,4-

disubstituted 1,2,3 triazoles is perhaps the most widely recognized and applied (Figure 2.8). This copper catalyzed version of a Huisgen cycloaddition was first reported in 2002 and remarkably is water compatible and can be catalyzed by a number of Cu(I) salts and coordination complexes.[77] In purely organic applications the catalytic Cu(I) is generally generated *in situ* via the addition of sodium ascorbate or ascorbic acid.[77] Although water or a polar organic solvent are used, these reaction conditions are generally incompatable with proteins due to potential damage to the protein caused by reactive species generated from reactions of Cu(I) with residual oxygen or by dehydroascorbate side reactions.[78]

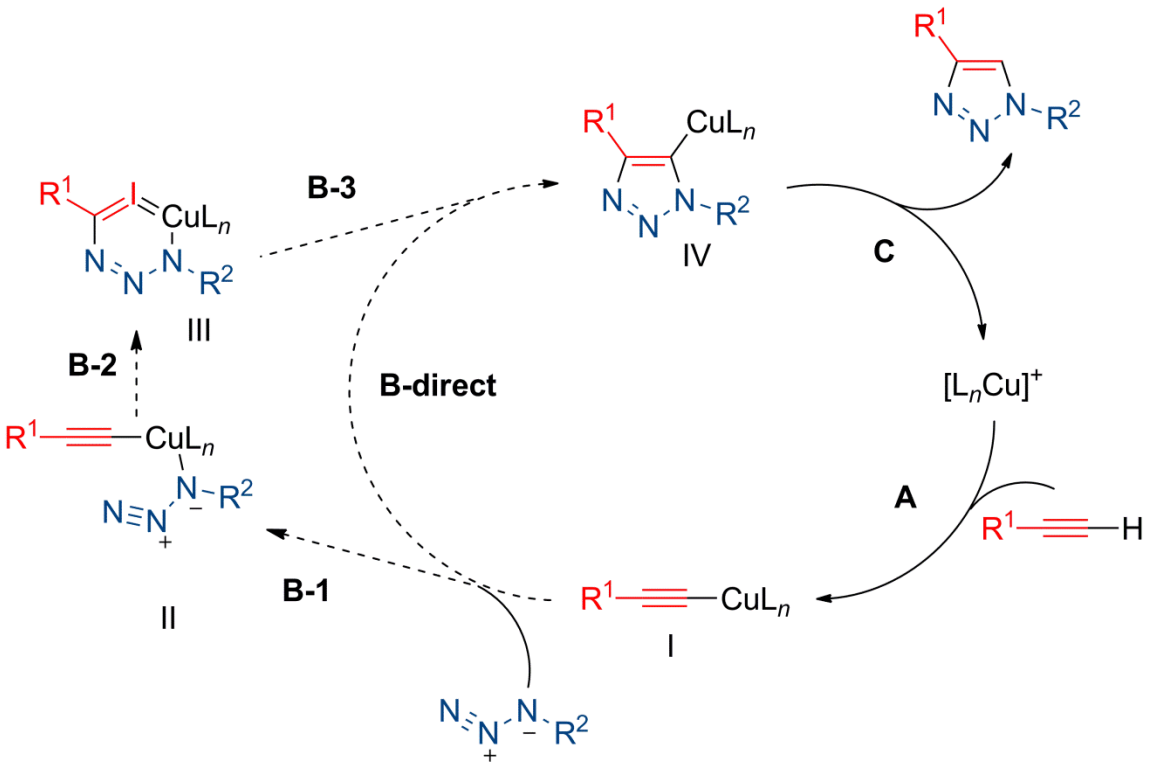

Figure 2.8: Proposed mechanism for copper catalyzed Huisgen azide-alkyne cycloaddition. In step A the terminal alkyne proton is abstracted and copper(I) acetylide **I** is formed. The subsequent formation of the triazole-copper complex **IV** in step B is expected to proceed via the annealing pathway (B-1 to B-2 to B-3) rather than the concerted direct pathway (B-direct). Finally in step C a proton replaces the copper on the triazole thereby egenerating the copper(I) catalyst.[77]

This chemistry has been extensively explored by the Finn group for application to protein cages with the development of reaction modifications to protect the protein component and ensuring retention of the copper catalyst activity. From the initial application of click chemistry for fluorescein labeling of CPMV the reaction has been significantly improved upon to include a wide range of coupling reactions. [79] Shortly after the first report, a modified procedure utilizing sulfonated bathophenanthroline as the copper catalyst ligand was described.[80,81] This ligand was included to ensure that the copper catalyst was in an active coordination environment rather than being potentially sequestered by interaction with the protein. Early applications of this approach include the click based attachment of Gd-MRI contrast agents to CPMV.[82]While effective, and a significant improvement over the initial report, the reagents still required that all reactions be performed in a strict inert atmosphere. Further improvements to the process were made by changing the copper ligand and through the addition of molecules (such as aminoguanidine for protection against protein damage) to the mixture, which allow the reaction to be mixed in a sealed vessel without extensive treatment to keep the reaction anoxic.[78] In this reaction mixture, any oxidized copper is regenerated by the presence of sodium ascorbate, while aminoguanidine acts as a radical scavenger protecting the protein from reactive species generated by the sodium ascorbate and copper. These modified conditions have provided a streamlined path towards a variety of protein-conjugate type syntheses.

While this reaction optimization is useful, especially for very sensitive proteins or for extended reaction condition exposures, these and other less optimized reaction

conditions have proven useful for the selective conjugation of molecules to the surface of VLPs. For example, use of MS2 and Qβ, with non-natural amino acids containing the necessary azide or alkyne functionalities, has allowed for improved attachement of large molecules like small DNAs, growth factors and PEG.[83] Similarly, click chemistry has proven effective for the selective modification of turnip yellow mosaic virus (TYMV) with a RGD peptide and courmarin dye where the reactive alkyne was introduced through EDC coupling of propargylamine to the native carboxyl groups in the protein.[84] In a more involved example, click chemistry was employed to introduce a polymer initiator onto the surface of Qβ and later the synthesized protein-polymer composite was labeled with small molecule dyes, again using click chemistry.[85] The success of these examples highlight the usefulness of the azide-alkyne click chemistry for the selective addition of large and small molecules to a variety of protein cages.

This reaction type, while useful for the specific coupling of molecules to proteins, can also be used iteratively for the stepwise formation of a polymer, similar to the formation of a dendrimer. Click chemistry has been applied towards the synthesis of addressable organic polymers inside both sHsp and the P22 VLP for the formation of an improved MRI contrast agent. To initiate the polymer synthesis in sHsp, a cysteine anchored alkyne was introduced on the interior of the protein followed by the use of the bathophenanthroline based click reaction conditions to add 2-azido-1-azidomethyl-ethylamine (an azide with pendant primary amine). Instead of stopping with the single click reaction the protein was purified and a further click reaction with tripropargyl amine (a branched alkyne) was undertaken. This product was further purified and subsequently

reacted with additional azide (Figure 2.9). Cycling the reagents in this manner for 3.5 generations lead to a polymer that filled the sHsp protein cage. Labeling of the construct, after each step of the reaction, indicated that no further addition of monomers occured after generation 2.5. Simlarly, cycling the reactants for 3.5 generations in P22 resulted in a multi-generation polymer, but due to the size of P22, the polymer did not fill the VLP. Using either the sHsp-polymer or P22-polymer construct, about 144 or 1,900 new addressable sites, respectively, can be labeled with a fluorophore or more substantively with a Gd based MRI contrast agent.[37,38 64]

It was this successful formation of organic polymers inside a protein, that provided inspiration, while the mild conditions developed by the Finn group made it possible to subject the protein scaffold to the many iterations required to synthesize the protein-MOP described in Chapter 5.

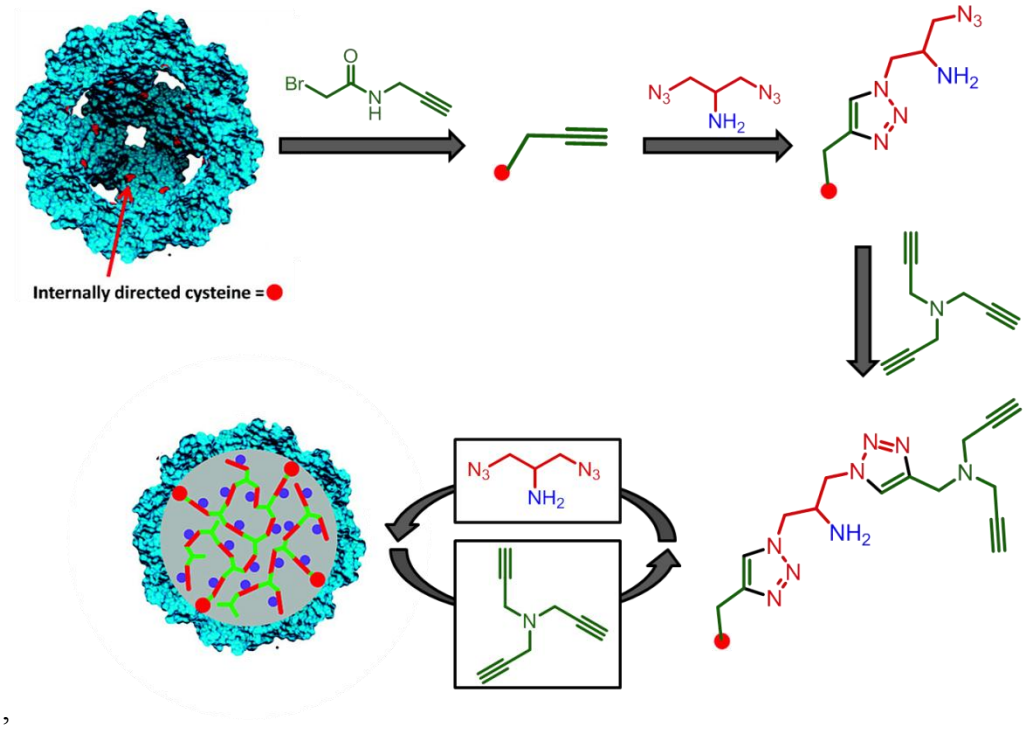

Figure 2.9: Synthetic scheme for the formation of a generational polymer inside sHsp. The internally directed cysteine (red dot) is G41C. The azide and alkyne steps are repeated until no further addition to the polymer is detected. Adopted from Abedin (2009).[37]

Atom Transfer Radical Polymerization

Atom transfer radical polymerization (ATRP) is a living radical metal catalyzed method that in bulk leads to polymer chains with low polydispersity. Reactions proceeding via the mechanism shown in Figure 2.10 were first demonstrated with the polymerization of styrene and methacrylates at elevated temperature. [86,87] Since then this method has been successfully applied to a wide range of monomers including styrene, acrylonitrile, acrylates, methacrylates, acrylamides, and methacrylamides.[88] For each of these monomers optimization of the reaction conditions, metal ligand, and halide initiator is essential for satisfactory polymerization.[89]

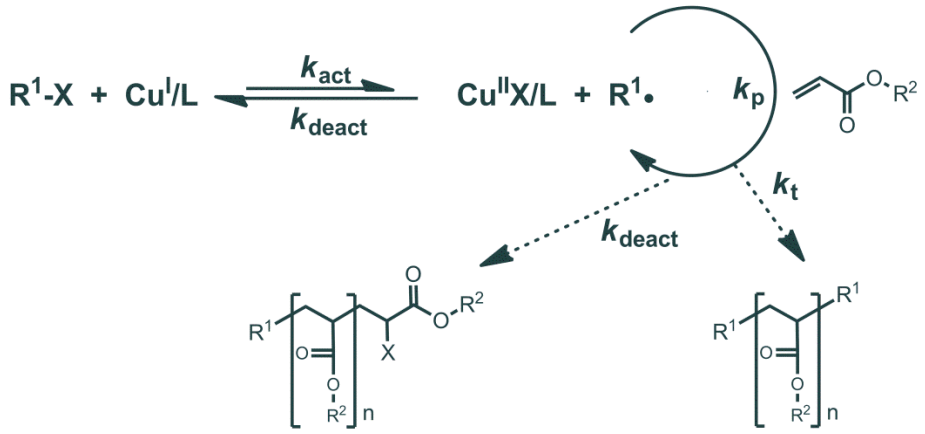

Figure 2.10: Reaction mechanism for ATRP. The reaction is activated through the abstraction of the halide (X) from the initiator (R^1-X) by the reduced metal complex. This process is reversible and the presence of the resulting oxidized metal complex helps modulate the rates of activation (k_{act}) and deactivation (k_{deact}). The selected monomer (here an acrylate) is added to radical species at a monomer and reaction condition dependent rate of propagation (k_p). Deactivation and subsequent reactivation of the polymer chain occurs as well as chain-to-chain termination.

An important advance in this polymerization technique has been the application of ATRP to biomolecules. Although the polymer can be made and characterized separately then attached to the biomolecule (grafted-to), just like polymers synthesized by other methods, one potential advantage of ATRP is that the polymer can also be grown directly from the biomolecule (grafted-from). The first report of this method describes the modification of strepavidin with a modified biotin initiator for the successful growth of N-isopropylacrylamide polymers (NIPAM) (Figure 2.11).[90] Another early report of this method describes the use of BSA or lysozyme with a NIPAM polymer grown from a cysteine attached initiation site. [91] Further work has focused on adding PEG-like based polymers to a variety of proteins for improved pharmacokinetic properties,[92-96] such as the C-terminal growth of oligo(ethylene glycol) methyl ether methacrylate (OEGMA)

from GFP and related N-terminal growth of OEGMA from myoglobin.[97,98] More recently poly(OEGMA) has been grafted from the exterior of the Qβ VLP with some success.[85] While each of these studies improves the knowledge of the polymerization process when anchored to a biomolecule a select few monomers are used and all but one use monomeric proteins.

The range of protein-polymer composites described in Chapters 5, 6, and 7 build upon the previous ATRP based protein-polymer work to demonstrate spatial control of the polymerization. In addition, by relying on the robust nature of ATRP, the range of materials made using the grafted-from approach was exploited, highlightling the potential for dramatic expansion of applications using these materials.

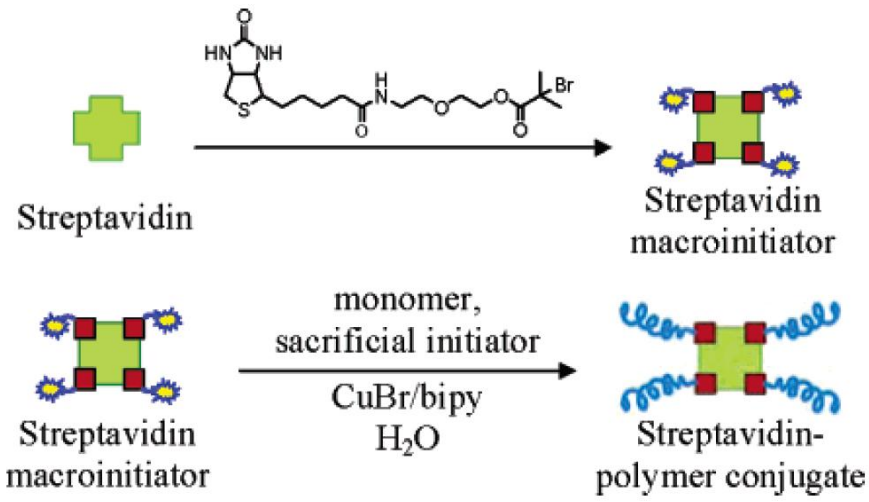

Figure 2.11: Synthetic scheme for the formation of streptavidin anchored poly(NIPAM) where a biotin containing initiator is bound to the streptavidin prior to polymerization.[90]

MANUSCRIPT IN CHAPTER 3

MONITORING BIOMIMETIC PLATINUM NANOCLUSTER FORMATION USING MASS SPECTROMETRY AND CLUSTER-DEPENDENT H_2 PRODUCTION

Contributions of Authors and Co-Authors

Manuscripts in Chapters 3, 4, and 6

Author: Sebyung Kang

Contributions: Designed and carried out the mass spectrometry experiments and wrote the manuscript.

Co-author: Janice Lucon

Contributions: Designed and carried out the synthesis and activity experiments and wrote the manuscript.

Co-author: Zachary B. Varpness

Contributions: Developed preliminary Pt particle inside protein cage methods.

Co-author: Lars Leipold

Contributions: Assisted in maintenance and interpretation of the mass spectrometry data.

Co-author: Masaki Uchida

Contributions: Assisted in experimental design.

Co-author: Debbie Willits

Contributions: Provided mutant making guidance.

Co-author: Mark Young

Contributions: Obtained funding and coordinated the project.

Co-author: Trevor Douglas

Contributions: Obtained funding, coordinated the project, and assisted with the design of the experiments. Discussed the results and edited the manuscript at all stages.

Manuscript Information Page

Authors: Sebyung Kang, Janice Lucon, Zachary B. Varpness, Lars Liepold, Masaki Uchida, DebbieWillits, Mark Young,and Trevor Douglas
Journal: Angewandte Chemie International Edition

Status of the manuscript:
____ Prepared for submission to a peer-reviewed journal
____ Officially submitted to a peer-reviewed journal
____ Accepted by a peer-reviewed journal
_X__ Published in a peer-reviewed journal

Publisher: Wiley-VHC
Issue in which manuscript appears: Volume 47, 7845-7848 (2008)

CHAPTER 3

MONITORING BIOMIMETIC PLATINUM NANOCLUSTER FORMATION USING MASS SPECTROMETRY AND CLUSTER-DEPENDENT H_2 PRODUCTION

Published: *Angewandte Chemie International Edition*, **2008**, 47, 7845-7848.

Sebyung Kang[1], Janice Lucon[1], Zachary B. Varpness[1], Lars Liepold[1], Masaki Uchida[1], Debbie Willits[2], Mark Young[2], and Trevor Douglas[1]

1 Chemistry and Biochemistry Department, Montana State University, Bozeman, Montana, 59717

2 Department of Plant Sciences, Montana State University, Bozeman, Montana, 59717

Introduction

Protein cages, such as ferritins, viruses, and heat shock proteins, have been used as size-constrained reaction vessels to spatially limit nanoparticle growth, to encapsulate preformed nanomaterials, or for covalent attachment of organic molecules.[6,25,32,33,53,76,99] Although protein cages have been widely used as powerful templates for nanomaterials syntheses, the processes of metal ion accumulation and core formation within a protein cage are still poorly understood. This is mainly due to the lack of appropriate analytical tools that detect multiple transient state species simultaneously with sufficient resolution and accuracy. While most spectroscopic techniques provide averaged information of populations in a mixture, mass spectrometry can simultaneously resolve individual molecular masses present in a mixture.[100,101] Therefore, it is possible to concurrently detect multiple populations distributed within an ensemble and monitor their changes

individually instead of averaging all signals. With the invention of soft ionization methods, such as electrospray ionization (ESI)[102] and matrix assisted laser desorption ionization (MALDI)[103], it has become possible to measure the intact mass of noncovalently associated macromolecular complexes[104-106] and isolated colloids.[107-109] Mass measurement of giant noncovalent protein complexes have been extensively studied[110-113] and preservation of solution structures in the gas phase inside mass spectrometers has been well demonstrated.[104-106] We used this approach to monitor Pt^{2+} binding and Pt^0 nanocluster formation in a protein cage template.

Herein, we have genetically and chemically modified Listeria innocua Dps (LiDps) for the controlled synthesis of platinum nanoclusters, analyzed the Pt^0 nanocluster growth by noncovalent mass spectrometry, and verified the activity of these nanoclusters as hydrogen production catalysts. This is the first report to precisely follow the transition from metal binding through nucleation and nanocluster formation using mass spectrometry.

Results and Discussion

The Dps (DNA binding protein from starved cells) from the Gram-positive bacterium Listeria innocua prevents oxidative damage of DNA by accumulating iron atoms within its central cavity to produce an iron oxide core similar to that of ferritins.[39,40] The LiDps consists of 12 identical 18 kDa subunits that self-assemble into a hollow protein cage having tetrahedral 23 symmetry (Figure 3.1).[39] The LiDps is consequently smaller than ferritin with an outer diameter of 9 nm and an inner cavity diameter of 5 nm with 0.8 nm pores at the three fold axis where molecules can pass

through to the interior (Figure 3.1).[39] The LiDps has been used for mineralizing metal oxides, such as iron and cobalt oxides, and cadmium sulfide.[41,44,46] Herein we have extended this approach to encapsulate Pt^0 nanoparticles using the LiDps cage. We genetically modified the LiDps to enable site selective chemical modification to the interior of the LiDps cage by substitution of serine at position 138, located in the middle of helix E, with cysteine (S138C; Figure 3.1). We synthesized 5-iodoacetoamido-1,10 phenanthroline (iodo-phen)[114] and labeled the introduced cysteines of the S138C mutant with no alteration of the protein cage architecture (Appendix A, Figure A1). Covalent attachment of metal binding ligands to the interior surface of the LiDps was expected to induce binding of Pt^{2+}ions and facilitate nucleation of Pt^{2+}ions.

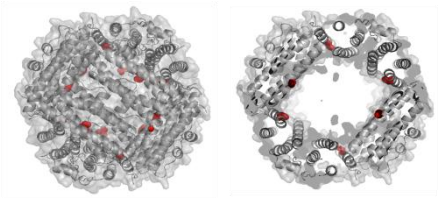

Figure 3.1: Surface and ribbon diagram representations of LiDps (PDB 1QGH) looking down the twofold symmetry axis (left) and a clipped view showing the interior space of the cage (right). Serine 138 residues substituted with cysteines, in the S138C mutant, are indicated in red.

The extent of of reaction between the iodo-phen and LiDps cysteine thiols to form the corresponding thioether with loss of I- (Appendix A, Figure A2) was evaluated by measuring the molecular masses of subunits using electrospray ionization time-of-flight mass spectrometry (ESI-TOF MS) using previously described methods.[60,115] Attachment of the phenanthroline moiety to the LiDps subunit resulted in a 236 unit mass increase (Appendix A, Figure A2). Two major populations were detected from the iodo-phen

treated S138C LiDps. Component analysis of the charge state distributions revealed that the dominant species in the iodo-phen treated S138C LiDps sample were a 18301.4 Da subunit (85%) and a 18065.4 Da subunit (15%). These observed masses are in an excellent agreement with the values predicted for a LiDps protein subunit modified with a single phenanthroline moiety (18300.7 Da) and the unlabeled subunit (18064.7 Da; Figure 3.2A). Wild type (wt) LiDps, which does not have an intrinsic cysteine, was treated in parallel as a control and no modification was observed under identical reaction condition (Appendix A, Figure A3).

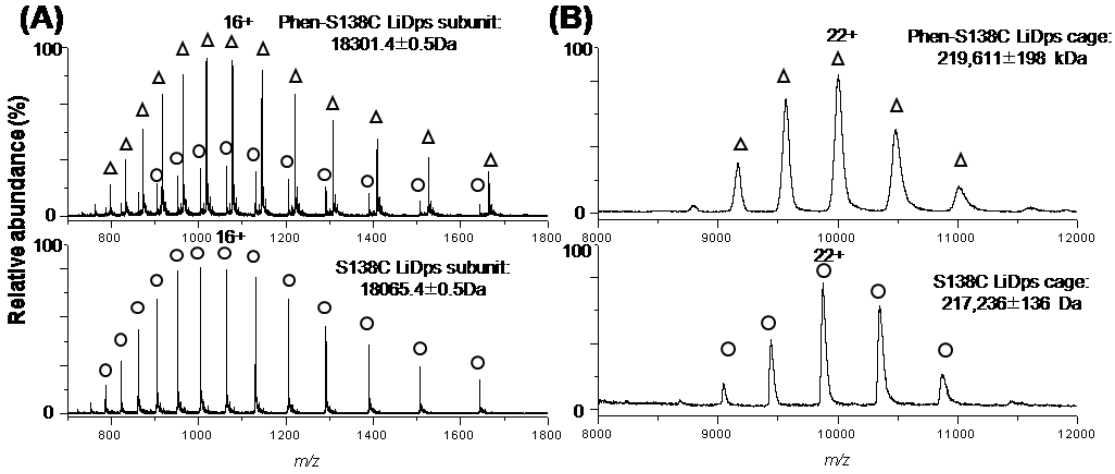

Figure 3.2: Mass spectrometric analyses of the subunit and intact LiDps before and after treatment with 5-iodoacetamido-1,10-phenanthroline; charge state distributions for modified (triangle) and unmodified S138C LiDps cages (circle) are shown. A) Mass spectra of subunits. Charged peaks (16+) of subunit either unmodified or modified with a single phenanthroline moiety are indicated. B) Noncovalent mass spectra of intact LiDps cages with charged peaks (22+) of iodo-phen treated and untreated cages indicated.

We confirmed the dodecameric cage architecture of the LiDps by measuring the intact cage masses of the S138C and phen-conjugated S138C LiDps (phen-S138C LiDps) (Figure 3.2B). The typical charge state distribution of dodecameric LiDps was observed

with unlabeled S138C LiDps (Figure 2B, bottom panel). The charge state distribution of the phen-S138C LiDps cage was shifted to higher m/z and its mass increase was 2375 Dz, which corresponds to addition of 10.1 phenanthroline moieties (236 Da) per cage on average (Figure 3.2B, top panel and inset values). The mass increase for the intact phen-S138C LiDps agreed well with the extent of modification determined by subunit mass analysis (Figure 3.2).

For monitoring Pt^{2+} ion binding, phen-S138C LiDps was treated with various amounts (0, 12, 24, 48, 100, and 200 Pt^{2+}/cage) of Pt^{2+} ions and equilibrated at 4 ^{o}C overnight. Unbound Pt^{2+} ions were removed by size exclusion chromatography (SEC) and the Pt^{2+}-phen-S138C Dps complexes were analyzed by noncovalent mass spectrometry. Wt and unlabeled S138C LiDps were also treated in parallel to investigate the direct role of the phenanthroline moiety in Pt^{2+} ion binding. While phen-S138C LiDps contained 43 Pt^{2+} ions with a theoretical loading of 200 Pt^{2+}/cage (Figure 3.3), unmodified S138C and wt LiDps contained 23 and 16 Pt^{2+} ions, respectively, at equivalent Pt^{2+} ion loading (Appendix A, Figure A4) suggesting that the phenanthroline moiety facilitates additional Pt^{2+} ion binding.

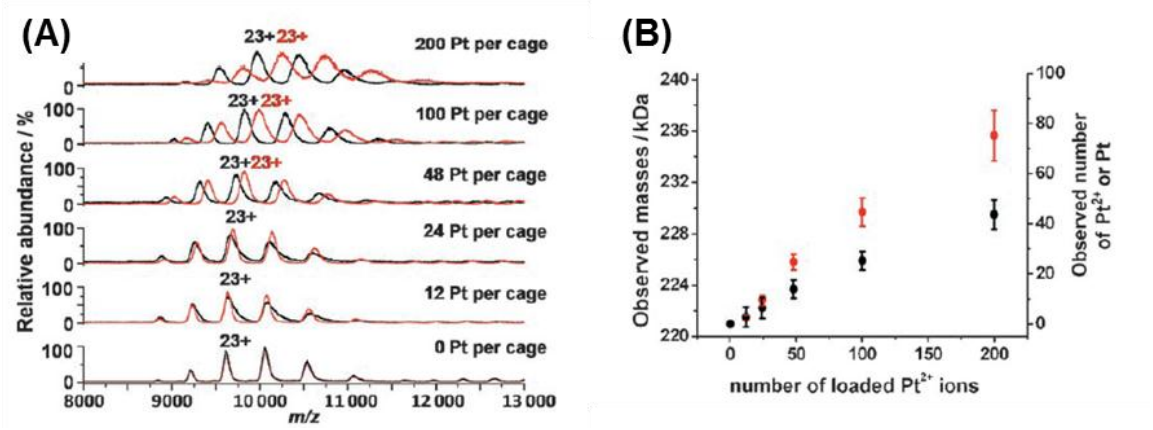

Figure 3.3: (A) Overlaid mass spectra of the Pt^{2+} ion bound (black) and Pt^{0} mineralized (red) phen-S138C LiDps cages at various loading ratios of Pt^{2+} (0, 12, 24, 48, 100, and 200 Pt^{2+} ions per cage, bottom to top). Charged peaks (23+) of the cages are indicated. (B) Plots of the observed masses (left y axis) and converted numbers (right y axis) of Pt^{2+} ion bound (black circles) and Pt^{0} mineralized (red circles) phen-S138C LiDps cages according to the initial Pt^{2+} ion loadings. Deviations of Pt^{2+}-ion or Pt^{0}-atom contents in the broadened peaks were determined by calculating the half width at the half height of each peak and comparing to a 0 loading control.

In order to follow Pt^{0} nanocluster formation, phen-S138C LiDps was incubated with the same range of Pt^{2+} ion loadings (0, 12, 24, 48, 100, and 200 Pt^{2+}/cage) at 4 ^{o}C overnight and subsequently photoreduced. Analysis of the reaction product by SEC revealed that the Pt^{0} mineralized phen-S138C LiDps eluted at the same position as the untreated control phen-S138C LiDps. This unaltered elution profile indicates that the Pt^{2+} binding and Pt^{0} mineralization occur selectively within the inner cavity of the cages and does not alter the cage architecture (Appendix A, Figure A5). However, uncontrolled particle growth was observed through a shift in the SEC profile with wt and unlabeled S138C LiDps cages under identical reaction condition (Appendix A, Figure A6).

Charge state distributions of both Pt^{2+} ion bound (black) and Pt^{0} nanoclustered phen-S138C LiDps (red) were shifted to higher m/z compared to the untreated phen-

S138C LiDps in accordance with the increasing numbers of Pt^{2+} loaded (Figure 3.3A). Only one population was observed at each Pt^{2+} loading (Figure 3.3A) implying that binding or nanocluster formation events occur homogeneously throughout the cage population rather than in an all-or-nothing manner. However, peak broadening at the high Pt^{2+} loadings was observed (Figure 3.3A) indicating that individual phen-S138C LiDps contain slightly different amounts of Pt^{2+} or Pt^0 within a narrow distribution with a maximum deviation of 10 Pt^0 at loading of 200 Pt^{2+}/cage as shown in Figure 3B. Charge state distributions of Pt^0 nanoclustered phen-S138C LiDps were shifted to higher m/z compared to that of Pt^{2+} ion bound phen-S138C LiDps suggesting increased Pt^{2+} incorporation upon photoreduction (Figure 3.3A). Based on the mass calculations, 2.8, 6.3, 13.9, 25.3, and 43.5 Pt^{2+} ions were bound to phen-S138C LiDps with theoretical Pt^{2+} ion loadings of 12, 24, 48, 100, and 200 Pt^{2+} ions per cage, respectively, whereas Pt^0 nanoclusters containing 2.4, 9.4, 24.8, 44.6, and 75 Pt^0 were formed in phen-S138C LiDps with the same range of Pt^{2+} ion loadings (Figure 3.3B). Taken together these results suggest that the introduced Pt^{2+} ions first enter the cages and bind to the covalently attached phenanthroline moiety and that free Pt^{2+} ions inside are recruited by the pre-bound Pt^{2+} ions upon photoreduction to form the Pt^0 nanoclusters.

To verify core formation, we attempted to observe the Pt^0 nanoclusters inside the cages using transmission electron microscopy (TEM), but we could not detect Pt^0 cores inside phen-S138C LiDps (Appendix A, Figure A7). However, a core size of 75 Pt^0 is estimated to have an approximately 1 nm diameter which is at the detection limit of the

instrument. Therefore, we may not have detected distinct cores because of technical limitations rather than the lack of core formation.

Pt^0 nanoparticles are known to be excellent catalysts for proton reduction and hydrogen production.[116,117] It has been suggested that their catalytic activity is dependent upon the Pt^0 particle size.[118] We have previously demonstrated efficient hydrogen production using the Pt^0 mineralized heat shock protein cages in conjunction with a photochemical system.[32] To move toward a more simple assay, we have implemented a photosystem based on $[Ir(ppy)_2(bpy)]^+$ (ppy = 2-phenylpyridine; bpy = 2,2'-bipyridine) which has been shown to act as a mediatorless photocatalyst for hydrogen production in conjunction with Pt^0 colloid.[119] We used the Ir based photocatalyst as a tool to investigate the loading required to create catalytic Pt^0 clusters for hydrogen production (Figure 3.4 and Appendix A, Figure A8). The Ir complex only control corroborated previous reports that the complex can produce small amounts of hydrogen without a Pt catalyst present.[119] While the phen-S138C LiDps samples with equal to or less than 45 Pt^0 (theoretical loading of 100 Pt^{2+}/cage) produced hydrogen near baseline levels, the 75 Pt^0 (theoretical loading of 200 Pt^{2+}/cage) containing phen-S138C LiDps generated approximately four times more hydrogen than the background level (Figure 3.4B and Appendix A, Figure A8). These data support the idea that the 75 Pt atoms form a sufficiently large nanocluster rather than multiple nanoclusters in the phen-S138C LiDps. In contrast, the 45 Pt^0, or lower Pt^0, containing cages appear to have failed to form a sufficiently large cluster to catalyze hydrogen production.

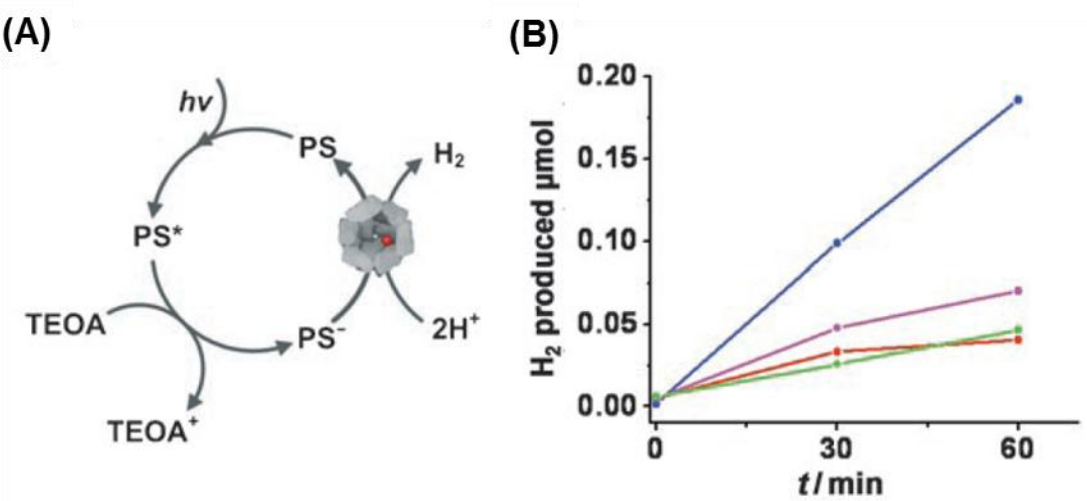

Figure 3.4: Hydrogen production from the Pt^0 mineralized phen-S138C LiDps. (A) Schematic representation of the light-mediated hydrogen production from Pt^0 nanoclustered phen-S138C LiDps. The photosensitizer (PS) employed in this process is [Ir(ppy)2(bpy)]+. (B) Time dependent hydrogen production of Ir complex only (red), 25 Pt^0 (green), 44 Pt^0 (magenta), and 75 Pt^0 (blue) mineralized phen-S138C LiDps.

Conclusion

In conclusion, we have successfully resolved Pt^{2+} ion binding and Pt^0 nanocluster formation inside the protein cages at near atomic resolution using mass spectrometry. In addition, we have demonstrated catalytic Pt^0 nanocluster dependant hydrogen production within the LiDps cage. This high resolution analysis has been made possible by using the genetically engineered and chemically functionalized LiDps for directed nanocluster growth. Better understanding of biomimetic mineralization processes may give us greater insight into controlled material synthesis under the mild conditions. In particular, thoroughly elucidating the relationship between Pt^0 nanocluster sizes and the total quantity of hydrogen produced may lead to the development of more efficient hydrogen production systems

Experimental

Mutagenesis, Protein Expression, and Purification.

Cysteine substitution of serine 138 was generated by Quick change PCR protocol using pET-30b based plasmids encoding genes for LiDps. The amplified DNAs were transformed into competent E.coli strain BL21 (DE) and S138C LiDps was over-expressed in E. coli and purified as previously described.[41]

Phen Modification of the S138C LiDps and Purification.

Synthesis of 5-iodoacetamido-1,10-phenanthorline (iodo-phen) was carried out as previously described.[114] The final product was confirmed by mass spectrometry. The S138C LiDps was incubated with 3 molar equivalents of iodo-phen at 4oC overnight. Reactions were loaded onto a 10 x 300 mm Superose 6 (Amersham Bioscience) size exclusion column and eluted with buffer containing 50 mM MES, 100mM NaCl (pH6.5) at a rate of 0.5 mL/min.

Mass Spectrometry.

Subunit masses of the iodo-phen treated and untreated S138C LiDps cages were analyzed by ESI-Q-TOF mass spectrometry (Q-TOF Premier, Waters) interfaced to a Waters UPLC and autosampler. Samples were loaded onto the BioBasic SEC-300 column (5 μm, 250 L × 1.0 mm I.D, Thermo Scientific) and eluted with the buffer containing 40% isopropanol, 59.9% water, and 0.1% formic acid isocratically with a rate of 25 μl/min. Mass spectra were acquired in the range of m/z 50–5,000 and processed using component analysis from MassLynx version 4.1 to obtain average masses from multiple

charge state distributions. Mass analyses of the intact LiDps cages were carried out on samples in 10 mM triethylammonium acetate buffer (pH 6.8).[120] Spectra were acquired in the range of m/z 50-30,000 by directly infusing samples into the mass spectrometer at a flow rate of 20 µL/min. Source and desolvation temperatures were 80°C and 120°C, respectively. Collisional focusing, which facilitated the focusing and transmission of ionized LiDps cages in vacuo, was achieved by increasing the source pressure to approximately 7.0 mbar.[121] The capillary voltage and the sample cone voltage were 3,000 V and 50 V, respectively. Pressure in the collision cell and the TOF tube were maintained at 1.0 × 10-2 mbar and 2.0 x 10-6 mbar, respectively. Mass calibration was accomplished by directly infusing aqueous CsI (50 mg/mL) at 0.5 µL/min. Charge states and masses were obtained from the spectral data using MassLynx version 4.1 software (Waters). All assigned masses were manually verified. Deviations of the Pt^{2+} ion and Pt^{0} contents in the broadened peaks were determined by calculating the half-width at the half-height of each peak and comparing with a 0 loading control.

<u>Pt^{2+} Ion Binding and Pt^{0} Nanocluster Formation.</u>

Phen-S138C LiDps (200 µl at 1 mg/mL in 50mM MES, 100mM NaCl, pH6.5) was mixed with the appropriate amount of 2 mM K_2PtCl_4 for a theoretical loading of either 0, 12, 24, 48, 100, or 200 Pt^{2+} per cage. To each sample 25mM MES (pH 6.5) was added for a final volume of 400 µl. After incubating at 4°C overnight, a four-fold excess of 4 mM sodium citrate was added to each cuvette and then they were immediately illuminated with a 150 W Xe arc lamp (175 W, Lambdz-LS, Sutter Instruments) equipped with an IR filter (10 cm water filter) and a UV cutoff filter (UV absorbing glass) for 45

min. The light flux was measured using an Extech Instrument EasyView light meter. The sample temperature was maintained at 40 oC with a water bath.[122,123] After mineralization, each sample was loaded onto a 10 x 300 mm Superose 6 (Amersham Bioscience) size exclusion column and eluted with 50 mM MES, 100 mM NaCl (pH 6.5) at a rate of 0.5 mL/min.

Light Induced Hydrogen Production.

The remaining 0, 48, 100, and 200 Pt^{2+}/cage samples (approximately 0.62 nM) were mixed with 53.5 µl of 33 mM $[Ir(ppy)_2(bpy)]PF_6$ and 2,000 µl of a acetonitrile/ water/ triethanolamine (TEOA) mixture (9:3:1).[119] The photosensitizer only control was mixed in the same manner adding 53.5 µl extra 9:3:1 acetonitrile/ water/ TEOA to make the same final volume. Samples were septum sealed and degassed under N_2 and vacuum alternatively three times. Each sample was illuminated for 1 hr at 25^{o}C with the same lamp used for photoreduction. Headspace samples were analyzed on a Shimadzu GC-8A TCD with a 1.83 m x 0.32 cm 80/100 Porapak Supelco column using argon as carrier gas.[32] Bulk H_2 gas was used as a standard to quantify the sample H_2 production.

MANUSCRIPT IN CHAPTER 4

A CLICK CHEMISTRY BASED COORDINATION POLYMER INSIDE SMALL HEAT SHOCK PROTEIN

Contributions of Authors and Co-Authors

Manuscripts in Chapters 3, 4, and 6

Author: Janice Lucon

Contributions: Designed and carried out the experiments and wrote the manuscript.

Co-author: Md Joynal Abedin

Contributions: Assisted in the initial training for organic and click reactions.

Co-author: Masaki Uchida

Contributions: Assisted in experimental design.

Co-author: Lars O. Liepold

Contributions: Provided mass spectrometry assistance

Co-author: Craig C. Jolley

Contributions: Assisted in the interpretation of the occupancy of the construct.

Co-author: Mark Young

Contributions: Obtained funding and coordinated the project.

Co-author: Trevor Douglas

Contributions: Obtained funding, coordinated the project, and assisted with the design of the experiments. Discussed the results and edited the manuscript at all stages.

Manuscript Information Page

Authors: Janice Lucon, Md Joynal Abedin, Masaki Uchida, Lars Liepold, Craig C. Jolley, Mark Young, and Trevor Douglas

Journal: Chemical Communications

Status of the manuscript:
____ Prepared for submission to a peer-reviewed journal
____ Officially submitted to a peer-reviewed journal
____ Accepted by a peer-reviewed journal
__X_ Published in a peer-reviewed journal

Publisher: The Royal Society of Chemistry
Issue in which manuscript appears: Volume 46, 264-266 (2010)

CHAPTER 4

A CLICK CHEMISTRY BASED COORDINATION POLYMER INSIDE SMALL HEAT SHOCK PROTEIN

Published: *Chemical Communications*, **2010**, 46, 264-266.

Janice Lucon[1,2], Md Joynal Abedin[1,2], Masaki Uchida[1,2], Lars Liepold[1,2], Craig C. Jolley[1,3], Mark Young[3,4], and Trevor Douglas[1,2]

[1] *Chemistry and Biochemistry Department, Montana State University, Bozeman, Montana, 59717*
[2] *Center for Bio-Inspired Nanomaterials, Montana State University, Bozeman, Montana, 59717*
[3] *Astrobiology Biogeocatalysis Research Center, Montana State University, Bozeman, Montana, 59717*
[4] *Department of Plant Sciences, Montana State University, Bozeman, Montana, 59717*

Abstract

A branched iron–phenanthroline based coordination polymer has been constructed in a water based system using a click chemistry approach to link monomeric coordination complexes together within a protein cage nanoarchitecture, which acts both as a template and a sized constrained reaction environment.

Introduction

Metal-organic frameworks and coordination polymers are an exciting class of materials with novel mechanochemical properties and diverse applications including gas storage, catalysis and drug delivery.[124-129] The utility of this growing class of materials

has expanded to include controlled encapsulation and release of drugs where it is of particular importance to have protected particles on the nanoscale.

Virus capsids and other protein cages have been extensively employed as nanoscaffolds for the size constrained synthesis of minerals and polymers, presentation of antibodies and glycans, and transport of contrast agents and dyes with materials, catalytic, and medical applications.[25,27,130-134] The particle to particle uniformity of the protein cage allows for the exquisite control over the size of materials contained within the structure. The use of engineered specific chemical modification sites on the cage architecture has allowed control over the number and location of attached dyes, organometallics, tethererd targeting moieties and initiation sites of polymers. By taking advantage of the features of protein cages as synthetic containers, new routes toward coordination polymer synthesis with uniform particle size and mulifunctionality can be developed.

Results and Discussion

Initial attempts to create an encapsulated coordination polymer within a protein cage utilized the attachment of a single 1,10-phenanthroline (phen) ligand to unique cysteine residues on the interior of a protein cage. The 12 nm exterior diameter protein cage was a mutant of the 24 subunit small heat shock protein from Methanococcus jannaschii bearing an internal cysteine residue (sHsp G41C). Titration of the sHsp G41C-phen construct with Fe(II) resulted in 0.3 Fe(II)/subunit with an associated increased in absorbance at 530 nm suggesting the formation of a $Fe(phen)_3^{2+}$ complex, with phenanthrolines contributed from adjacent subunits, blocking the possibility of

propagating the polymer and suggesting that the protein cage has significant conformational flexibility.

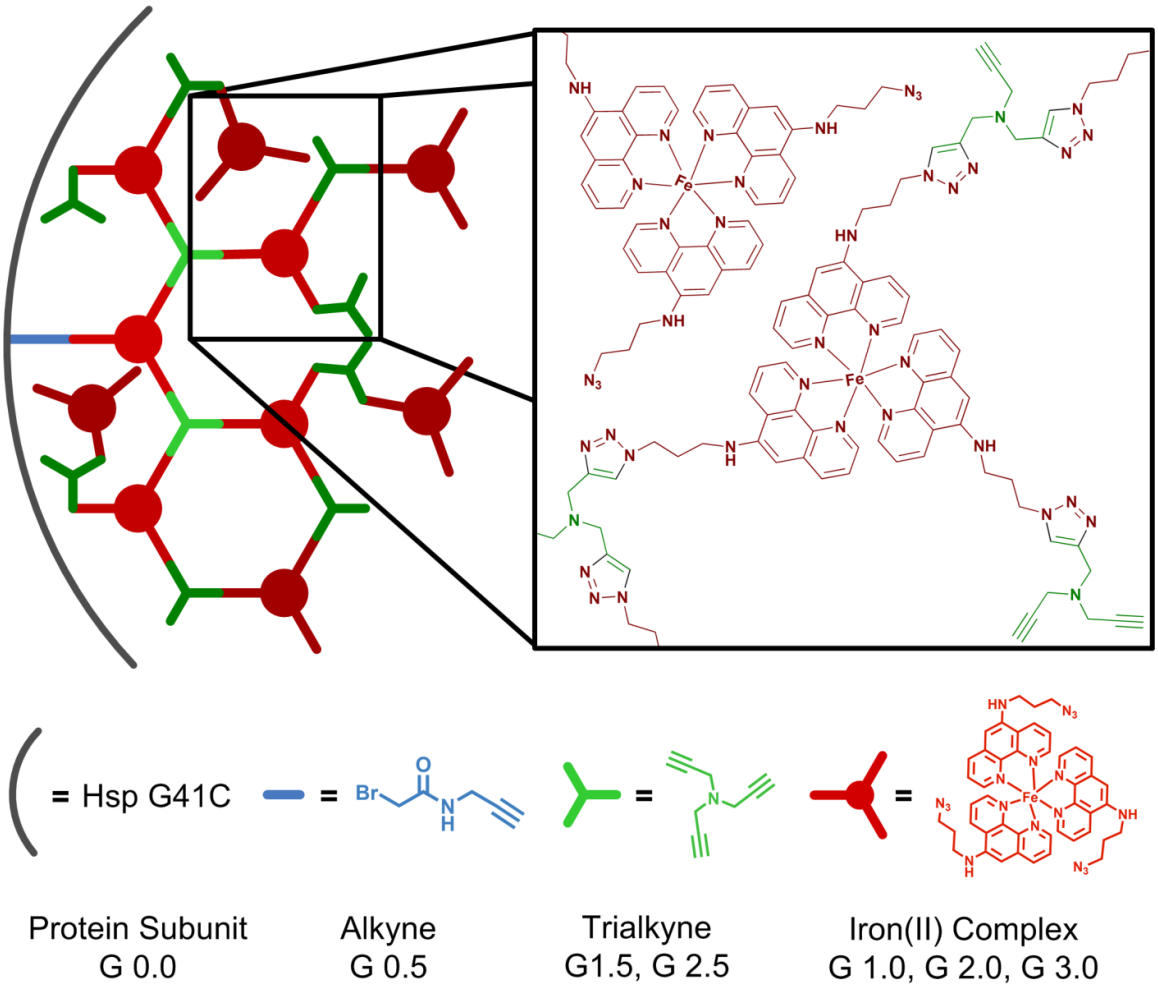

Figure 4.1: Model scheme for the stepwise formation of a coordination polymer inside sHsp G41C starting at the internal cysteine of each protein subunit. Each generation is added through the introduction of either an alkyne or azide functional group containing compound.

Thus, we took the approach of pre-forming the metal coordination complexes and polymerizing these building blocks through a Cu(I) catalyzed ‘click’ reaction via pendant azide and alkyne moieties through the formation of a 1,4-disubstituted 1,2,3-triazole. In

particular this ligand based method allows for specific stepwise additions of different metal coordination centers that may not otherwise polymerize under mild aqueous reaction conditions. This coupling reaction was selected due to its demonstrated compatibility with proteins and high reaction specificity having been used extensively for the attachment of a variety of ligands to proteins[135] and generation of related branched organic polymers within the sHsp G41C construct.[37]

We applied this ligand-ligand coupling approach, as summarized in Figure 4.1, to create a branched coordination polymer, which was grown in a stepwise manner with discrete generations. The genetically introduced interior cysteine (G41C) was the polymer initiation site, established by reaction with N-propargyl bromoacetamide to generate a protein bound alkyne functionality, identified as generation 0.5 (G0.5). The first Cu(I) catalyzed click reaction was between the this cage bound alkyne and a Fe(II) $(phenanthroline)_3$ coordination complex, bearing pendant azide groups, to form generation 1.0 (G1.0). The exposed branching azide functional groups on the coordination complex were subsequently reacted with tripropargylamine to form generation 1.5 (G1.5), with further branching of the polymer. The azide coordination complex and alkyne linkers were added and coupled alternatively through G3.0 at which point no further increase in polymerization was observed.

The cysteine reactive alkyne, N-propargyl bromoacetamide, used to form G0.5 was synthesized according to established proceedures[79] and was reacted with the protein (sHsp G41C, 50 mM phosphate, 100 mM NaCl, pH 7.5 buffer) in a 6-fold molar excess with respect to cysteine at room temperature for 3 hrs. This labeling reaction was

quenched with an equimolar addition of dithiothreitol and allowed to react for an additional 30 min followed by dialysis. Analysis of the product by subunit MS ESI-TOF) revealed greater than 80% single labeling of the subunits with trace (<5%) double labeled subunit due to reaction with available lysine residues in addition to the cysteine with the remainder of subunits staying unlabeled.

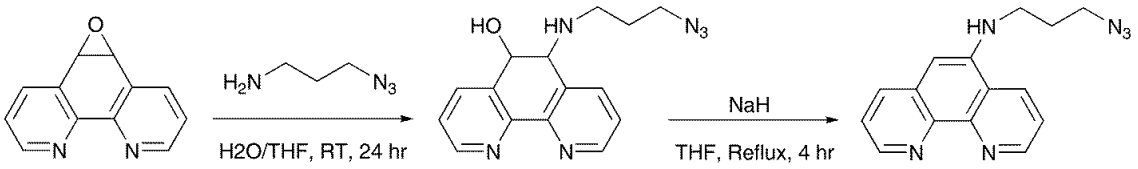

Figure 4.2: N-(3-azidopropyl)-1,10-phenanthrolin-5-amine (az-phen) synthesis scheme. Additional reaction details are contained in the Appendix B.

The azide containing phenanthroline ligand used in the Fe(II) coordination complex was synthesized in two steps (summarized in Figure 4.2) starting with the reaction of 5,6-epoxy-5,6-dihydro-1,10-phenanthroline with 3-azidopropylamine[37] followed by dehydration with sodium hydride to form the fully aromatized N-(3-azidopropyl)-1,10-phenanthrolin-5-amine (az-phen).[136] The desired Fe(II) coordination complex formed instantaneously at room temperature when a fresh aqueous solution containing ammonium iron(II) sulfate hexahydrate was mixed in a 1:3 ratio with a methanol solution of 5-aminoazido-1,10-phenanthroline to yield $Fe(az\text{-}phen)_3^{2+}$ as indicated by the solution turning a bright red color. The desired complex was precipitated using ammonium hexafluorophosphate and recrystallized from methylene chloride and ether. The identity of the resulting material was verified by mass spectrometry and NMR (Appendix B) indicating a low spin d6 Fe(II) complex.

Each generation of the polymer (G1.0-G3.0) was constructed (Figure 4.1) by click-based coupling to the previous generation of either Fe(azide-phen)$_3^{2+}$ (G1.0, G2.0, G3.0) or tripropargylamine (G1.5, G2.5) in the presence of $CuSO_4$ mixed with tris(hydroxypropyl)triazolylmethyl-amine, aminoguanidine and sodium ascorbate.[78,137] The reaction was allowed to proceed for 1 hr at room temperature followed by dialysis and size exclusion chromatography to remove small molecule reactants. Alternatively the click coupling was catalyzed using the Cu(I) catalyst, $Cu(CH_3CN)_4(OTf)$, in the presence of sulfonated bathophenanthroline as previously described with commensurate polymerization observed but increased protein loss.[37,82,135] All samples and data described in this manuscript were formed using the $CuSO_4$/ascorbate based reaction protocol. No precipitation occurred with the protein in solution, suggesting that the polymerization reaction is spatially localized to within the cage-like structure of the sHsp. However, when the reaction components were mixed at an equivalent concentration, in the absence of the protein cage, a dark red precipitate formed over the same reaction period, due to unconstrained bulk polymerization.

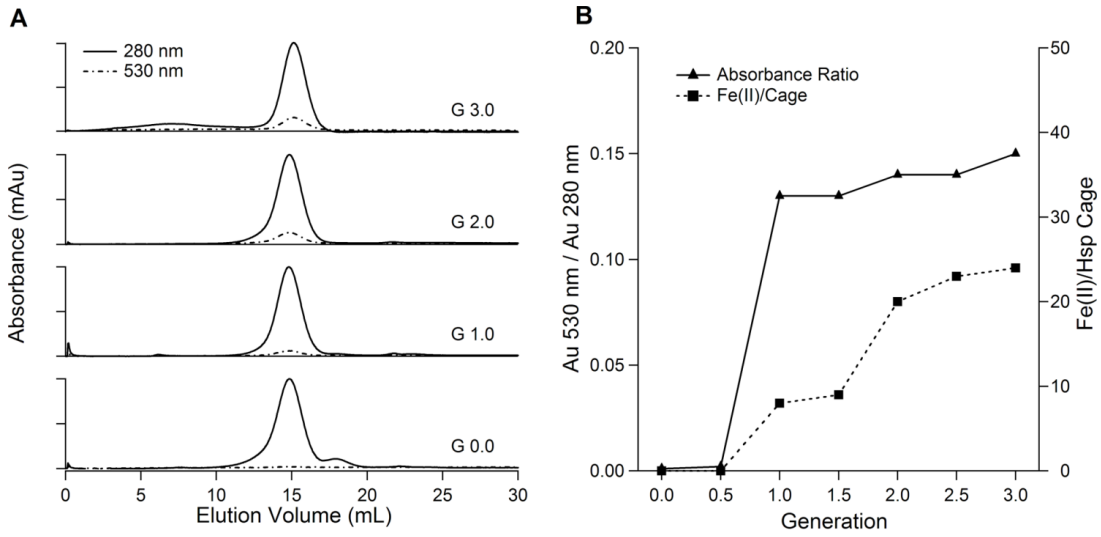

Figure 4.3: Size exclusion chromatography of sHsp G41C generations. (A) The solid line is the absorbance at 280 nm and the dashed line is the absorbance at 530 nm. (B) The ratio of the absorbance at 530 to 280 nm at each generation and the equivalent number of Fe(II) moieties per a cage. The absorbance at 530 nm is only due to the $Fe(az\text{-}phen)_3^{2+}$, while the absorbance at 280 nm is from both the protein and the $Fe(az\text{-}phen)_3^{2+}$.

Size exclusion chromatography elution profiles of each generation, (Figure 4.3A) exhibited nearly identical elution times to that of the starting material sHsp G41C. The absorbance of the $Fe(azide\text{-}phen)_3^{2+}$ complex, which has a maxima at 530 nm, co-eluted with the protein indicating that the complex is tightly associated with the protein cage. As additional $Fe(azide\text{-}phen)_3^{2+}$ moieties were added to the growing branched polymer with each integer generation (Figure 4.3B), the ratio of the absorbance at 530 nm to 280 nm increased. Little to no increase in the absorbance ratio and number of irons per a cage were observed in the half generations as expected. In a similar fashion, the ratio at G3.0 rose to the level observed in G2.0, but did not exceed the value indicating that there was no further extension of the polymer. The protein at each generation was quantified using the Bradford assay. Using the extinction coefficient at 530 nm (8.8 mM-1) the

concentration of Fe(azide-phen)$_3^{2+}$ in each generation was calculated to obtain the number of Fe/cage to be 8, 9, 20, 23, and 24 for G1.0. G1.5, G2.0, G2.5, and G3.0, respectively.

The number of irons incorporated is reasonable based on an initial labeling efficiency of the cage of 80% with the bromo-alkyne (G0.5) followed by 45% reaction efficiency for the addition of the first Fe complex (G1.0). The next two generations (G1.5, G2.0) have a combined efficiency of 50% with either the trialkyne generation or the second addition of the Fe complex being more efficient than G1.0. The fact that no further increase in the number of irons incorporated into generation (G3.0) is evidence that all the accessible alkynes have been reacted.

The volume occupied by the coordination polymer, predicted by molecular modeling of the monomers, and based on the number of irons/cage, is about 20% of the interior volume of the cage. This filled volume compares well with the click based organic polymer inside sHsp G41C with a nearly equivalent (18%) portion of the interior volume occupied at the final generation.[37]

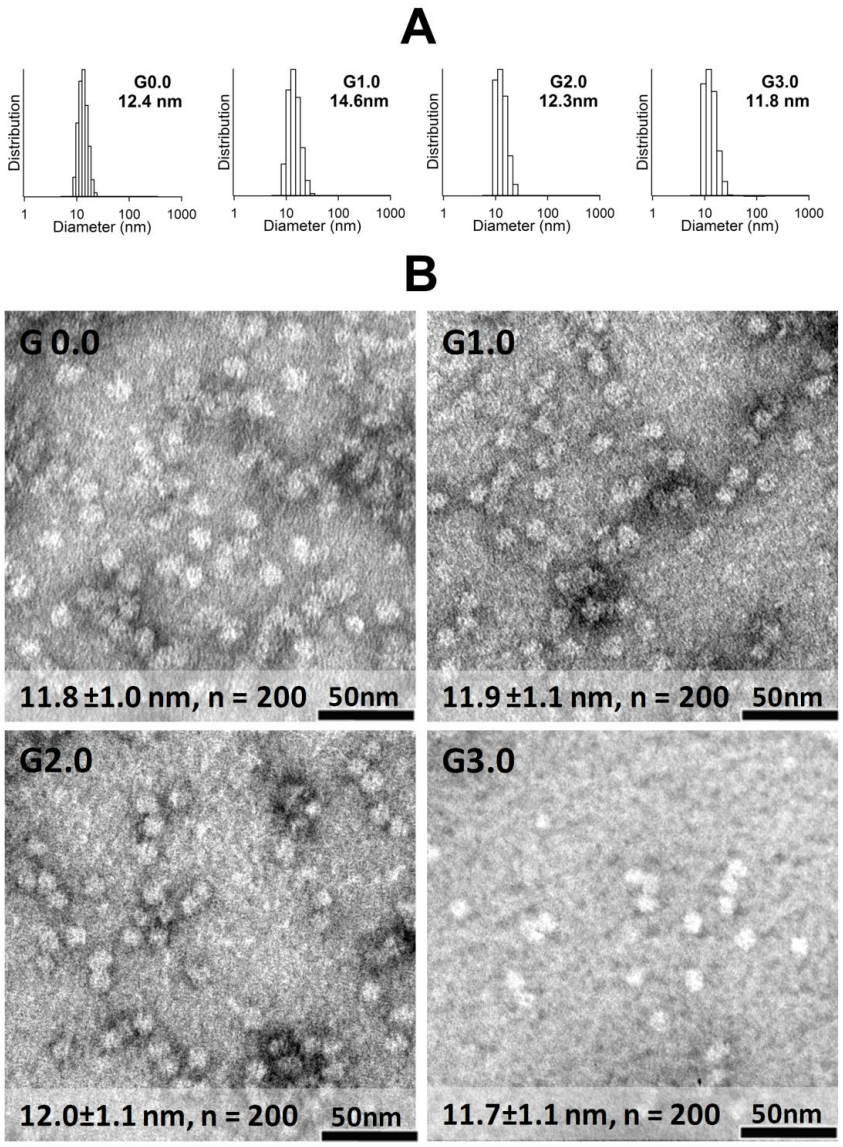

Figure 4.4: Comparison of the size of the native protein cage (sHsp G41C G0.0) with the generations where the Fe(II) coordination complex was added (G1.0, G2.0, G3.0) evaluated by DLS (A) and TEM (B). The values presented in (A) are the mean hydrodynamic diameter of the DLS distribution. The samples in (B) were stained with 2% uranyl acetate for visualization of the protein cage.

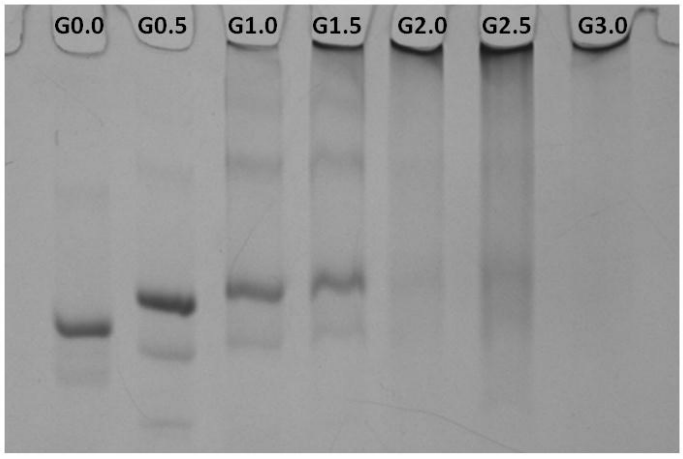

Figure 4.5: Coomassie stained acid urea denaturing gel evidence of cross-linking of the protein subunits. The bands below the main subunit band are a degradation product of the sHsp protein.[53]

The size distributions of the protein-coordination polymer samples were nearly identical to the native sHsp G41C G0.0 when investigated by SEC, dynamic light scattering (DLS) and transmission electron microscopy (TEM) (Figure 4.4). DLS for the G41C G0.0, G1.0, G2.0, and G3.0 samples revealed particle diameters of 12.4, 14.6, 12.3, and 11.8 nm respectively. Negative stain TEM revealed intact cage-like architectures 12 nm in diameter for each of the generations. Collectively these data confirm that the cage structure remains intact during the synthesis with the polymer constrained to the interior of the cage.

Using acid urea denaturing conditions to effectively dissociate the native protein cage into subunits (G0.0, Figure 4.5) each polymer generation was treated and run on an acid urea gel to confirm that a polymer was formed inside the cage thereby cross-linking the subunits.[138] As the generations increase across the gel, the monomer, which is dominant in G0.0 and G0.5, gradually decreases with a parallel increase in intensity at the

top of the gel. This indicates that there is a steady increase in mass of the sHsp with increasing generation. Pale pink bands could be seen at the top band in lanes G1.5 to G3.0 before staining for protein indicating the presence of the $Fe(azide\text{-}phen)_3^{2+}$ polymer complex. Treating G3.0 with the strong iron chelator, deferoxamine, in a ratio of 10:1 compared to sample iron, removed the iron from the coordination complex eliminating the pink sample color.

Conclusion

In summary, we have constructed a branched coordination polymer selectively within the protein cage of sHsp, which extends across the interior cavity of the sHsp G41C cage protein. This polymer was initiated at the genetically introduced cysteine residue on each subunit and preceded by first forming the coordination complex and then synthesizing the coordination polymer using a ligand-ligand click based reaction allowing the cage architecture to be retained while cross-linking the subunits.

CHAPTER 5

USING THE INTERIOR CAVITY OF THE P22 CAPSID FOR SITE-SPECIFIC INITIATION OF ATOM TRANSFER RADICAL POLYMERIZATION

Introduction

The use of protein-polymer composite materials is a growing field that takes advantage of the monodispersity of biomolecules while imparting new materials properties via polymer conjugation. Much of the work in this area has been focused on site-specific conjugation of polymers to monomeric proteins, but when more complex multimeric biomolecules are employed not only is the polymer location on the primary sequence of interest, but also the spatial relationship between the polymer and the overall protein architecture becomes important.

The use of virus-like particle (VLP) proteins, which form symmetric protein shells defining an interior cavity, relies on two distinct environments that can be modified - either the exposed exterior or the confined interior. Utilizing the exterior surface, polymer formation or attachment has been employed as a means of appending molecules of interest designed to alter VLP solubility, increase stability, or introduce new functionalities.[85,139] In this chapter the use of atom transfer radical polymerization (ATRP) for directed polymer synthesis constrained within a virus like particle derived from the bacteriophage P22 (Figure 5.1) is described. This method is rapid and results in products with low polydispersity, is also promiscuous with respect to the range of

monomers that can be used, and the simplicity of the ATRP initiator means that it can be readily attached to the protein cage in a site-specific manner.

To demonstrate that the ATRP driven strand and crosslinked polymer growth can be applied to the P22 VLP system with spatial control, two P22 point mutants (K118C or S39C) were considered. For this initial study a neutral very water soluble monomer (TRIS-acrylamide) was selected for use with or without the addition of bisacrylamide as a crosslinker. Although both the K118C and S39C initiation sites were effective polymerization locations, based on this test series the S39C location was determined to be a more robust internal polymer directing site for selective internal polymerization.

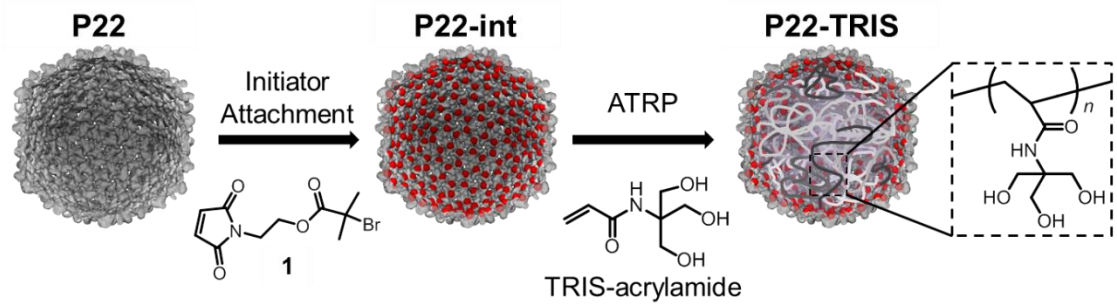

Figure 5.1: Synthesis of the polymer P22 VLP composite. P22 modified with a cysteine reactive ATRP initiator (**1**) is used as macroinitiator for ATRP growth of poly(TRIS-acrylamide) strands or a poly(TRIS-acrylamide) network crosslinked with bisacrylamide inside the virus like particle.

Results and Discussion

Each of the two mutants used in this study contain a single point mutation in the wild-type P22 coat protein, K118C and S39C, which introduces an addressable thiol in each for attachment of an ATRP initiator (1). The K118C mutation site is located in the long helix (helix 1) and was developed prior to this work, where it was demonstrated that

once the capsid is expanded the K118C location labels well.[59] The facial exposure of this site in the expanded morphology of P22 appears to be exterior facing according to the structural models (Figure 5.2), but previous work with this mutant indicates that this site may be interior facing making this an interesting mutation site for further study.[59,64] Due to the labeling efficiency, improvement of the K118C mutation in the expanded morphology over the empty shell morphology the expanded morphology of the capsids was selected for this study. To complement the apparently exterior exposed K118C mutant, the S39C mutant, located on an interior exposed flexible loop, was designed specifically such that the thiol is exposed exclusively to the interior according to the P22 structural models (Figure 5.3). The complete characterization of this new mutant is described in Chapter 6.

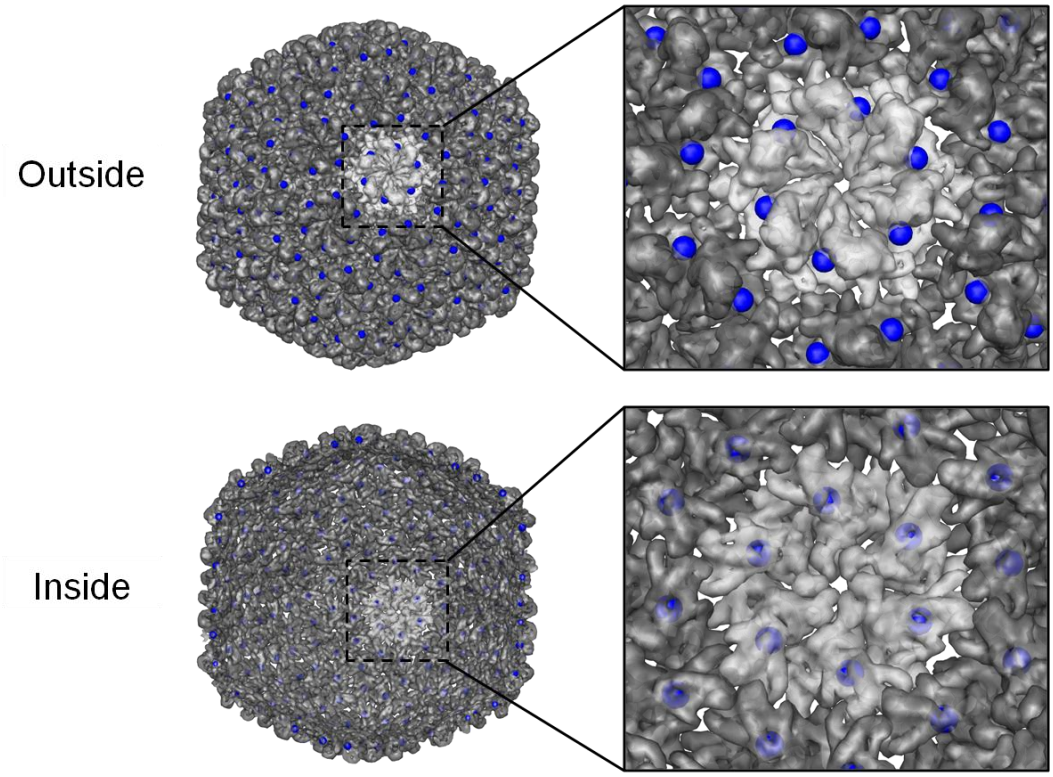

Figure 5.2: Structural model of the expanded morphology of the P22 capsid that shows the location of the K118C mutation. The location of the modified residue, K118C (in blue) was derived from a structural model of P22 using coordinate data [140] deposited as Protein Data Bank file 2XYZ. Both a view of the exterior of the capsid (top) and a half shell cut-away view revealing the interior (bottom) of the capsid are included.

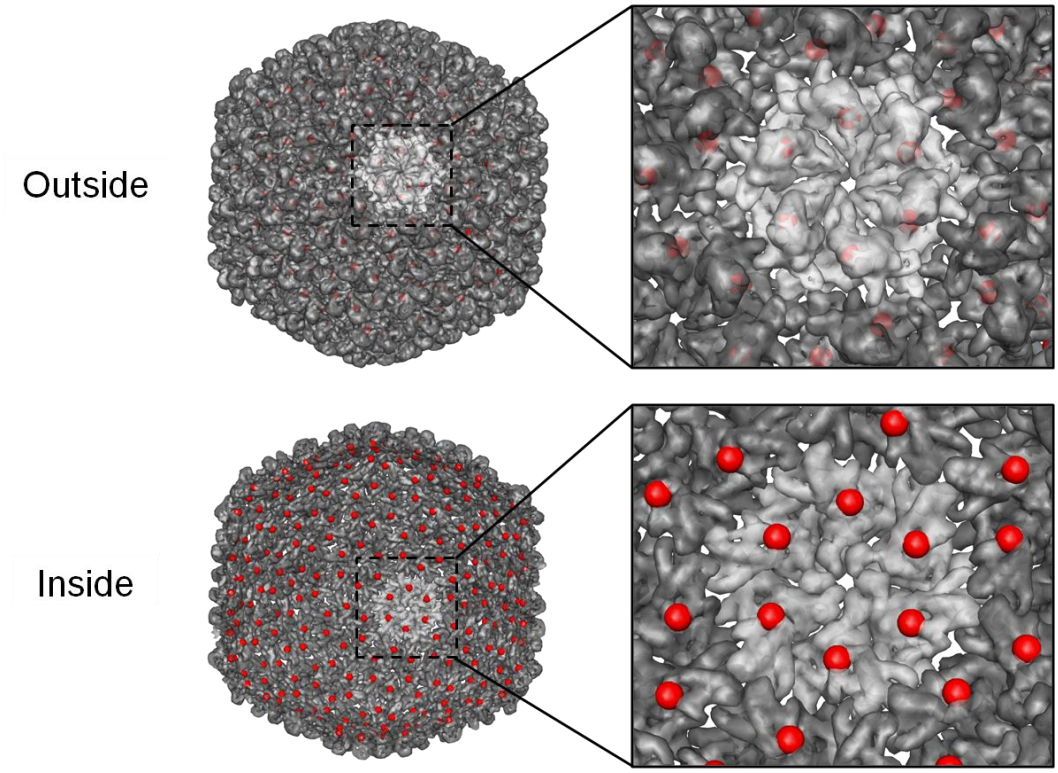

Figure 5.3: Structural model of the expanded morphology of the P22 capsid that shows the location of the S39C mutation. The location of the modified residue, S39C (in red) was derived from a structural model of P22 using coordinate data [140] deposited as Protein Data Bank file 2XYZ. Both a view of the exterior of the capsid (top) and a half shell cut-away view that revealed the interior (bottom) of the capsid are included and illustrate that, according to this model, this mutation site is interior exposed.

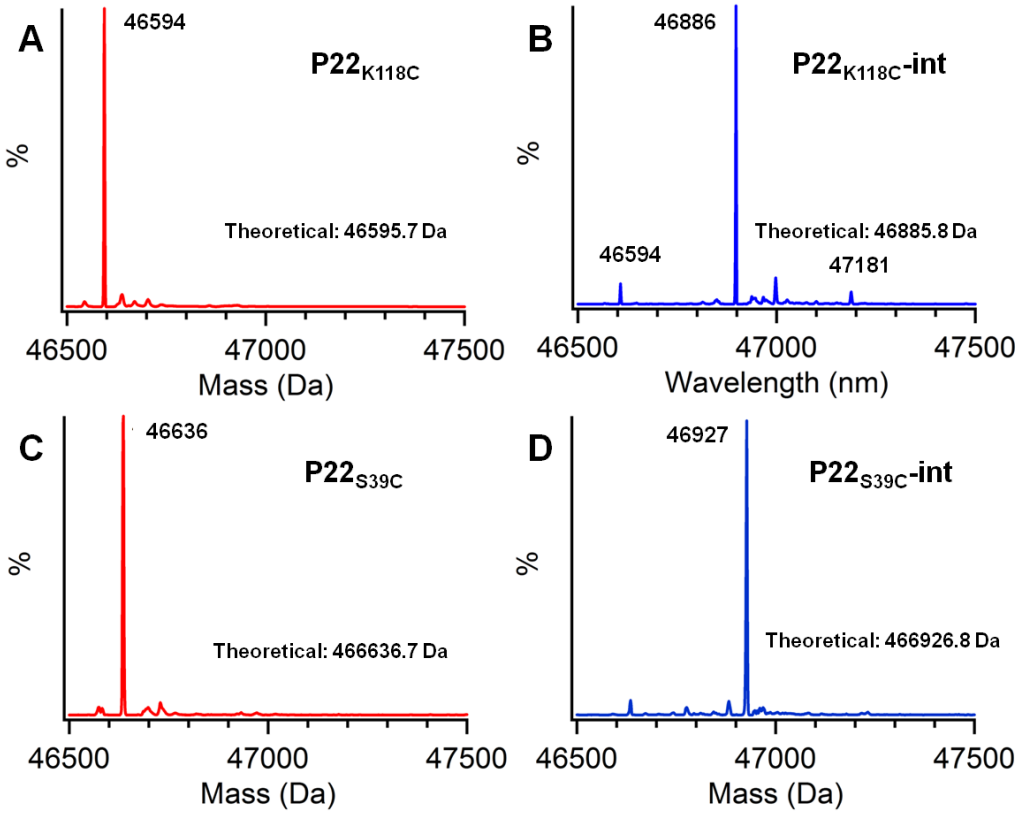

Figure 5.4: Representative subunit mass spectrometry analysis of $P22_{S39C}$ and $P22_{K118C}$ macroinititators.

To make the P22 macroinitiators, the P22 mutants (K118C and S39C) were labeled with initiator **1**. This cysteine reactive ATRP initiator was chosen because of its good labeling and initiation as well as a demonstrated compatibility with biomolecules.[91,141] It was synthesized through modification of established protocols and selectively reacted with $P22_{K118C}$ and $P22_{S39C}$ to make the macroinitiators, $P22_{K118C}$-int and $P22_{S39C}$-int, respectively. Both mutants reacted with near quantitative single labeling of the introduced cysteine as observed by subunit mass spectrometry (Figure 5.4).

Initial efforts were directed towards the P22-int macroinitiator constructs under a range of TRIS-acrylamide monomer loadings and reaction temperatures using standard ATRP biomolecule conditions with a Cu(I)/bipyridine catalyst.[142] Athough polymerization was observed as an increase in mass and distribution of the P22 subunit band by SDS-PAGE gels under all the tested conditions it was the midrange polymerization (2,600 monomers/subunit) and temperature conditions (23ºC) which were selected for further investigation and are described here. To make the protein-linear polymer conjugates ($P22_{S39C}$-TRIS and $P22_{K118C}$-TRIS), TRIS-acrylamide was the only monomer in solution, while for the protein-crosslinked polymer samples ($P22_{S39C}$-xTRIS and $P22_{K118C}$-xTRIS) bis-acrylamide was added as 20% of the total monomer present. In each sample, after 3 hr reaction time, the synthesis was halted by exposing the sample to air and the protein-polymer conjugate (P22-TRIS or P22-xTRIS) was purified away from remaining monomers and the copper catalyst using a commercial desalting spin column, which separates large macromolecular complexes from small molecular species.

Each of the reactions was observed to proceed rapidly and exhibit increased subunit mass by denaturing gel analysis, as indicated by the shift to higher molecular mass within 5 min of reaction initiation, with only minor additional mass increase up to 180 min (Figure 5.5A, 5.6A, 5.7A, 5.8A). By this analysis method, it appeared that not all of the initiator labeled subunits produced sufficiently long polymer chains for a mass shift to become apparent. Others have also observed this incomplete initiation in both monomeric and multimeric systems when making grafted-from protein-polymer composites.[85,91,141,142] Significantly when the crosslinker, bis-acrylamide, was included in

the reaction additional blurred bands, corresponding to multimers of subunits, were observed in the P22-xTRIS samples (Figure 5.7A and 5.8A) indicating that the subunints were covalently connected through the crosslinked polymer. The intensity of the upper bands observed in the $P22_{S39C}$-xTRIS described are rather more pronounced than usually observed in this mutant for samples treated under similar conditions, which may indicate that the reaction worked particularly well in in this specific instance. Even so, compared to the $P22_{S39C}$ construct significantly less subunit-to-subunit crosslinking was observed in the $P22_{K118C}$ construct indicating that the growing strands may be more spatically separated.

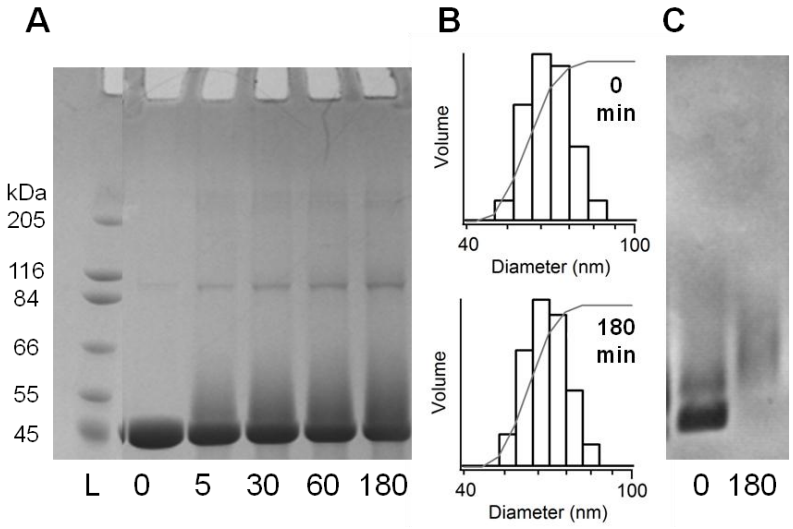

Figure 5.5: Characterization of the $P22_{S39C}$-TRIS reaction. A) SDS-PAGE gel showing increase in Mw with increasing reaction time from 0 to 180 min (L is the Mw ladder). B) DLS of P22 sample before and after 180 min polymerization reaction showing an unchanged diameter (63 nm). C) Native agarose gel electrophoresis showing almost the same migration behavior before and after polymerization.

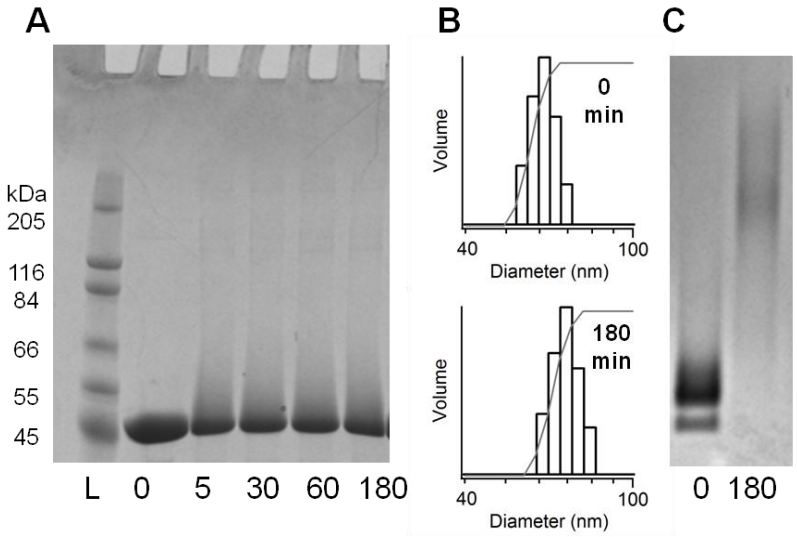

Figure 5.6: Characterization of the $P22_{K118C}$-TRIS reaction. A) SDS-PAGE gel showing increase in Mw with increasing reaction time from 0 to 180 min (L is the Mw ladder). B) DLS of P22 sample before and after 180 min polymerization reaction showing a changed diameter (60 nm to 68 nm). C) Native agarose gel electrophoresis showing a large difference in migration consistent with some polymer on the exterior surface.

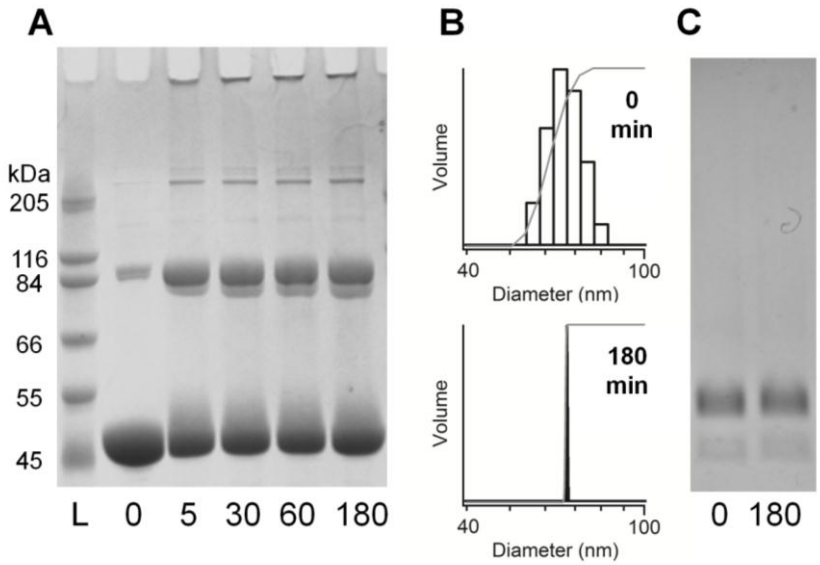

Figure 5.7: Characterization of the $P22_{S39C}$-xTRIS reaction. A) SDS-PAGE gel showing increase in Mw with increasing reaction time from 0 to 180 min (L is the Mw ladder). B) DLS of P22 sample before and after 180 min polymerization reaction showing an unchanged diameter (67 nm). C) Native agarose gel electrophoresis showing identical migration behavior before and after polymerization.

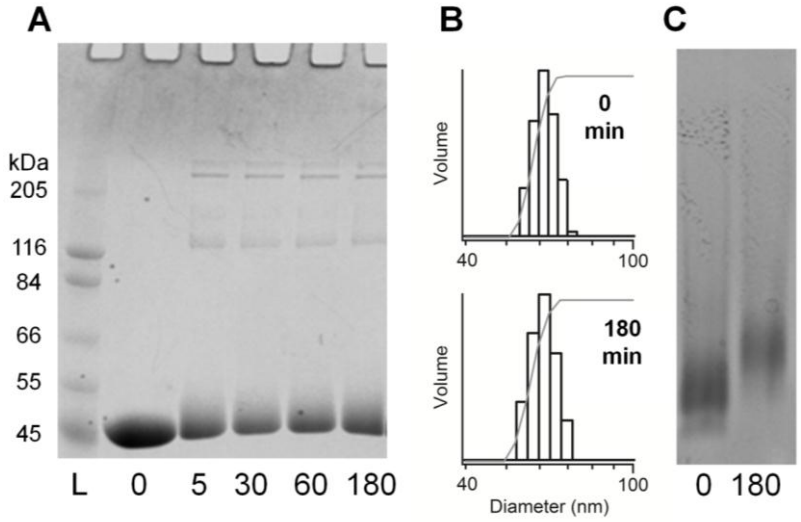

Figure 5.8: Characterization of the $P22_{K118C}$-xTRIS reaction. A) SDS-PAGE gel showing increase in Mw with increasing reaction time from 0 to 180 min (L is the Mw ladder). B) DLS of P22 sample before and after 180 min polymerization reaction showing an unchanged diameter (62 nm). C) Native agarose gel electrophoresis showing almost the same migration behavior before and after polymerization.

Additional data supporting the presence of polymer was obtained using multi-angle light scattering (MALS), which can be used to obtain the total mass of a composite. In each sample a similar mass increase over starting material was observed. When the intact $P22_{S39C}$ constructs were measured using multi-angle light scattering (Figure 5.9 and 5.10) the molecular mass of the entire composite increased from 21.7 MDa ($P22_{S39C}$-int) to 23.4 MDa ($P22_{S39C}$-TRIS) and from 18.7 MDa ($P22_{S39C}$-int) to 20.1 MDa ($P22_{S39C}$-xTRIS). These mass increases correspond to the incorporation of about 9,000 monomers/cage (21 monomers/subunit) and 8,000 monomers/cage (19 monomers/subunit) for $P22_{S39C}$-TRIS and $P22_{S39C}$-xTRIS, respectively. A similar increase was observed for the $P22_{K118C}$-linear polymer construct going from 19.9 MDa ($P22_{K118C}$-int) to 21.0 MDa ($P22_{K118C}$-TRIS) and corresponding to the incorporation of roughly

6,000 monomers/cage (14 monomers/subunit) (Figure 5.11). Comparison of the $P22_{K118C}$ crosslinked sample indicated a slightly larger mass increase going from 19.9 MDa ($P22_{K118C}$-int) to 22.3 MDa ($P22_{K118C}$-xTRIS), which is roughly 13,000 monomers/cage (32 monomers/subunit). For these samples, the data were fit using the simplest data processing method, which requires the use of a single specific refractive index increment (dn/dc, 0.185), which was possible since the dn/dc for acrylamides (0.16-0.19)[143] is close to that of protein (0.185). Some of the variation in the observed P22-int mass from the theoretical mass of 19.6 MDa is due to residual P22 scaffold protein present in the capsids used as starting material in some of the samples.

To determine the location of the polymer, whether exposed to the exterior or confined to the interior of the P22, the size of the P22-polymer constructs were compared to their initial macroinitiator P22 complex using DLS, SEC, and native agarose gels. In both $P22_{S39C}$ samples the data suggest the diameter remained the same before and after polymerization indicating that the polymer is confined to the interior of the capsid in these constructs. By DLS the particle diameters were measured to be 63±8 nm ($P22_{S39C}$-int) and 63±7 nm ($P22_{S39C}$-TRIS) for the uncrosslined sample (Figure 5.5B), while the crosslinked sample (Figure 5.7B) had diameters of 67±7 ($P22_{S39C}$-int) and 67±1 nm ($P22_{S39C}$-xTRIS). The difference in the starting initiator diameter is partially due to differences in the degree of expansion of the P22 capsid material used in the experiments. Purification by SEC of $P22_{S39C}$-TRIS and $P22_{S39C}$-xTRIS compared to their respective starting $P22_{S39C}$-int resulted in identical time, further confirming that the protein cage is unchanged in diameter and thus the polymer is likely confined to the interior of the

protein cage (Figure 5.9 and 5.10). In addition, analysis of the native constructs by agarose gel electrophoresis (Figure 5.5C and 5.7C) exhibited only a minor shift in electrophoretic mobility upon polymerization indicating that the addition of the polymer did not contribute significantly to an increased cross-sectional area. Based on these data, the S39C mutation appears to clearly direct growth such that the polymer is localized on the interior of the capsid under both reaction conditions.

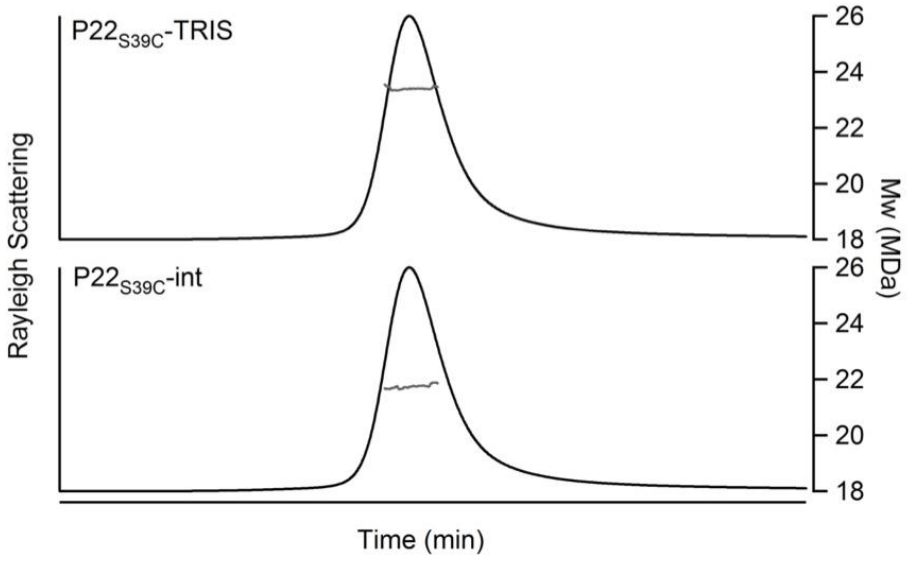

Figure 5.9: Size exclusion chromatography and multiangle light scattering of $P22_{S39C}$ before and after polymerization. No change in elution volume or particle diameter was observed between the samples but an increase in Mw of 1.7 MDa was observed between the samples.

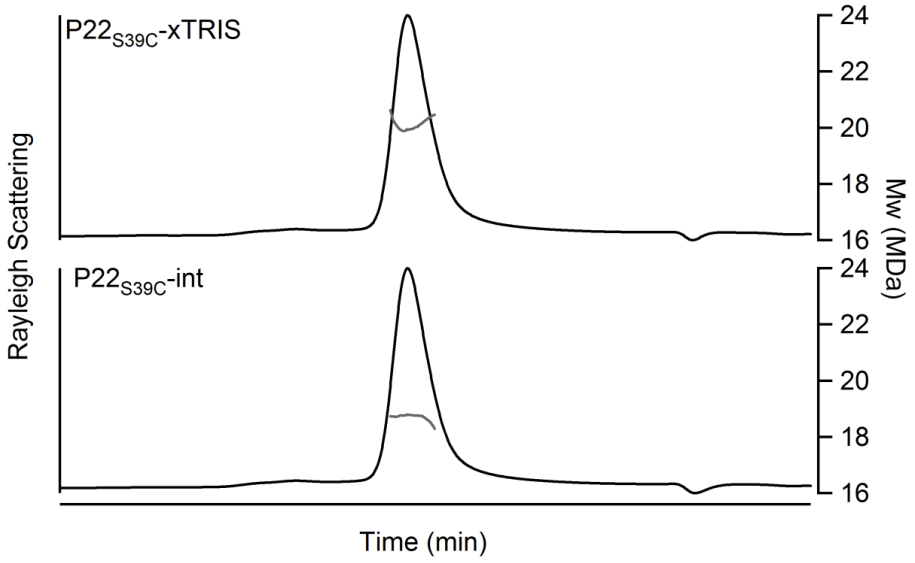

Figure 5.10: Size exclusion chromatography and multiangle light scattering of $P22_{S39C}$ before and after crosslinked polymerization. No change in elution volume or particle diameter was observed between the samples but an increase in Mw of 1.4 MDa was observed between the samples.

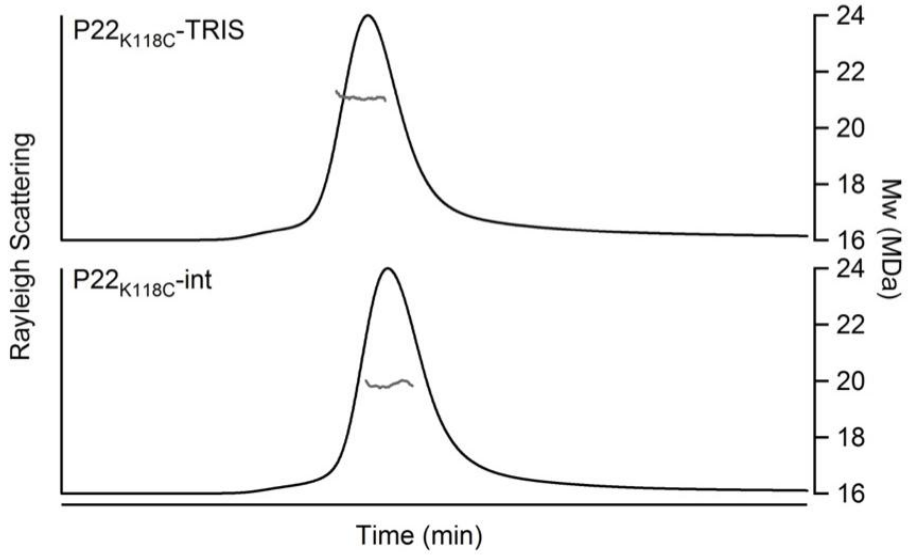

Figure 5.11: Size exclusion chromatography and multiangle light scattering of $P22_{K118C}$ before and after polymerization. A change in elution volume and particle diameter was observed in the sample after polymerization consistent with some polymer on the exterior surface. An increase in Mw of 1.1 MDa was observed between the samples.

Unlike the S39C constructs, when the $P22_{K118C}$-int was treated to make $P22_{K118C}$-TRIS, the construct exhibited an increase in diameter of about 8 nm, from 60 ± 5 nm to 68 ± 6 nm, as measured by DLS suggesting partial growth of the polymer on the exterior of the cage (Figure 5.6). Upon analysis by size exclusion chromatography it was apparent that the $P22_{K118C}$-TRIS increased in size compared to $P22_{K118C}$-int as evidenced by a shift to earlier elution time, indicating the formation of a larger particle (Figure 5.11). Also analysis of the native constructs by agarose gel electrophoresis indicated a significant shift in electrophoretic mobility suggesting that the cross-sectional area of the construct was significantly altered by the growth of the polymer.

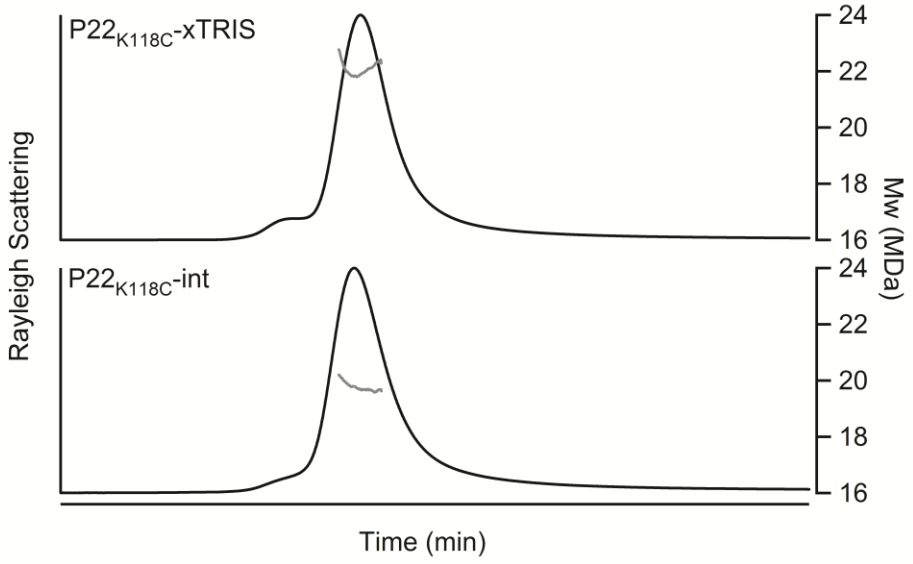

Figure 5.12: Size exclusion chromatography and multiangle light scattering of $P22_{K118C}$ before and after crosslinked polymerization. No shift in elution time was observed indicating that the particle dimeter remains constrant and an increase on 2.3 MDa mass was observed between the samples.

Suprisingly when the $P22_{K118C}$-int was treated to make $P22_{K118C}$-xTRIS, the construct did not exhibit an increase in diameter starting at 62 ± 5 nm and ending at 62 ± 4 nm, as measured by DLS (Figure 5.8B) suggesting the small amount of crosslinking observed by denaturing gel may be sufficient to limit growth of this polymer to the interior. Analysis of $P22_{K118C}$-xTRIS by size exclusion chromatography confirmed this observation as no shift in elution time was measured (Figure 5.12). In addition, analysis of the native constructs by agarose gel electrophoresis indicated only a minor shift in electrophoretic mobility further suggesting that the cross-sectional area of the construct was not altered by the growth of the polymer.

Taken together, the $P22_{K118C}$-TRIS and $P22_{K118C}$-xTRIS data support a model where the K118C mutation site can access both the exterior and interior environments. Addition of a crosslinking agent appears to be sufficient in this case to cause the majority of growth to be interior directed, where the crosslinking limits the flexibility of the polymer sufficiently to restrict interior-exterior sampling of the polymer. This is in agreement with the apparent internal directing behavior of this mutant when a multi generation organic crosslinked click chemistry based polymer is formed originating from this site.[64] This data also reinforces the shortfalls of depending solely on structural models, of large macromolecular constructs such as P22, to predict mutation site behavior. In the structural model (Figure 5.2) the K118C site appears to be mostly exterior exposed, but this model does not reflect the potential dynamic nature of this region which could reasonably cause the site to be alternately interior and exterior facing. Although the K118C construct is not ideal for our intended purpose, of directed interior

polymerization, this mutation site may be useful for future use as a switchable or externally modified polymer-VLP.

Conclusion

The $P22_{S39C}$-based macroinitiator effectively directs both linear strand and crosslinked polymer growth to the VLP interior, resulting in confined polymer growth as the protein shell acts as a barrier, leaving only the protein shell exposed to the bulk solution. The $P22_{K118C}$-based macroinitiator presents a less ideal location, directing polymer less predictably such that in this particular monomer case is inside directing with crosslinker present and outside directing without. Due to the simplicity, modular nature, and potential loading capacity of the ATRP based approach taken to make these P22-polymer internal composites, this same method is further explored in the following chapters to make a range of novel VLP-polymer composites.

Experimental

Materials.

All reagents were analytical grade and purchased from either Sigma-Aldrich or Fisher Scientific and used as received unless otherwise noted. Dichloromethane was distilled over calcium hydride prior to use. All water was deionized using a NANOpure water purification system. Mutagenesis and purification of P22 were completed according to established protocols. Dynamic light scattering measurements were taken on a 90Plus particle size analyzer (Brookhaven). Multi-angle light scattering measurements

were collected using a Heleos (Wyatt) instrument with a size exclusion column and using a dn/dc value of 0.185 for all samples.

Synthesis of 2-Bromoisobutyrate Ethoxy Maleimide (**1**).

Compound **1** was synthesized by a modification of the procedures previously reported.[91,141] Ethanol-maleimide (200 mg, 1.42 mmol) was mixed on ice with triethylamine (197 ul, 1.42 mmol) in 5 mL dry dichloromethane. 2-bromo-2-methylpropionylbromide (266 ul, 2.13 mmol) was added dropwise. The reaction was allowed to warm to room temperature and was determined by thin layer chromatography to have reached completion after 1.5 hr. The solvent was removed and the product was subsequently cleaned via column chromatography (silica gel, dichloromethane) with a yield of 76%. ^{1}H NMR (500 MHz, $CDCl_3$) δ = 1.87 (s, 6H, CH_3); 3.84 (t, J = 5.5, 2H, NCH_2); 4.31 (t, J = 5.5, 2H, OCH_2); 6.71 (s, 2H, CH_{vinyl}). ^{13}C δ = 30.59 (CH_3), 36.57(NCH_2), 62.88(OCH_2), 134.26(CH_{vinyl}).

P22-int Macroinitiator Formation Conditions**.**

P22(S39C) or P22(K118C) in PBS, pH 7.6 (4 mL, 7.2 mg/mL) was infused with 156 µL of **1** (80 mM inDMSO, 10 fold excess per a subunit). The mixture was allowed to react for 3 hrs at room temperature. After 3 hrs the reaction was quenched with DTT (156 µL , 80 mM in water). To remove excess DTT and 1, the protein was pelleted at 48,000 rpm for 50 minutes in an ultra centrifuge (Sorvall) followed by resuspension into PBS, pH 7.6. By subunit mass spectrometry >95% of the subunits were labeled.

P22-TRIS Polymer Formation Conditions.

Each sample was made in a small crimp-top vial with the addition of 2500 μL monomer solution (2 wt% TRIS-acrylamide or 2 wt% 16:4 TRIS-acrylamide:bis-acrylamide, PBS, pH 7.6) and 875 μL PBS buffer (100 mM sodium phosphate, 50 mM NaCl, pH 7.6). To this mixture, 875 μL of P22-int (6.0 mg/mL, 0.11 μmoles subunit, pH 7.6) was added followed by pump and back filling with Ar 4 times to deaerate the mixture. The metal catalyst solution was made in a second vial using 10 mL deionized water degassed by bubbling Ar through the liquid for 20 minutes, to which was added 7.0 mg CuBr (0.049mmoles) and 15.6 mg 2,2'-bipyridine (0.10 mmoles). The vial was immediately sealed and sonicated for 5 min. To the monomer-protein vial, 750 μL of the metal catalyst solution was added and the vial was maintained at 23 ºC for the remaining duration of the experiment with time course aliquots taken at 0, 5,30, 60, and 180 min. Each timed sample was quenched by exposure to air and the protein-polymer composite was purified away from unreacted monomer and the copper catalyst using a spin column (Biorad, Micro Bio-Spin Columns P-30, PBS, pH 7.6).

Denaturing Gel Assay.

P22-int macroinitiators and P22-polymer composites were analyzed using SDS-PAGE on 10-20% gradient Tris-glycine gels (Lonza). Protein was detected by staining with Coomassie blue.

Native Agarose Gel Assay.

P22-int macroinitiators and P22-polymer composites were analyzed on 0.8% native agarose gel using 40 mM Tris-base, 5 mM sodium acetate, 1 mM EDTA, pH 8.2 running buffer and were run for 3 hrs at 65 volts.

Subunit Mass Spectrometry.

Subunit masses of the P22 coat and P22-int macroinitiators were analyzed by ESI-Q-TOF mass spectrometry (Q-TOF Premier, Waters) interfaced to a Waters Acquity UPLC and autosampler. [50] Mass spectra were acquired in the range of m/z 50-5000 and processed using the MaxEnt 1 algorithm for MassLynx version 4.1 to obtain deconvoluted average masses from multiple charge state distributions.

MANUSCRIPT IN CHAPTER 6

USING THE INTERIOR CAVITY OF THE P22 CAPSID FOR SITE-SPECIFIC INITIATION OF ATOM TRANSFER RADICAL POLYMERIZATION WITH HIGH DENSITY CARGO LOADING

Contributions of Authors and Co-Authors

Manuscripts in Chapters 3, 4, and 6

Radical Polymerization with High-Density Cargo Loading

Author: Janice Lucon

Contributions: Designed and carried out the experiments and wrote the manuscript.

Co-author: Shefah Qazi

Contributions: Characterized the samples by NMR and analyzed the relaxivity data.

Co-author: Masaki Uchida

Contributions: Assisted in experimental design and the initial characterization of the S39C mutant.

Co-author: Gregory J. Bedwell

Contributions: Characterized the samples by analytical ultracentrifugation.

Co-author: Ben LaFrance

Contributions: Assisted in the initial characterization of the S39C mutant.

Co-author: Peter E. Prevelige, Jr

Contributions: Obtained funding and coordinated the project.

Co-author: Trevor Douglas

Contributions: Obtained funding, coordinated the project, and assisted with the design of the experiments. Discussed the results and edited the manuscript at all stages.

Manuscript Information Page

Authors: Janice Lucon, Shefah Qazi, Masaki Uchida, Gregory J. Bedwell, Ben LaFrance, Peter E. Prevelige, Jr, and Trevor Douglas
Journal: Nature Chemistry

Status of the manuscript:
____ Prepared for submission to a peer-reviewed journal
____ Officially submitted to a peer-reviewed journal
____ Accepted by a peer-reviewed journal
_X__ Published in a peer-reviewed journal

Publisher: Nature Publishing Group
Issue in which manuscript appears: Volume 4, 781-788 (2012), Cover

CHAPTER 6

USING THE INTERIOR CAVITY OF THE P22 CAPSID FOR SITE-SPECIFIC INITIATION OF ATOM TRANSFER RADICAL POLYMERIZATION WITH HIGH DENSITY CARGO LOADING

Published: *Nature Chemistry*, **2012**, 4, 781-788 (Cover).

Janice Lucon[1,2], Shefah Qazi[1,2], Masaki Uchida[1,2], Gregory J. Bedwell[3], Ben LaFrance[1,2], Peter E. Prevelige, Jr.[3], and Trevor Douglas[1,2]

[1] Chemistry and Biochemistry Department, Montana State University, Bozeman, Montana, 59717
[2] Center for Bio-Inspired Nanomaterials, Montana State University, Bozeman, Montana, 59717
[3] Department of Microbiology, University of Alabama at Birmingham, Birmingham, Alabama, 35294

Abstract

Virus-like particles (VLPs) have emerged as important and versatile architectures for chemical manipulation in the development of functional hybrid nanostructures. Here we demonstrate a successful site -selective initiation of atom transfer radical polymerization reactions to form an addressable polymer constrained within the interior cavity of a VLP. Potentially, This protein–polymer hybrid of P22 and cross-linked poly(2-aminoethyl methacrylate) could be useful as a new high-density delivery vehicle for the encapsulation and delivery of small -molecule cargos. In particular, the encapsulated polymer can act as a scaffold for the attachment of small functional molecules, such as

fluorescein dye or the magnetic resonance imaging (MRI) contrast agent Gd-diethylenetriaminepentacetate, through reactions with its pendant primary amine groups. Using this approach, a significant increase in the labelling density of the VLP, compared to that of previous modifications of VLPs, can be achieved. These results highlight the use of multimeric protein–polymer conjugates for their potential utility in the development of VLP-based MRI contrast agents with the possibility of loading other cargos.

Introduction

The use of protein–polymer composite materials for medical and materials applications is a growing field that aims to take advantage of the exquisite monodispersity and bioactivity of biomolecules and also impart new material properties via polymer conjugation. When a responsive polymer is selected, new thermo-, light- and pH -sensitive macromolecular materials can be produced to control more fully the activity and phase solubility of the biomolecule.[93,94] By adding a specific polymer to the biomolecule, the composite material may exhibit improved retention, lowered immunogenicity and increased bioavailability.[95,96,144] To attain the desired final material properties, careful selection of both the protein and the polymer components is essential. Much of this work focused on the site-specific conjugation of polymers to monomeric proteins, but when more complex multimeric biomolecules are employed, not only is the polymer location on the primary sequence of interest, but also the spatial relationship between the polymer and the overall protein architecture becomes increasingly important.

In particular, the use of virus-like particle (VLP) proteins, which are a special class of multimeric proteins that form symmetric protein shells surrounding an empty interior space, relies on two distinct environments that can be modified, either the exposed exterior or the confined interior. For the exterior surface, polymer formation or attachment was employed as a method to append molecules of interest designed to alter VLP solubility, increase stability or introduce new functionalities.[85,139] Electrostatic interactions were used in several systems to package existing polymers or guide capsid assembly around polymers and polymer–nanoparticle composites to provide a charge -dependent occupation of the interior space.[6,7,10,21,145,146] Synthesis of polymers in the interior space was limited to small protein cages, which were employed as a synthesis chamber for an untethered oligomer or for the development of an anchored addressable network.[36,37]

We reported previously the use azide–alkyne ‘click’ chemistry to construct an anchored polymer network inside a small protein -cage architecture.[37,38,147] In this stepwise synthesis approach, polymer growth was directed to the protein -cage interior, which resulted in a protein-confined hyperbranched polymer. The protein shell acted as a barrier that limited the polymer size and left only the protein exterior exposed to the bulk solution. By labelling the resulting protein–polymer construct with a Gd-based magnetic resonance imaging (MRI) contrast agent, an enhanced magnetic resonance contrast agent was obtained, which highlights the utility of using the interior space to maximize cargo loading.[38] While this method is effective, the stepwise nature of the polymerization reaction makes the process onerous for larger constrained polymer syntheses. A

preferable alternative route to achieve an anchored addressable polymer is to proceed via a continuous polymerization of simple monomers from an easily modified initiator. Of the several suitable continuous biomolecule-anchored polymerization methods, we chose to use atom -transfer radical polymerization (ATRP) as it is particularly suited to an improved formation of polymer inside a protein cage. This method is not only rapid, but also results in products with relatively low polydispersity in bulk solutions and is promiscuous with respect to the range of monomers that can be used. Also, the simplicity of the ATRP initiator means that it can be attached readily to the protein cage in a site-specific manner, and thereby we can control the site of polymer initiation. Thus, by combining ATRP with a container-like protein, the formation of a polymer scaffold constrained to the interior of a VLP architecture can be afforded in a single short reaction.

Here we report the use of ATRP to make addressable polymer networks within the confines of the bacteriophage P22 -based VLP (Figure 6.1). The 2-aminoethyl methacrylate (AEMA) monomer was selected because the primary amine-rich polymer synthesized within the P22 capsid could be modified subsequently with the small molecules of interest, which resulted in very high -density loadings of the capsid. The use of the AEMA network as a scaffold was demonstrated through the attachment of either fluorescein isothiocyanate (FITC) or Gd-DTPA-NCS (DTPA = diethylenetriaminepentacetate). Using this method, we can achieve a substantial increase in the degree of labeling per VLP compared to that given in previous reports, which demonstrates the potential capacity of the capsid interior for directed cargo loading.

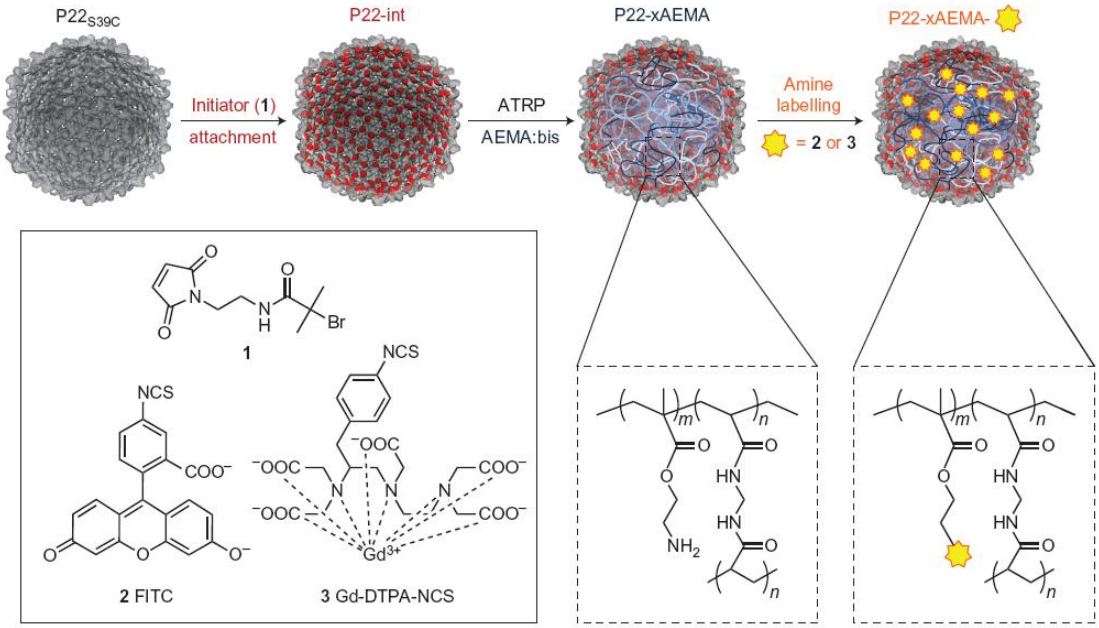

Figure 6.1: Schematic of the internally initiated ATRP polymerization within the P22 VLP. $P22_{S39C}$ modified with a cysteine-reactive ATRP initiator (1) was used as the macroinitiator and a size-constrained reaction vessel for ATRP growth of poly(AEMA) strands, cross-linked with bisacrylamide, inside the P22 VLP architecture to make P22-xAEMA. Subsequently, this internal polymer scaffold was modified with primary amine-reactive labeling agents, either (2) or (3), to introduce a high density of new functionality to the construct.

Results and Discussion

In this work we utilized a VLP (derived from the bacteriophage P22) that consists of 420 subunits arranged on an icosahedral lattice with a resulting exterior diameter of 64 nm and an unoccupied internal cavity with a 54 nm in diameter.[58] Recombinant expression in Escherichia coli requires co-expression of the coat protein and scaffold protein for self-assembly. This VLP is capable of transformation into a series of distinct morphologies, which includes the procapsid (PC) morphology that contains the scaffold protein, an empty shell (ES) form in which the scaffold protein is removed, an expanded

form (EX) and a wiffleball (WB) structure in which all 12 pentamers are removed (Appendix C, Figure C1). The EX form most closely mimics the morphology found in the DNA containing infectious virion and is the form used in this study To attain the EX form, the scaffold protein is removed from the PC using successive guanidine.HCl extractions followed by heating at 65 8C, which generates the capsid in its EX morphology. A new P22 mutant was designed for use with ATRP that contained a single - point mutation in the wild-type coat protein ($P22_{S39C}$) and introduced an addressable thiol suitable for the attachment of an initiator (1). This site was selected specifically such that the introduced thiol could be exposed exclusively to the interior according to the currently available P22 structural models (Figure 6.2).[56,140] Although the wild-type protein contains an intrinsic cysteine (C405) it was not removed because previous studies demonstrated that this site is not addressable.[59,148] This new mutant was characterized and behaves in the same manner as the wild-type P22 capsid, going through the same series of morphological transformations. To obtain the EX morphology, the scaffold protein was removed from $P22_{S39C}$ to generate the ES, heated to 65ºC, and subsequently analyzed to ensure the formation of the EX morphology (Figure 3). The characteristic shift of the particles to a lower electrophoretic mobility was observed on heating, consistent with expansion of the capsid. Precipitation of the protein was observed only at temperatures greater than 80 C, which indicates that the protein architecture is relatively thermostable (Appendix C, Figure C2). The size of the VLP, by dynamic light scattering (DLS), increased as expected from 60±4 nm (PC morphology) to 71±5 nm, consistent with the known range of values for the P22 particle in either the EX or WB morphologies (Figure

6.3D). By transmission electron microscopy (TEM) the overall structure of the VLP was retained and, after heating to 75 ºC large pores became apparent in the structure (Figure 6.3C), which is a characteristic of the WB morphology.

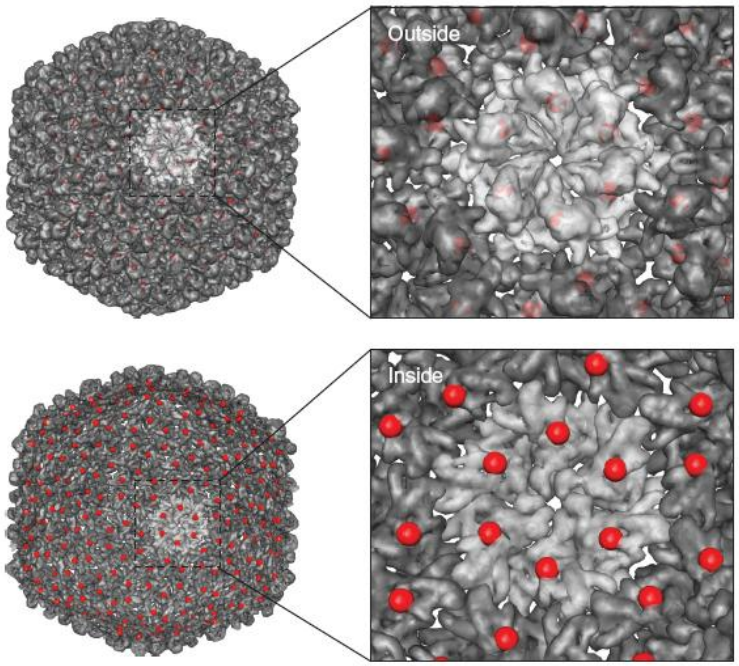

Figure 6.2: Structural model of the expanded morphology of the P22 capsid that shows the location of the S39C mutation. The location of the modified residue, S39C (in red) was derived from a structural model of P22 using coordinate data [140] deposited as Protein Data Bank file 2XYZ. Both a view of the exterior of the capsid (top) and a half shell cut-away view that revealed the interior (bottom) of the capsid are included and illustrate that, according to this model, this mutation site is interior exposed.

To make the P22 macroinitiator, the $P22_{S39C}$ mutant was labeled with initiator 1, an amide derivative of a previously reported ATRP initiator. This cysteine -reactive ATRP initiator (Figure 6.1) was selected because of its efficient labeling, satisfactory initiation and demonstrated compatibility with biomolecules. Initiator 1, unlike the ester-containing form previously reported, is expected to be less susceptible to bond

cleavage.[91,141] It was synthesized through the modification of established protocols and selectively reacted with $P22_{S39C}$ to make $P22_{S39C}$-int with near-quantitative single labeling of the introduced cysteine, as observed by subunit mass spectrometry (Appendix C, Figure C3).

Using the $P22_{S39C}$-int macroinitiator construct, cross-linked AEMA polymer strands were synthesized inside this protein cage to make P22-xAEMA under standard ATRP biomolecule conditions using a Cu(I)/bipyridine To explore the range of reaction conditions available to the $P22_{S39C}$ system for internally directed polymerization reactions, initially a selection of AEMA:bisacrylamide monomer to subunit ratios (3,000–26,000) and temperatures (23, 40 and 60 ºC) as well as catalyst -loading ratios, were investigated. Samples were monitored by gel electrophoresis and DLS to determine reaction completion and suitable conditions (an example comparison is shown in Appendix C, Figure C4). The purified protein–polymer hybrid constructs were stable after polymerization and only at the highest temperature and loading conditions did the diameter of the cage increase significantly, which indicates that under most of the tested conditions the VLP effectively constrains the polymer growth to the interior of the capsid. From these test reactions it was apparent that the monomer loading had a greater impact on the extent of polymerization than the temperature of the reaction, and that the reactions were effectively complete after less than three hrs.

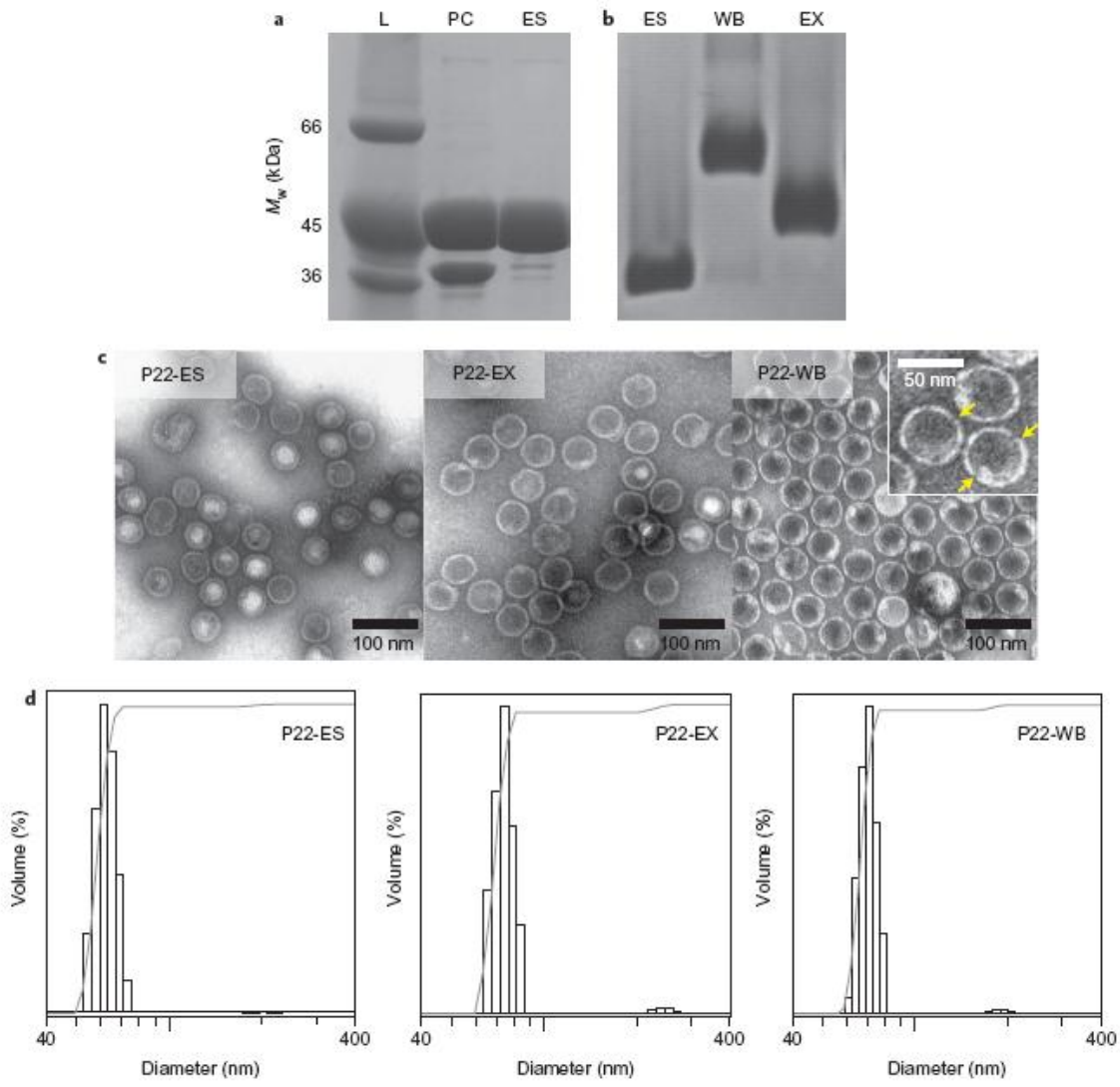

Figure 6.3: Characterization of the $P22_{S39C}$ mutant to verify morphological transformation. A) SDS-PAGE of the purified P22 before (PC) and after (ES) extraction of the scaffold protein. The lower band corresponds to scaffold (33.6 kDa) and the upper band is coat protein (46.6 kDa). L is the molecular weight standards. B) Native agarose gel of the P22 Es, EX and WB structures. The observed shift in mobility indicates the temperature-induced transformation from ES to EX and WB morphologies. C) Negatively stained TEM images of the ES, EX, and WB morphologies show the degree of particle-size homogeneity. The inset shows the appearance of small voids (yellow arrows) in the shell of the WB morphology. D) DLS of the three morphological forms (ES, EX, and WB). The measured hydrodynamic diameter for the expansion from ES (60 ± 4 nm) to EX (71 ± 5 nm) and WB (68 ± 4 nm) is as expected.

To verify further that our selected P22 mutant was confining the polymer, we compared the behavior of $P22_{S39C}$ to a second mutant of P22 coat protein ($P22_{K118C}$), described previously, and which has a reactive cysteine site predicted to be partially exposed to the exterior (Appendix C, Figure C5). [59] Both mutants were labeled with an ATRP initiator (Appendix C, Figures C6 and C7) and analyzed under simple polymerization conditions. We used the AEMA without addition of bisacrylamide at a loading of 26,000 monomers/subunit of the partially exterior-exposed $P22_{K118C}$ to make $P22_{K118C}$-AEMA, which resulted in dramatically different material properties compared to those of the $P22_{S39C}$ treated under the same conditions ($P22_{S39C}$-AEMA) and emphasizes the importance of site specificity for polymer initiation and growth in these protein architectures. When the initiator-labeled $P22_{K118C}$ was treated to make $P22_{K118C}$-AEMA, the construct exhibited an increase in diameter of about 20 nm, from 60 ± 3 nm to 81 ± 4 nm, as measured by DLS, which suggests the growth of polymer on the exterior of the cage (Appendix C, Figure C8), but the $P22_{S39C}$ -based sample diameter remained constant before (67 ± 4 nm) and after (67 ± 4 nm) polymerization. In addition, unlike $P22_{S39C}$-AEMA, the $P22_{K118C}$-AEMA hybrid was not very stable. Although no precipitation was observed under the reaction conditions, mass precipitation of the $P22_{K118C}$-AEMA occurred on purification. This loss could be alleviated partially by increasing the ionic strength of the buffer (>250 mM NaCl). Taken together, these data support a model in which the initiation site determines the overall access of the AEMA polymer to the exterior environment and when the polymer growth is exposed to the exterior of the cage, the protein–polymer composite destabilizes significantly. We

directed our efforts to the interior -facing $P22_{S39C}$-int macroinitiator construct at a midrange monomer loading (6,000 monomers/subunit) with bisacrylamide present and moderate temperature conditions (23ºC) for further investigation with four experimental replicates. After three hrs of reaction time, the synthesis was halted by exposing each sample to air and the protein–polymer conjugate ($P22_{S39C}$-xAEMA) was purified away from the remaining AEMA and bisacrylamide monomers and the copper catalyst by pelleting the protein construct using ultracentrifugation, which easily separates large macromolecular complexes from small molecular species. The resulting construct exhibited a dramatic shift in electrophoretic mobility, by native agarose gel, which indicates that the P22-int had become P22-xAEMA (Fig. S9). On a subunit basis an increased subunit mass (by denaturing gel analysis) was observed, as indicated by a shift to a higher molecular mass (Fig. 4A and Appendix C, Figure C9). By this analysis method, it appears that not all of the initiator-labeled subunits produced sufficiently long polymer chains for a mass shift to be apparent. Others also observed this incomplete initiation in both monomeric and multimeric systems when making grafted-from protein–polymer composites.[85,91,141,142]

To confirm that the polymer was confined to the interior of the P22, the size of the $P22_{S39C}$-xAEMA construct was compared to that of the initial macroinitiator P22 complex. When the particles were visualized using TEM, the morphology of P22 after the reaction was unchanged from that before (Figure 6.4B). The average particle diameter was 51±3 nm in the unpolymerized $P22_{S39C}$-int and remained the same (53±3 nm) after the reaction. In addition, the hydrodynamic diameter, as measured by DLS, remained

unchanged on polymer formation (Figure 6.4C). The particle diameters were 70±10 nm and 71±3 nm, respectively, for $P22_{S39C}$-int and $P22_{S39C}$-xAEMA, which further confirms that the polymer was confined to the interior of the protein cage.

Multiangle light scattering (MALS) was used to analyze further the $P22_{S39C}$-xAEMA construct for the radius and molecular weight (Figure 6.5). According to this method the radius of the particles remained nearly constant, measured as 29.3 nm ($P22_{S39C}$-int) and 28.2 nm ($P22_{S39C}$-xAEMA), but the molecular weight increased on polymerization. Using the standard refractive index increment (dn/dc) for protein (0.185) and the published value for AEMA (0.153) [149] , the MALS data from the $P22_{S39C}$-int and $P22_{S39C}$-xAEMA samples were fitted to obtain molecular weights. The measured molecular weight for $P22_{S39C}$-int was 18.9 ± 0.2 MDa, consistent with the predicted value for the EX morphology of P22, but the $P22_{S39C}$-xAEMA had a combined molecular weight of 20.2 ± 0.6 MDa, with 18.7 ± 0.5 MDa contributed from the protein and 1.5 ± 0.4 MDa contributed from the polymer. This mass increase corresponds to the addition of 12,000 ± 3,000 AEMA monomers/VLP or 28 ± 7 AEMA monomers/subunit, on average.

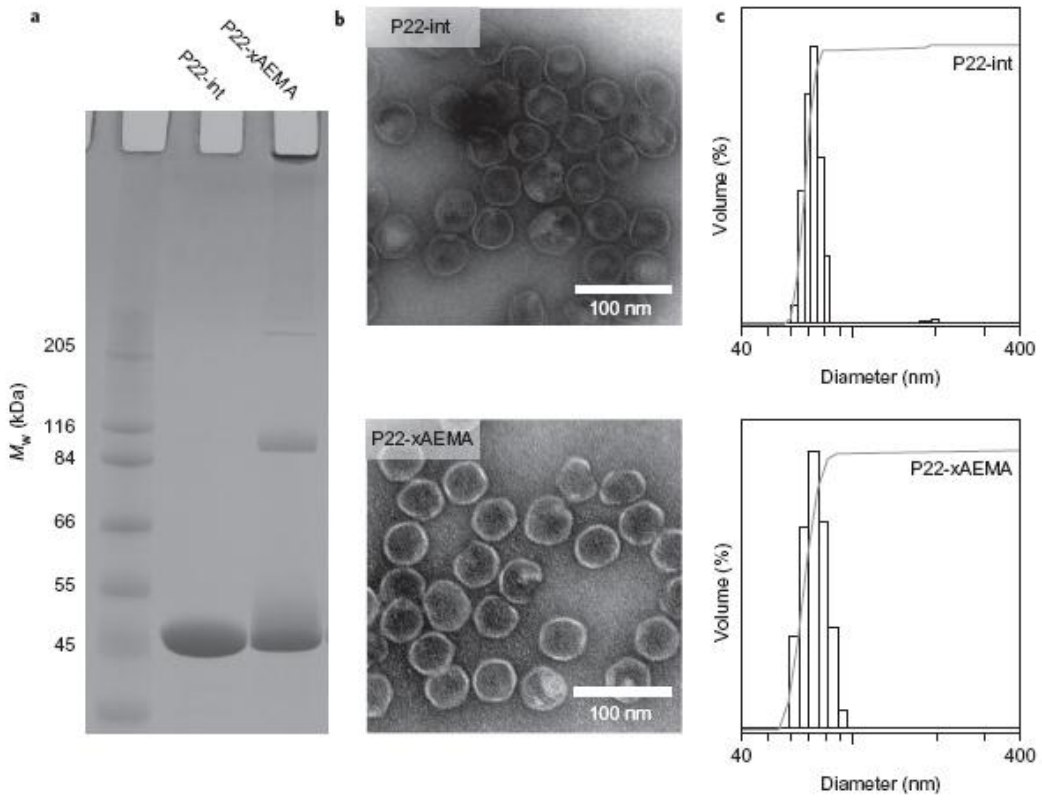

Figure 6.4: Size and morphological characterization of the $P22_{S39C}$-xAEMA composite and $P22_{S39C}$-int. A) Representative SDS-PAGE gel of $P22_{S39C}$-int and $P22_{S39C}$-xAEMA. The polymerized sample shows some streaking to higher Mw, which indicates the range of polymer chain lengths appended to the subunits as compared to the starting P22. In addition, highly cross-linked material can be observed in the well at the top of the gel. B) TEM images of $P22_{S39C}$-int (top) and $P22_{S39C}$-xAEMA (bottom) illustrate that the $P22_{S39C}$-xAEMA retains the size and shape homogeneity of the P22 capsid after the polymerization reaction. C) DLS of $P22_{S39C}$-int (top) and $P22_{S39C}$-xAEMA (bottom). The modified sample is monodisperse and has the same average diameter as that of the starting $P22_{S39C}$-int.

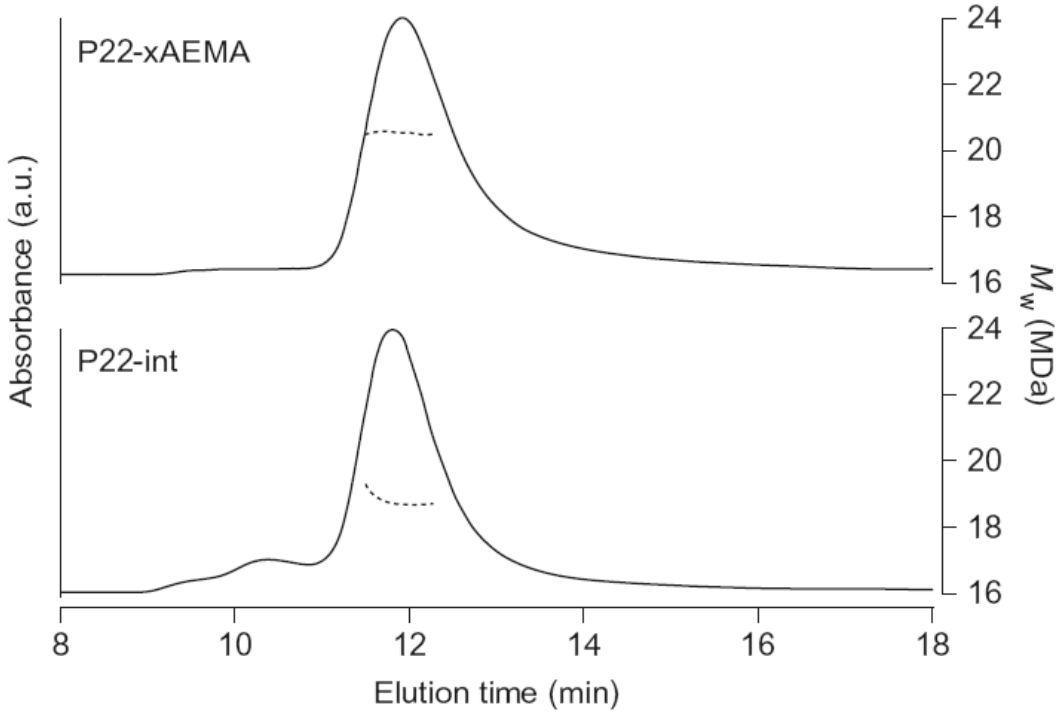

Figure 6.5: Molecular weight increase as a result of polymerization, monitored by MALS. Using size exclusion chromatography, both $P22_{S39C}$-xAEMA and $P22_{S39C}$-int exhibit the same elution time when monitored by absorbance (continuous line) at 280 nm, which indicates retention of the particle size. Fitting the MALS data across the elution profile reveals the molecular weight of the material (dashed line), which increases substantially for the $P22_{S39C}$-xAEMA (top) compared to the $P22_{S39C}$-int (bottom). a.u. = arbitrary units.

The internally directed $P22_{S39C}$-xAEMA polymerization resulted in the introduction of a large number of addressable amines sequestered within the protein cage. To demonstrate that the introduced amines on the poly(AEMA) inside the $P22_{S39C}$-xAEMA construct were addressable, FITC (2) was used as an amine -specific labeling agent. Both the $P22_{S39C}$-xAEMA and $P22_{S39C}$-int control were incubated with a 100 -fold excess of FITC per subunit to give $P22_{S39C}$-xAEMA-FITC and $P22_{S39C}$-int-FITC, respectively. Excess FITC was removed by pelleting the protein twice using

ultracentrifugation followed by resuspension before analysis. The difference in the degree of labeling between the $P22_{S39C}$-int-FITC and $P22_{S39C}$-xAEMA-FITC was significant enough to be readily discernible (Appendix C, Figure C10).

When the fluorescently labeled $P22_{S39C}$-xAEMA construct was analyzed using gel electrophoresis the fluorescein signal was observed to migrate with the protein. Under denaturing sodium dodecyl sulfate polyacrylamide gel electrophoresis (SDS–PAGE) conditions, the fluorescein migrated with the subunit and with the polymer-modified subunit, which indicates that the fluorescent dye was bound covalently to the construct and not just sorbed onto the protein–polymer composite (Appendix C, Figure C11). When analyzed by native agarose gel electrophoresis, a net shift in the electrophoretic mobility of the $P22_{S39C}$-xAEMA and $P22_{S39C}$xAEMA-FITC was observed, caused by the polymer and FITC altering the charge of the construct (Figure 6.6A). The observed shift indicates that the polymer and dye were associated tightly with the protein cage. The $P22_{S39C}$-xAEMA-FITC was labeled to the extent that the migration of a distribution of species was visible prior to staining under ambient light, but $P22_{S39C}$-int-FITC was observed only weakly (Figure 6.6B). In contrast, the emission signal of the $P22_{S39C}$xAEMA-FITC distribution was depressed in intensity compared to that of the much less heavily labelled $P22_{S39C}$-int-FITC (Figure 6.6C), which probably results from self-quenching of the fluorophore caused by the abundance of polymer-bound fluorescein in close proximity. This apparent loss of fluorescence intensity was confirmed by solution -phase analysis of the constructs, in which a greater than 95% reduction in fluorescence was observed in the $P22_{S39C}$-xAEMA-FITC compared to $P22_{S39C}$-int-FITC (Appendix C, Figure C12). Similar

quenching was shown in systems with high fluorophore concentrations, such as micelles, where derivatives of fluorescein can lose more than 98% of their fluorescence signal because of proximity and dimerization effects. [150,151]

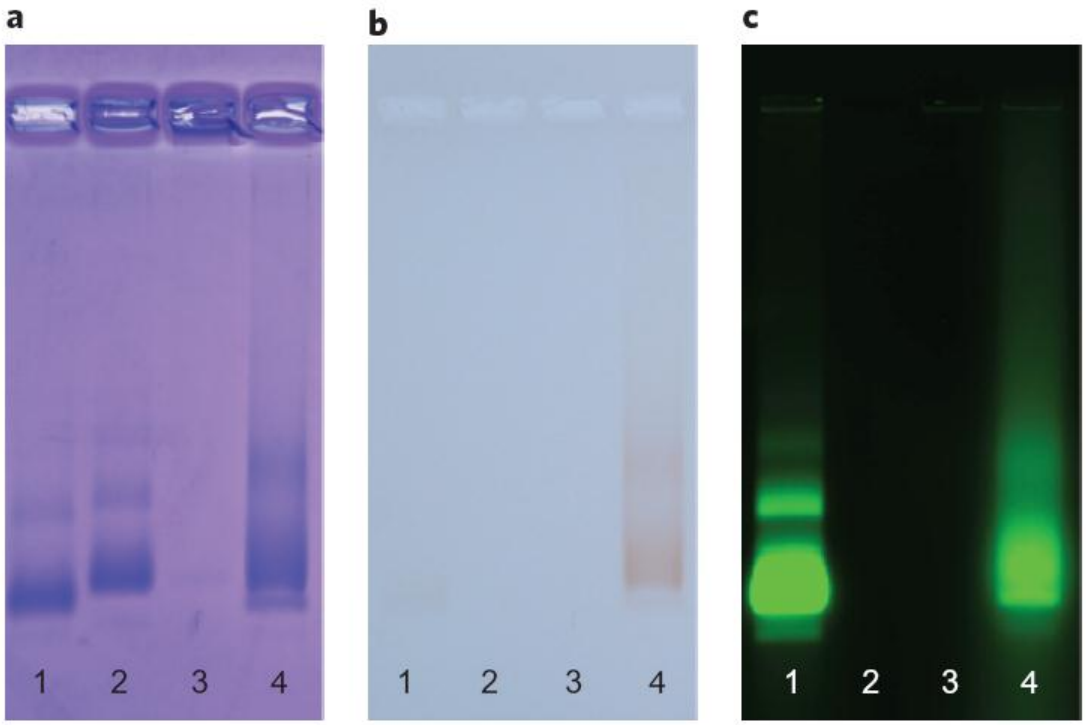

Figure 6.6: Polymer formation and covalent modification with FITC was verified by native agarose gel electrophoresis. (A-C) Three different views of the same native agarose gel with $P22_{S39C}$-int-FITC (lane 1), $P22_{S39C}$-int (lane 2), $P22_{S39C}$-xAEMA (lane 3), and $P22_{S39C}$-xAEMA-FITC (lane 4). A) The gel was stained with Coomassie to detect the protein component. The $P22_{S39C}$-xAEMA runs slightly out of the well in the opposite direction to the other proteins due to the net positive charge on the poly(AEMA) at the running-buffer pH. Labeling this construct with the negatively charged FITC reverses the effective net charge on the construct and results in a shift in migration direction. B) The unstained gel under ambient light. The $P22_{S39C}$-int-FITC sample is faintly visible and the $P22_{S39C}$-xAEMA-FITC sample is clearly visible, which signifies the relative degree of FITC labeling in each sample. C) The unstained gel illuminated with a laser at 488 nm and detected at 520 nm to highlight FITC. The $P22_{S39C}$-int-FITC is considerably brighter than the $P22_{S39C}$-xAEMA-FITC, which indicates the relative degree of fluorescence quenching in each sample.

After demonstrating polymerization within the P22 capsid and the postsynthetic modification of the functional groups, we explored the $P22_{S39C}$-xAEMA composite system as a potential T1 contrast agent through the attachment of Gd-DTPA-NCS (3) to the encapsulated polymer. Gd-DTPA-NCS was added, in a 100 -fold excess per subunit, to the $P22_{S39C}$-xAEMA or $P22_{S39C}$-int and allowed to react overnight, followed by pelleting by ultracentrifugation and resuspension of the protein twice in each of four experimental replicates. The resulting material ($P22_{S39C}$-xAEMA-Gd or $P22_{S39C}$-int-Gd) was analyzed for both sulfur and gadolinium content by inductively couple plasma mass spectrometry (ICP-MS) to determine both the Gd and protein concentrations. To rule out the possibility of simple electrostatic interaction between the polymer and Gd-DTPA, controls with both $P22_{S39C}$-xAEMA and $P22_{S39C}$-int were incubated and isolated, under the same conditions as above, with Magnevist (Gd-DTPA), which lacks the aminereactive isothiocyanate. When these constructs were analyzed by native agarose gel electrophoresis (Appendix C, C13), a net shift in the electrophoretic mobility of the $P22_{S39C}$-xAEMA-Gd was observed, caused by the polymer and Gd-DTPA-NCS altering the net charge of the construct, but the $P22_{S39C}$-xAEMAMagnevist sample retained the same low electrophoretic mobility as that of the $P22_{S39C}$-xAEMA, which provides evidence that there were no significant electrostatic interactions between $P22_{S39C}$-xAEMA and Gd-DTPA.

The Gd-DTPA loading per P22 was determined quantitatively for each of the constructs from the ICP-MS data. The $P22_{S39C}$-xAEMA-Gd contained 28 times more Gd/VLP than the $P22_{S39C}$-int-Gd control (320 Gd/VLP, <1 Gd/subunit), where

endogenous lysines were modified, which indicated that it is largely the polymer that is being labeled rather than the protein shell. The low reactivity of the endogenous P22 lysines was reported previously, with only a few of the 20 lysines per subunit observed to be reactive.[115] This minimal background reactivity is advantageous because it means that in the $P22_{S39C}$-xAEMA sample the vast majority (>95%) of the addressable sites are located on the encapsulated polymer. If necessary, endogenous lysines could be blocked chemically prior to polymerization.[37] The $P22_{S39C}$-xAEMA-Gd loading per cage was 9,100 ± 800 Gd/VLP (22 ± 2 Gd/subunit), which corresponds to an internal concentration of 150 mM Gd within the VLP. This is significantly more Gd, both on a per-cage and per-subunit basis, than that in previous reports using VLPs, with values that ranged from less than 1.0/subunit to 6.6/subunit (60/VLP to 650/VLP), and highlights the advantage of using the full capacity of the interior volume.[38,82,85,131,152-156]. In addition, both the $P22_{S39C}$-xAEMA and $P22_{S39C}$-int incubated with Magnevist (Gd-DTPA) contained Gd levels below the lower limit of quantification, which demonstrates that the Gd detected is attached covalently to the protein–polymer construct rather than associated via electrostatic interactions under the labeling reaction conditions.

To verify that the high loading observed was reasonable and occurred homogeneously across the population of P22 capsids, the particles were analyzed by analytical ultracentrifugation to investigate differences in sedimentation velocity (Figure 6.7). The measured sedimentation value of the $P22_{S39C}$-xAEMA (167 S) falls within the range observed for $P22_{S39C}$-int (142 S) and the scaffold protein-filled PC morphology (191 S), which indicates that the polymer content does not exceed the packing observed

in the naturally occurring self-assembled system. Covalent modification of polymer with Gd-DTPA-NCS to make $P22_{S39C}$-xAEMA-Gd resulted in a shift to a higher S value (227 S), which is consistent with the efficient incorporation of additional mass via Gd-DTPA-NCS to the interior of the VLP.

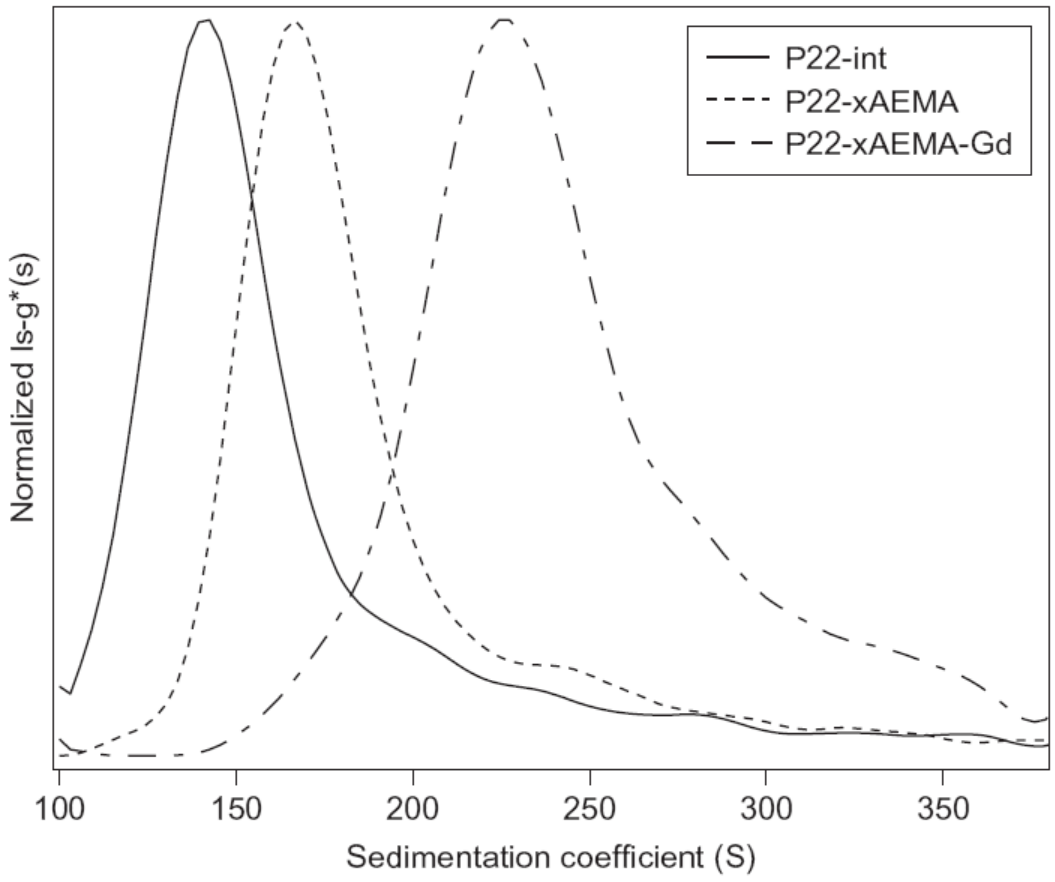

Figure 6.7: Analysis of sample population homogeneity by analytical ultracentrifugation. Samples were centrifuged at 5,000-7,000 rpm and absorbance data were acquired at 280 nm and modeled to calculate the apparent sedimentation coefficient distribution ls-g*(s) for each sample. The measured sedimentation value of the $P22_{S39C}$-xAEMA (167 S) shows an increase from that of $P22_{S39C}$-int (142 S) and covalent modification of polymer with Gd-DTPA-NCS to make $P22_{S39C}$-xAEMA-Gd resulted in a shift to a higher S value (227 S), consistent with the incorporation of additional mass via Gd-DTPA-NCS labeling of the polymer. These data indicate that there is a homogeneous shift in the entire population to higher S values with each modification.

The 1H relaxivity of water in the presence of these highly loaded $P22_{S39C}$-xAEMA-Gd particles and $P22_{S39C}$-int-Gd was measured at 60 MHz (1.4 T), using an inversion recovery -pulse sequence. The $P22_{S39C}$-xAEMA-Gd and $P22_{S39C}$-int-Gd had ionic relaxivities (r1) of 22.0 $mM^{-1}s^{-1}$ and 23.5 $mM^{-1}s^{-1}$, respectively. The observed improvement in r1 for both constructs is consistent with an enhancement over free Gd-DTPA (4.0 mM-1s-1) due to an increase in the rotational correlation time that arises from tethering the chelate to a large supramolecular particle.[38,131] In addition, because the ionic relaxivity is enhanced similarly in both constructs it can be concluded that the polymer does not restrict water exchange significantly between the bulk and the interior of the $P22_{S39C}$-xAEMA-Gd composite, as water restriction would lessen the observed enhancement, as is seen in some micelles and liposomes.[157,158]

In addition to the ionic relaxivity enhancement, each $P22_{S39C}$-xAEMA-Gd carries 9,100 ± 800 Gd/VLP, which leads to a per particle relaxivity of 200,000 $mM^{-1}s^{-1}$. The particle relaxivity of $P22_{S39C}$-xAEMA-Gd dramatically exceeds that of the $P22_{S39C}$-int-Gd control (7,500 $mM^{-1}s^{-1}$) and those in previous reports of VLP nanoparticle -based MRI contrast agents, with values that fall in the range of 103–104 $mM^{-1}s^{-1}$. [38,82,85,131,152-156] The particle relaxivity is also higher than those observed for many other macromolecular assemblies, such as micelles, liposomes and polymers, which places this construct comfortably in the upper end of observed macromolecular relaxivities for its size.[157-161]

Conclusion

In summary, the application of ATRP for site-directed polymer formation inside a VLP results in an anchored network that is unparalleled for labeling purposes and utilizes

the previously largely untapped interior volume of the VLP. The $P22_{S39C}$-based macroinitiator effectively directs polymer growth to the VLP interior, which results in a confined polymer growth because the protein shell acts as a barrier to unconstrained polymer growth, to leave only the protein shell exposed to the bulk solution. By selecting an appropriate macroinitiator and monomer, this new multimeric protein–polymer composite acts as a scaffold for the attachment of small molecules of interest, such as the fluorophore FITC or paramagnetic MRI contrast agents (here, Gd-DTPA-NCS). The introduced polymer scaffold results in a significantly increased number of labels per cage compared to those of other VLP -based systems. The improvement in labeling is important for the delivery of contrast agent on a per-particle basis as it allows for a high concentration delivery of contrast agent or other cargo molecules of interest. This material exhibits an order -of -magnitude improvement in relaxivity per particle over that of existing VLP systems. The use of this material as a targeted MRI contrast agent is particularly interesting because of the high relaxivity and is an application we are exploring further. As a consequence of the simplicity, modular nature and loading level of the ATRP -based approach taken to make these P22–polymer internal composites, currently this same method is being employed to make a range of novel VLP– polymer composites with biomedical and catalytic applications.

Experimental

All materials were analytical grade and purchased from either Sigma-Aldrich or Fisher Scientific and used as received unless otherwise noted. Dichloromethane was distilled over calcium hydride prior to use. All water was deionized using a NANOpure

water purification system. Dynamic light scattering measurements were taken on a 90Plus particle size analyzer (Brookhaven).

Mutagenesis.

The P22(S39C) point mutation was made using established polymerase chain reaction protocols (Qiagen) using pET-11a based plasmids encoding genes for scaffolding and coat protein. The amplified DNA was transformed into E. coli strain BL21 (DE) and selected for ampicillin resistance.[59]

Protein Purification.

Transformed BL21 (DE3) *E. coli* were grown in 1L cultures inoculated with 1 mL starter culture at 37°C with vigorous shaking overnight. The bacteria were then centrifuged away from the media at 3700 g for 20 minutes. The cell pellets were resuspended in PBS pH 7.2 and were incubated with DNAse, RNAse, and lysozyme (all Sigma-Aldrich) for 30 minutes on ice. Cells were lysed further by sonication on ice. The cell debris was removed via centrifugation at 12,000 g for 45 minutes. The supernatant was then loaded on a 35% sucrose cushion and centrifuged at 48,000 rpm for 50 minutes in an ultra centrifuge (Sorvall). The resulting virus pellet was resuspended in PBS pH 7.0, spun at 17,000 rpm for 20 minutes to remove particulates and lipid providing 135 mg of P22 procapsid (PC). Scaffold protein was extracted using 0.5 M guanidine-HCl in 4 repeated cycles. The P22 empty shells were then dialyzed against PBS pH 7.0 overnight resulting in 86 mg (64% yield) P22 empty shell (ES). The empty shell P22 was heat treated for 20 min at 65^{o}C to transform the protein into its expanded form as previously described and analyzed.[59] The heat treated samples were purified by pelleting as above,

followed by resuspension into PBS pH 7.6 in preparation for protein labeling yielding 58 mg (68% yield form ES) of P22 expanded shell (EX) from 1L of initial *E. coli* culture.

Synthesis of 2-Bromoisobutyryl Aminoethyl Maleimide (**1**).

1 was synthesized by a modification of the procedures previously reported.[91,141] N-2-aminoethyl-maleimide (250 mg, 0.98 mmol) was mixed on ice with triethylamine (300 µL, 2.2 mmol) in 5 mL dry dichloromethane. 2-bromo-2-methylpropionylbromide (200 µL, 1.6 mmol) was added dropwise. The reaction was allowed to warm to room temperature and was subsequently extracted 3 times from dichloromethane and water followed by drying over anhydrous sodium sulfate. The crude product was cleaned via column chromatography (silica gel, 10% ethyl acetate in dichloromethane) with a yield of 80%. ^{1}H NMR (500 MHz, $CDCl_3$) δ = 1.89 (s, 6H, CH_3); 3.46 (dd, J = 5.5, 5.5, 2H, NCH_2); 3.72 (dd, J = 5.0, 1.5, 2H, NCH_2); 6.71 (s, 2H, CH_{vinyl}), 6,97 (s, NH). ^{13}C δ = 32.54 (CH_3), 37.34 (NCH_2), 39.84 (NCH_2), 62.51 (C), 134.59(CH_{vinyl}), 170.96 (CO), 172.74 (CO). ESI-MS: *m/z* calculated 289.0188, 291.0167 (MH^+), found *m/z* 289.0192, 291.0179.

P22-int Macroinitiator Formation Conditions**.**

$P22_{S39C}$ in PBS, pH 7.6 (4 mL, 7.2 mg/mL) was infused with 156 µL of **1** (80 mM inDMSO, 10 fold excess per a subunit). The mixture was allowed to react for 3 hrs at room temperature. After 3 hrs the reaction was quenched with DTT (156 µL, 80 mM in water). To remove excess DTT and **1**, the protein was pelleted at 48,000 rpm for 50 minutes in an ultra centrifuge (Sorvall) followed by resuspension into PBS, pH 7.6. By subunit mass spectrometry >95% of the subunits were labeled. Yield: quantitative.

P22-AEMA Polymer Formation Conditions.

Each experimental replicate was made in a large crimp-top vial with the addition of 20 mL monomer solution (4 wt% 16:4 AEMA:bis-acrylamide in PBS, pH 8.0) and 11 mL buffer (PBS, pH 8.0) followed by pH adjustment with concentrated sodium hydroxide solution as needed back to pH 8.0. To this mixture, 6 mL of P22-int (8.0 mg/mL, 1.0 μmoles subunit, pH 8.0) was added followed by pump and back filling with Ar 4 times to deaerate the mixture. The metal catalyst solution was made in a second crimp vial where 19.2 mg CuBr (0.13 mmoles), 29.9 mg CuBr2 (0.13 mmoles), and 83.5 mg 2,2'-bipyridine (0.53 mmoles) followed by the addition of 10 mL deionized water which had been degassed by bubbling Ar through the liquid for 20 minutes. The vial was subsequently sonicated for 5 min to obtain a dark brown solution. To the monomer-protein vial, 3 mL of the metal catalyst solution was added and the vial was maintained at 23 ºC for the remaining duration of the experiment. After 3 hr the reaction was quenched by exposure to air and the protein-polymer composite was purified away from unreacted monomer and the copper catalyst by pelleting and resupending the protein 2 times into 100 mM sodium carbonate with 50 mM NaCl buffer, pH 9.0. Yield: 38.7 mg (81%).

FITC (**2**) Labeling Conditions**.**

To 2.0 mL $P22_{S39C}$-xAEMA (0.086 μmoles subunit, carbonate buffer, pH 9.0) at 2 mg/mL, 343 μL FITC (8.6 mmoles, 25 mM in DMSO) was added dropwise while vortexing the protein solution. The mixture was allowed to sit overnight at 4 ºC followed by purification away from excess FITC by pelleting and resuspending (carbonate buffer, pH 9.0) the protein twice over.

Gd-DTPA-NCS (**3**) Labeling Conditions**.**

Gd-DTPA-NCS was made according to established procedures.[38] Briefly, 2.80 mg (4.31 μmoles) DTPA-NCS was dissolved in 40 μL of 1M sodium bicarbonate and 200 μL water. Once the DTPA-NCS was completely dissolved, 5.27 μL $GdCl_3$ (900 mM in water, 4.74 μmoles) was added to the solution and stirred for 3 hrs at room temperature. The solution was subsequently diluted to 10 mM with DMSO (186 μL) and added to the protein-polymer conjugate as follows. To 4.0 mL (0.17 μmoles subunit, 2 mg/mL carbonate buffer, pH 9.0) $P22_{S39C}$-AEMA, 1700 μL (17 μmoles) Gd-DTPA (10 mM in DMSO/H_2O) was added dropwise while vortexing the protein solution. The mixture was allowed to sit overnight at 4 ºC followed by purification away from excess Gd-DTPA by pelleting and resuspending the protein twice. Yield: 5.2 mg (65%).

Subunit Mass Spectrometry.

Subunit masses of the P22 coat and P22-int macroinitiators were analyzed by ESI-Q-TOF mass spectrometry (Q-TOF Premier, Waters) interfaced to a Waters Acquity UPLC and autosampler. [50] Samples were loaded onto a BioBasic-300 SEC column (5 μm, 250 L x 1.0 mm I.D., Thermo Scientific) and eluted with buffer containing 40% isoproanol, 59.9% water, and 0.1% formic acid isocratically with a rate of 25 μL/min. Mass spectra were acquired in the range of m/z 50-5000 and processed using the MaxEnt 1 algorithm for MassLynx version 4.1 to obtain deconvoluted average masses from multiple charge state distributions.

Transmission Electron Microscopy.

The P22-int macroinitiators and P22-polymer composites were imaged by transmission electron microscopy (Leo 912 AB) by negatively staining the sample with 1% uranyl acetate on formvar carbon coated grids. For the diameter measurements 200 particles were measured for each sample.

Denaturing Gel Assay.

P22-int macroinitiators and P22-polymer composites were analyzed using SDS-PAGE on 10-20% gradient Tris-glycine gels (Lonza). Fluorescence imaging of the gels was carried out on a Typhoon TRIO (GE Healthcare) gel scanner with excitation at 488 nm and detection at 526 nm. Protein was detected by staining with Coomassie blue.

Native Agarose Gel Assay.

P22-int macroinitiators and P22-polymer composites were analyzed on 0.8% native agarose gel using 40 mM Tris-base, 5 mM sodium acetate, 1 mM EDTA, pH 8.2 running buffer and were run for 3 hrs at 65 volts. Fluorescence imaging of the gels was carried out on a Typhoon TRIO (GE Healthcare) gel scanner with excitation at 488 nm and detection at 526 nm. Protein was detected by staining with Coomassie blue.

Multi-Angle Light Scattering.

P22-int and P22-xAEMA samples were separated over a WTC-0100S (Wyatt Technologies) size exclusion column at flow rate of 0.7 mL/min (Agilent 1200 HPLC) in 50 mM phosphate, 500 mM sodium chloride, pH 8.0. Each sample injection was 25 μL and the samples were run in triplicate. Elution profiles were for mass analysis were

detected using a UV-Vis detector (Agilent), aWyatt HELEOS multi angle light scattering detector, and a Wyatt Optilab rEX differential refractometer. Using the elution profile data the number average molecular weight, Mn, was calculated with Astra 5.3.14 software (Wyatt Technologies) using a dn/dc for protein of 0.185 and a dn/dc for the polymer component of 0.153.[149]

Analytical Ultracentrifugation**.**

Sedimentation velocity experiments were performed in an XL-A ultracentrifuge (Beckman Coulter, Fullerton, CA) using a AN-60Ti rotor. Epon double-sector centerpieces were filled with 390 μL or 400 μL of sample and the corresponding reference buffer, respectively. The samples were centrifuged at 20°C and 5,000-7,000 rpm. Absorbance data were acquired at wavelength of 280nm. The raw data were analyzed using SEDFIT software, implementing the ls-g*(s) model. Input parameters such as buffer density and viscosity were determined using Sednterp software.

Relaxivity Measurements.

T1 measurements were carried out on Anasazi FT-NMR 60MHz (1.41 T) spectrometer for all samples. Each P22-xAEMA-Gd (0.61 mM Gd, 1.3 mg/mL protein) experimental replicate was diluted with 67% D_2O in H_2O to yield a dilution series with concentrations of 0.20, 0.068, 0.023 mM Gd. The longitudinal relaxation rate constant (T1) at each dilution was measured using an inversion recovery pulse sequence (90º pulse width of 6.3 μs with 8 experiments of 1 scan) at 298 K, where the relaxation delay was set to six times the estimated T1 (Figure Appendix C, Figure C12A-C). To attain the actual T1 value, the following equation for T1 relaxation:

$$M_z = A(1-\exp(-t/T1))+B$$

was fit to the experimental data acquired at each dilution where A, B, and T1 were used as fitting parameters.[162] The plot of inverse T1 versus Gd (mM) for the 3 dilutions was used to determine relaxivity values (r1), where relaxivity per Gd is equal to the slope of the line (Appendix C, Figure C12D) and relaxivity per VLP was calculated by multiplying the slope by Gd/VLP.

Protein and Gd Concentration.

The protein concentration was determined by analyzing samples for sulfur content and Gd concentration by inductively couple plasma mass spectrometry (ICP-MS) at Energy Labs (Billings, MT). Samples were submitted in triplicate and average concentrations were reported. The protein concentration was obtained by subtracting from the detected sulfur concentration the Gd contribution due to sulfur in the DTPA-NCS chelator. The remaining sulfur content was converted to subunit concentration using a conversion factor of 13 thiols per a subunit (the initial Met in the P22 coat sequence is never present in the final protein according to mass spectrometry).

CHAPTER 7

ADDITIONAL COMPOSITES MADE USING ATRP AND THE P22 MACROINITIATOR

Introduction

Protein-polymer composites made using cage-like proteins present abundant opportunities for design, which have been explored in previous chapters. Some additional promising directions in polymerization of these templates, focused on new monomers, are explored in this chapter.

Like other living radical polymerization techniques, one of the advantages of ATRP is that this technique works well for a variety of monomers, which include methacrylates, methacrylamides, and acrylamides. But current literature on grafted-from protein-polymer composites has been by large limited to just two types of monomers – N-isopropylacrylamide (NIPAM) and PEG-methacrylates. Although poly-PEG methacrylates are of high interest due to their potential use as solubility and immune response modification additions to protein based systems [97,144,163] and poly(NIPAM), a thermoresponsive polymer, allows for temperature selective recovery of the protein from solution [90,164], these are not the only monomers of potential interest.

In particular additions that can serve as addressable sites are of interest as demonstrated in Chapter 6 are compeling for further exploration. Although the AEMA monomer explored in the previous chapter is successfull having other means to attain the same end would be desireable. The ester bond in the AEMA is one weakness in the

polymer that could be avoided through the use of an acrylamide or methacrylamide based monomer. Another alternative method to make an addressable polymer is to use a carboxylic acid containing monomer which could then be used to couple primary amine containing molecules of interest to the protein-polymer composite. In an even more simplified approach the monomer could potentially have the dye molecule already attached prior to polymerization so that no additional steps to label the composite are required after polymerization.

One of the interesting aspects of using ATRP to graft-from the interior of a VLP is that there are several confounding factors that could be impacting the polymerization and distribution of polymer chain lengths appended to each subunit. Of these factors, the impact of crowding from the proximity of the 420 initiation sites and the potential diffusion altering effect of the protein cage are of special interest.[165] Selecting simple neutral monomers and associated crosslinking monomers such as the TRIS-acrylamide and bis-acrylamide described in Chapter 5 could present opportunities to better understand these reactions.

One property that makes the heavily studied NIPAM system so appealing is that is is a stimulus responsive polymer changing its macrostructure upon change in temperature. Unlike most materials, poly(NIPAM) shrinks when heated above about 32 ºC. This property makes it an interesting internal tether for the irreversable thermoswitchable P22.

Coordination complexes have proven to be abundantly useful as dyes, photosensensitizers, and photodynamic therapy agents. By developing coordination

complexes suitable for ATRP the first steps toward a P22 contained metal-based catalytic material can be accomplished.

To begin exploring the range of monomers suitable for formation of P22-polymer constructs that meet the above mentioned applications a selection of acrylamides, methacrylates, methacrylamides, and metal bound or metal binding monomers were tested in preliminary experiments with P22 macroinitiators (Figure 7.1). The basic characterization of each of these constructs is described in this chapter.

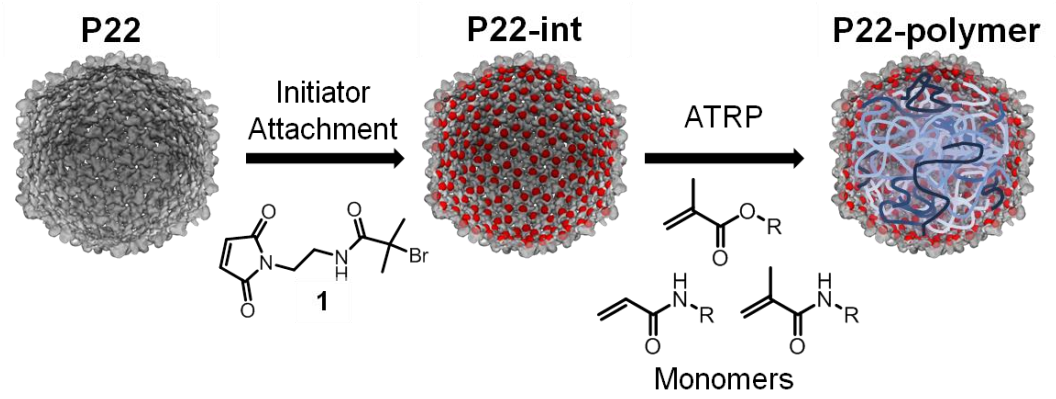

Figure 7.1: Assembly of the internal polymer P22 VLP. $P22_{S39C}$ modified with a cysteine reactive ATRP initiator (**1**) used as macroinitiator for ATRP growth of polymers attached to the virus like particle. The nature of the introduced polymer is dependent on both the monomer class and the side chain (R) on the monomer.

Results and Discussion

In each of the following tests the P22 capsid with the S39C mutation was employed and the reactions were performed with 2% by weight monomer in the reaction solution for 3 hrs at room temperature in phosphate buffer (pH 8.0), unless otherwise stated. These reactions were purified using spin columns (Micro Bio-Spin 30, Bio-Rad) which are size exclusion gel containing columns that sufficiently separate the very small

excess reaction components from the finished protein-polymer composite for initial analysis.

Methacrylic Acid (MAA)

The addition of a poly-methacrylic acid (PMAA) to a protein cage could be advantageous for a variety of reasons and thus is worth developing. The ability to introduce a negatively charged polymer inside the P22 architecture could provide an interesting counterbalance to the positively charged AEMA polymer described in the previous chapter. Much like the AEMA the MAA can also serve as a potential label scaffold. Having this polymer available may open the range of labeling agents that could be appended to molecules that are not available as AEMA reactive agents, but contain a primary amine, which can be appended to the poly(MAA) via EDC coupling. The net negative internal charge that is created by adding the poly(MAA) may make cages modified with this polymer more amenable to internal mineralization as the metal ion to be mineralized should be electrostatically attracted to the interior of the protein much like in the case of adding a poly(EA) peptide to the interior of P22.[16]

The $P22_{S39C}$-MAA composite was made under standard conditions and purified via ultracentrifugal pelleting of the sample. When the $P22_{S39C}$-MAA was tested it exhibited increased subunit mass by denaturing gel analysis, as indicated by the shift to higher molecular mass (Figure 7.2). Though the shift is less pronounced than that seen in the $P22_{S39C}$-AEMA samples (Chapter 6), this difference may be due to the AEMA strongly interacting with the coomassie dye used to stain the gels while the MAA does not. When the intact $P22_{S39C}$-MAA construct was compared using multi-angle light

scattering the molecular mass of the entire composite increased from 18.7 MDa ($P22_{S39C}$-int) to 19.6 MDa ($P22_{S39C}$-MAA). This mass increase corresponds to the incorporation of, on average, about 13,000 monomers/cage (31 monomers/subunit) into polymer strands (Figure 7.3).

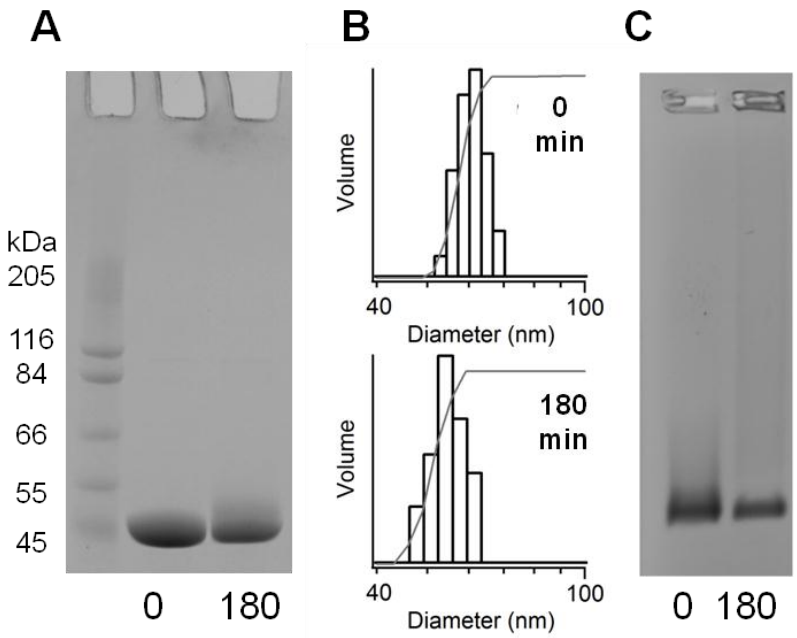

Figure 7.2: Characterization of the $P22_{S39C}$-MAA reaction. A) SDS-PAGE gel showing some increase in Mw. B) DLS of the sample before and after the polymerization reaction. C) Native agarose gel electrophoresis showing the same migration behavior before and after polymerization.

To confirm that this polymer was confined to the interior of the P22, the size of the $P22_{S39C}$-MAA construct was compared to the initial macroinitiator P22 complex. The average hydrodynamic particle diameter was 62±4 nm in the unpolymerized $P22_{S39C}$-int and apparently decreased in size slightly (55±5 nm) after the reaction as measured by DLS (Figure 7.2). When purified by SEC both $P22_{S39C}$-int and $P22_{S39C}$-MAA eluted at the same time further confirming that the polymer is confined to the interior of the protein

cage (Figure 7.3). In addition analysis of the native constructs by agarose gel electrophoresis revealed matching electrophoretic mobility (Figure 7.2). Because there is no change in migration, the charges associated with the MAA must be balanced under the running conditions used in this analysis, otherwise the $P22_{S39C}$-MAA would be expected to migrate farther than the unmodified material.

Altogether, although the observed mass increase was not particularly large nor was a complete shift observed in the SDS-PAGE gel, this monomer may be a successful means to introduce negative charge to the protein cage or as an alternative addressable labeling site. With further reaction optimization and confirmation of the predicted potential labeling and mineralization effects the potential of the composite could be more fully realized.

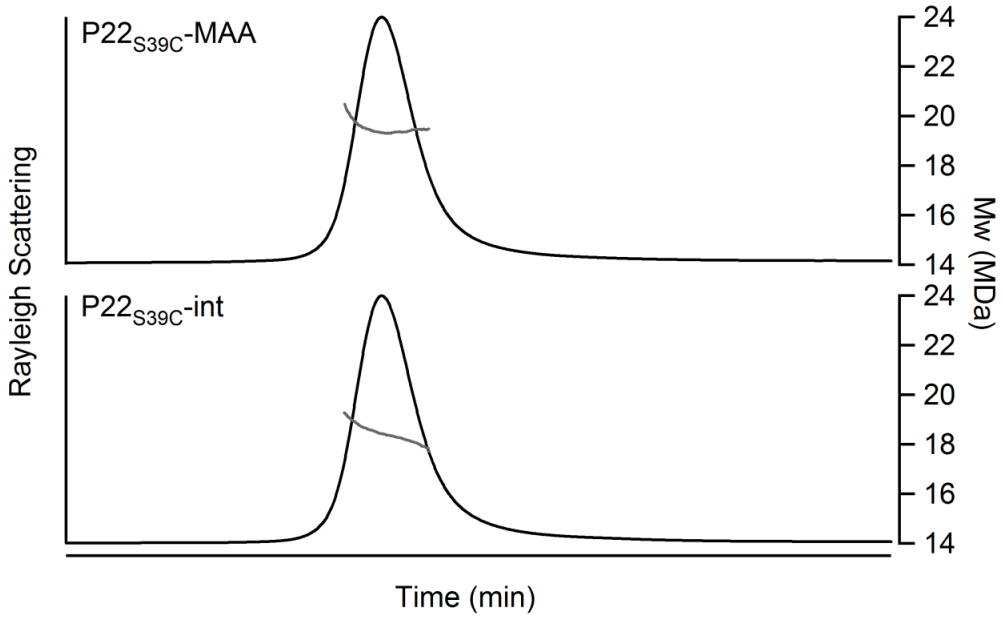

Figure 7.3: Size exclusion chromatography and multiangle light scattering of $P22_{S39C}$-MAA before and after polymerization. No change in elution volume or particle diameter was observed between the samples, but an increase in Mw of 1.1 MDa was observed between the samples.

Acrylamide (Acryl)

As one of the simplest possible monomers, acrylamide could be important as a control monomer or as a spacer monomer in a copolymer with bulky side groups. In addition, the neutral nature of the acrylamide monomer opens the possibility of using mass spectrometry methods such as MALDI to analyze the polymer chain lengths associated with each subunit rather than just the entire composite mass as measured by MALS. This additional characterization data on the ATRP reaction could be instrumental as a means to determine the relative impact surface effects and protein cage diffusion limitations on the polymerization.

The $P22_{S39C}$-Acryl composite described here was made under standard conditions and purified via ultracentrifugal pelleting of the sample. The $P22_{S39C}$-Acryl reactions exhibited increased subunit mass by denaturing gel analysis, as observed by the shift to higher molecular mass (Figure 7.4), indicating that sufficiently long polymer chains for a mass shift to become apparent were present. When the intact $P22_{S39C}$-Acryl construct was analyzed using multi-angle light scattering the molecular mass of the entire composite increased from 18.6 MDa ($P22_{S39C}$-int) to 18.7 MDa ($P22_{S39C}$-Acryl). This mass increase corresponds to the incorporation of, on average, about 2,700 monomers/cage (6.4 monomers/subunit) into polymer strands (Figure 7.5).

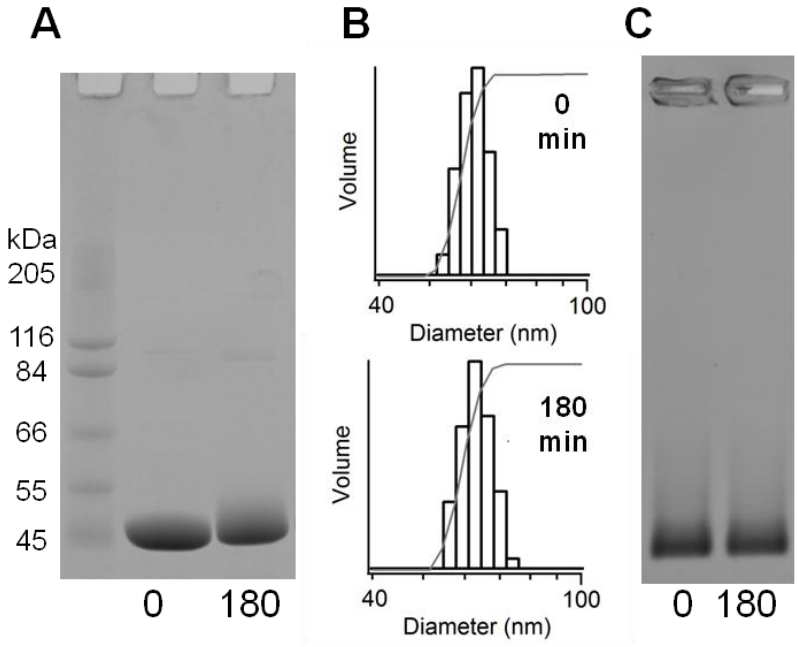

Figure 7.4: Characterization of the $P22_{S39C}$-Acryl reaction. A) SDS-PAGE gel showing increase in Mw. B) DLS of the sample before and after the polymerization reaction showing an unchanged diameter. C) Native agarose gel electrophoresis showing the same migration behavior before and after polymerization.

To confirm that this polymer was confined to the interior of the P22, the size of the $P22_{S39C}$-Acryl construct was compared to the initial macroinitiator P22 complex. The average hydrodynamic particle diameter was 62±4 nm in the unpolymerized $P22_{S39C}$-int and remained the same (64±5 nm) after the reaction as measured by DLS (Figure 7.4). When analyzed by SEC, both $P22_{S39C}$-int and $P22_{S39C}$-Acryl eluted at the same time further confirming that the polymer is confined to the interior of the protein cage (Figure 7.5). When the native construcs where analyzed by agarose gel electrophoresis they appeared to have identical electrophoretic mobilities indicating that the addition of the polymer does not contribute significantly to an increased cross-sectional area (Figure 7.4).

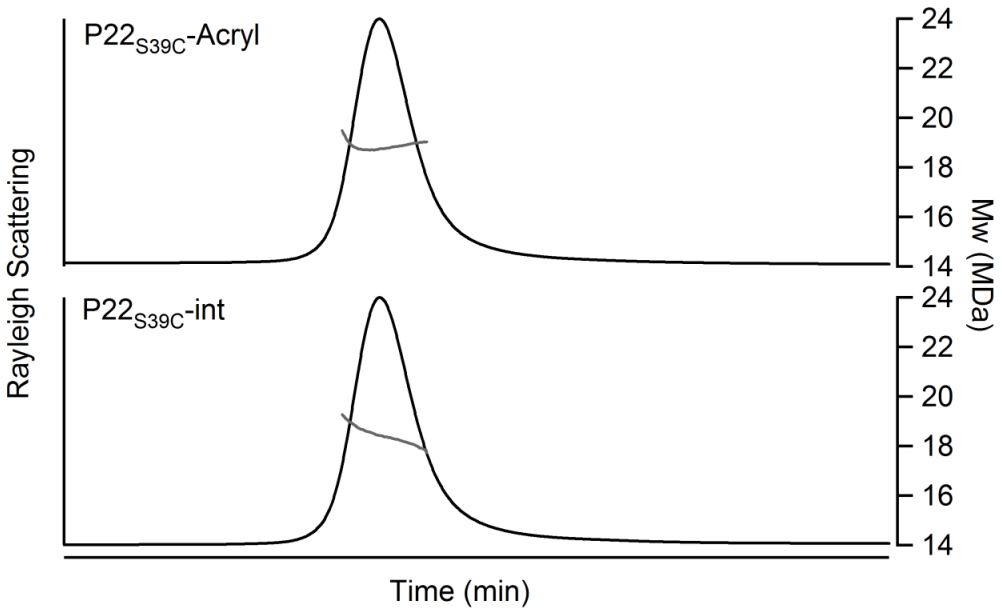

Figure 7.5: Size exclusion chromatography and multiangle light scattering of $P22_{S39C}$ before and after polymerization. No change in elution volume or particle diameter was observed between the samples, but an increase in Mw of 0.2 MDa was observed between the samples.

Although a small mass increase and some evidence for increased subunit mass was observed, to more fully utilize this monomer it would be desireable to optimize the reaction conditions specifically for this monomer. The limited degree of polymerization was not unexpected as acrylamides are known to be less ideal for ATRP reactions than methacrylates, but optimization using a different Cu catalyst chelator may prove effective.[89] Alternatively, development of the P22 as a RAFT macroinitiator may result in the desired result.[166]

Acrylamide-Bisacrylamide (xAcryl)

The ability to readily make both standed and crosslinked polymers is one of the many advantages of the ATRP methodology. Changing the degree of crosslinking could have a dramatic impact on the physical properties of the protein cage including an increase in the Young's modulus and theromostability of the construct. The samples below were made specifically to test whether the same degree of crosslinking could be attained using ATRP with this monomer combination as that observed in P22 with several generations of a click chemistry synthesized polymer.[64]

Samples were synthesized without addition of bis-acrylamide (1:0) and at loadings of 4:1 or 1:1 acrylamide to bis-acrylamide, respectively. Each $P22_{S39C}$-xAcryl reaction exhibited increased subunit mass by denaturing gel analysis, as observed by the shift to higher molecular mass (Figure 7.6), indicating that sufficiently long polymer chains had formed for a mass shift to become apparent. As the amount of crosslinker was increased from 1:0 to 4:1 to 1:1 a significant shift to dimer and other multimers was observed. When the intact $P22_{S39C}$-xAcryl constructs were compared using multi-angle light scattering the molecular mass of each composite increased from 18.6 MDa ($P22_{S39C}$-int) to 18.7, 19.0, or 19.2 MDa for loadings of 1:0, 4:1, and 1:1, respectively. In each case, these mass increases correspond to the incorporation of about 2,700 (1:0), 4,500 (4:1), and 5,800 monomers/cage on average (Figure 7.7).

To confirm that this polymer was confined to the interior of the P22, the size of the $P22_{S39C}$-xAcryl constructs were compared to the initial macroinitiator P22 complex. The average hydrodynamic particle diameter was 62±4 nm in the unpolymerized $P22_{S39C}$-

int and remained the same (64±5 nm (1:0), 64±5 nm (4:1), 60±3 nm (1:1)) after the reaction as measured by DLS (Figure 7.6). When analyzed by SEC, both $P22_{S39C}$-int and each $P22_{S39C}$-xAcryl exhibited the same elution time, further confirming that the polymer is confined to the interior of the protein cage (Figure 7.7). In addition analysis of the native constructs by agarose gel electrophoresis showed no change in electrophoretic mobility indicating that the addition of the polymer does not contribute significantly to an increased cross-sectional area (Figure 7.6).

Although complete crosslinking of the subunits was not observed in these samples, using alternative monomers that exhibit a higher degree of incorporation may produce the desired level of crosslinking. Also, further optimization of the reaction conditions for these acrylamides may result in the desired degree of crosslinking. Even with the current degree of crosslinking differences in the cage mechanical and thermoresponsive properties may be apparent.

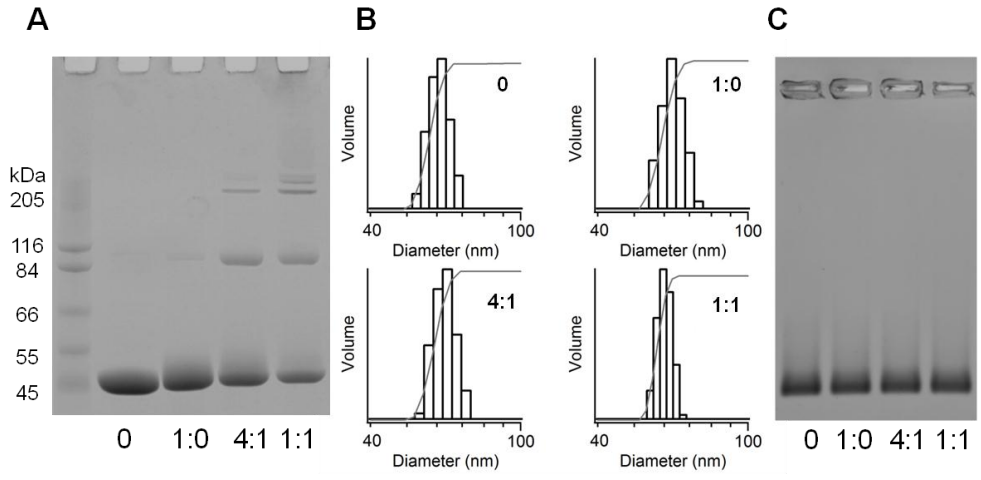

Figure 7.6: Characterization of the $P22_{S39C}$-xAcryl reactions. A) SDS-PAGE gel showing increased subunit crosslinking with increased proportion of bisacrylamide. B) DLS of each sample showing unchanged diameter. C) Native agarose gel electrophoresis showing identical migration behavior before and after polymerization.

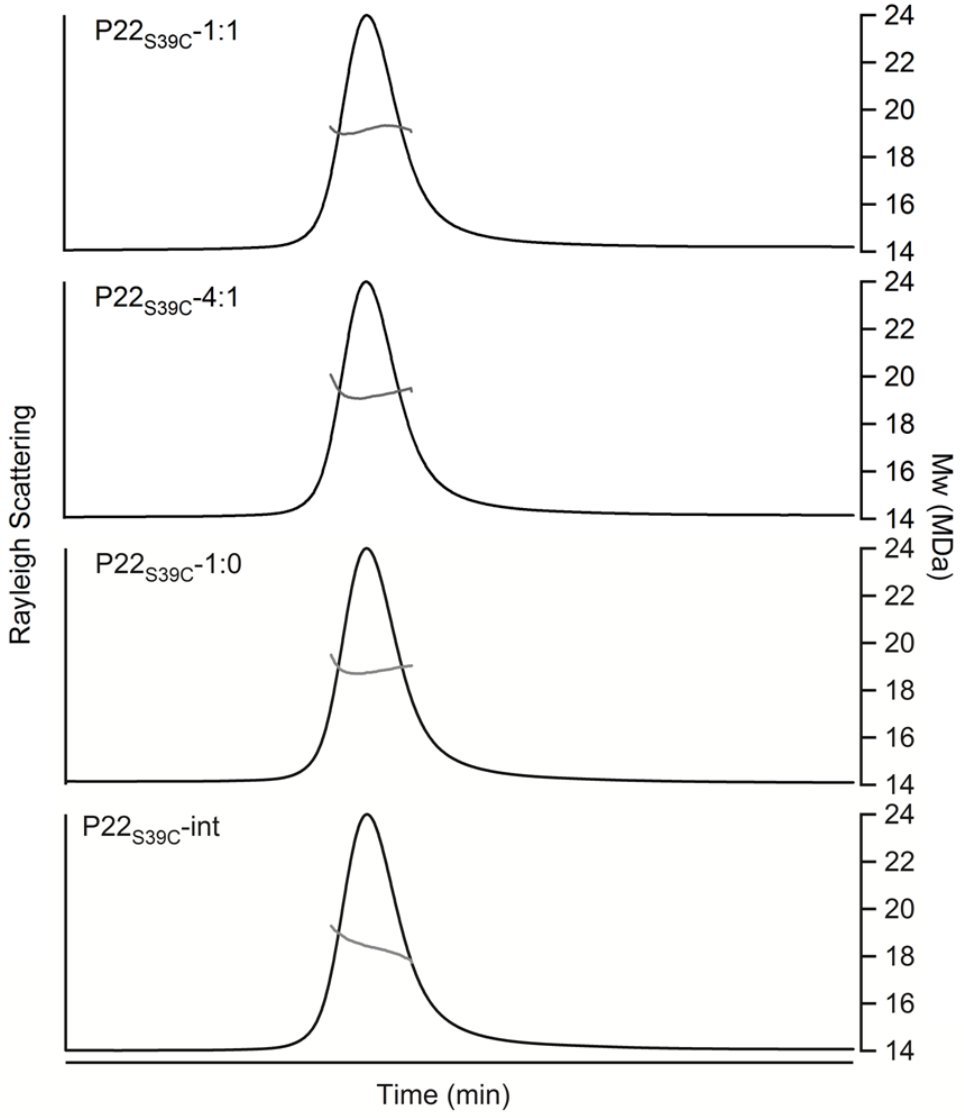

Figure 7.7: Size exclusion chromatography and multiangle light scattering of $P22_{S39C}$ before and after polymerization. No change in elution volume or particle diameter was observed between the samples, but an increase in Mw was observed in each sample compared to the starting material.

N-Isopropylacrylamide (NIPAM)

The use of stimuls responvie materials is of continuing interest for advance materials design. NIPAM is of interest due to its structural transisition to a more compact arrangement which occurs at near body temperature (~32 ºC).[167] This property has been exploited for the selective recovery of monomeric protein modified with poly(NIPAM).[90] For P22 not only could this monomer be used on the exterior of the P22 for a similar recovery results, but also on the interior. This poly(NIPAM) transition occurs counter to the thermo-driven expansion of P22, which occurs at about 65 ºC, so this polymer could serve as a means to raise the P22 expansion transition temperature, halt transformation, or even revert the expanded morphology back to the empty shell morphology.

The $P22_{S39C}$-NIPAM composite was made under standard conditions where the sample was at room temperature (~24 ºC) and purified via ultracentrifugal pelleting of the sample where the ultracentrifuge chamber was set at (4 ºC). The $P22_{S39C}$-NIPAM reactions proceeded rapidly and exhibited increased subunit mass by denaturing gel analysis, as indicated by the shift to higher molecular mass (Figure 7.8). By this analysis method it appeared that not all of the initiator labeled subunits produced sufficiently long polymer chains for a mass shift to become apparent. When the intact $P22_{S39C}$-NIPAM construct was compared using multi-angle light scattering the material apparently precipitated on the column as observed by a significant decrease in signal intensity (Figure 7.9). This protein loss is potentially due to the $P22_{S39C}$-NIPAM precipitating due to having crossed the polymer lower critical solution temperature of about 32 ºC somewhere in the HPLC-MALS system, which had a tendency to be much warmer than

room temperature due to excess heat in the instrument stack. Alternatively, the polymer may be partially localized on the exterior, as the agarose gel (Figure 7.8 C) may indicate, which could also cause the protein-polymer composite to be retained on the HPLC-MALS column.

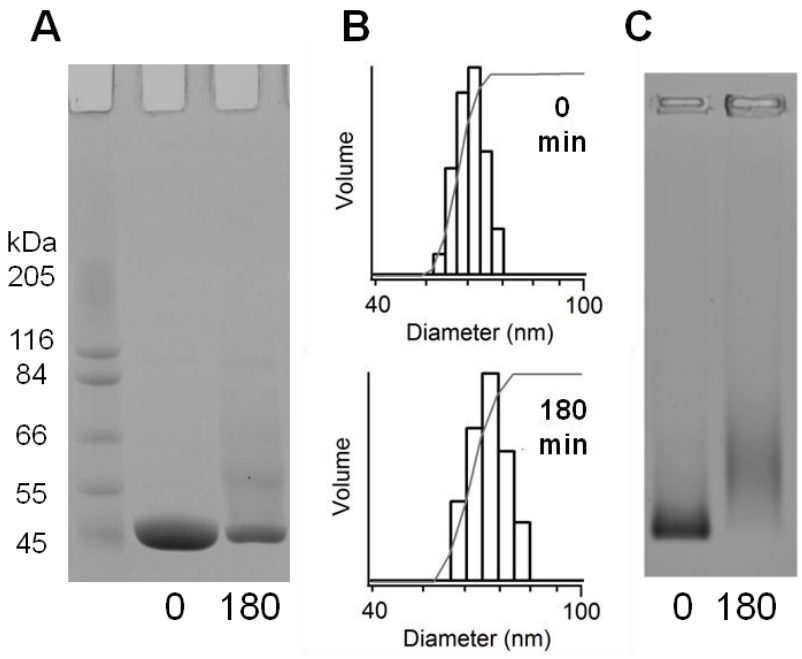

Figure 7.8: Characterization of the $P22_{S39C}$-NIPAM reaction. A) SDS-PAGE gel showing increase in Mw. B) DLS of P22 sample before and after the polymerization reaction showing slightly increased diameter (from 62±4 to 67±6 nm). C) Native agarose gel electrophoresis showing a small shift in migration behavior before and after polymerization.

To confirm that this polymer was confined to the interior of the P22, the size of the $P22_{S39C}$-NIPAM construct was compared to the initial macroinitiator P22 complex. The average hydrodynamic particle diameter was 62±4 nm in the unpolymerized $P22_{S39C}$-int and increased slightly (67±6 nm) after the reaction as measured by DLS (Figure7.8). In addition analysis of the native constructs by agarose gel electrophoresis indicated only

a minor shift in electrophoretic mobility indicating that the addition of the polymer is not dramatically altering the cross-sectional area of the composite (Figure 7.8).

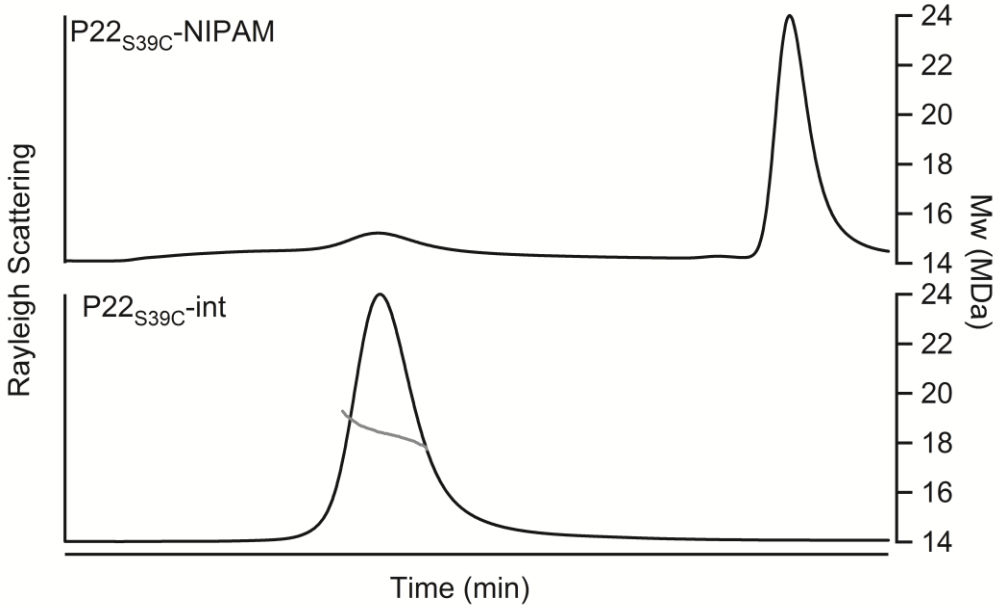

Figure 7.9: Size exclusion chromatography and multiangle light scattering of $P22_{S39C}$-NIPAM before and after polymerization. A significant reduction in signal intensity was observed at the expected elution volume and a later peak appeared indicating that the material was altered under the elution conditions.

Based on the data presented it is clear that some NIPAM was appended to the P22 macroinitator. It is clear from the poor elution of the construct when analyzed by MALS that this composite will require extra care when handling to avoid undesired temperature driven behavior. A simple means to assess the behavior of this construct with changes in temperature would be to do vary the temperature and measure the change in diameter by DLS and the amount of protein still in solution by UV-vis. If increased quantity of

NIPAM is desired then it may be beneficial to alter the reaction conditions[90,91] or utilize a different Cu catalyst ligand.[168,169]

Aminopropylmethacrylamide (APMA)

The formation of an addressable polymer inside the P22 is a highly desirable construct as described in the previous chapter. Although the P22-AEMA construct previously described has proven to be effective, the methacrylate can be more readily hydrolytically cleaved than an acrylamide bond and the presence of the ester can allow the AEMA monomer to rearrange under certain pH conditions to form the more stable methacrylamide-alcohol (Figure 7.10).[149] Thus the use of an acrylamide or methacrylamide with a primary amine side chain becomes more desirable because the pH driven arrangement and cleavage do not occur with these molecules. So, as an alternative to the AEMA, aminopropylmethacrylamide (APMA) was selected and tested.

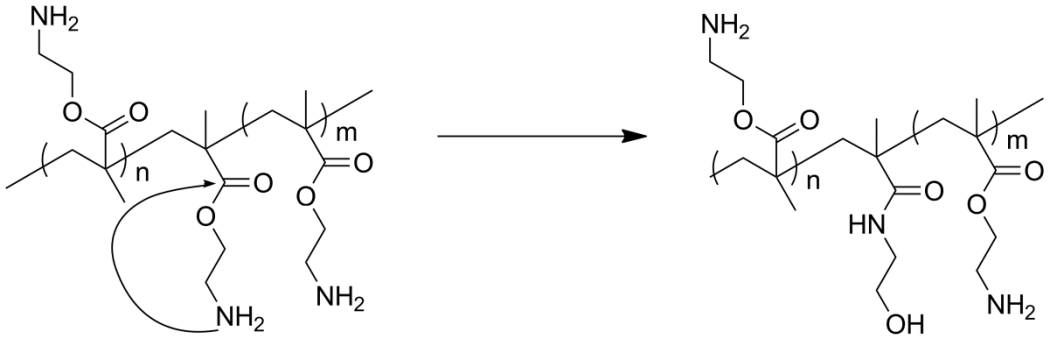

Figure 7.10: Potential undesireable rearrangement of AEMA.

The P22-APMA was made under the same conditions used to make the P22-AEMA described in Chapter 6, but was purified only via spin column rather through protein pelleting by ultracentrifugation. Compared to the P22-AEMA the P22-APMA

exhibited poor increases in subunit mass by denaturing gel analysis, as indicated by a weaker shift to higher molecular mass (Figure 7.11). By this analysis method it appeared that the APMA polymer chains are insufficiently long for a shift in subunit mass to become apparent. In comparison analysis of the native construct by agarose gel electrophoresis indicated significant shift in electrophoretic mobility much like in the P22-AEMA samples indicating that there is enough APMA addition to the P22 to cause some charge change, but not enough to be readily visible on the denaturing gel (Figure 7.11).

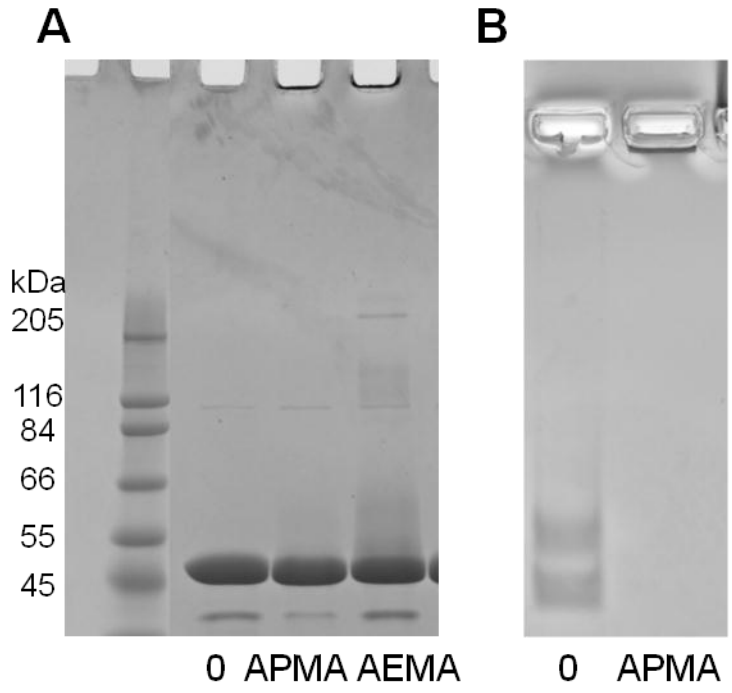

Figure 7.11: Characterization of the $P22_{S39C}$-APMA reaction. A) SDS PAGE gel showing little to no increase in the APMA sample where an AEMA polymerization under the same conditions exhibits a mass increase B) Native agarose gel electrophoresis showing a shift in migration behavior before and after polymerization for the $P22_{S39C}$-APMA sample.

Based on this initial work, it appears that APMA is not an ideal alternative to AEMA for use as a primary amine containing monomer for ATRP reactions under these conditions. Some of the reason for is lower polymerization is likely due to the methacrylamide backbone of this monomer, which although used for ATRP reactions is usually initiated under diffent condtions.[170] An alternative approach to using this monomer would be to develop a means to use this monomer in a RAFT type polymerization, which is well suited for methacrylamides, where the P22 is modified with a RAFT initiator.[171,172]

Bis-Methacrylate-AEMA (xAEMA)

Although bisacrylamide has been demonstrated in the previous chapters to be an effective crosslinking monomer for both acrylamides (TRIS-acrylamide) and methacrylates (AEMA) it would be potentially beneficial to be able to match the monomer and crosslinker functionality (ie. acrylamide with acrylamide and methacrylate with methacrylate) to more closely match the chain elongation and deactivation rates of the monomer and crosslinker. Of the methacrylate based crosslinkers, ethylene glycol dimethacrylate (bis-methacrylate) is likely to have the best water solubility due to its small size and was therefore selected for this test. Unfortunately even this small methacrylate had poor water solubility even with increasing the percentatge of organic solvent up to 30% acetonitrile of the reaction volume with bis-methacrylate droplets visible in the reaction mixture. But even with the poor solubility some incorporation into the monomer was observed when a copolymer of 16:4 AEMA:bis-methacrylate (2% reaction solution) was tested in purely aqueous buffer.

Similar to the bisacrylamide crosslinked AEMA previously described, the AEMA and bis-methacrylate reaction mixture still resulted in rapid reactions and increased subunit mass by denaturing gel analysis (Figure 7.12). Significantly a second band and other higher bands are observed in the gel corresponding to dimer and higher order coupling of subunits by the crosslinked polymer, even though the crosslinker has low solubility. Just like with the bisacrylmide crosslinked samples, by this analysis method it appeared that not all of the initiator labeled subunits produced sufficiently long polymer chains for a mass shift to become apparent. Futhermore, the expected shift in electrophoretic mobility is observed when the samples are analyzed by agarose gel electrophoresis indicating that the AEMA is also incorporated (Figure 7.13)

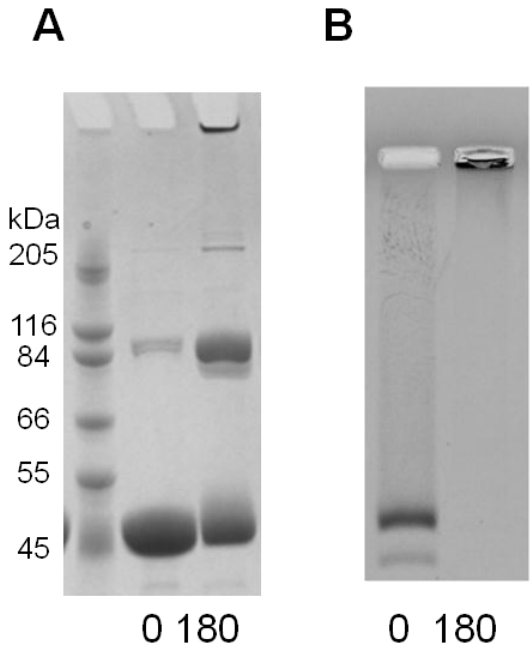

Figure 7.12: Characterization of the $P22_{S39C}$-xAEMA reaction. A) SDS PAGE gel showing increase in Mw and formation of covalently linked multimers. B) Native agarose gel electrophoresis showing the expected shift in electrophoretic mobility due to the addition of the positively charged AEMA.

Even though this monomer has poor water solubility, it appears that it has sufficient solubility to be incorporated at a reasonable level. Thus this crosslinker may be a useful alternative to the use of bis-acrylamide in the future for the formation of protein-crosslinked polymer constructs. Further optimization of the reaction conditions may lead to improved crosslinking and bis-methacrylate solubility.

Coumarin Acrylamide

The ATRP polymerization method allows for rapid incorporation of addressable sites within a VLP as described in the previous chapter, but to incorporate a dye or other visualizing agent a second labeling step is still required. To make protein-polymer composites with the dye intrinsic to the system requires that the monomer side group be the dye.

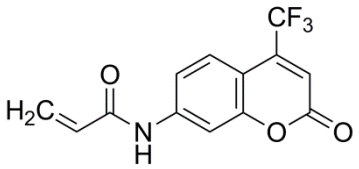

Figure 7.13: The coumarin monomer (7-[4-(Trifluoromethyl)coumarin]acrylamide)

As a test case, acrylamide-coumarin was selected and run as a copolymer with TRIS-acrylamide at a 1:30 with a final solution concentration of about 1% monomers in a pH 7.6 phosphate buffer solution. Unfortunately this monomer was much too insoluble in aqueous conditions even with greater than 10% DMSO present in the solution to lead to any measurable incorporation of dye into the growing polymer. Analysis of the material by UV-vis showed no absorbance at 342 nm and no fluorescence was observed upon

excitation with UV light after polymerization indicating that no detectable quantity of the coumarin monomer was incorporated. In the future using a dye monomer with sufficient solubility, perhaps through a charge on the molecule like that in acrylamide-fluorescein, may allow a copolymer of the dye monomer and a second highly soluble monomer (acrylamide, TRIS-acrylamide, etc) an intrinsic dye polymer to be made.

$[Fe(meth\text{-}phen)_3]^{2+}$

The use of this Fe monomer (Figure 7.14) for the formation of a crosslinked coordination polymer in P22 is a follow-on from the work in Chapter 4, where a $Fe(phen)_3$ monomer was polymerized using click chemistry. The $Fe(phen)_3$ functionality is well worth revisitng with application to the larger protein cage as the complex is a well behaved model complex for other potentially interesting coordination complexes. In addition, this complex itself is a good dye and can act as a reversible (with the addition of a siderophore like deferoxime) crosslinking agent.

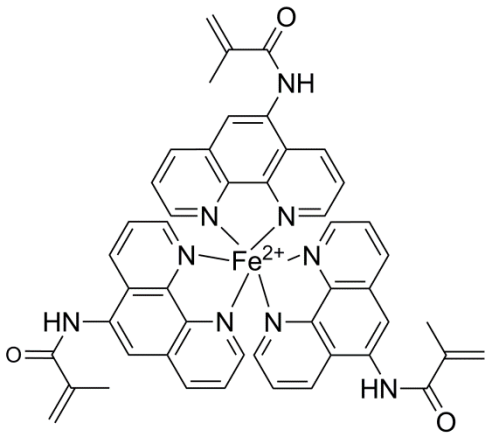

Figure 7.14: The $[Fe(meth\text{-}phen)_3]^{2+}$ monomer.

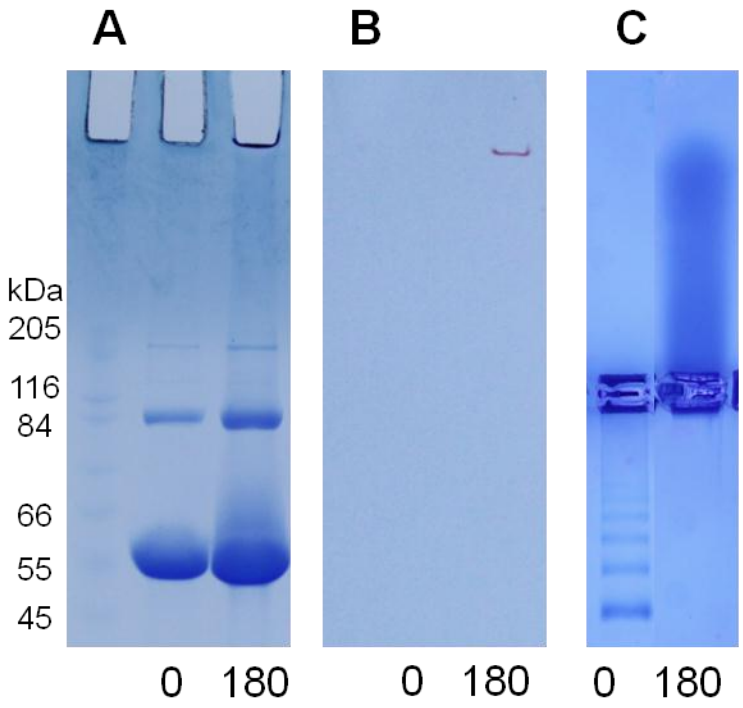

Figure 7.15: Characterization of the $P22_{S39C}$-Fe sample. A) Stained SDS-PAGE gel showing a shift to higher molecular weight and subunit crosslinking. B) Unstained SDS-PAGE gel where a pink hue from the Fe complex in visible in the top of the well where highly crosslinked material is located. C) Native agarose gel electrophoresis showing the expected reversal in migration direction due to addition of the positively charged AEMA and Fe monomers.

Because $[Fe(meth\text{-}phen)_3]^{2+}$ is both bulky and a crosslinking agent, this monomer was tested as a copolymer with AEMA at a 1:49 ratio. The Fe monomer had poor solubility in pure aqueous conditions, so the reaction was run with 20% EtOH present. The sample was purified using spin concentration followed by spin column purification. The P22-$Fe(meth\text{-}phen)_3$ (P22-Fe) reactions proceeded rapidly and exhibited increased subunit mass by denaturing gel analysis, as indicated by the shift to higher molecular mass (Figure 7.15). Significantly, a second band and other higher bands are observed in the gel corresponding to dimer and higher order coupling of subunits by the crosslinked

polymer, indicating that the trifunctional Fe complex was incorporated. A greater degree of crosslinking may be observed if acid urea denaturing conditions like those used in Chapter 4 were employed, as the SDS-PAGE conditions were observed to distrupt some proportion of the Fe-phen bonds in that case.[147] Further evidence of polymerization is observed in the unstained gel (Figure 7.15) where a pink hue from the iron complex is visible in the highly crosslinked material at the top of the gel. In addition the direction of migration on a native agarose gel is reversed as is expected for the addition of the positively charged AEMA and Fe monomers (Figure 7.15).

Preliminary quantification of the amount of iron incorporated into the protein was carried out using uv-vis spectroscopy (Figure 7.16) based on the extinction coefficient of the Fe complex at 510 nm (6.4 mM^{-1}) and assuming a quantitative yield of protein. From this data there were about 1000 Fe incorporated per cage. This is in the range expected as the AEMA alone incorporates about 12,000 monomers per cage (Chapter 6), so for the 2% loading of the trivalent monomer about 700 monomers would be expected to be incorporated. But before any additional conclusions about the relative incorporation rates of the two monomers are drawn, the amount of iron compared to protein should be quantified by a more precise method such as ICP-MS and the samples should be purified by the purification method used in Chapter 6, which more thoroughly eliminates any free AEMA polymer carryover compared to the purification method used for this sample.

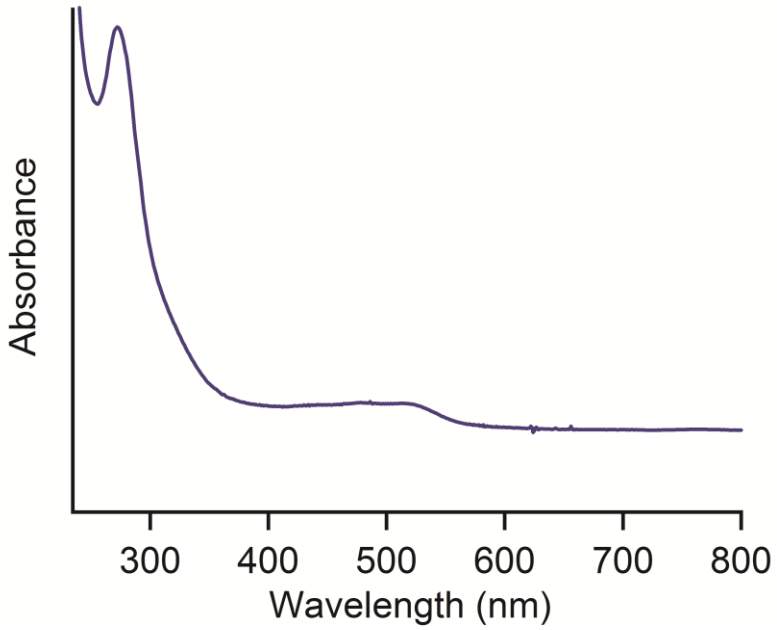

Figure 7.16: Uv-vis profile of the $P22_{S39C}$-Fe.

One of the largest concerns about this monomer was that it exhibits poor aqueous solubility, but the addition of the EtOH had the desired effect to such a degree that the proportion of Fe complex in the reaction mixture could readily be increased. In the future improved analysis of the composite using ICP to obtain a more precise Fe to protein ratio and using acid urea gels for the denaturing gel analysis to get a better measure of the degree of crosslinking will significantly improve the understanding of this reaction. In addition, better incorporation may be observed when the composite is a copolymer with a neutral or negatively charged monomer as opposed to the positively charged AEMA monomer.

[Ru(meth-phen)$_3$]$^{2+}$

Tris-phen and closely related tris-bpy ruthenium complexes have proven to be abundantly useful as dyes, photosensensitizers, and photodynamic therapies. While protein associated Ru complexes have been used to kill cells and activate hydrogenase[134,173] the use of Pt metal or coordination complexes of Co are coupled to the Ru complex for the production of hydrogen[174,175] is of particular interest. By developing a Ru complex (Figure 7.17) suitable for ATRP the first steps toward a molecular P22-metal based catalytic material can be accomplished.

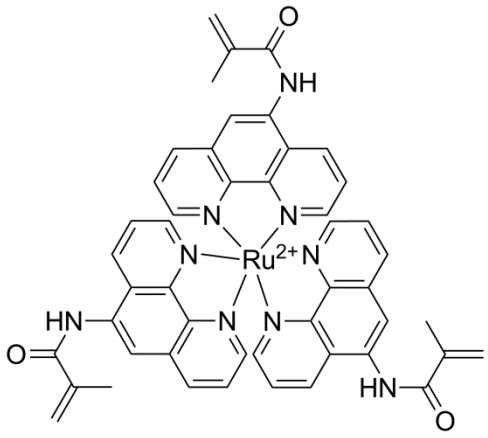

Figure 7.17: The [Ru(meth-phen)$_3$]$^{2+}$ monomer.

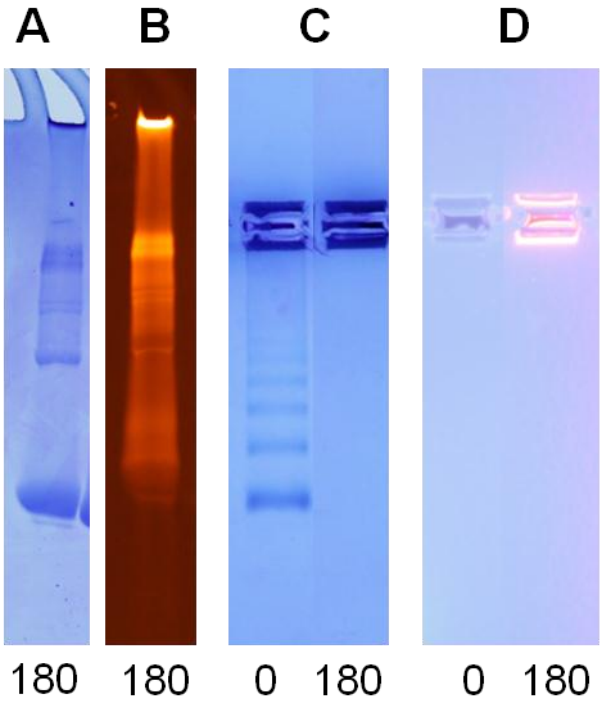

Figure 7.18: Characterization of the $P22_{S39C}$-Ru sample. A) Stained SDS-PAGE gel showing a shift to higher molecular weight and subunit crosslinking. B) Unstained SDS-PAGE gel illuminated under UV light where the fluorescence from the Ru complex in visible where polymerized material is present. C) Stained native agarose gel showing the expected reversal in migration direction due to addition of the positively charged AEMA and Ru monomers. D) Unstained native agarose gel illuminated under UV light where the Ru complex fluorescence is visible.

Because $[Ru(meth\text{-}phen)_3]^{2+}$ is both bulky and a crosslinking agent this monomer was tested as a copolymer with AEMA at a 1.2% loading. The Ru monomer had poor solubility in pure aqueous conditions, so the reaction was run with 30% EtOH present which successfully kept the Ru monomer in solution. The sample was purified using spin concentration followed by spin column purification. The P22-$Ru(meth\text{-}phen)_3$ (P22-Ru) reactions exhibited increased subunit mass by denaturing gel analysis, as indicated by the shift to higher molecular mass (Figure 7.18). Significantly a second band and other

higher bands are observed in the gel corresponding to dimer and higher order coupling of subunits by the crosslinked polymer, indicating that the trifunctional Ru complex was incorporated. The presence of the Ru complex in these bands was verified by the fluorescence observed in the UV illuminated unstained gel (Figure 7.18). Further evidence of incorporation is that, as expected for the addition of the positively charged AEMA and Ru monomers, the direction of migration on a native agarose gel is reversed and the Ru fluorescence co-migrates with the intact protein cage (Figure 7.18).

Preliminary quantification of the amount of ruthenium incorporated into the protein was based on the absorbance of the sample at 450 nm using an extinction coefficient for the Ru complex of 13.5 mM^{-1} and assuming a quantitative protein yield. From these data we concluded that approximately 800 Ru were incorporated per cage. This is in the range expected as the AEMA alone incorporates about 12,000 monomers per cage (Chapter 6), so for the 1.2% loading of the trifunctional monomer about 400 monomers would be expected to be incorporated. Before any additional conclusions about the relative incorporation of the two monomers can be drawn, the amount of ruthenium compared to protein should be quantified by a more precise method such as ICP-MS and the samples should be purified by the purification method used in Chapter 6, which more thoroughly eliminates any free AEMA polymer carryover compared to the method used for this sample.

One reason for pursuing a Ru based polymer is that this complex could be used as a photosensitizer for catalytic hydrogen production from water when it is coupled to metallic platinum (Figure 7.19).[32] To begin testing the potential of using the P22-Ru for

the directed mineralization of Pt inside the P22 (Figure 7.20), the sample in mineralization buffer (200 mM EDTA, 50 mM MES, 100 mM NaCl, pH 6.5) was incubated overnight with an aged aqueous K_2PtCl_4 solution at a loading of 1,000, 5,000, or 10,000 Pt ions per cage. On the following day, each solution was illuminated with a high intensity LED light (455 nm) for 1.5 hrs. The samples were then centrifuged at 17,000 gs for 20 min to remove any resulting precipitate then purified away form excess Pt ions through spin concentration and spin columns. The resulting UV-vis spectra of the P22-Ru-Pt composites are contained in Figure 7.21. In each of the Pt treated P22-Ru samples the sample shows an increase in absorbance in the range of 350 nm, which is indicative of the formation of Pt nanoparticles. In control reactions with P22-int treated with Pt in the same manner there was no change in the spectra.

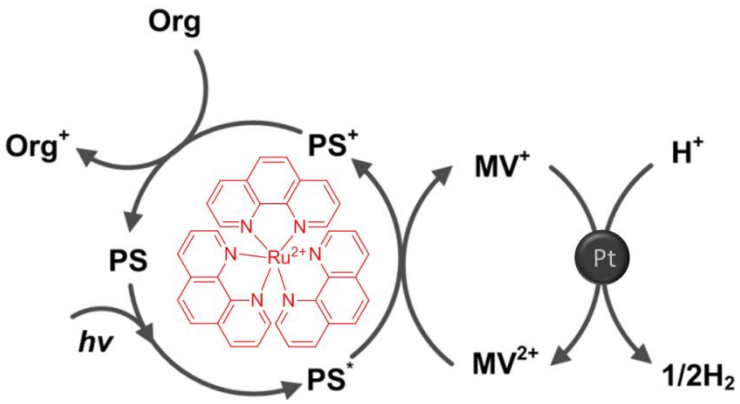

Figure: 7.19 A Ru-Pt photocatalytic cycle. Here the Ru complex is the photosensitizer (PS) which when excited by light transfers an excited electron to the methyl viologen (MV) electron mediator which in conjunction with the Pt nanoparticle catalyzes the formation of hydrogen equivalents from water. To complete the cycle the Ru complex is regenerated to its initial oxidation state by obtaining an electron from the sacrificial reductant (Org).

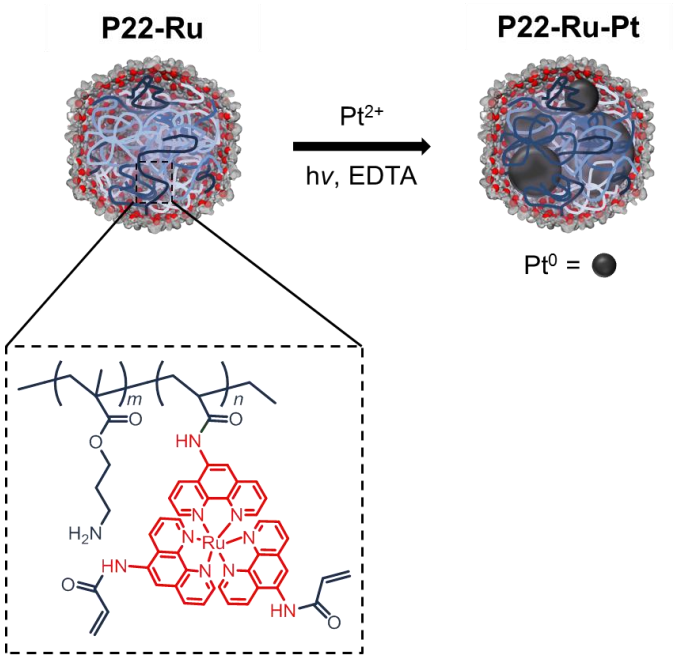

Figure 7.20: Scheme for formation of Pt nanoparticles inside P22

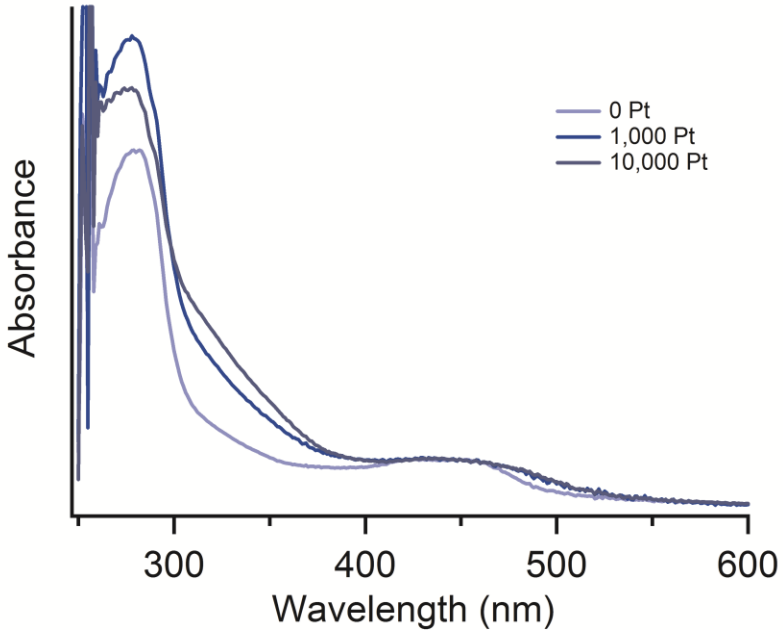

Figure 7.21: Uv-vis profile of the $P22_{S39C}$-Ru-Pt samples. Each sample is standardized based on the Ru absorbance at 410 nm.

Based on this preliminary experiment it appears that it is possible to readily form a P22-Ru material with this Ru monomer. Use of this composite to form a P22-Ru-Pt construct also appears to be successful. Futher work to thoroughly quantify the amount of Ru and Pt incorportated into the P22 will be instrumental to further use of this material. Additional testing to ensure that the P22-Ru-Pt complex can catalytically produce H2 from water will further confirm the success of this process. Modification of the reaction conditions to use a different co-monomer and to increase the molar proportion of Ru present, as the complex was suffenciently soluble, could serve to easily increase the number of Ru incorporated per cage.

Other Metal Binding Monomers

Much like the phenanthroline complexes described above, the potential uses of metal binding monomers inside a protein cage are numerous. So, not only meth-phenanthroline, but also meth-pyridine was synthesized. These two monomers (Figure7.22), in preliminary tests suffered from poor solubility in the reaction solution. In addition both monomers will be binding competitors for the catalytic copper. The meth-phen is expected to readily substitute for the unmodified bipyridine used in the catalyst, thereby trapping the Cu into the protein-polymer complex. Because the binding affininty of pyridine for copper is less than that of bipyridine, the deactivation of the catalyst and entrapment of Cu in the composite is less of a concern with the meth-pyridine. Efforts are ongoing to find suitable reaction conditions and to make the desired phenanthroline or pyridine based polymer.

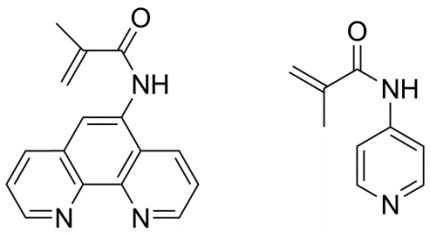

Figure 7.22: The meth-phen (left) and meth-pyrine (right) monomers.

Conclusion

Expansion of the range of protein-polymer composites could have impacts on light-harvesting materials, stimulus responsive materials, analysis of these composites, and open new means to package molecules into this composite. Each of the monomers investigated in this chapter, with the exception of the coumarin monomer, appear promising for their respective applications.

As with any polymerization technique some monomers will be better suited than others under the established conditions, so careful consideration of whether the monomer is a methacrylate vs acrylamide vs methacrylamide can have a significant impact on the successful formation of the desired composite. Future investigations would be well served to consider alterations to the type of Cu ligand utilized in the reaction to optimize the rates of chain growth and termination to realize maximal polymer incorporation. Altering the reaction composition to increase the percentage of the new monomer and switching from the use of AEMA as a co-monomer to a neutral, well behaved species may serve to futher increase the degree of desired polymerization.

One of the most substantial limitations to the use of some of the ATRP monomers investigated was lack of water solubility. Here we found that, provided the protein to be

modified is not significantly destabilized in organic solvents addition of DMSO, ethanol, or acetonitrile to the polymerization reaction can serve to balance monomer solubility with protein stability. In several cases adding an organic cosolvent has the desired effect (coordination complexes, bis-methacrylate), while in others the desired monomer is just too water insoluble (coumarin) to be suitable for the grafting from ATRP approach.

Although each of the monomers in this and previous chapters were explored for use as internal polymers these and other monomers could have significant applications if polymerized from exterior facing initiation sites. Some potential applications are similar to those found in the literature using monomeric proteins, which inherently place the polymer exposed to the exterior. Modification of these proteins leads to materials that can be used thermoresponsive recovery or are shielded from the immune system. Modification of P22 in this way should result in similar materials, but with the added benefit of having an interior volume, which could be otherwise modified making these materials particularly suited to use as tectons in a higher order structure. Thus polymerization attempts with other mutation sites than those already explored is also highly desireable.

Experimental

All reagents were analytical grade and purchased from either Sigma-Aldrich or Fisher Scientific and used as received unless otherwise noted. All water was deionized using a NANOpure water purification system. Mutagenesis and purification of P22 were completed according to established protocols as described in Chapter 6. Cysteine reactive initiators were synthesized and reacted with protein as described in Chapter 6.

Methacrylic acid, acrylamide, N-isopropylacrylamide, bis-methacrylate, TRIS-acrylamide, and coumarin-acrylamide were purchased from Sigma-Aldrich and used without further purification. N-(3-Aminopropyl)methacrylamide was purchased from Polysciences. Synthesis protocols for all other monomers are contained in Appendix D. Dynamic light scattering measurements were taken on a 90Plus particle size analyzer (Brookhaven). Multi-angle light scattering measurements were collected using a Heleos (Wyatt) instrument with a size exclusion column and using a dn/dc value of 0.185 for all samples.

CHAPTER 8

CONCLUSION

In this and other work, protein cages have been used to make a variety of protein-based composite materials. All of these syntheses are at some level inspired by the processes used by Nature to form protein-mineral and protein-nucleic acid based structures. Often these synthetic materials are made with a biomimetic approach using mild reaction conditions in an aqueous environment. As this field has expanded the potential applications of these materials has become more diverse to include materials aimed toward energy, electronics, and medical applications. While much of the field is application driven, these studies also serve to improve our understanding of the native protein behavior and processes.

Mimicking the piecewise synthesis of mineral inside ferritin, which relies on interior-exterior differentiation, in Chapter 3 the mineralization of Pt nanoparticles in LiDps protein was accomplished through the attachment of phenanthroline, a metal binding ligand, to the interior of the protein. Without this chemical modification, it was not possible to synthesize the Pt nanoparticles under mild conditions with spatial control. The use of native mass spectrometry to resolve the number of Pt atoms bound or mineralized in this protein cage under these conditions made it possible to measure the differences in the loading ratio even though the synthesized particles were too small to visualize using other methods. Inspired by the success of the mass spectrometry method developed in this work a similar approach was used as the basis for experiments which allowed the ferrihydrite mineralization process in LiDps to be modeled, thereby

increasing our understanding of the natural LiDps mineralization process. In addition of being a developmental model for native mass spectrometry quantification of mineralization, the LiDps-Pt was shown to be capable of catalytic hydrogen production using an established photocatalytic hydrogen production reaction scheme. Since the nanoparticles were active catalysts, further work to establish the relationship between Pt nanocluster size and hydrogen produced may lead to the development of more efficient hydrogen production systems through Pt particle size optimization.

In Chapter 4, changing the synthetic units involved in the piecewise formation of a MOP proved essential to the successful formation of a sHsp-MOP composite in. By preforming the metal complex and then completing the organic ligand with azide-alkyne click chemistry, a new approach for making protein-coordination complex materials was established. While this model system demonstrated a spatially controlled synthesis with initiation from the interior of a protein cage, this proof-of-concept material did not fully utilize some of the advantages inherent to the synthetic design. The approach taken, of forming the coordination complex first, allows coordination complexes which require protein incompatible synthetic conditions to be directly incorporated into the polymer network. Thus, this method then could provide a means to incorporate a large number of photosensitizers, like Ru complexes, into the interior of a protein substrate, which would not be possible using the standard coordination complex formation driven assembly for making MOPs. In addition, the generational nature of the click chemistry polymerization allows for improved control over the monomer arrangement compared to other

polymerization approaches like ATRP, which does not have a way to control the ‘nearest neighbor’ of each monomer.

Although ATRP cannot control the arrangement of monomers in a copolymer, the continuous nature of this reaction outweighs its detractions in many instances. The use of ATRP made possible the internally confined grafted-from polymer described in Chapter 5. This primary amine rich polymer begins to take advantage of the previously largely untapped interior volume of the P22, where internal occupancy otherwise relied on genetic modification of the scaffold protein. The use of AEMA to form the polymer results in a scaffold, which can be subsequently labeled with molecules of interest such as fluorophores or MRI contrast agents in such a manner that the same approach could be applied to other protein-based systems. The labeled P22-polymer composite in chapter 5 had an order-of-magnitude improvement in relaxivity on a particle basis over other VLP based contrast agents and was competitive with other macromolecular MRI contrast agent vehicles, but was more monodisperse. Due to the promising medical applications of this material work to make further improvements in the MRI contrast agent carrier through targeting the construct to specific tissues is ongoing.

The usefulness of the ATRP approach is not limited to synthesis with AEMA, rather this method opens the possibility of forming a wide range of polymers, which could not be attained using other methods. Because the virus inspired polymer encapsulation approach relies on electrostatic interactions, the range of polymers that can be encapsulated is inherently limited, but ATRP has no such limitation. The neutral P22-TRIS-acrylamide composites made using ATRP in Chapter 4 has served to alter our view

of the K118C initiation site. Previously the site was interpreted to be more interior facing than the new structural models and the results of this study suggest, which indicate that the site is likely interfacial, sampling both the interior and exterior of the capsid. Furthermore, preliminary data on a range of P22-polymer constructs where the polymer is an acrylamide, meth-acrylamide, or meth-acrylate indicate that metal binding, thermoresponsive, and crosslinked polymers can be made inside P22. The success fo these polymerization attempts emphasizes the diverse rang eof constructs attainable using this synthetic method. While many of these constructs showed sufficient polymerization, further optimization of the reaction conditions for the specific monomers may lead to improved polymerization.

Altogether, several new piecewise synthetic methods were developed, which expanded the range of materials synthetically attainable for protein based composites. Modification of the interior through genetic and chemical modification proved essential to the success of these syntheses. Using one these materials a new analysis procedure was developed, which opened a new means to study mineralization in protein cages. The approach required for successful formation of a MOP in the protein cage used here is one that could be used for inclusion of additional coordination complexes and is a method that could be used in bulk. The ATRP route developed to make polymers inside P22 is of a sufficiently general design to be applicable to a wide array of monomers, which could be used for a wide range of applications. Furthermore, each synthetic method used to make the protein-metal, protein-MOP, and protein-polymer composites described can be

readily transferred or subtly modified for use with other protein systems and developed further for energy, electronics, or medicine applications.

APPENDICES

APPENDIX A

SUPPORTING INFORMATION FOR CHAPTER 3

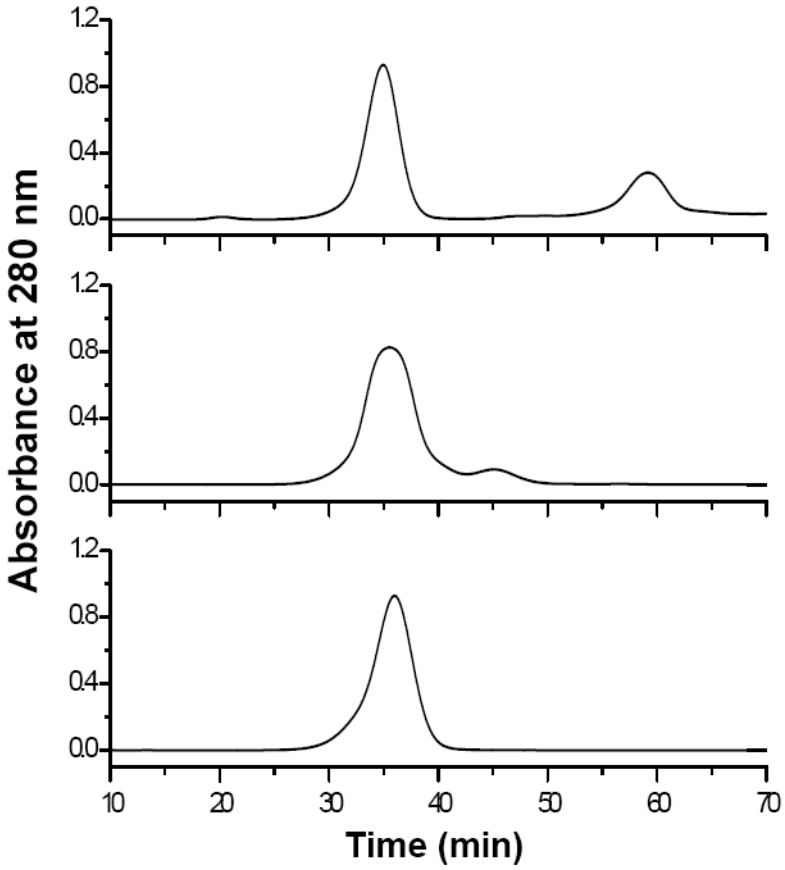

Figure A1: Size exclusion elution profiles of wild type (bottom), untreated (middle) and iodo-phen treated.

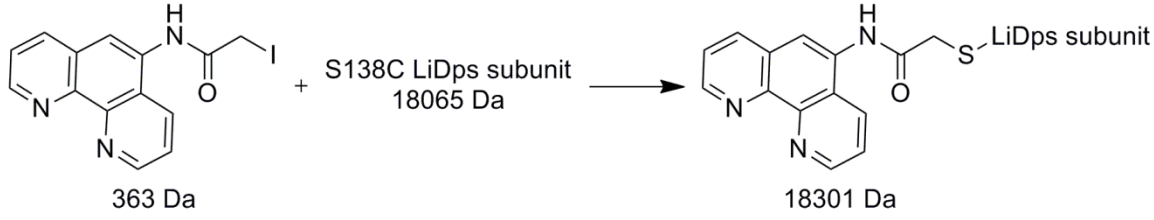

Figure A2: Reaction scheme of covalent attachment of 5-iodoacetoamido-1,10-phenanthroline to the S138C

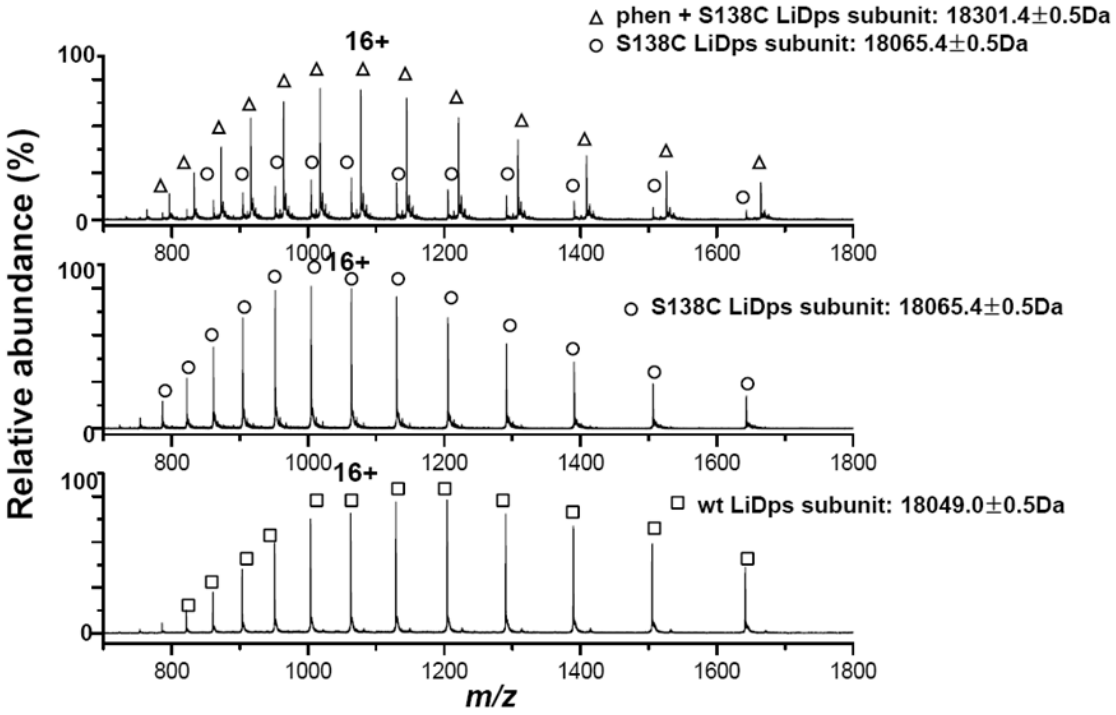

Figure A3: Subunit mass spectrometric analyses of the iodo-phen treated S138C and wt LiDps. Mass spectra of the iodo-phen treated S138C (top) and wt (bottom) LiDps and untreated S138C LiDps (middle) subunits. Two dominate Gaussian chage state distributions were observed in the iodo-phen treated S138C LiDps and are labeled as triangles and circles (top). Only one Gaussian charge state distribution was observed in the wt and untreated S138C LiDps and labeled as open squares (bottom) and open circles (middle). Charged peaks (16+ of either a single phen labeled and unlabeled subunit are indicated. Component analyses of tow dominant charge state distributions of iono-phen treated S138C LiDps showed masses of a single phenanthroline moiety attached (open triangles, calc. 18300.7 Da; obs. 18301.4 Da) and the unlabeled (open circles, calc. 18064.7 Da; obs. 18065.4 Da) subunits. Component analysis of charge state distributions of iodo-phen treated wt LiDps showed mass of unmodified wt (open sqaures, calc. 18048.6 Da; obs. 18049.0 Da) subunit.

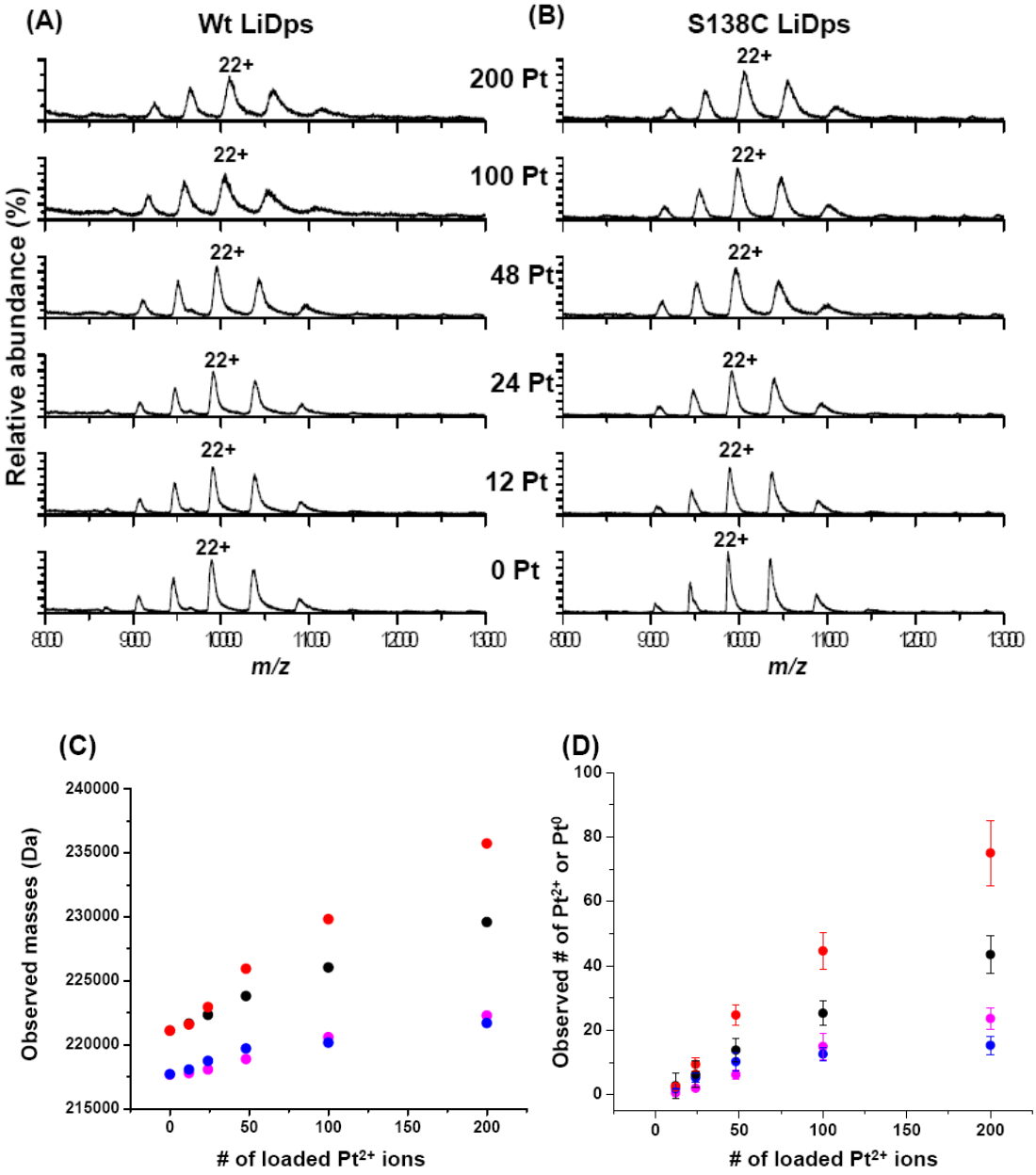

Figure A4: Non-covalent mass spectra of Pt^{2+} ion bound LiDps cages and plots of observed masses. Mass spectra of the Pt^{2+} ion bound wt (A) and S138C (B) LiDps cages at various loadings of Pt^{2+} (0, 12, 24, 48, 100, and 200 Pt^{2+} /cage, bottom to top). Charged peaks (22+) of the cages are indicated. (B) Plots of the observed masses (C) and converted numbers (D) of the Pt^{2+} ion bound phen-S138C (black circles), wt (blue circles), S138C (magenta circles) LiDps, and the Pt^{0} mineralized (red circles) phen-S138C LiDps cages according to the initial Pt^{2+} input numbers. Deviations of Pt^{2+} ion or Pt^{0} contents in the broadened peaks were determined by calculating half-width at the halfheight of each peak and comparing to a 0 loading control.

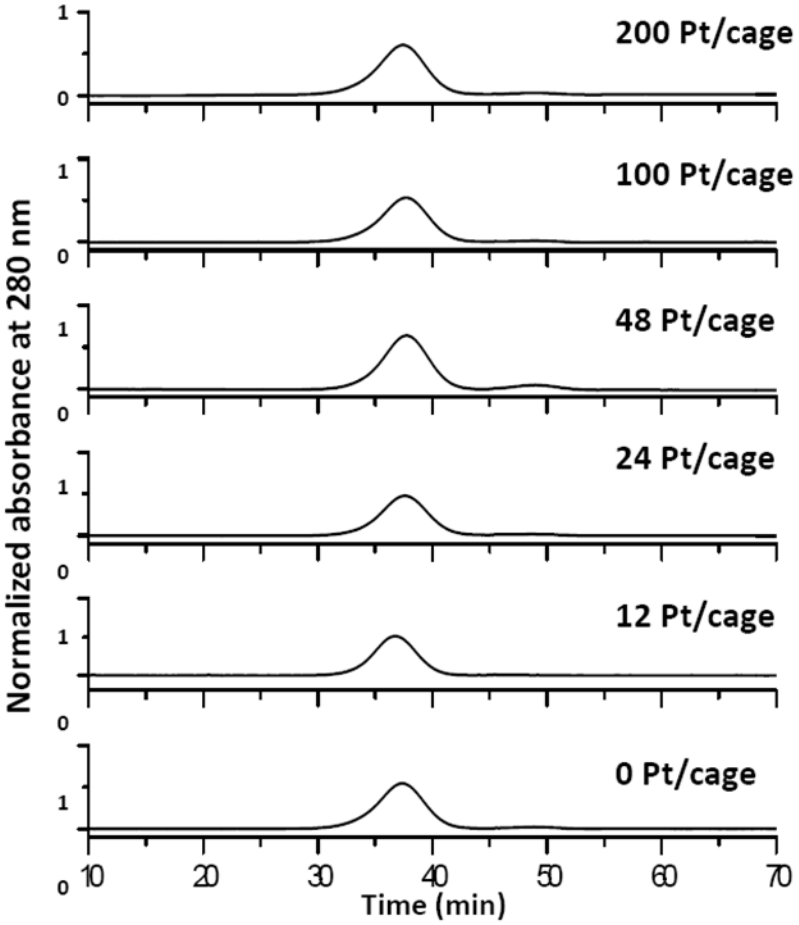

Figure A5: Size exclusion profiles of the Pt^0 mineralized phen-S138C LiDps. Initial inputs (0, 12, 24, 48, 100,and 200 Pt^{2+} /cage, bottom to top) of the Pt^{2+} ions are indicated at the each panel.

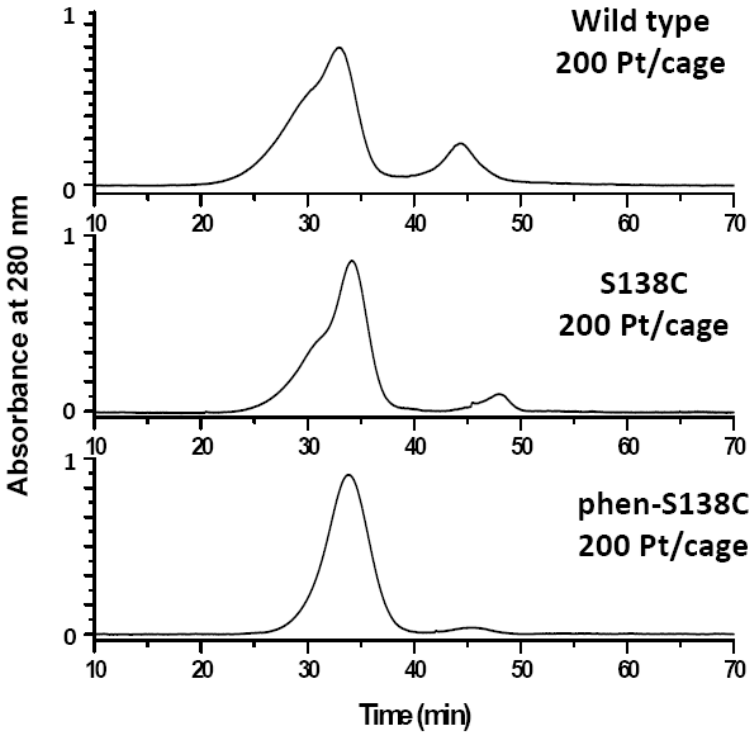

Figure A6: Size exclusion profiles of the Pt^0 mineralized (theoretical loading of 200 Pt^{2+} /cage) wild type (top), S138C (middle), and phen-S138C LiDps.

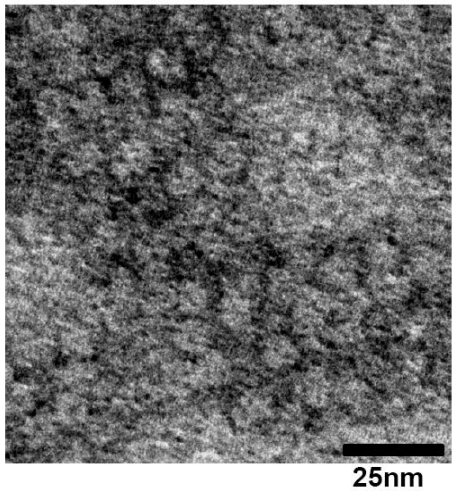

Figure A7: Transmission electron micrograph of the 75 Pt^0 containing phen-S138C LiDps (theoretical loading of 200 Pt^{2+}/cage) stained with 2% uranyl acetate.

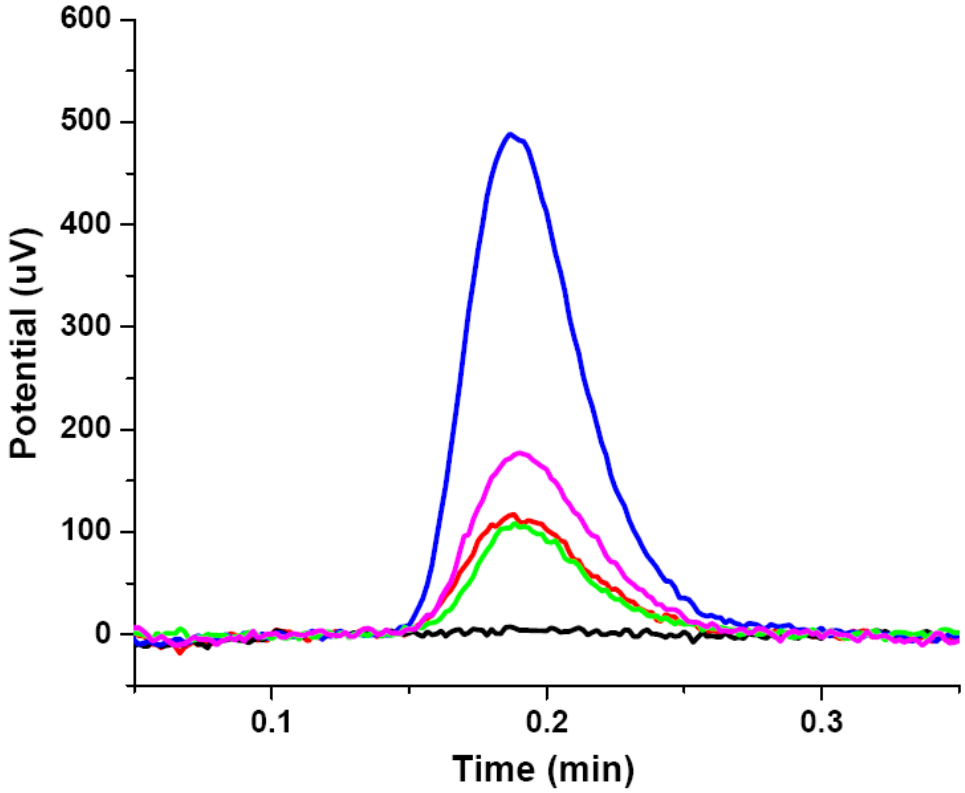

Figure A8: Hydrogen production from the Pt^0 mineralized phen-S138C LiDps. (A) Gas chromatographic traces of blank (black), Ir complex only (red), 25 Pt^0 (green), 44 Pt^0 (magenta), and 75 Pt^0 (blue) mineralized phen-S138C LiDps after 1hr of illumination.

APPENDIX B

SUPPORTING INFORMATION FOR CHAPTER 4

Experimental Section

Materials.

All reagents were purchased from Aldrich Chemical Co. or Fisher Scientific and used without further purification. All water was purified through a Nanopure system to 18.2 MΩ resistivity before use. Tetrahydrofuran was distilled over sodium metal and benzophenone under nitrogen.

N-(3-azidopropyl)-1,10-phenanthrolin-5-amine (az-phen).

In a flask, under argon**,** 0.50 g 5,6-epoxy-5,6-dihydro-1,10-phenanthroline (0.50 g, 25 mmoles) was dissolved in 6 mL water and 3 mL THF.[136] To this solution 3-azidopropylamine (76.5 mmoles, 3-fold excess) was added dropwise.[37] This reaction was stirred at room temperature for 24 hrs followed by extraction 3 times with methylene chloride. The organic layer was dried over anhydrous sodium sulfate and the solvent was removed using a rotary evaporator. The crude compound was purified by column chromatography (silica gel, 9:1 CH_2Cl_2:TEA) to yield a dark yellow oil in near quantitative yield. The entire product from step 1 was added to a solution containing 0.7 g 95% NaH (12-fold excess) in 75 mL dry THF under Ar and refluxed for 4 hrs. The reaction was cooled to room temperature and 20 mL MeOH was slowly added dropwise to quench the reaction. The solvents were removed by rotary evaporation and the product was dissolved in 150 mL water followed by extraction 4 times with methylene chloride. The crude final product was purified by column chromatography (silica gel, 9:1 CH_2Cl_2:TEA) resulting in a yellow solid (0.24g, 35% yield). ^{1}H NMR ($CDCl_3$, 500 MHz): δ 9.06 (d, J = 4.5, 1H), 8.89 (d, J = 2.5, 1H), 8.33 (d, J = 8.5, 1H), 8.03 (d, J = 8.0,

1H), 7.56 (q, J = 4.5, 1H), 7.54 (q, J = 4.5, 1H), 6.63 (s, 1H), 4.91 (s, br, NH), 3.57 (t, J = 6.5, 2H), 3.47 (t, J = 6.5, 2H), 2.10 (m, J = 6.5, 2H). LC-MS: M + H 279.1388 (found), M + H 279.1358 (calculated).

Caution: Exercise extra caution when handling the reagents in this reaction scheme as azides can be an explosion hazard.

Fe(az-phen)$_3$(PF_6)$_2$.

A fresh aqueous solution containing ammonium iron(II) sulfate hexahydrate (329 μmoles) was mixed in a 1:3 molar ratio with a solution of 5-aminopropylazide-1,10-phenanthroline (987 μmoles) instantly forming a dark red solution. The solution was allowed to stir at room temperature for 30 min followed by precipitation by adding a saturated aqueous solution of ammonium hexafluorophosphate dropwise to the mixture. The red solid was collected through filtration and washed with ether and water. The dark red powder was recrystallized from dichloromethane and ether to yield the final product Fe(az-phen)$_3$(PF_6)$_2$ (0.25 g, 64% yield). ^{1}H NMR ($CDCl_3$, 500 MHz): δ 8.61 (t, J = 6.5, 1H), 8.20 (t, J = 7.5, 1H), 7.61 (td, J = 5.0, 20.5, 1H), 7.54 (m, J = 5.5, 1H), 7.35 (m, J = 3.5, 1H), 7.22 (td, J = 5.0, 24.0, 1H), 6.98 (d, J = 3.5, 1H), 5.86 (d, J = 3.0, 1H, NH), 3.54 (t, J = 6.5, 2H), 3.50 (d, J = 6.0, 2H), 2.06 (m, J = 6.5, 2H). LC-MS: M + H 890.3658 (found), M + H 890.3189 (calculated).

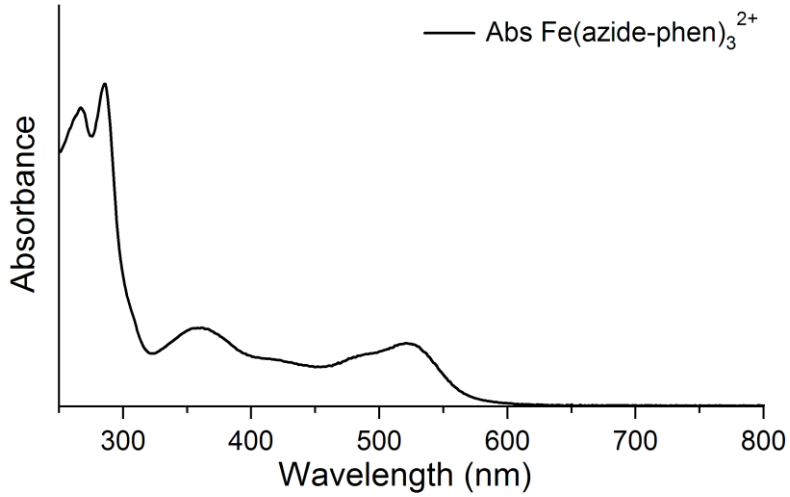

Figure B1: Uv-vis trace of Fe(az-phen)$_3^{2+}$ in water.

sHsp G41C Cage Purification and Characterization.

Methanococcus jannaschii sHsp G41C was purified from an *E. coli* heterologous expression system as previously described.[176] One liter cultures of *E. coli* (BL21 [DE3] B strain) containing pET-30a(+) sHsp16.5 plasmid were grown overnight in LB medium with kanamycin added (37°C, 220 rpm). Cells were harvested by centrifugation at 3700*g* for 15 min and resuspended in 30 mL of 100 mM HEPES, 50 mM NaCl, pH 8.0. Lysozyme, DNase, and RNase were added to the final concentrations of 50, 60, and 100 μg/mL, respectively. The sample was incubated for 30 min at room temperature, French pressed (American Laboratory Press Co., Silver Springs, MD), and sonicated on ice (Branson Sonifier 250, Danbury, CT, power 4, duty cycle 50%, 3 × 5 min with 3 min intervals). Bacterial cell debris was removed via centrifugation for 20 min at 12 000*g*. The supernatant was heated for 15 min at 65 °C, thereby denaturing many *E. coli*

proteins. The supernatant was centrifuged for 20 min at 12 000*g* and purified by gel filtration chromatography (Superose-6, Bio-Rad Duoflow, Hercules, CA).

Coordination Polymer Synthesis Inside sHsp G41C

sHsp G41C-alkyne Conjugate (G0.5). sHsp G41C (30 mg, 2.0 mg/mL, 1.8 μmoles subunit) in phosphate buffer (100mM phosphate, 5 mM EDTA, 100mM NaCl, pH 7.6) was reacted at room temperature for 3 hrs with N-propargylbromoacetamide (100mM, 11 μmoles, dissolved in DMF) at a 6-fold excess relative to subunit protein. The reaction was quenched with an equimolar (11 μmoles) amount of 2-mercaptoethanol followed by dialysis (100mM HEPES, 50 mM NaCl, pH 7.5) with near quantitative yield as measured by absorbance at 280 nm using the published extinction coefficient (9322 M^{-1} cm^{-1}) for SHsp.[177]

sHsp G41C-alkyne-iron Conjugate (G1.0). sHsp G41C-alkyne (20 mg, 2.0 mg/mL, 1.2 μmoles subunit) in 100mM HEPES, 50 mM NaCl, pH 7.5 was added to 35 mL solution (25 mL water, 10 mL buffer) containing $Fe(azide\text{-}phen)_3^{2+}$ (4 μmoles). To this solution a mixture of CuSO4 (0.17 μmoles) and TBTA-OH (4.25 μmoles), 100mM aminoguanidine in water (34 μmoles), and freshly made 100mM sodium ascorbate (34 μmoles) were added sequentially with thorough mixing between each additional reagent. This solution was allowed to mix at room temperature for 1 hr followed by dialysis and size exclusion chromatography on a Superose 6 column (Amersham Bioscience).

sHsp G41C-alkyne-iron-alkyne Conjugate (G1.5). sHsp G41C-alkyne (14 mg, 2.0 mg/mL, 0.85 μmoles subunit) in 100mM HEPES, 50 mM NaCl, pH 7.5 was added to 40 mL solution (30 mL water, 10 mL buffer) containing tripropargylamine (5 μmoles). To

this solution a mixture of CuSO4 (0.225 μmoles) and TBTA-OH (5.5 μmoles), 100mM aminoguanidine in water (44 μmoles), and freshly made 100mM sodium ascorbate (44 μmoles) were added sequentially with thorough mixing between each additional reagent. This solution was allowed to mix at room temperature for 1 hr followed by dialysis and size exclusion chromatography on a Superose 6 column (Amersham Bioscience).

sHsp G41C-alkyne-iron-alkyne-iron Conjugate (G2.0). sHsp G41C-alkyne (6 mg, 2.0 mg/mL, 0.36 μmoles subunit) in 100mM HEPES, 50 mM NaCl, pH 7.5 was added to 40 mL solution (30 mL water, 10 mL buffer) containing $Fe(azide\text{-}phen)_3^{2+}$ (5 μmoles). To this solution a mixture of CuSO4 (0.225 μmoles) and TBTA-OH (5.5 μmoles), 100mM aminoguanidine in water (44 μmoles), and freshly made 100mM sodium ascorbate (44 μmoles) were added sequentially with thorough mixing between each additional reagent. This solution was allowed to mix at room temperature for 1 hr followed by dialysis and size exclusion chromatography on a Superose 6 column (Amersham Bioscience).

sHsp G41C-alkyne-iron-alkyne-iron-alkyne Conjugate (G2.5). sHsp G41C-alkyne (2 mg, 2.0 mg/mL, 0.12 μmoles subunit) in 100mM HEPES, 50 mM NaCl, pH 7.5 was added to 15 mL solution (30 mL water, 10 mL buffer) containing tripropargylamine (3.3 μmoles). To this solution a mixture of CuSO4 (0.15 μmoles) and TBTA-OH (3.7 μmoles), 100mM aminoguanidine in water (30 μmoles), and freshly made 100mM sodium ascorbate (30 μmoles) were added sequentially with thorough mixing between each additional reagent. This solution was allowed to mix at room temperature for 1 hr followed by dialysis and size exclusion chromatography on a Superose-6 column (Amersham Bioscience).

sHsp G41C-alkyne-iron-alkyne-iron-alkyne-iron Conjugate (G3.0): sHsp G41C-alkyne (0.5 mg, 2.0 mg/mL, 0.03 μmoles subunit) in 100mM HEPES, 50 mM NaCl, pH 7.5 was added to 14 mL solution (10 mL water, 4 mL buffer) containing Fe(azide-phen)$_3^{2+}$ (1.8 μmoles). To this solution a mixture of CuSO4 (0.08 μmoles) and TBTA-OH (1.8 μmoles), 100mM aminoguanidine in water (15 μmoles), and freshly made 100mM sodium ascorbate (15 μmoles) were added sequentially with thorough mixing between each additional reagent. This solution was allowed to mix at room temperature for 1 hr followed by dialysis and size exclusion chromatography on a Superose-6 column (Amersham Bioscience).

sHsp G41C coordination polymer composite analysis. sHsp G41C and each coordination polymer generation were characterized by SEC (Superose 6, Bio-Rad Duoflow), DLS (Brookhaven 90Plus, Brookhaven, NY), TEM (Leo 912 AB), SDS-PAGE, and mass spectrometry (NanoAcquity/Q-Tof Premier; Waters, Milford, MA). The protein concentration was determined by absorbance at 280 nm using the published extinction coefficient (9322 M^{-1} cm^{-1}).[52] The assembled protein cages at each generation including the native sHsp G41C were imaged by transmission electron microscopy by negatively staining the sample with 2% uranyl acetate on formvar carbon coated grids.

Each sHsp G41C click generation was prepped for an acid urea gel in 4 x loading buffer (5% acetic acid, 6 M urea, and 30% glycerol) and heated at 60^{o}C for 6 min. The gel was prepared according to general protocols [138] with 12% acrylamide and 40% urea and run at 150V followed by coomassie blue staining/destaining.

Mass Spectrometry.

MS analyses were performed on a ESI-Q-TOF mass spectrometer (Q-TOF Premier, Waters). SHsp G41C and each generation (0.1-2 μL, 1.0 mg/mL) were injected onto a BioBasic SEC-300 (Thermo Scientific) column and eluted with 40% IPA, 0.1% formic acid. Deconvoluted spectra were generated with the software MaxEnt1 provided by Waters. The organic ligand and iron coordination complex were analyzed using C18 column (218TP5115, Vydac, Deerfield, IL) and eluted with a water-acetonitrile linear gradient (eluent A, 0.1% formic acid in water; eluent B, 0.1% formic acid in acetonitrile).

APPENDIX C

SUPPORTING INFORMATION FOR CHAPTER 6

Mutagenesis.

The P22(S39C) point mutation was made using established polymerase chain reaction protocols (Qiagen) using pET-11a based plasmids encoding genes for scaffolding and coat protein. The amplified DNA was transformed into E. coli strain BL21 (DE) and selected for ampicillin resistance.[59]

Protein Purification.

Transformed BL21 (DE3) E. coli were grown in 1L cultures inoculated with 1 mL starter culture at 37°C with vigorous shaking overnight. The bacteria were then centrifuged away from the media at 3700 g for 20 minutes. The cell pellets were resuspended in PBS pH 7.2 and were incubated with DNAse, RNAse, and lysozyme (all Sigma-Aldrich) for 30 minutes on ice. Cells were lysed further by sonication on ice. The cell debris was removed via centrifugation at 12,000 g for 45 minutes. The supernatant was then loaded on a 35% sucrose cushion and centrifuged at 48,000 rpm for 50 minutes in an ultra centrifuge (Sorvall). The resulting virus pellet was resuspended in PBS pH 7.0, spun at 17,000 rpm for 20 minutes to remove particulates and lipid providing 135 mg of P22 procapsid (PC). Scaffold protein was extracted using 0.5 M guanidine-HCl in 4 repeated cycles. The P22 empty shells were then dialyzed against PBS pH 7.0 overnight resulting in 86 mg (64% yield) P22 empty shell (ES). The empty shell P22 was heat treated for 20 min at 65^{o}C to transform the protein into its expanded form as previously described and analyzed.[59] The heat treated samples were purified by pelleting as above, followed by resuspension into PBS pH 7.6 in preparation for protein labeling yielding 58 mg (68% yield form ES) of P22 expanded shell (EX) from 1L of initial E. coli culture.

Subunit Mass Spectrometry.

Subunit masses of the P22 coat and P22-int macroinitiators were analyzed by ESI-Q-TOF mass spectrometry (Q-TOF Premier, Waters) interfaced to a Waters Acquity UPLC and autosampler.[50] Samples were loaded onto a BioBasic-300 SEC column (5 μm, 250 L x 1.0 mm I.D., Thermo Scientific) and eluted with buffer containing 40% isoproanol, 59.9% water, and 0.1% formic acid isocratically with a rate of 25 μL/min. Mass spectra were acquired in the range of m/z 50-5000 and processed using the MaxEnt 1 algorithm for MassLynx version 4.1 to obtain deconvoluted average masses from multiple charge state distributions.

Transmission Electron Microscopy.

The P22-int macroinitiators and P22-polymer composites were imaged by transmission electron microscopy (Leo 912 AB) by negatively staining the sample with 1% uranyl acetate on formvar carbon coated grids. For the diameter measurements 200 particles were measured for each sample.

Denaturing Gel Assay.

P22-int macroinitiators and P22-polymer composites were analyzed using SDS-PAGE on 10-20% gradient Tris-glycine gels (Lonza). Fluorescence imaging of the gels was carried out on a Typhoon TRIO (GE Healthcare) gel scanner with excitation at 488 nm and detection at 526 nm. Protein was detected by staining with Coomassie blue.

Native Agarose Gel Assay.

P22-int macroinitiators and P22-polymer composites were analyzed on 0.8% native agarose gel using 40 mM Tris-base, 5 mM sodium acetate, 1 mM EDTA, pH 8.2 running buffer and were run for 3 hrs at 65 volts. Fluorescence imaging of the gels was carried out on a Typhoon TRIO (GE Healthcare) gel scanner with excitation at 488 nm and detection at 526 nm. Protein was detected by staining with Coomassie blue.

Analytical Ultracentrifugation.

Sedimentation velocity experiments were performed in an XL-A ultracentrifuge (Beckman Coulter, Fullerton, CA) using a AN-60Ti rotor. Epon double-sector centerpieces were filled with 390 μL or 400 μL of sample and the corresponding reference buffer, respectively. The samples were centrifuged at 20°C and 5,000-7,000 rpm. Absorbance data were acquired at wavelength of 280nm. The raw data were analyzed using SEDFIT software, implementing the ls-g*(s) model. Input parameters such as buffer density and viscosity were determined using Sednterp software.

Relaxivity Measurements.

T1 measurements were carried out on Anasazi FT-NMR 60MHz (1.41 T) spectrometer for all samples. Each P22-xAEMA-Gd (0.61 mM Gd, 1.3 mg/mL protein) experimental replicate was diluted with 67% D2O in H2O to yield a dilution series with concentrations of 0.20, 0.068, 0.023 mM Gd. The longitudinal relaxation rate constant (T1) at each dilution was measured using an inversion recovery pulse sequence (90º pulse width of 6.3 μs with 8 experiments of 1 scan) at 298 K, where the relaxation delay was

set to six times the estimated T1 (Figure C12 A-C). To attain the actual T1 value, the following equation for T1 relaxation:

$$Mz = A(1-\exp(-t/T1))+B$$

was fit to the experimental data acquired at each dilution where A, B, and T1 were used as fitting parameters.[162] The plot of inverse T1 versus Gd (mM) for the 3 dilutions was used to determine relaxivity values (r1), where relaxivity per Gd is equal to the slope of the line (Figure C12 D) and relaxivity per VLP was calculated by multiplying the slope by Gd/VLP.

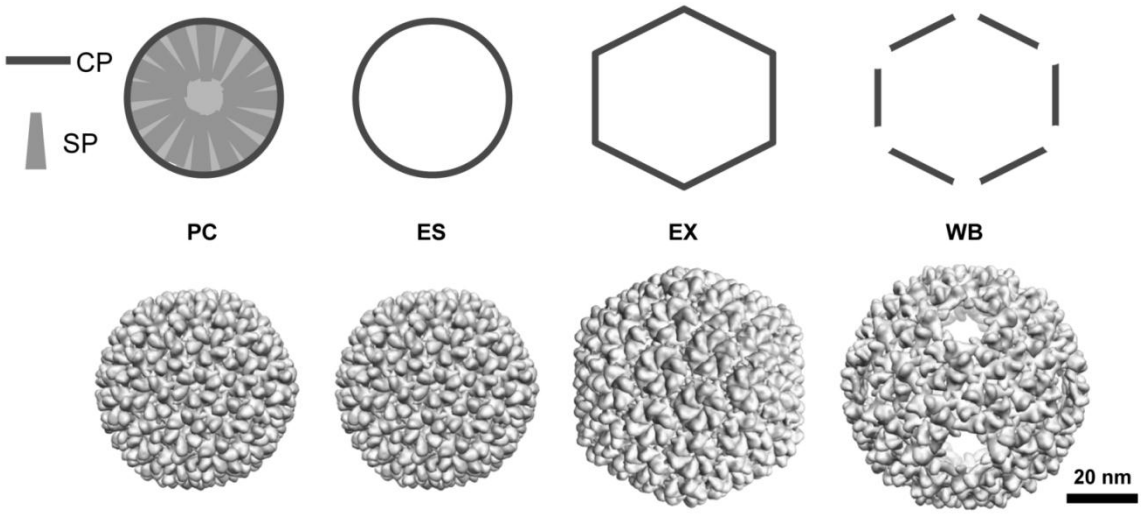

Figure C1: Four unique morphological forms of P22. The coat protein (CP) and scaffold protein (SP) are expressed in *E. coli*. The purified protein architecture is in the procapsid state (PC) containing both CP and SP. After extraction with guanidine•HCl only CP remains in the empty shell (ES) state. If the VLP is heated to 65 ºC the shell enlarges to form the expanded shell (EX) state used in this paper. If instead the ES is heated to 75 ºC the wiffleball (WB) state can be made, where pentons are missing from the icosahedral vertices. PDB ID 3IYI, 2XYZ, 3IYH.

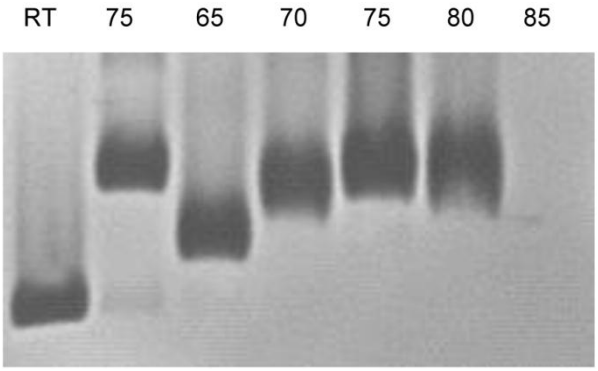

Figure C2: Agarose gel of $P22_{S39C}$-ES heated at different temperatures. Gel labels are heating temperatures in ºC. The states at 65 ºC and 75 ºC correspond to the EX and WB states, respectively. Precipitation occurred while heating at 85 ºC resulting in complete loss of protein.

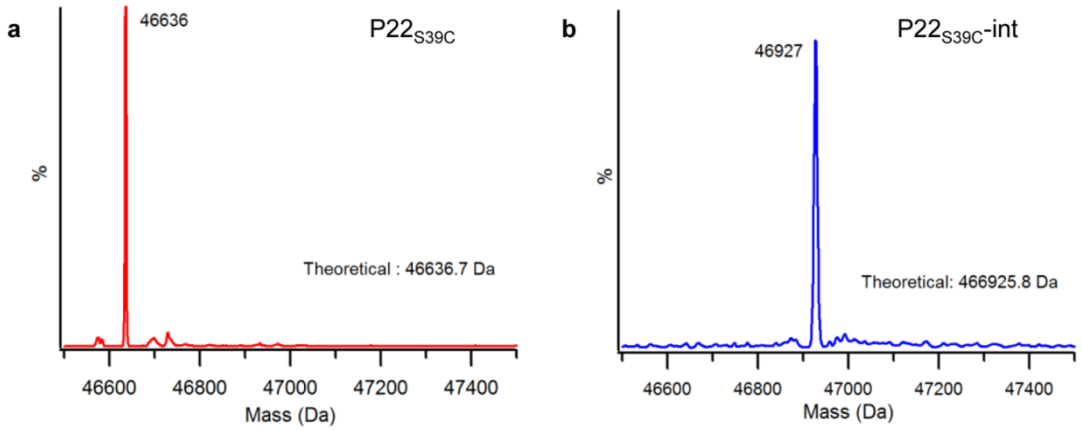

Figure C3: Subunit mass spectrometry characterization of the $P22_{S39C}$ macroinitiator. A) The mass observed is in agreement with the expected mass of the $P22_{S39C}$ mutant B) The only mass observed corresponds to the $P22_{S39C}$-int indicating that all of the subunits have reacted and that there is no significant multiple labeling of the subunits.

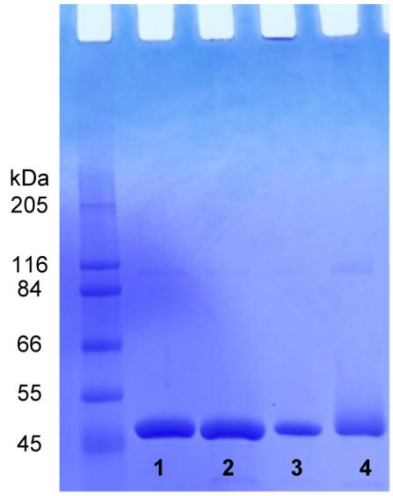

Figure C4: Denaturing gel electrophoresis of P22-polymer samples made with varying amounts of metal catalyst. The amount of catalyst per protein subunit ranged from 0 eq. (lane 1), 10 eq. (lane 2), 40 eq. (lane 3), to 100 eq. (lane 4). Based on this gel 100 eq was determined to be the most effective of these tested conditions.

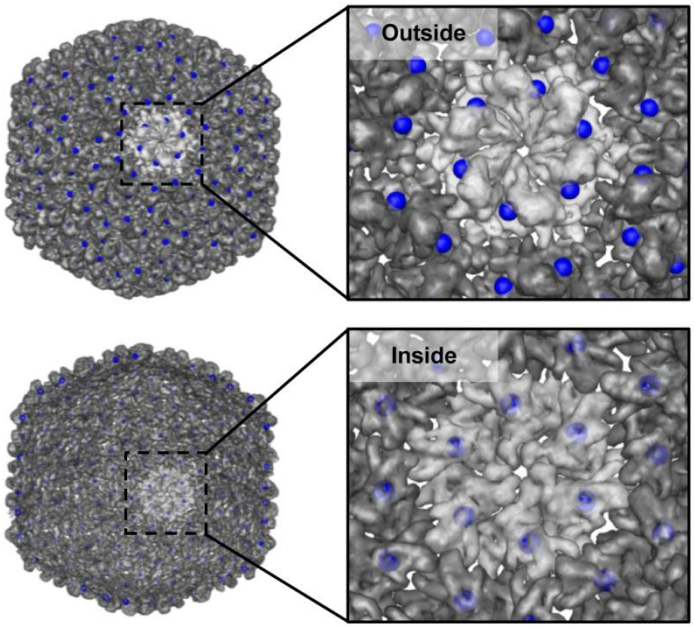

Figure C5: Structural model of the P22 capsid expanded morphology showing the location of the K118C mutation. Location of the modified residue, K118C (in blue), derived from the structural model of P22 using coordination data deposited as PDB file 2XYZ. Both a view of the exterior of the capsid (top) and a half shell cut-away view revealing the interior (bottom) are shown, to illustrate the location of the mutation site.

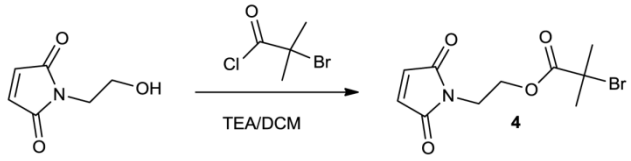

Figure C6: Synthesis of 2-bromoisobutyrate ethoxy maleimide (**4**). **4** was synthesized by a modification of the procedures previously reported.[91,141]

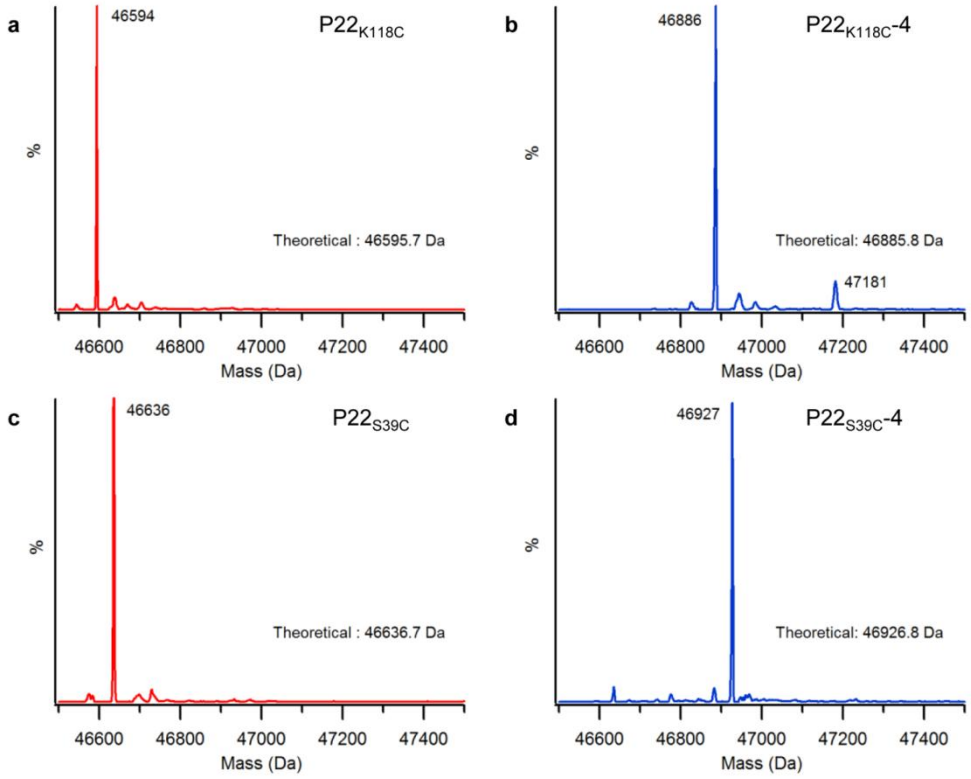

Figure C7: Subunit mass spectrometry characterization of the $P22_{S39C}$-4 and $P22_{K118C}$-4 macroinitiators. A) The mass observed is in agreement with the expected mass of the $P22_{K118C}$ mutant. B) The majority mass observed corresponds to the $P22_{K118C}$-**4** indicating that most of the subunits have reacted and that there is less than 5% double labeling (47181 Da) of the subunits. C) The mass observed is in agreement with the expected mass of the $P22_{S39C}$ mutant D) The only mass observed corresponds to the $P22_{S39C}$-**4** indicating that all of the subunits have reacted and that there is no significant multiple labeling of the subunits.

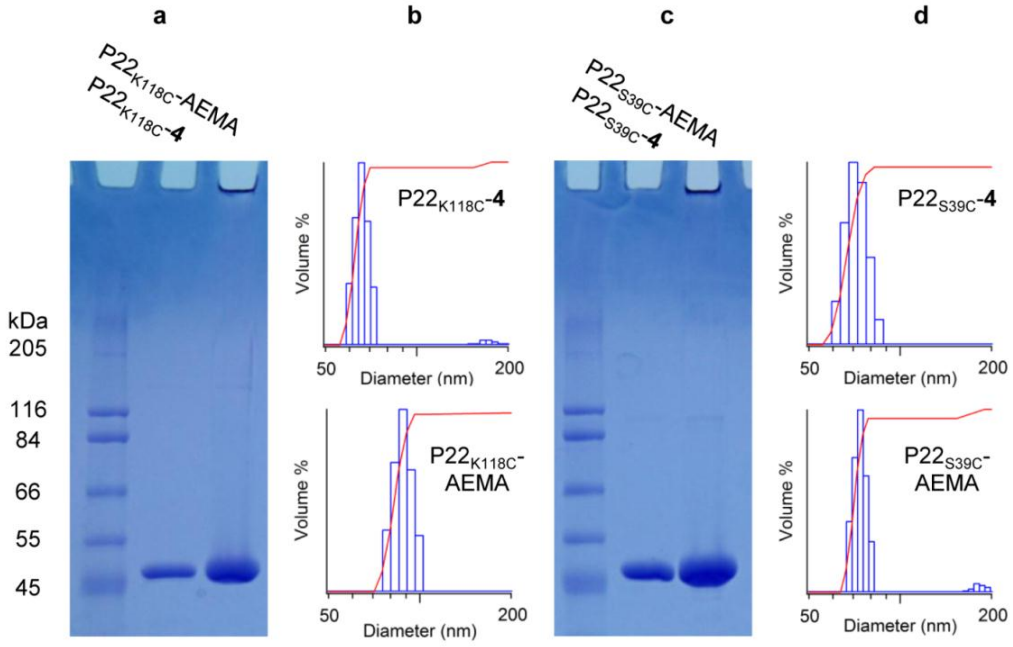

Figure C8: Basic analysis of $P22_{K118C}$-AEMA and $P22_{S39C}$-AEMA. The $P22_{K118C}$-AEMA composite exhibits increased subunit mass, but concomitantly increases in diameter, while the $P22_{S39C}$-AEMA retains its initial diameter. A) $P22_{K118C}$-AEMA analyzed by SDS-PAGE. B) Dynamic light scattering of $P22_{K118C}$-AEMA indicates that at least some of the polymer is on the exterior of the cage through the increase in diameter from 60 ± 3 nm to 81 ± 4 nm. C) $P22_{S39C}$-AEMA analyzed by SDS-PAGE. B) Dynamic light scattering of $P22_{S39C}$-AEMA indicates that the polymer is on the interior of the cage through retention of diameter changing from 72 ± 5 nm to 68 ± 4 nm.

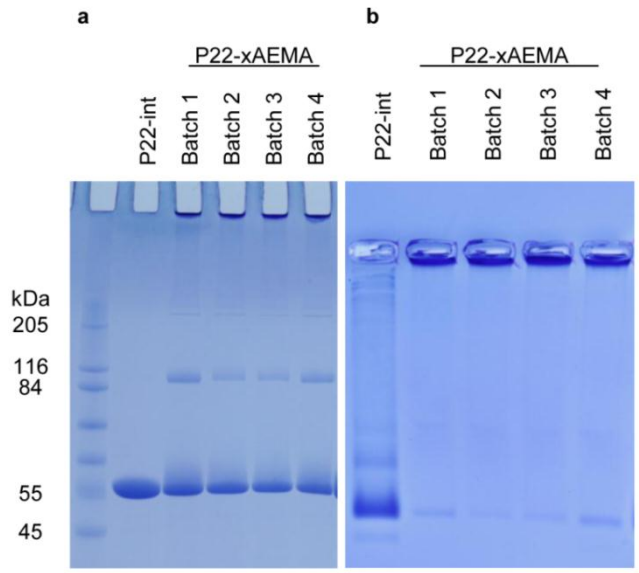

Figure C9: Gel analysis comparison of 4 experimental replicates of the $P22_{S39C}$-xAEMA synthesis. A) When subjected to denaturing gel condition a streak to higher molecular mass and the appearance of dimer due to subunit crosslinking is observed indicating the growth of crosslinked polymer chains on the subunits in each batch. B) When each batch is analyzed by native agarose gel conditions a uniform shift in mobility compared to $P22_{S39C}$-int is observed.

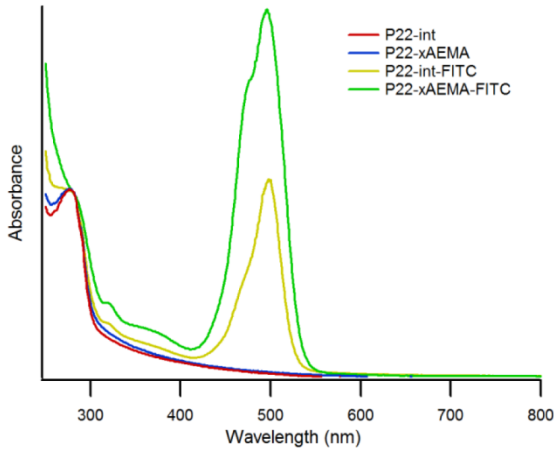

Figure C10: Representative absorbance profiles of the $P22_{S39C}$-int, $P22_{S39C}$-xAEMA, $P22_{S39C}$-int-FITC, and $P22_{S39C}$-xAEMA-FITC. The $P22_{S39C}$-int-FITC is labeled on the intrinsic lysine residues of the protein, while the $P22_{S39C}$-xAEMA-FITC has labeling both on the lysines and the AEMA introduced primary amines. FITC is the contributor to the absorbance at 495 nm, while both the protein-polymer composite and FITC absorb at 280 nm.

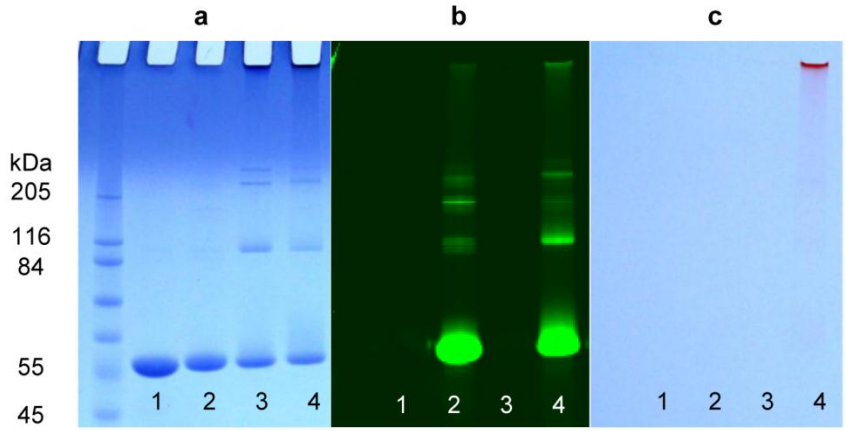

Figure C11: Verification of FITC covalent attachment by denaturing gel electrophoresis. Three different views of the same SDS-PAGE denaturing gel electrophoresis of $P22_{S39C}$-int (lane 1), $P22_{S39C}$-int-FITC (lane 2), $P22_{S39C}$-xAEMA (lane 3), and $P22_{S39C}$-xAEMA-FITC (lane 4). A) The gel after Coomassie staining highlighting the protein component of the samples with the unmodified subunit appearing at about 46 kDa and the modified subunits (lanes 3 and 4) streaking to higher molecular weights. B) Both the $P22_{S39C}$-int-FITC and $P22_{S39C}$-xAEMA-FITC subunits are visible when the fluorescent signal from the FITC is visualized. C) The gel under ambient light. Only the $P22_{S39C}$-xAEMA-FITC is visible as orange streak.

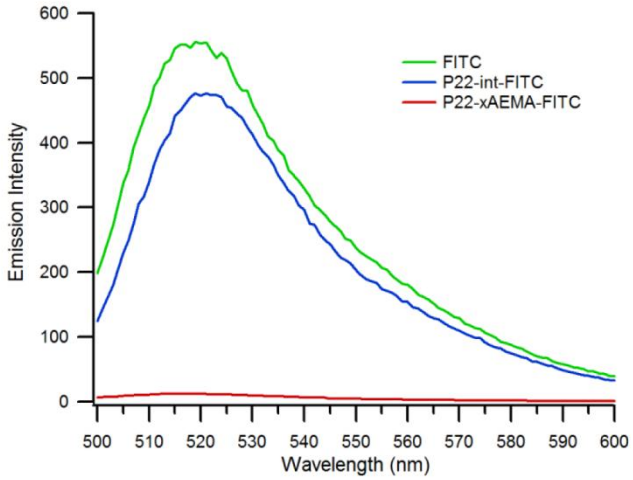

Figure C12: Representative fluorescence emission profiles for FITC labeled samples. In this dataset $P22_{S39C}$-int-FITC and $P22_{S39C}$-xAEMA-FITC compared to free FITC. Each sample had equivalent absorbance at 495 nm and was measured in pH 9.0 buffer. The excitation wavelength was 488 nm and fluorescence emission was detected over the charted range.

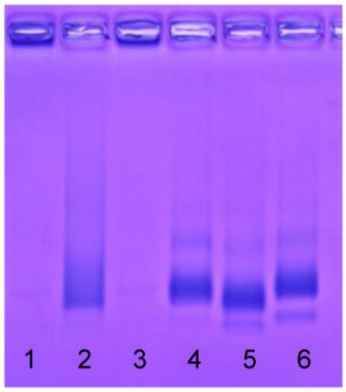

Figure C13: Covalent attachment of Gd-DTPA-NCS monitored by native agarose gel electrophoresis. Native agarose gel analysis of $P22_{S39C}$-xAEMA (lane 1), $P22_{S39C}$-xAEMA-Gd (lane 2), $P22_{S39C}$-xAEMA-magnevist (lane 3), $P22_{S39C}$-int (lane 4), $P22_{S39C}$-int-Gd (lane 5), and $P22_{S39C}$-int-magnevist (lane 6). The attachment of Gd-ATPA-NCS to the polymerized sample has the same effect on electrophoretic mobility as observed in the FITC labeled sample described in Figure 6.

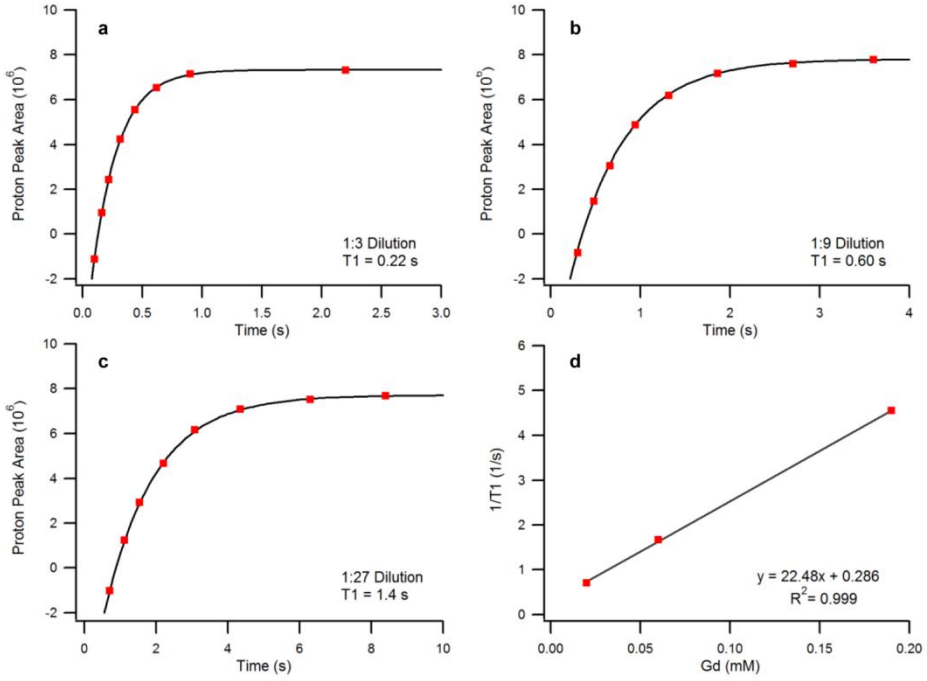

Figure C14: Representative $P22_{S39C}$-xAEMA-Gd data used for relaxivity calculations. A) Raw relaxivity data for the 1:3 dilution sample fit to find T1 at 0.20 mM Gd. B) Raw relaxivity data for the 1:9 dilution sample fit to find T1 at 0.068 mM Gd. C) Raw relaxivity data for the 1:27 dilution sample fit to find T1 at 0.023 mM Gd. D) Plot of 1/T1 values determined in panels A-C fit to determine the ionic relaxivity (r1).

APPENDIX D

COORDINATION COMPLEX, LIGAND, AND ORGANIC MOLECULE SYNTHESIS

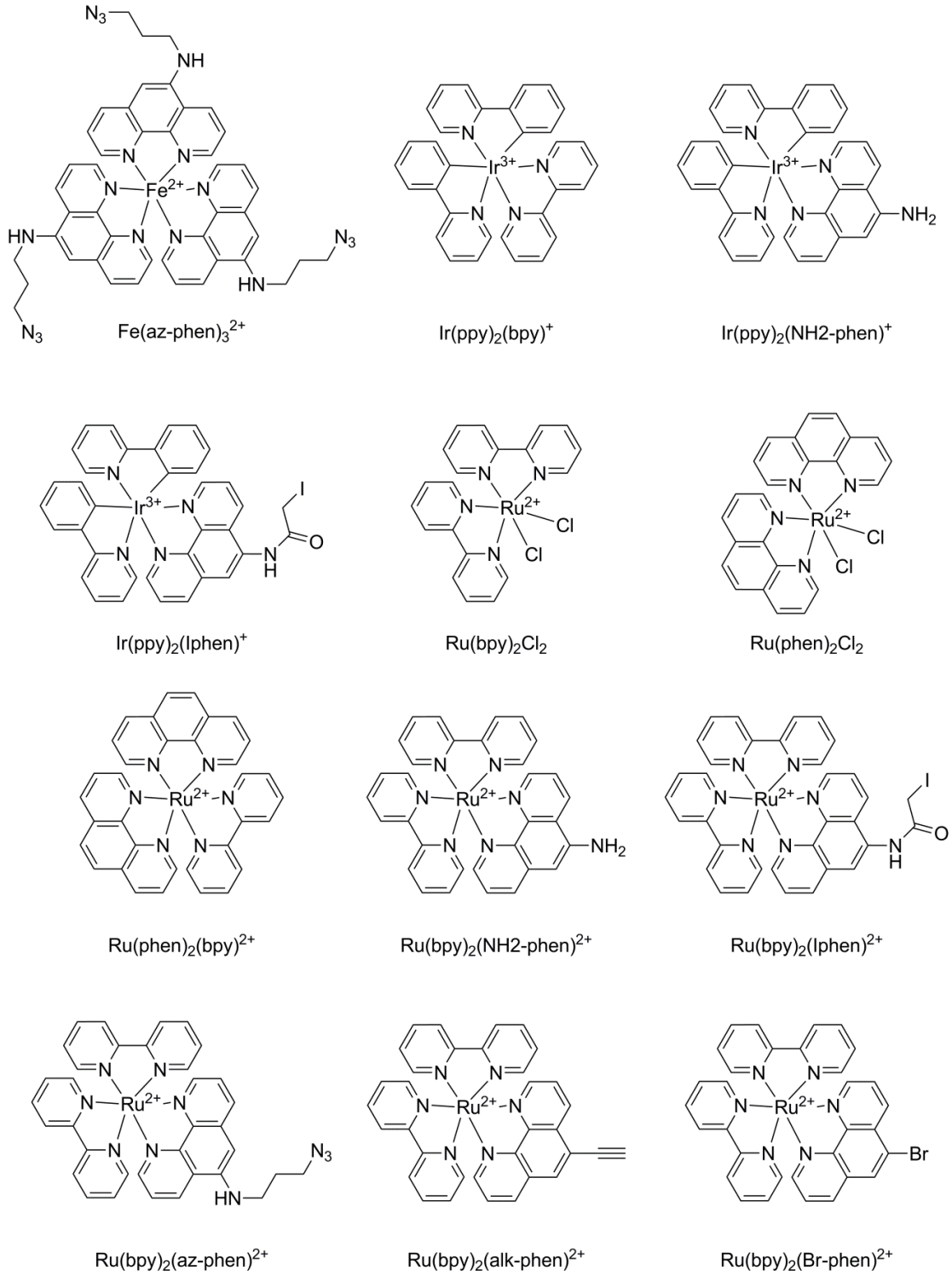

Figure D1: Coordination complexes.

Synthesis of $[Fe(az\text{-}phen)_3](PF_6)_2$.

A fresh aqueous solution containing ammonium iron(II) sulfate hexahydrate (329 μmoles) was mixed in a 1:3 molar ratio with a solution of 5-aminopropylazide-1,10-phenanthroline (987 μmoles) instantly forming a dark red solution. The solution was allowed to stir at room temperature for 30 min followed by precipitation by adding a saturated aqueous solution of ammonium hexafluorophosphate dropwise to the mixture. The red solid was collected through filtration and washed with ether and water. The dark red powder was recrystallized from dichloromethane and ether to yield the final product $Fe(az\text{-}phen)_3(PF_6)_2$ (0.25 g, 64% yield). 1H NMR (CDCl3, 500 MHz): δ 8.61 (t, J = 6.5, 1H), 8.20 (t, J = 7.5, 1H), 7.61 (td, J = 5.0, 20.5, 1H), 7.54 (m, J = 5.5, 1H), 7.35 (m, J = 3.5, 1H), 7.22 (td, J = 5.0, 24.0, 1H), 6.98 (d, J = 3.5, 1H), 5.86 (d, J = 3.0, 1H, NH), 3.54 (t, J = 6.5, 2H), 3.50 (d, J = 6.0, 2H), 2.06 (m, J = 6.5, 2H). LC-MS: M + H 890.3658 (found), M + H 890.3189 (calculated).

Synthesis of $[Ir(ppy)_2(bpy)]Cl$.

$Ir(ppy)_2(bpy)Cl$ was synthesized using established literature methods.[178] MS: M+ 657.0 (found), 657.2 (calculated).

Synthesis of $[Ir(ppy)_2(NH2\text{-}phen)]Cl$**.**

$Ir(ppy)_2(NH2\text{-}phen)Cl$ was synthesized using established literature methods.[178] MS: M+ 696.0 (found), 696.2 (calculated).

Synthesis of $[Ir(ppy)_2(Iphen)]PF_6$.

In a flask 250 mg (0.30 mmoles) $Ir(ppy)_2(NH2\text{-}phen)PF_6$ and 1.1 g (3.2 mmoles) iodoacetic anhydride were dissolved in 10 mL acetonitrile. The reaction was allowed to mix at room temperature overnight. In the morning the reaction was rotovaped to dryness, responded in methanol, then precipitated with aqueous ammonium hexafluorophosphate to yield 124 mg (0.12 mmoles, 41%) of a pale yellow powder. MS: M+ 863.9 (found), 864.1 (calculated).

Synthesis of $Ru(bpy)_2Cl_2$.

$Ru(bpy)_2Cl_2$ was synthesized according to literature methods using the protocol established for $Ru(phen)_2Cl_2$.[179]

Synthesis of $Ru(phen)_2Cl_2$.

$Ru(phen)_2Cl_2$ was synthesized according to literature methods.[179] In brief, 2.0 g (7.6 mmoles) $RuCl_3$ hydrate, 3.3 g (17 mmoles) 1,10-phenanthroline, and 3.3 g (76 mmoles) lithium chloride were dissolved in 13 mL DMF and allowed to sit for about 1 hr. This mixture was then refluxed for 8 hrs under argon. After cooling slightly acetone was added and the reaction placed at 4 ºC. The vessel sides were scraped every few days to encourage crystal formation from the dark purple mixture. After about 1 month sufficient crystals had formed. These were collected via vacuum filtration and washed with acetone three times to yield 8.15 g (14.9 mmoles, 88% yield) of purple microcrystals of the desired product. The small amount of $Ru(phen)_3Cl_2$ contaminate present as red crystals can be removed by washing the solid with cold methanol before using this material in further reactions.

Synthesis of $[Ru(phen)_2(bpy)](PF_6)_2$.

The small amount of $Ru(phen)_3Cl_2$ contaminate present as red crystals in the starting material was removed by soaking the material in cold methanol and removing the supernatant before using the remaining solid in further reactions. In a round bottom flask 200 mg (0.35 mmoles) $Ru(phen)_2Cl_2$ and 65 mg (0.41 mmoles) 2,2'-bipyridine were suspended in 10 mL methanol. This mixture was refluxed under argon for 4 hrs then filtered and added 6 mL water was added and the product was precipitated using aqueous NH_4PF_6. The precipitate was washed with water and ether then further cleaned on a silica gel column (1% sat aq potassium nitrate, 9% water, 90% acetonitrile). The product fractions were rotovaped to dryness, dissolved in methanol, and then reprecipitated with aqueous NH_4PF_6. The resulting microcrystals were collected via vacuum filtration and washed with water and ether to yield 88 mg (0.097 mmoles, 28% yield) of the desired product. MS: M 2+ 309.0662 (found), 309.0552 (calculated).

Synthesis of $[Ru(bpy)_2(NH2\text{-}phen)](PF_6)_2$.

$[Ru(bpy)_2(NH2\text{-}phen)](PF_6)_2$ was synthesized according to previously published procedures.[180] In brief, 0.350 g (0.725 mmol) $[Ru(bpy)_2Cl_2]$ and 0.142 g (0.725 mmol) of 5-amino-1,10-phenanthroline were added to 25 mL of methanol and allowed to reflux under argon for 3 h. The red solution was gravity filtered and an aqueous saturated solution of ammonium hexafluorophosphate was added to the warm mixture. The precipitate was collected and washed with cold water and ether to obtain the desired product with a 68% yield. MS: M 2+ 304.4 (found), 304.6 (calculated).

Synthesis of $[Ru(bpy)_2(Iphen)_2](PF_6)_2$.

$[Ru(bpy)_2(Iphen)_2](PF_6)_2$ was made via a modification of the literature method. Instead of making the Iphen before coordination to the Ru the Iphen ligand in this procedure is made from NH2-phen already coordinated to the Ru. This reaction order rearrangement helps prevent the undesired substitution of iodine for chlorine in the Iphen, which would lead to reduced cysteine labeling efficiency. In a flask 1.0 g (1.1 mmoles) $[Ru(bpy)_2(NH2\text{-}phen)_2](PF_6)_2$ and 4.0 g (11 mmoles) iodoacetic anhydride were dissolved in 30 mL acetonitrile and allowed to stir at room temperature overnight under argon. The reaction was subsequently rotovaped to dryness and the oil was dissolved in methanol followed by precipitation of the desired product by adding aqueous NH_4PF_6. The solid was collected and washed with water and ether to yield 1.2 g (1.1 mmoles, quantitive yield). MS: M 2+ 388.4 (found), 388.5 (calculated).

Synthesis of $[Ru(bpy)_2(az\text{-}phen)](PF_6)_2$.

In a round bottom flask 77 mg (0.16 mmoles) $Ru(bpy)_2Cl_2$ and 50 mg (0.18 mmoles) az-phen were suspended in 5 mL methanol. This mixture was refluxed under argon for 4 hrs then filtered and the product was precipitated using aqueous NH_4PF_6. The precipitate was washed with water and ether to yield 78 mg (0.08 mmoles, 50%) of product. MS: M 2+ 346.0 (found), M 2+ 346.1 (calculated).

Synthesis of $[Ru(bpy)_2(alk\text{-}phen)](PF_6)_2$.

In a round bottom flask 150 mg (0.31 mmoles) $Ru(bpy)_2Cl_2$ and 70 mg (0.34 mmoles) alk-phen were suspended in 10 mL methanol. This mixture was refluxed under argon for 4 hrs then filtered and the product was precipitated using aqueous NH_4PF_6. The

precipitate was washed with water and ether to yield 110 mg (0.12 mmoles, 40%) of product. MS: M 2+ 309.0 (found), M 2+ 309.1 (calculated).

Synthesis of $[Ru(bpy)_2(Br\text{-}phen)](PF_6)_2$.

In a round bottom flask 1.7 g (3.5 mmoles) $Ru(bpy)_2Cl_2$ and 1.0 g (3.8 mmoles) Br-phen were suspended in 50 mL methanol. This mixture was refluxed under argon for 4 hrs then 20 mL water was added and the product was precipitated using aqueous NH_4PF_6. The precipitate was washed with water and ether to yield 3.0 g (3.1 mmoles, 88%) of product as bright red microcrystals. MS: M 2+ 336.9 (found), 337.0 (calculated).

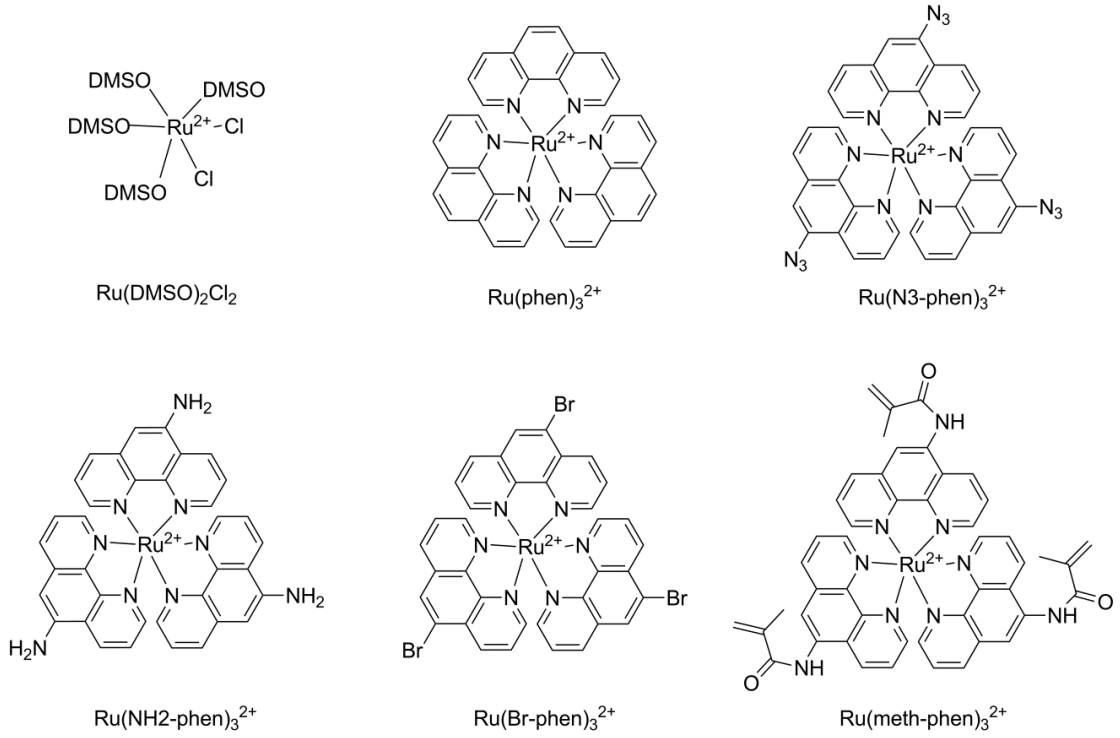

Figure D2: Coordination complexes derived from $Ru(DMSO)_4Cl_2$.

Synthesis of $Ru(DMSO)_4Cl_2$.

The $Ru(DMSO)_4Cl_2$ was made through the application of published procedures.[181,182] In brief, in a 100 mL round bottom flask 1.0 g (3.8 mmoles) ruthenium chloride hydrate was mixed with 5 mL DMSO and placed under argon. This mixture was refluxed in a sand bath (190 ºC) for about 7 minutes until the reaction turned brown-yellow. Do not reflux any longer than necessary for the color change otherwise the DMSO begins to degrade forming strongly scented compounds. The reaction was immediately cooled on an icebath and subsequently rotovaped (70 ºC water bath, high vac) until crystals began to form. Dry acetone (10 mL) was added and the flask was placed on ice for 30 min to complete the crystallization. The pale yellow crystals were collected via vacuum filtration and washed 3 times with 10 mL acetone and 3 times with 10 mL ether yielding 1.48 g (3.06 mmoles, 77%). If the crystals are not sufficiently pure at this point the product can be further purified by recrystallizing for hot DMSO.

Synthesis of $[Ru(phen)_3](PF_6)_2$.

To 66 mg (0.14 mmoles) $RuDMSO_4Cl_2$ and 91 mg (0.45 mmoles) 1,10-phenanthroline 3 mL of ethylene glycol was added. The mixture was heated at 120 ºC using a sandbath for 4 hrs. To the hot mixture about 5 mL water was added followed by a saturated solution of ammonium hexafluorophosphate (aq). The resulting bright orange precipitate was collected by vacuum filtration and washed with water and ether with a yield of 68.1 mg (0.073 mmoles, 53%). MS: M 2+ 321.05 (found), 321.06 (calculated).

Synthesis of [Ru(N3-phen)$_3$](PF$_6$)$_2$.

To 110 mg (0.23 mmoles) $RuDMSO_4Cl_2$ and 200 mg (0.90 mmoles) 5-azido1,10-phenanthroline (N3-phen) 10 mL of ethylene glycol was added. The mixture was heated at 120 ºC using a sandbath for 5 hrs. To the hot mixture about 10 mL water was added followed by a saturated solution of ammonium hexafluorophosphate (aq). The resulting orange precipitate was collected by vacuum filtration and washed with water and ether with a yield of 381 mg (0.36 mmoles, >100%).

Synthesis of [Ru(NH2-phen)$_3$](PF6)$_2$).

To 726 mg (1.5 mmoles) $RuDMSO_4Cl_2$ and 1460 mg (7.5 mmoles) 5-amino1,10-phenanthroline (NH2-phen) 50 mL of ethylene glycol was added. The mixture was heated at 120 ºC using a sandbath for 5 hrs. To the hot mixture about 100 mL water was added followed by a saturated solution of ammonium hexafluorophosphate (aq). The resulting brown-orange precipitate was collected by vacuum filtration and washed with water and ether with a yield of 1.91g (0.36 mmoles, >100%). MS: M 2+ 343.5 (found), 343.6 (calculated).

Synthesis of [Ru(Br-phen)$_3$](PF$_6$)$_2$.

To 242 mg (0.5 mmoles) $RuDMSO_4Cl_2$ and 650 mg (2.5 mmoles) 5-bromo-1,10-phenanthroline (Br-phen) 20 mL of ethylene glycol was added. The mixture was heated at 120 ºC using a sandbath for 5 hrs. To the hot mixture about 50 mL water was added followed by a saturated solution of ammonium hexafluorophosphate (aq). The resulting yellow-orange precipitate was collected by vacuum filtration and washed with water and

ether with a yield of 890 mg (0.76 mmoles, >100%). MS: M 2+ 438.8 (found), 438.9 (calculated).

Synthesis of $[Ru(Br\text{-}bpy)_3](PF_6)_2$.

To 242 mg (0.5 mmoles) $RuDMSO_4Cl_2$ and 587 mg (2.5 mmoles) 4-bromo-2,2'-bipyridine (Br-bpy) 20 mL of ethylene glycol was added. The mixture was heated at 120 ºC using a sandbath for 5 hrs. To the hot mixture about 50 mL water was added followed by a saturated solution of ammonium hexafluorophosphate (aq). The resulting orange-red precipitate was collected by vacuum filtration and washed with water and ether with a yield of 536 mg (0.48 mmoles, 96%). MS: M 2+ 403.8 (found), 403.9 (calculated).

Synthesis of $[Ru(meth\text{-}phen)_3](PF_6)_2$.

In a dry flask 100 mg (0.13 mmoles) $[Ru(NH2\text{-}phen)_3](PF_6)_2$ was suspended in 5 mL dry dichloromethane and 122 µL (0.88 mmoles) triethylamine. To this suspension 84 µL (0.88 mmoles) methacrylolchloride was added dropwise. The suspension gradually dissolved completely giving a very dark black-red solution. After mixing overnight at room temperature the reaction was rotovaped to dryness and the resulting solid was dissolved in 5 mL methanol. Addition of 5 mL water and a saturated solution of ammonium hexafluorophosphate (aq) resulted in an orange-red precipitate, which was collected by vacuum filtration and washed 3 times with water and ether. Crude yield 240 mg (0.203 mg, 77%). The product was further purified over a silica gel column (1% sat potassium nitrate (aq), 9% water, 90% acetonitrile) with collection of the red band.

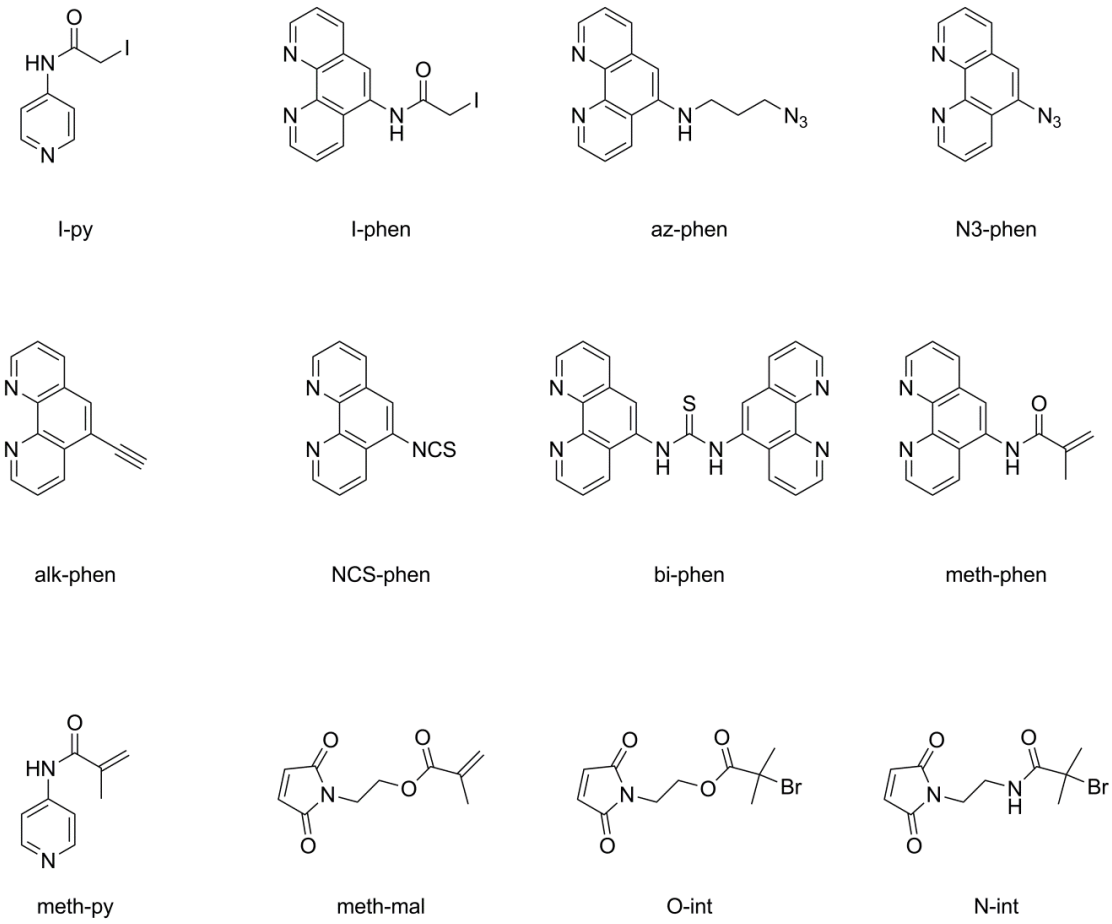

Figure D3: Ligands and molecules for ATRP.

Synthesis of 4-iodoacetamido-pyridine (I-py).

In a flask 175 mg (1.87 mmole) 4-amino-pyridine was dissolved in 4 mL dry THF with sonication. To this solution 1.0 g (2.8 mmole) iodoacetic anhydride was added followed by an additional 1 mL dry THF. The flask was placed under argon and allowed to stir at 4C in the dark overnight. The tan precipitate that formed over that time was collected via vacuum filtration and washed with a saturated solution of sodium carbonate followed by 2 times rinsing with cold water to yield 232 mg (0.88 mmoles, 47%) of pure product.

Synthesis of 5-iodoacetamido-1,10-phenanthroline (I-phen).

Synthesis was carried out as previously described.[114]

Synthesis of N-(3-azidopropyl)-1,10-phenanthrolin-5-amine (az-phen, azide-phen).

In a flask, under argon**,** 0.50 g 5,6-epoxy-5,6-dihydro-1,10-phenanthroline (0.50 g, 25 mmoles) was dissolved in 6 mL water and 3 mL THF. To this solution 3-azidopropylamine (76.5 mmoles, 3-fold excess) was added dropwise. This reaction was stirred at room temperature for 24 hrs followed by extraction 3 times with methylene chloride. The organic layer was dried over anhydrous sodium sulfate and the solvent was removed using a rotary evaporator. The crude compound was purified by column chromatography (silica gel, 9:1 CH_2Cl_2:TEA) to yield a dark yellow oil in near quantitative yield. The entire product from step 1 was added to a solution containing 0.7 g 95% NaH (12-fold excess) in 75 mL dry THF under Ar and refluxed for 4 hrs. The reaction was cooled to room temperature and 20 mL MeOH was slowly added dropwise to quench the reaction. The solvents were removed by rotary evaporation and the product was dissolved in 150 mL water followed by extraction 4 times with methylene chloride. The crude final product was purified by column chromatography (silica gel, 9:1 CH_2Cl_2:TEA) resulting in a yellow solid (0.24g, 35%). 1H NMR (CDCl3, 500 MHz): δ 9.06 (d, J = 4.5, 1H), 8.89 (d, J = 2.5, 1H), 8.33 (d, J = 8.5, 1H), 8.03 (d, J = 8.0, 1H), 7.56 (q, J = 4.5, 1H), 7.54 (q, J = 4.5, 1H), 6.63 (s, 1H), 4.91 (s, br, NH), 3.57 (t, J = 6.5, 2H), 3.47 (t, J = 6.5, 2H), 2.10 (m, J = 6.5, 2H). LC-MS: M + H 279.1388 (found), M + H 279.1358 (calculated).

Caution: Exercise extra caution when handling the reagents in this reaction scheme as azides can be an explosion hazard.

Synthesis of 4-azidophenanthroline (N3-phen).

In a flask, 1.00 g 5,6-epoxy-5,6-dihydro-1,10-phenanthroline (5.08 mmoles) and 1.00 g sodium azide (15.4 mmoles) were dissolved in 40 mL water and 20 mL THF. While crystals gradually formed as this reaction was stirred at room temperature overnight. In the morning 20 mL additional water was added to the reaction and the flask was placed on ice for 1 hr followed by collection of the crystals by vacuum filtration. The resulting solid was washed 3 times with 10 mL cold water. This solid then dissolved in 20 mL DMSO mixed with 240 μL 2M NaOH (aq). The solution initially was brown but in less than 0.5 hr turns a brilliant green. After 3 hrs the reaction was quenched by adding 120 mL water, turning the reaction yellow, and the flask was placed at 4 C overnight. The crystals that formed were collected by vacuum filtration and washed 3 times with 10 mL cold water to yield 2.9 mmoles (57%) of pure product. ^{1}H NMR (500 MHz, DMSO-d6) δ 9.15 (dd, J = 4.1, 1.3 Hz, 2H), 9.02 (dd, J = 4.1, 1.3 Hz, 2H), 8.49 (ddd, J = 18.3, 8.2, 1.4 Hz, 4H), 7.92 (s, 1H), 7.78 (ddd, J = 27.0, 8.2, 4.3 Hz, 3H). 13C NMR (DMSO, 500 MHz): δ 150.88, 149.36, 135.16, 130.90, 128.28, 123.84, 123.48, 113.51

Caution: Exercise extra caution when handling the reagents in this reaction scheme as azides can be an explosion hazard.

Synthesis of 4-alkyn-1,10-phenanthroline (alk-phen).

Alk-phen was made through the application of established procedures. In brief, to 1.00 g (3.9 mmole) 5-bromo-1,10-phenanthroline, 375 mg (0.59 mmoles)

$Pd(II)(Ph_3P)_2Cl_2$, and 170 mg (0.86 mmole) in a round bottom flask 50 mL dry tetrahydrofuran and 10 mL dry diisopropyl amine were added under argon. While stirring at room temperature, 900 μL (6.3 mmole) trimethylsilyl acetylene was added dropwise over several minutes. This mixture was allowed to stir for 2 days then rotovaped to dryness. The resulting black solid was resuspended in 40 mL methanol and 20 mL water and to this 200 mg potassium cyanide was added. This mixture was sonicated for 1.5 hrs then extracted 4 times from dichloromethane and water. The black organic layer was dried over sodium sulfate then rotovaped to dryness. The resulting black solid was purified on an alumina column (0.1% TFA, 2% methanol, 98% dichloromethane) to yield 374 mg (1.8 mmoles, 47%) of a pale yellow powder. ^{1}H NMR (500 MHz, Chloroform-d) δ 9.23 (ddd, *J* = 12.5, 4.3, 1.4 Hz, 2H), 8.78 (dd, *J* = 8.2, 1.4 Hz, 1H), 8.24 (dd, *J* = 8.1, 1.3 Hz, 1H), 8.11 (s, 1H), 7.75 (dd, *J* = 8.2, 4.3 Hz, 1H), 7.67 (dd, *J* = 8.1, 4.3 Hz, 1H), 3.57 (s, 1H), 1.62 (s, 1H).

Synthesis of 5-thiourea-1,10-phenanthroline (NCS-phen).

The NCS-phen was made the application of a procedure previously described for the formation of isothiocyanates.[183] A 50 mL round-bottomed flask was charged with 5-amino-1,10-phenanthroline (488 mg, 2.5 mmol), THF (10 mL), and sodium hydride (91 mg, 3.8 mmol). The flask was set in an ice bath under Ar atmosphere and the chemicals were stirred and mixed thoroughly. Carbon disulfide (480 mL, 8 mmol) was slowly injected via a syringe pump over 1 hr as the reaction was brought up to room temperature. The mixture was then refluxed at 40 ºC for 20 hr while maintaining an Ar atmosphere. The reaction was cooled on an ice bath followed by the addition of p-

toluenesulfonyl chloride (524 mg, 2.75 mmol) and triethylamine (760 mL, 5.5 mmol) and was subsequently stirred for 3 hr at room temperature. Dichloromethane (15 mL) and 1N hydrochloric acid were added to the reaction flask. The water layer was then washed twice with 10 mL of dichloromethane to remove residual reactants.

Synthesis of 1,3-di-1,10-phenanthrolin-5-ylthiourea (bi-phen).

The bi-phen linker was made in situ through the application of a procedure previously described for the formation of isothiocyanates.[183] A 50 mL round-bottomed flask was charged with 5-amino-1,10-phenanthroline (488 mg, 2.5 mmol), THF (10 mL), and sodium hydride (91 mg, 3.8 mmol). The flask was set in an ice bath under Ar atmosphere and the chemicals were stirred and mixed thoroughly. Carbon disulfide (480 mL, 8 mmol) was slowly injected via a syringe pump over 1 hr as the reaction was brought up to room temperature. The mixture was then refluxed at 70 ºC for 20 hr while maintaining an Ar atmosphere. The reaction was cooled on an ice bath followed by the addition of p-toluenesulfonyl chloride (524 mg, 2.75 mmol) and triethylamine (760 mL, 5.5 mmol) and was subsequently stirred for 3 hr at room temperature. Dichloromethane (15 mL) and 1N hydrochloric acid were added to the reaction flask. The water layer was then washed twice with 10 mL of dichloromethane to remove residual reactants. The organic layer was discarded, while the water layer was stored at 4 ºC overnight, resulting in a pale orange precipitate which was isolated on a glass filter, washed with diethyl ether, and dried in a desiccator. The product was characterized by NMR and LC/MS. ^{1}H NMR: (500 MHz, DMSO-d6) (ppm) 9.30 (dd, J=5 Hz, J=35 Hz, 4H), 9.19 (dd, J=6.5 Hz, J=44.5 Hz, 4H), 8.63 (s, 2H) and 8.27–8.22 (m, 4H). ^{13}C NMR: (500 MHz, DMSO-d6)

(ppm) 183.7, 148.9, 142.4, 138.8, 136.7. 136.5, 135.0, 129.2, 127.5, 125.6, 125.5, 123.7. LC/MS: M+H 433.124 (found), M+H 433.123 (calculated).

Synthesis of 5-methacryamido-1,10-phenanthroline (meth-phen).

In a dry flask 200mg (1.0 mmoles) 5-amino-1,10-phenanthroline was dissolved in 5 mL dry dichloromethane and 400 μL dry triethylamine. This mixture was placed on ice and 220 μL (2.2 mmoles) methacrylol chloride was added dropwise. The mixture was allowed to mix on ice for 6 hrs and then extracted three times with dichloromethane from water. The organic layer was dried over anhydrous sodium sulfate and then cleaned over a silica gel column (1% sat aq potassium nitrate, 9% water, 90% acetonitrile). The organic layer was rotovaped to remove the acetonitrile then extracted three times with dichloromethane from water and dried over sodium sulfate to yield 240 mg (0.9 mmoles, 88%) of the desired product. MS: M+H 264.1178 (found), 264.1137 (calculated). ^{13}C NMR (500 MHz, Chloroform-d) δ 167.90, 149.79, 149.63, 146.01, 144.28, 139.90, 135.73, 130.69, 130.42, 127.90, 124.56, 123.28, 122.51, 121.11, 120.82, 18.80.

Synthesis of 4-methacryamido-pyridine (meth-py).

In a dry flask 1.00 g (10.6 mmoles) 4-amino pyridine was suspended in 12.5 mL dry dichloromethane and 1.6 mL dry triethylamine. This mixture was placed on ice and 1.20 mL (12.5 mmoles) methacrylol chloride diluted into 12.5 mL dry dichloromethane was added dropwise. The mixture was allowed to mix on ice for 4 hrs and then extracted three times with dichloromethane from water. The organic layer was dried over anhydrous sodium sulfate and then cleaned over a silica gel column (1:1 ethylacetate:dichloromethane). Yielding 1.0 g (6.4 mmoles, 60%) of the desired product

as a white powder. ^{1}H NMR (500 MHz, Chloroform-d) δ 8.47 (d, *J* = 6.2 Hz, 2H), 8.01 (s, 1H), 7.51 (d, *J* = 6.3 Hz, 2H), 5.79 (s, 1H), 5.51 (s, 1H), 2.03 (s, 3H).

Methacrylate maleimide (meth-mal).

In a dry flask 200 mg (1.4 mmoles) N-(2-hydroxyethyl)maleimde[184] was dissolved in 5 mL dry dichloromethane and 200 µL (1.4 mmoles) dry triethylamine. This mixture was placed on ice and 150 µL (1.6 mmoles) methacrylol chloride was added dropwise. The mixture was allowed to mix on ice overnight, rotovaped to dryness, and then cleaned over a silica gel column (97% dichloromethane 3% methanol). The first fractions were combined to yield 180 mg (0.85 mmoles, 60%) of product as a white powder.

Note: Although this monomer could be successfully appended to active cystienes followed by ATRP, it should not be employed as a free monomer as the unprotected maleimide can form undesired alternative ATRP couplings.

Synthesis of 2-bromoisobutyrate ethoxy maleimide (O-int).

O-int was synthesized by a modification of the procedures previously reported.[91,141] N-(2-hydroxyethyl)maleimide[184] (200 mg, 1.42 mmol) was mixed on ice with triethylamine (197 ul, 1.42 mmol) in 5 mL dry dichloromethane. 2-bromo-2-methylpropionylbromide (266 ul, 2.13 mmol) was added dropwise. The reaction was allowed to warm to room temperature and was determined by thin layer chromatography to have reached completion after 1.5 hr. The solvent was removed and the product was subsequently cleaned via column chromatography (silica gel, dichloromethane) with a yield of 76%. ^{1}H NMR (500 MHz, $CDCl_3$) δ = 1.87 (s, 6H, CH_3); 3.84 (t, J = 5.5, 2H,

NCH_2); 4.31 (t, J = 5.5, 2H, OCH_2); 6.71 (s, 2H, CH_{vinyl}). ^{13}C NMR (500 MHz, $CDCl_3$) δ = 30.59 (CH_3), 36.57(NCH_2), 62.88(OCH_2), 134.26(CH_{vinyl}).

Synthesis of 2-bromoisobutyryl aminoethyl maleimide (N-int).

N-int was synthesized by a modification of the procedures previously reported.[91,141] N-2-aminoethyl-maleimide (250 mg, 0.98 mmol) was mixed on ice with triethylamine (300 ul, 2.2 mmol) in 5 mL dry dichloromethane. 2-bromo-2-methylpropionylbromide (200 ul, 1.6 mmol) was added dropwise. The reaction was allowed to warm to room temperature and was subsequently extracted 3 times from dichloromethane and water followed by drying over anhydrous sodium sulfate. The crude product was cleaned via column chromatography (silica gel, 10% ethyl acetate in dichloromethane) with a yield of 80%. ^1H NMR (500 MHz, $CDCl_3$) δ = 1.89 (s, 6H, CH_3); 3.46 (q, J = 5.6, 2H, NCH_2); 3.72 (dd, J = 6.4, 4.6, 2H, NCH_2); 6.71 (s, 2H, CH_{vinyl}), 6,97 (s, NH). ^{13}C NMR (500 MHz, $CDCl_3$) δ = 32.54 (CH_3), 37.34 (NCH_2), 39.84 (NCH_2), 62.51 (C), 134.59(CH_{vinyl}), 170.96 (CO), 172.74 (CO). ESI-MS: *m/z* calculated 289.0188, 291.0167 (MH^+), found *m/z* 289.0192, 291.0179.

REFERENCES CITED

1 Manne, S. *et al.* Atomic-force microscopy of the nacreous layer in mollusk shells. *Proceedings of the Royal Society B-Biological Sciences* **256**, 17-23 (1994).

2 Schäffer, T. E. *et al.* Does abalone nacre form by heteroepitaxial nucleation or by growth through mineral bridges? *Chemistry of Materials* **9**, 1731-1740 (1997).

3 Bruet, B. J. F. *et al.* Nanoscale morphology and indentation of individual nacre tablets from the gastropod mollusc Trochus niloticus. *Journal of Materials Research* **20**, 2400-2419 (2005).

4 Addadi, L. & Weiner, S. Biomineralization - a pavement of pearl. *Nature* **389**, 912-& (1997).

5 Aizenberg, J., Muller, D. A., Grazul, J. L. & Hamann, D. R. Direct fabrication of large micropatterned single crystals. *Science* **299**, 1205-1208 (2003).

6 Douglas, T. & Young, M. Host-guest encapsulation of materials by assembled virus protein cages. *Nature* **393**, 152-155 (1998).

7 Comellas-Aragones, M. *et al.* Controlled integration of polymers into viral capsids. *Biomacromolecules* **10**, 3141-3147 (2009).

8 Kwak, M. *et al.* Virus-like particles templated by DNA micelles: a general method for loading virus nanocarriers. *J. Am. Chem. Soc.* **132**, 7834-+ (2010).

9 Ng, B. C., Chan, S. T., Lin, J. & Tolbert, S. H. Using polymer conformation to control architecture in semiconducting polymer/viral capsid assemblies. *Acs Nano* **5**, 7730-7738 (2011).

10 Hu, Y. F., Zandi, R., Anavitarte, A., Knobler, C. M. & Gelbart, W. M. Packaging of a polymer by a viral capsid: The interplay between polymer length and capsid size. *Biophys. J.* **94**, 1428-1436 (2008).

11 Worsdorfer, B., Pianowski, Z. & Hilvert, D. Efficient in vitro encapsulation of protein cargo by an engineered protein container. *J. Am. Chem. Soc.* **134**, 909-911 (2012).

12 Minten, I. J., Hendriks, L. J. A., Nolte, R. J. M. & Cornelissen, J. Controlled encapsulation of multiple proteins in virus capsids. *J. Am. Chem. Soc.* **131**, 17771-17773 (2009).

13 Fiedler, J. D., Brown, S. D., Lau, J. L. & Finn, M. G. RNA-directed packaging of enzymes within virus-like particles. *Angew. Chem., Int. Ed.* **49**, 9648-9651 (2010).

14 Rhee, J. K. *et al.* Colorful virus-like particles: Fluorescent protein packaging by the Q beta capsid. *Biomacromolecules* **12**, 3977-3981 (2011).

15 O'Neil, A., Reichhardt, C., Johnson, B., Prevelige, P. E. & Douglas, T. Genetically programmed in vivo packaging of protein cargo and its controlled release from bacteriophage P22. *Angew. Chem., Int. Ed.* **50**, 7425-7428 (2011).

16 Reichhardt, C. *et al.* Templated assembly of organic-inorganic materials using the core shell structure of the P22 bacteriophage. *Chem. Commun.* **47**, 6326-6328 (2011).

17 Patterson, D. P., Prevelige, P. E. & Douglas, T. Nanoreactors by programmed enzyme encapsulation inside the capsid of the bacteriophage P22. *Acs Nano* **6**, 5000-5009 (2012).

18 Patterson, D. P. *et al.* Virus-like particle nanoreactors: Programmed encapsulation of the thermostable CelB glycosidase inside the P22 capsid. *Soft Matter* **8**, 10158-10166 (2012).

19 Chen, C. *et al.* Nanoparticle-templated assembly of viral protein cages. *Nano Lett.* **6**, 611-615 (2006).

20 Tsvetkova, I. *et al.* Pathway switching in templated virus-like particle assembly. *Soft Matter* **8**, 4571-4577 (2012).

21 Dixit, S. K. *et al.* Quantum dot encapsulation in viral capsids. *Nano Lett.* **6**, 1993-1999 (2006).

22 Swift, J., Butts, C. A., Cheung-Lau, J., Yerubandi, V. & Dmochowski, I. J. Efficient self-assembly of Archaeoglobus fulgidus ferritin around metallic cores. *Langmuir* **25**, 5219-5225 (2009).

23 Valero, E. *et al.* Magnetic nanoparticles-templated assembly of protein subunits: A new platform for carbohydrate-based MRI nanoprobes. *J. Am. Chem. Soc.* **133**, 4889-4895 (2011).

24 Hennequin, B. *et al.* Aqueous near-infrared fluorescent composites based on apoferritin-encapsulated PbS quantum dots. *Advanced Materials* **20**, 3592-+ (2008).

25 Uchida, M. *et al.* Biological containers: Protein cages as multifunctional nanoplatforms. *Advanced Materials* **19**, 1025-1042 (2007).

26 Klem, M. T., Young, M. & Douglas, T. Biomimetic synthesis of photoactive alpha-Fe_2O_3 templated by the hyperthermophilic ferritin from Pyrococus furiosus. *Journal of Materials Chemistry* **20**, 65-67 (2010).

27 Ueno, T. *et al.* Size-selective olefin hydrogenation by a Pd nanocluster provided in an apo-ferritin cage. *Angew. Chem., Int. Ed.* **43**, 2527-2530 (2004).

28 Kramer, R. M., Li, C., Carter, D. C., Stone, M. O. & Naik, R. R. Engineered protein cages for nanomaterial synthesis. *J. Am. Chem. Soc.* **126**, 13282-13286 (2004).

29 Warne, B., Kasyutich, O. I., Mayes, E. L., Wiggins, J. A. L. & Wong, K. K. W. Self assembled nanoparticulate Co : Pt for data storage applications. *Ieee Transactions on Magnetics* **36**, 3009-3011 (2000).

30 Ueno, T. *et al.* Process of accumulation of metal ions on the interior surface of apo-ferritin: Crystal structures of a series of apo-ferritins containing variable auantities of Pd(II) ions. *J. Am. Chem. Soc.* **131**, 5094-5100 (2009).

31 Suzuki, M. *et al.* Preparation and catalytic reaction of Au/Pd bimetallic nanoparticles in Apo-ferritin. *Chem. Commun.*, 4871-4873 (2009).

32 Varpness, Z., Peters, J. W., Young, M. & Douglas, T. Biomimetic synthesis of a H_2 catalyst using a protein cage architecture. *Nano Lett.* **5**, 2306-2309 (2005).

33 Klem, M. T. *et al.* Bio-inspired synthesis of protein-encapsulated CoPt nanoparticles. *Advanced Functional Materials* **15**, 1489-1494 (2005).

34 Knez, M. *et al.* Biotemplate synthesis of 3-nm nickel and cobalt nanowires. *Nano Lett.* **3**, 1079-1082 (2003).

35 Dujardin, E., Peet, C., Stubbs, G., Culver, J. N. & Mann, S. Organization of metallic nanoparticles using tobacco mosaic virus templates. *Nano Lett.* **3**, 413-417 (2003).

36 Abe, S. *et al.* Polymerization of phenylacetylene by rhodium complexes within a discrete space of apo-ferritin. *J. Am. Chem. Soc.* **131**, 6958-6960 (2009).

37 Abedin, M. J., Liepold, L., Suci, P., Young, M. & Douglas, T. Synthesis of a cross-linked branched polymer network in the interior of a protein cage. *J. Am. Chem. Soc.* **131**, 4346-4354 (2009).

38 Liepold, L. O. *et al.* Supramolecular protein cage composite MR contrast agents with extremely efficient relaxivity properties. *Nano Lett.* **9**, 4520-4526 (2009).

39 Ilari, A., Stefanini, S., Chiancone, E. & Tsernoglou, D. The dodecameric ferritin from Listeria innocua contains a novel intersubunit iron-binding site. *Nature Structural Biology* **7**, 38-43 (2000).

40 Stefanini, S., Cavallo, S., Montagnini, B. & Chiancone, E. Incorporation of iron by the unusual dodecameric ferritin from Listeria innocua. *Biochemical Journal* **339**, 775-775 (1999).

41 Allen, M., Willits, D., Mosolf, J., Young, M. & Douglas, T. Protein cage constrained synthesis of ferrimagnetic iron oxide nanoparticles. *Advanced Materials* **14**, 1562-+ (2002).

42 Usselman, R. J. *et al.* Two-component magnetic structure of iron oxide nanoparticles mineralized in Listeria innocua protein cages. *Journal of Applied Physics* **107** (2010).

43 Kang, S., Jolley, C. C., Liepold, L. O., Young, M. & Douglas, T. From metal binding to nanoparticle formation: Monitoring biomimetic iron oxide synthesis within protein cages using mass spectrometry. *Angew. Chem., Int. Ed.* **48**, 4772-4776 (2009).

44 Allen, M., Willits, D., Young, M. & Douglas, T. Constrained synthesis of cobalt oxide nanomaterials in the 12-subunit protein cage from Listeria innocua. *Inorganic Chemistry* **42**, 6300-6305 (2003).

45 Resnick, D. A. *et al.* Magnetic properties of Co_3O_4 nanoparticles mineralized in Listeria innocua Dps. *Journal of Applied Physics* **99** (2006).

46 Iwahori, K. *et al.* Cadmium sulfide nanoparticle synthesis in Dps protein from Listeria innocua. *Chemistry of Materials* **19**, 3105-3111 (2007).

47 Okuda, M. *et al.* Bio-templated CdSe nanoparticle synthesis in a cage shaped protein, Listeria-Dps, and their two dimensional ordered array self-assembly. *Chem. Commun.* **46**, 8797-8799 (2010).

48 Suci, P., Kang, S., Gmur, R., Douglas, T. & Young, M. Targeted Delivery of a Photosensitizer to Aggregatibacter actinomycetemcomitans Biofilm. *Antimicrobial Agents and Chemotherapy* **54**, 2489-2496 (2010).

49 Suci, P. A., Kang, S., Young, M. & Douglas, T. A Streptavidin-Protein Cage Janus Particle for Polarized Targeting and Modular Functionalization. *J. Am. Chem. Soc.* **131**, 9164-+ (2009).

50 Kang, S. *et al.* Controlled assembly of bifunctional chimeric protein cages and composition analysis using noncovalent mass spectrometry. *J. Am. Chem. Soc.* **130**, 16527-16529 (2008).

51 Kim, R., Kim, K. K., Yokota, H. & Kim, S. H. Small heat shock protein of Methanococcus jannaschii, a hyperthermophile. *Proc. Natl. Acad. Sci. U S A* **95**, 9129-9133 (1998).

52 Kim, K. K., Kim, R. & Kim, S. H. Crystal structure of a small heat-shock protein. *Nature* **394**, 595-599 (1998).

53 Flenniken, M. L., Willits, D. A., Brumfield, S., Young, M. J. & Douglas, T. The small heat shock protein cage from Methanococcus jannaschii is a versatile nanoscale platform for genetic and chemical modification. *Nano Lett.* **3**, 1573-1576 (2003).

54 Varpness, Z., Suci, P. A., Ensign, D., Young, M. J. & Douglas, T. Photosensitizer efficiency in genetically modified protein cage architectures. *Chem. Commun.*, 3726-3728 (2009).

55 Johnson, J. E. Virus particle maturation: Insights into elegantly programmed nanomachines. *Current Opinion in Structural Biology* **20**, 210-216 (2010).

56 Parent, K. N. *et al.* P22 coat protein structures reveal a novel mechanism for capsid maturation: Stability without auxiliary proteins or chemical crosslinks. *Structure* **18**, 390-401 (2010).

57 Teschke, C. M., McGough, A. & Thuman-Commike, P. A. Penton release from P22 heat-expanded capsids suggests importance of stabilizing penton-hexon interactions during capsid maturation. *Biophys. J.* **84**, 2585-2592 (2003).

58 Earnshaw, W., Casjens, S. & Harrison, S. C. Assembly of head of bacteriophage P22: x-ray diffraction from heads, proheads and related structures *Journal of Molecular Biology* **104**, 387-410 (1976).

59 Kang, S. *et al.* Implementation of P22 viral capsids as nanoplatforms. *Biomacromolecules* **11**, 2804-2809 (2010).

60 Kang, S., Lander, G. C., Johnson, J. E. & Prevelige, P. E. Development of bacteriophage P22 as a platform for molecular display: Genetic and chemical modifications of the procapsid exterior surface. *Chembiochem* **9**, 514-518 (2008).

61 Teschke, C. M. & Parent, K. N. 'Let the phage do the work': Using the phage P22 coat protein structures as a framework to understand its folding and assembly mutants. *Virology* **401**, 119-130 (2010).

62 Parent, K. N., Suhanovsky, M. M. & Teschke, C. M. Polyhead formation in phage P22 pinpoints a region in coat protien required for conformational switching. *Molecular Microbiology* **65**, 1300-1310 (2007).

63 Shen, L. M., Bao, N. Z., Prevelige, P. E. & Gupta, A. Fabrication of ordered nanostructures of sulfide nanocrystal assemblies over self-assembled genetically engineered P22 coat protein. *J. Am. Chem. Soc.* **132**, 17354-17357 (2010).

64 Qazi, S. *et al.* P22 viral capsids as nanocomposite high-relaxivity MRI contrast agents. *Molecular Pharmaceutics* (2012).

65 Uchida, M. *et al.* Site-directed coordination chemistry with P22 virus-like particles. *Langmuir* **28**, 1998-2006 (2012).

66 Song, Y. J. *et al.* Controlled synthesis of 2-D and 3-D dendritic platinum nanostructures. *J. Am. Chem. Soc.* **126**, 635-645 (2004).

67 Brugger, P. A., Cuendet, P. & Gratzel, M. Ultrafine and specific catalysts affording efficient hydrogen evolution from water under visible-light illumination. *J. Am. Chem. Soc.* **103**, 2923-2927 (1981).

68 Chen, D. H., Yeh, J. J. & Huang, T. C. Synthesis of platinum ultrafine particles in AOT reverse micelles. *Journal of Colloid and Interface Science* **215**, 159-166 (1999).

69 Eklund, S. E. & Cliffel, D. E. Synthesis and catalytic properties of soluble platinum nanoparticles protected by a thiol monolayer. *Langmuir* **20**, 6012-6018 (2004).

70 Zhao, S. Y., Chen, S. H., Wang, S. Y., Li, D. G. & Ma, H. Y. Preparation, phase transfer, and self-assembled monolayers of cubic Pt nanoparticles. *Langmuir* **18**, 3315-3318 (2002).

71 Jiang, D. L. *et al.* Photosensitized hydrogen evolution from water using conjugated polymers wrapped in dendrimeric electrolytes. *J. Am. Chem. Soc.* **126**, 12084-12089 (2004).

72 Keller, P. & Moradpour, A. Is there a particle-size dependence for the mediation by colloidal redox catalysts of the light-induced hydrogen evolution from water. *J. Am. Chem. Soc.* **102**, 7193-7196 (1980).

73 Narayanan, R. & El-Sayed, M. A. Shape-dependent catalytic activity of platinum nanoparticles in colloidal solution. *Nano Lett.* **4**, 1343-1348 (2004).

74 Narayanan, R. & El-Sayed, M. A. Effect of catalytic activity on the metallic nanoparticle size distribution: Electron-transfer reaction between Fe(CN)(6) and thiosulfate ions catalyzed by PVP-platinum nanoparticles. *Journal of Physical Chemistry B* **107**, 12416-12424 (2003).

75 Chen, J. Y., Lim, B., Lee, E. P. & Xia, Y. N. Shape-controlled synthesis of platinum nanocrystals for catalytic and electrocatalytic applications. *Nano Today* **4**, 81-95 (2009).

76 Knez, M. *et al.* Biotemplate synthesis of 3-nm nickel and cobalt nanowires. *Nano Lett.* **3**, 1079-1082 (2003).

77 Rostovtsev, V. V., Green, L. G., Fokin, V. V. & Sharpless, K. B. A stepwise Huisgen cycloaddition process: Copper(I)-catalyzed regioselective "ligation" of azides and terminal alkynes. *Angew. Chem., Int. Ed.* **41**, 2596-+ (2002).

78 Hong, V., Presolski, S. I., Ma, C. & Finn, M. G. Analysis and optimization of copper-catalyzed azide-alkyne cycloaddition for bioconjugation. *Angew. Chem., Int. Ed.* **48**, 9879-9883 (2009).

79 Wang, Q. *et al.* Bioconjugation by copper(I)-catalyzed azide-alkyne 3+2 cycloaddition. *J. Am. Chem. Soc.* **125**, 3192-3193 (2003).

80 Sen Gupta, S. *et al.* Accelerated bioorthogonal conjugation: A practical method for the ligation of diverse functional molecules to a polyvalent virus scaffold. *Bioconjugate Chemistry* **16**, 1572-1579 (2005).

81 Sen Gupta, S., Raja, K. S., Kaltgrad, E., Strable, E. & Finn, M. G. Virus-glycopolymer conjugates by copper(I) catalysis of atom transfer radical polymerization and azide-alkyne cycloaddition. *Chem. Commun.*, 4315-4317 (2005).

82 Prasuhn, D. E., Yeh, R. M., Obenaus, A., Manchester, M. & Finn, M. G. Viral MRI contrast agents: coordination of Gd by native virions and attachment of Gd complexes by azide-alkyne cycloaddition. *Chem. Commun.*, 1269-1271 (2007).

83 Patel, K. G. & Swartz, J. R. Surface functionalization of virus-like particles by direct conjugation using azide-alkyne click chemistry. *Bioconjugate Chemistry* **22**, 376-387 (2011).

84 Zeng, Q. B. *et al.* Chemoselective modification of turnip yellow mosaic virus by Cu(I) catalyzed azide-alkyne 1,3-dipolar cycloaddition reaction and its application in cell binding. *Bioconjugate Chemistry* **22**, 58-66 (2011).

85 Pokorski, J. K., Breitenkamp, K., Liepold, L. O., Qazi, S. & Finn, M. G. Functional virus-based polymer–protein nanoparticles by atom transfer radical polymerization. *J. Am. Chem. Soc.* **133**, 9242-9245 (2011).

86 Wang, J. S. & Matyjaszewski, K. Controlled living radical polymerization: Atom-transfer radical polymerization in the prescence of transition-metal complexes. . *J. Am. Chem. Soc.* **117**, 5614-5615 (1995).

87 Wang, J. S. & Matyjaszewski, K. Controlled living radical polymerization: halogen atom-transfer radical polymerization promoted by a Cu(i)-Cu(ii) redox process. . *Macromolecules* **28**, 7901-7910 (1995).

88 Odian, G. *Principles of polymerization, 4th ed.*, 316-319 (Wiley-Isnterscience, 2004).

89 Matyjaszewski, K. Atom transfer radical polymerization (ATRP): Current status and future perspectives. *Macromolecules* **45**, 4015-4039 (2012).

90 Bontempo, D. & Maynard, H. D. Streptavidin as a macroinitiator for polymerization: In situ protein-polymer conjugate formation. *J. Am. Chem. Soc.* **127**, 6508-6509 (2005).

91 Heredia, K. L. *et al.* In situ preparation of protein: "Smart" polymer conjugates with retention of bioactivity. *J. Am. Chem. Soc.* **127**, 16955-16960 (2005).

92 Nicolas, J., Mantovani, G. & Haddleton, D. M. Living radical polymerization as a tool for the synthesis of polymer-protein/peptide bioconjugates. *Macromolecular Rapid Communications* **28**, 1083-1111 (2007).

93 Krishna, O. D. & Kiick, K. L. Protein- and peptide-modified synthetic polymeric biomaterials. *Biopolymers* **94**, 32-48 (2010).

94 Grover, G. N. & Maynard, H. D. Protein-polymer conjugates: Synthetic approaches by controlled radical polymerizations and interesting applications. *Current Opinion in Chemical Biology* **14**, 818-827 (2010).

95 Klok, H. A. Peptide/protein-synthetic polymer conjugates: quo vadis. *Macromolecules* **42**, 7990-8000 (2009).

96 Thordarson, P., Le Droumaguet, B. & Velonia, K. Well-defined protein-polymer conjugates-synthesis and potential applications. *Applied Microbiology and Biotechnology* **73**, 243-254 (2006).

97 Gao, W. P., Liu, W. G., Christensen, T., Zalutsky, M. R. & Chilkoti, A. In situ growth of a PEG-like polymer from the C terminus of an intein fusion protein improves pharmacokinetics and tumor accumulation. *Proc. Natl. Acad. Sci. U S A* **107**, 16432-16437 (2010).

98 Gao, W. P. *et al.* In situ growth of a stoichiometric PEG-like conjugate at a protein's N-terminus with significantly improved pharmacokinetics. *Proc. Natl. Acad. Sci. U S A* **106**, 15231-15236 (2009).

99 Mann, S. & Ozin, G. A. Synthesis of inorganic materials with complex form. *Nature* **382**, 313-318 (1996).

100 Poliakov, A. *et al.* Macromolecular mass spectrometry and electron microscopy as complementary tools for investigation of the heterogeneity of bacteriophage portal assemblies. *Journal of Structural Biology* **157**, 371-383 (2007).

101 Sobott, F., Benesch, J. L., Vierling, E. & Robinson, C. V. Subunit exchange of multimeric protein complexes. Real-time monitoring of subunit exchange between small heat shock proteins by using electrospray mass spectrometry. *Journal of Biological Chemistry* **277**, 38921-38929 (2002).

102 Fenn, J. B., Mann, M., Meng, C. K., Wong, S. F. & Whitehouse, C. M. Electrospray ionization for mass spectrometry of large biomolecules. *Science* **246**, 64-71 (1989).

103 Tanaka, K. *et al.* Protein and polymer analyses up to m/z 100 000 by laser ionization time-of-flight mass spectrometry. *Rapid Commun Mass Spectrom.* **2**, 151-153 (1988).

104 Benesch, J. L. & Robinson, C. V. Mass spectrometry of macromolecular assemblies: preservation and dissociation. *Current Opinion in Structural Biology* **16**, 245-251 (2006).

105 Bothner, B. & Siuzdak, G. Electrospray ionization of a whole virus: analyzing mass, structure, and viability. *Chembiochem* **5**, 258-260 (2004).

106 Heck, A. J. R. & van den Heuvel, R. H. H. Investigation of intact protein complexes by mass spectrometry. *Mass Spectrometry Reviews* **23**, 368-389 (2004).

107 Dass, A., Stevenson, A., Dubay, G. R., Tracyt, J. B. & Murray, R. W. Nanoparticle MALDI-TOF mass spectrometry without fragmentation: Au-25(SCH2CH2Ph)(18) and mixed monolayer Au-25(SCH2CH2Ph)(18-x)(L)(x). *J. Am. Chem. Soc.* **130**, 5940-5946 (2008).

108 Tracy, J. B. *et al.* Poly(ethylene glycol) ligands for high-resolution nanoparticle mass spectrometry. *J. Am. Chem. Soc.* **129**, 6706-+ (2007).

109 Chaki, N. K., Negishi, Y., Tsunoyama, H., Shichibu, Y. & Tsukuda, T. Ubiquitous 8 and 29 kDa gold: Alkanethiolate cluster compounds: Mass-spectrometric determination of molecular formulas and structural implications. *J. Am. Chem. Soc.* **130**, 8608-+, doi:10.1021/ja8005379 (2008).

110 Kitagawa, N., Mazon, H., Heck, A. J. R. & Wilkens, S. Stoichiometry of the peripheral stalk subunits E and G of yeast V-1-ATPase determined by mass spectrometry. *Journal of Biological Chemistry* **283**, 3329-3337 (2008).

111 Esteban, O. *et al.* Stoichiometry and localization of the stator subunits E and G in Thermus thermophilus H+-ATPase/synthase. *Journal of Biological Chemistry* **283**, 2595-2603 (2008).

112 Fandrich, M. *et al.* Observation of the noncovalent assembly and disassembly pathways of the chaperone complex MtGimC by mass spectrometry. *Proc. Natl. Acad. Sci. U S A* **97**, 14151-14155 (2000).

113 Last, A. M. & Robinson, C. V. Protein folding and interactions revealed by mass spectrometry. *Current Opinion in Chemical Biology* **3**, 564-570 (1999).

114 Chen, C. H. B. & Sigman, D. S. Nuclease activity of 1,10-phenanthroline copper - sequence-specific targeting. . *Proc. Natl. Acad. Sci. U S A* **83**, 7147-7151 (1986).

115 Kang, S., Hawkridge, A. M., Johnson, K. L., Muddiman, D. C. & Prevelige, P. E. Identification of subunit-subunit interactions in bacteriophage P22 procapsids by chemical cross-linking and mass spectrometry. *Journal of Proteome Research* **5**, 370-377 (2006).

116 Esswein, M. J. & Nocera, D. G. Hydrogen production by molecular photocatalysis. *Chemical Reviews* **107**, 4022-4047 (2007).

117 Gratzel, M. Artificial photosynthesis - water cleavage into hydrogen and oxygen by visible-light. *Accounts of Chemical Research* **14**, 376-384 (1981).

118 Greenbaum, E. Interfacial photoreaction at the photosynthetic membrane interface: an upper limit for the number of platinum atoms required to form a hydrogen-evolving platinum. catalyst *Journal of Physical Chemistry* **92**, 4571-4574 (1988).

119 Tinker, L. L. *et al.* Visible light induced catalytic water reduction without an electron relay. *Chemistry-a European Journal* **13**, 8726-8732 (2007).

120 Lemaire, D., Marie, G., Serani, L. & Laprevote, O. Stabilization of gas-phase noncovalent macromolecular complexes in electrospray mass spectrometry using aqueous triethylammonium bicarbonate buffer. *Analytical Chemistry* **73**, 1699-1706 (2001).

121 Tahallah N., P. M., Maier CS., Heck AJ. The effect of the source pressure on the abundance of ions of noncovalent protein assemblies in an electrospray ionization orthogonal time-of-flight instrument. *Rapid Commun Mass Spectrom.* **15**, 596-601 (2001).

122 Wilenzic.R. M, Russell, D. C., Morriss, R. H. & Marshall, S. W. Uniform microcrystals of platinum and gold. . *Journal of Chemical Physics* **47**, 533-& (1967).

123 Klem, M. T., Mosolf, J., Young, M. & Douglas, T. Photochemical mineralization of europium, titanium, and iron oxyhydroxide nanoparticies in the ferritin protein cage. *Inorganic Chemistry* **47**, 2237-2239 (2008).

124 Alkordi, M. H., Liu, Y., Larsen, R. W., Eubank, J. F. & Eddaoudi, M. Zeolite-like metal-organic frameworks as platforms for applications: on metalloporphyrin-based catalysts. *J. Am. Chem. Soc.* **130**, 12639-12641 (2008).

125 Li, Q. W. *et al.* Docking in metal-organic frameworks. *Science* **325**, 855-859 (2009).

126 Tor, Y. Metal-containing oligomers, dendrimers and biopolymers. *Comptes Rendus Chimie* **6**, 755-766 (2003).

127 Horcajada, P. *et al.* Flexible porous metal-organic frameworks for a controlled drug delivery. *J. Am. Chem. Soc.* **130**, 6774-6780 (2008).

128 Rieter, W. J., Pott, K. M., Taylor, K. M. L. & Lin, W. B. Nanoscale coordination polymers for platinum-based anticancer drug delivery. *J. Am. Chem. Soc.* **130**, 11584-+ (2008).

129 Beck, J. B. & Rowan, S. J. Multistimuli, multiresponsive metallo-supramolecular polymers. *J. Am. Chem. Soc.* **125**, 13922-13923 (2003).

130 Kaltgrad, E. *et al.* On-virus construction of polyvalent glycan ligands for cell-surface receptors. *J. Am. Chem. Soc.* **130**, 4578-+ (2008).

131 Datta, A. *et al.* High relaxivity gadolinium hydroxypyridonate-viral capsid conjugates: Nanosized MRI contrast agents. *J. Am. Chem. Soc.* **130**, 2546-2552 (2008).

132 Soto, C. M. *et al.* Fluorescent signal amplification of carbocyanine dyes using engineered viral nanoparticles. *J. Am. Chem. Soc.* **128**, 5184-5189 (2006).

133 Huang, X. L. *et al.* Self-assembled virus-like particles with magnetic cores. *Nano Lett.* **7**, 2407-2416 (2007).

134 Suci, P. A., Varpness, Z., Gillitzer, E., Douglas, T. & Young, M. Targeting and photodynamic killing of a microbial pathogen using protein cage Architectures functionalized with a photosensitizer. *Langmuir* **23**, 12280-12286 (2007).

135 Gupta, S. S. *et al.* Accelerated bioorthogonal conjugation: A practical method for the ligation of diverse functional molecules to a polyvalent virus scaffold. *Bioconjugate Chemistry* **16**, 1572-1579 (2005).

136 Riklin, M., Tran, D., Bu, X. H., Laverman, L. E. & Ford, P. C. The synthesis of the ligand 5-bis[2-(3,5-dimethyl-1-pyrazolyl)ethyl]amine-1,10-phenanthroline and of its ruthenium(II) and rhenium(I) complexes: Binuclear species with Cu(I) and some photophysical properties. *Journal of the Chemical Society-Dalton Transactions*, 1813-1819 (2001).

137 Chan, T. R., Hilgraf, R., Sharpless, K. B. & Fokin, V. V. Polytriazoles as copper(I)-stabilizing ligands in catalysis. *Org. Lett.* **6**, 2853-2855 (2004).

138 Waite, J. H. & Benedict, C. V. Assay of dihyroxyphenyalanine (DOPA) in invertebrate structural proteins. . *Methods in Enzymology* **107**, 397-413 (1984).

139 Schlick, T. L., Ding, Z. B., Kovacs, E. W. & Francis, M. B. Dual-surface modification of the tobacco mosaic virus. *J. Am. Chem. Soc.* **127**, 3718-3723 (2005).

140 Chen, D. H. *et al.* Structural basis for scaffolding-mediated assembly and maturation of a dsDNA virus. *Proc. Natl. Acad. Sci. U S A* **108**, 1355-1360 (2011).

141 Mantovani, G. *et al.* Design and synthesis of N-maleimido-functionalized hydrophilic polymers via copper-mediated living radical polymerization: A suitable alternative to PEGylation chemistry. *J. Am. Chem. Soc.* **127**, 2966-2973 (2005).

142 Peeler, J. C. *et al.* Genetically encoded initiator for polymer growth from proteins. *J. Am. Chem. Soc.* **132**, 13575-13577 (2010).

143 Fevola, M. J., Bridges, J. K., Kellum, M. G., Hester, R. D. & McCormick, C. L. pH-responsive ampholytic terpolymers of acrylamide, sodium 3-acrylamido-3-methylbutanoate, and (3-acrylamidopropyl)trimethylammonium chloride. I. Synthesis and characterization. *Journal of Polymer Science Part a-Polymer Chemistry* **42**, 3236-3251 (2004).

144 Depp, V., Alikhani, A., Grammer, V. & Lele, B. S. Native protein-initiated ATRP: A viable and potentially superior alternative to PEGylation for stabilizing biologics. *Acta Biomaterialia* **5**, 560-569 (2009).

145 de la Escosura, A., Nolte, R. J. M. & Cornelissen, J. Viruses and protein cages as nanocontainers and nanoreactors. *Journal of Materials Chemistry* **19**, 2274-2278 (2009).

146 Aniagyei, S. E., DuFort, C., Kao, C. C. & Dragnea, B. Self-assembly approaches to nanomaterial encapsulation in viral protein cages. *Journal of Materials Chemistry* **18**, 3763-3774 (2008).

147 Lucon, J. *et al.* A click chemistry based coordination polymer inside small heat shock protein. *Chem. Commun.* **46**, 264-266 (2010).

148 Tuma, R., Prevelige, P. E. & Thomas, G. J. Mechanism of capsid maturation in a double-stranded DNA virus. *Proc. Natl. Acad. Sci. U S A* **95**, 9885-9890 (1998).

149 Alidedeoglu, A. H., York, A. W., Rosado, D. A., McCormick, C. L. & Morgan, S. E. Bioconjugation of D-glucuronic acid sodium salt to well-defined primary amine-containing homopolymers and block copolymers. *Journal of Polymer Science Part a-Polymer Chemistry* **48**, 3052-3061 (2010).

150 Weinstein, J. N., Yoshikami, S., Henkart, P., Blumenthal, R. & Hagins, W. A. Liposome-cell interaction: Transfer and intracellular release of a trapped fluorescent marker *Science* **195**, 489-492 (1977).

151 Chen, R. F. & Knutson, J. R. Mechanism of fluorescence concentration quenching of carboxyfluorescein in liposomes: Energy transfer to nonfluorescent dimers *Analytical Biochemistry* **172**, 61-77 (1988).

152 Allen, M. *et al.* Paramagnetic viral nanoparticles as potential high-relaxivity magnetic resonance contrast agents. *Magnetic Resonance in Medicine* **54**, 807-812 (2005).

153 Liepold, L. *et al.* Viral capsids as MRI contrast agents. *Magnetic Resonance in Medicine* **58**, 871-879 (2007).

154 Anderson, E. A. *et al.* Viral nanoparticles donning a paramagnetic coat: Conjugation of MRI contrast agents to the MS2 capsid. *Nano Lett.* **6**, 1160-1164 (2006).

155 Hooker, J. M., Datta, A., Botta, M., Raymond, K. N. & Francis, M. B. Magnetic resonance contrast agents from viral capsid shells: A comparison of exterior and interior cargo strategies. *Nano Lett.* **7**, 2207-2210 (2007).

156 Dunand, F. A., Borel, A. & Helm, L. Gd(III) based MRI contrast agents: Improved physical meaning in a combined analysis of EPR and NMR data? *Inorganic Chemistry Communications* **5**, 811-815 (2002).

157 Mulder, W. J. M., Strijkers, G. J., van Tilborg, G. A. F., Griffioen, A. W. & Nicolay, K. Lipid-based nanoparticles for contrast-enhanced MRI and molecular imaging. *NMR in Biomedicine* **19**, 142-164 (2006).

158 Ghaghada, K. B. *et al.* New dual mode gadolinium nanoparticle contrast agent for magnetic resonance imaging. *Plos One* **4**, 1-7 (2009).

159 Karfeld-Sulzer, L. S., Waters, E. A., Davis, N. E., Meade, T. J. & Barron, A. E. Multivalent protein polymer MRI contrast agents: Controlling relaxivity via modulation of amino acid sequence. *Biomacromolecules* **11**, 1429-1436 (2010).

160 Schuhmanngiampieri, G., Schmittwillich, H., Frenzel, T., Press, W. R. & Weinmann, H. J. In vivo and in vitro evaluation of Gd-DTPA-polylysine as a macromolecular contrast agent for magnetic resonance imaging. *Investigative Radiology* **26**, 969-974 (1991).

161 Ananta, J. S. *et al.* Geometrical confinement of gadolinium-based contrast agents in nanoporous particles enhances T(1) contrast. *Nature Nanotech.* **5**, 815-821 (2010).

162 Mitchell, D. G. & Cohen, M. *MRI principles*. 2 edn, 10-12 (Saunders, 2004).

163 Averick, S. *et al.* ATRP under biologically relevant conditions: grafting from a protein. *Acs Macro Letters* **1**, 6-10 (2012).

164 Zarafshani, Z., Obata, T. & Lutz, J. F. Smart PEGylation of Trypsin. *Biomacromolecules* **11**, 2130-2135 (2010).

165 Pyun, J., Kowalewski, T. & Matyjaszewski, K. Synthesis of polymer brushes using atom transfer radical polymerization. *Macromolecular Rapid Communications* **24**, 1043-1059 (2003).

166 Boyer, C. *et al.* Well-defined protein-polymer conjugates via in situ RAFT polymerization. *J. Am. Chem. Soc.* **129**, 7145-7154 (2007).

167 Tauer, K., Gau, D., Schulze, S., Volkel, A. & Dimova, R. Thermal property changes of poly(N-isopropylacrylamide) microgel particles and block copolymers. *Colloid and Polymer Science* **287**, 299-312 (2009).

168 Kizhakkedathu, J. N., Norris-Jones, R. & Brooks, D. E. Synthesis of well-defined environmentally responsive polymer brushes by aqueous ATRP. *Macromolecules* **37**, 734-743 (2004).

169 Ye, J. & Narain, R. Water-assisted atom transfer radical polymerization of N-isopropylacrylamide: Nature of solvent and temperature. *The Journal of Physical Chemistry B* **113**, 676-681 (2008).

170 Matyjaszewski, K. & Xia, J. H. Atom transfer radical polymerization. *Chemical Reviews* **101**, 2921-2990 (2001).

171 York, A. W. *et al.* Facile synthesis of multivalent folate-block copolymer conjugates via aqueous RAFT polymerization: Targeted delivery of siRNA and subsequent gene suppression. *Biomacromolecules* **10**, 936-943 (2009).

172 Paslay, L. C. *et al.* Antimicrobial poly(methacrylamide) derivatives prepared via aqueous RAFT polymerization exhibit biocidal efficiency dependent upon cation structure. *Biomacromolecules* **13**, 2472-2482 (2012).

173 Zadvornyy, O. A. *et al.* Photo-induced H-2 production by NiFe -hydrogenase from T. roseopersicina covalently linked to a Ru(II) photosensitizer. *Journal of Inorganic Biochemistry* **106**, 151-155 (2012).

174 Cropek, D. M. *et al.* A novel ruthenium(ii)-cobaloxime supramolecular complex for photocatalytic H_2 evolution: Synthesis, characterisation and mechanistic studies. *Dalton Transactions* **41**, 13060-13073 (2012).

175 Dempsey, J. L., Brunschwig, B. S., Winkler, J. R. & Gray, H. B. Hydrogen evolution catalyzed by cobaloximes. *Accounts of Chemical Research* **42**, 1995-2004 (2009).

176 Miura, A. *et al.* Floating nanodot gate memory devices based on biomineralized inorganic nanodot array as a storage node. *Japanese Journal of Applied Physics Part 2-Letters & Express Letters* **45**, L1-L3 (2006).

177 Kim, K. K. *et al.* Purification, crystallization, and preliminary x-ray crystallographic data analysis of small heat shock protein homolog from Methanococcus jannaschii, a hyperthermophile. *Journal of Structural Biology* **121**, 76-80 (1998).

178 Lo, K. K. W., Ng, D. C. M. & Chung, C. K. First examples of luminescent cyclometalated iridium(III) complexes as labeling reagents for biological substrates. *Organometallics* **20**, 4999-5001 (2001).

179 Sullivan, B. P., Salmon, D. J. & Meyer, T. J. Mixed phosphine 2-2'-bipyridine complexes of ruthenium. *Inorganic Chemistry* **17**, 3334-3341 (1978).

180 Ellis, C. D., Margerum, L. D., Murray, R. W. & Meyer, T. J. Oxidative electropolymerization of polypyridyl complexes of ruthenium. . *Inorganic Chemistry* **22**, 1283-1291 (1983).

181 Evans, I. P., Spencer, A. & Wilkinso.G. Dichlorotetrakis(dimethyl sulphoxide)ruthenium(ii) and its use as a source material for some new ruthenium(ii) complexes. . *Journal of the Chemical Society-Dalton Transactions*, 204-209 (1973).

182 Szafran, Z., Pike, R. M. & Singh, M. M. *Microscale inorganic chemistry: A comprehensive laboratory experience*. 218-224 (John Wiley and Sons, 1991).

183 Wong, R. & Dolman, S. J. Isothiocyanates from tosyl chloride mediated decomposition of in situ generated dithiocarbamic acid salts. *Journal of Organic Chemistry* **72**, 3969-3971 (2007).

184 Keller, K. A., Guo, J., Punna, S. & Finn, M. G. A thermally-cleavable linker for solid-phase synthesis. *Tetrahedron Letters* **46**, 1181-1184 (2005).